

CHEMIA

**STUDIA
UNIVERSITATIS BABEȘ-BOLYAI
CHEMIA**

4/2018

EDITORIAL BOARD OF STUDIA UNIVERSITATIS BABEȘ-BOLYAI CHEMIA

ONORARY EDITOR:

IONEL HAIDUC - Member of the Romanian Academy

EDITOR-IN-CHIEF:

LUMINIȚA SILAGHI-DUMITRESCU

EXECUTIVE EDITOR:

CASTELIA CRISTEA

EDITORIAL BOARD:

PAUL ȘERBAN AGACHI, Babeș-Bolyai University, Cluj-Napoca, Romania

LIVAIN BREAU, UQAM University of Quebec, Montreal, Canada

HANS JOACHIM BREUNIG, Institute of Inorganic and Physical Chemistry,
University of Bremen, Bremen, Germany

MIRCEA DIUDEA, Babeș-Bolyai University, Cluj-Napoca, Romania

JEAN ESCUDIE, HFA, Paul Sabatier University, Toulouse, France

ION GROSU, Babeș-Bolyai University, Cluj-Napoca, Romania

EVAMARIE HEY-HAWKINS, University of Leipzig, Leipzig, Germany

FLORIN DAN IRIMIE, Babeș-Bolyai University, Cluj-Napoca, Romania

FERENC KILAR, University of Pecs, Pecs, Hungary

BRUCE KING, University of Georgia, Athens, Georgia, USA

ANTONIO LAGUNA, Department of Inorganic Chemistry, ICMA, University of
Zaragoza, Zaragoza, Spain

JURGEN LIEBSCHER, Humboldt University, Berlin, Germany

KIERAN MOLLOY, University of Bath, Bath, UK

IONEL CĂȚĂLIN POPESCU, Babeș-Bolyai University, Cluj-Napoca, Romania

CRISTIAN SILVESTRU, Babeș-Bolyai University, Cluj-Napoca, Romania

<http://chem.ubbcluj.ro/~studiachemia/>; studiachemia@chem.ubbcluj.ro

http://www.studia.ubbcluj.ro/serii/chemia/index_en.html

YEAR
MONTH
ISSUE

Volume 63 (LXIII) 2018
DECEMBER
4

STUDIA UNIVERSITATIS BABEȘ-BOLYAI CHEMIA

4

ISSUE DOI:10.24193/subbchem.2018.4

STUDIA UBB EDITORIAL OFFICE: B.P. Hasdeu no. 51, 400371 Cluj-Napoca, Romania,
Phone + 40 264 405352, www.studia.ubbcluj.ro

CUPRINS – CONTENT – SOMMAIRE – INHALT

- ADRIAN PATRUT, NICOLAE ROBU, VASILE SAVU, ROXANA T. PATRUT, LASZLO RAKOSY, ILEANA-ANDREEA RAȚIU, DANIEL A. LOWY, DRAGOS MARGINEANU, KARL F. VON REDEN, Radiocarbon Investigation of the Pedunculate Oak of Botosana, Romania 7
- ROXANA NICOLA (CRIȘAN), OTILIA COSTIȘOR, CĂTĂLIN IANĂȘI, RADU LAZĂU, LIVIU SĂCĂRESCU, DANIEL NIŽNANSKY, AUREL ERCUȚA, ANA-MARIA PUTZ, CECILIA SAVII, Fractal Surface Maghemite Nanoparticles Prepared by Co-precipitation: the Influence of Iron Concentration and Base Nature 15
- DANA MARIA SABOU, IOAN BĂLDEA, Kinetic and Mechanistic Features of the Thiolactic Acid Oxidation by Chromium(VI) in Acidic Environment 31
- CARMEN SACALIS, FIRUTA GOGA, CRISTINA SOMESAN, Complexes of Selected Transition Metal Ions with *N*-Modified Glycine as Ligand 51

RADOSTINA ALEXANDROVA, RENI KALFIN, RAMONA TUDOSE, EUGENIA FAGADAR-COSMA, Comparative Cytotoxicity Assays Performed Using a Free Porphyrin and its Zn(II), Co(II) and Cu(II) Complexes. Influence of Optical and Aggregation Properties.....	65
CIPRIAN-VALENTIN MIHALI, CĂLIN FLAVIU LADAȘIU CIOLACU, LUCIAN FRENȚESCU, CONSTANTIN-MARIAN PETRESCU, IULIA MÂNDRUȚIU, DORIN BECHET, TIBERIU NISTOR, AUREL ARDELEAN, GHEORGHE BENGA, Determination of Plasma Phenylalanine Concentration by Two Dimensional Thin Layer Chromatography and High Performance Liquid Chromatography in Relation with Diagnosis of Phenylketonuria	79
CRISTIAN T. MATEA, TEODORA MOCAN, FLAVIU TABARAN, TEODORA POP, OFELIA MOSTEANU, LUCIAN MOCAN, CLAUDIU ZDREHUS, Evaluation of Capping Agents for Silver Nanoparticles	95
IRINA C. CHIȘ, ANDRA CLICHICI, RAMONA SIMEDREA, REMUS MOLDOVAN, VIORICA (LEORDEAN) LAZAR, SIMONA CLICHICI, OVIDIU ONIGA, CRISTINA NASTASĂ, The Effects of a New Chromenyl-methylene-thiazolidine-2,4-dione in Alleviating Oxidative Stress in a Rat Model of Streptozotocin-Induced Diabetes	103
ALINA DONICI, EMESE GAL, CLAUDIA CIMPOIU, CLAUDIU IOAN BUNEA, FLORIN DUMITRU BORA, Multi-Element Composition of Red and White Wines from Bujoru, Smulti and Oancea Wine Center, Romania	113
ANA-ANDREEA CIOCA, SORIN DANIEL DAN, VLĂDUȚA MĂRIOARA LUPĂU, LIORA MIHAELA COLOBATIU, MARIAN MIHAIU, The Effect of High Pressure Processing on Major Structural Proteins of Rainbow Trout Fish Fillets	129
MARIA GOREA, LILIANA BIZO, ADRIANA ȚĂNASE, Physical and Mechanical Properties of Some Plaster Mortars with Oxide Wastes..	137
SORIN-AUREL DORNEANU, ALEXANDRU-ANDREI AVRAM, ALEXANDRU-HORAȚIU MĂRINCAȘ, NICOLETA COTOLAN, TIBERIU FRENȚIU, PETRU ILEA, Influence of the Composition Evolution of Waste Computer Motherboards on their Recycling Strategy	147
IOAN AUREL CHERECHES, IOAN PETEAN, GERTRUD-ALEXANDRA PALTINEAN, AURORA MOCANU, LIANA MURESAN, GEORGE ARGHIR, MARIA TOMOAI-A-COTISEL, Airborne Particles Pollution in Dej City.....	159

DRAGICA BOJOVIĆ, MIOMIR ŠOŠKIĆ, VANJA TADIĆ, Comparative Study of Chemical Composition of the Essential Oils from <i>Satureja Cuneifolia</i> Ten. and <i>Satureja Montana</i> L., <i>Lamiaceae</i> Collected at National Park Lovćen, Montenegro.....	167
GULZIYA SEILKHANOVA, AKMARAL RAKHYM, ALEXANDRA CSAVDARI, Preliminary Assessment of Modified Kazakh Natural Zeolites as Possible Sorbents for MnO_4^- Removal from Aqueous Solutions	181

Studia Universitatis Babes-Bolyai Chemia has been selected for coverage in Thomson Reuters products and custom information services. Beginning with V. 53 (1) 2008, this publication is indexed and abstracted in the following:

- Science Citation Index Expanded (also known as SciSearch®)
- Chemistry Citation Index®
- Journal Citation Reports/Science Edition

RADIOCARBON INVESTIGATION OF THE PEDUNCULATE OAK OF BOTOSANA, ROMANIA

ADRIAN PATRUT^{a,*}, NICOLAE ROBU^b, VASILE SAVU^b,
ROXANA T. PATRUT^{a,c}, LASZLO RAKOSY^c, ILEANA-ANDREEA RAȚIU^a,
DANIEL A. LOWY^d, DRAGOS MARGINEANU^a, KARL F. VON REDEN^e

ABSTRACT. The article discloses the AMS (accelerator mass spectrometry) radiocarbon dating results of the pedunculate oak of Botoșana. Four wood samples were extracted from its trunk. Five segments extracted from these samples were analyzed by AMS radiocarbon. Their radiocarbon dates were found to be between 161 ± 21 BP and 260 ± 20 BP. These values correspond to calibrated ages of 235 – 365 years. The dating results extrapolated to the geometric center of the trunk indicate an age of 645 ± 50 years for the oak of Botoșana.

Keywords: AMS radiocarbon dating, *Quercus robur*, dendrochronology, age determination.

INTRODUCTION

The pedunculate oak (*Quercus robur* L.), also called European oak or English oak, belongs to the family Fagaceae and is native to Europe, western Asia and northern Africa. This upright, columnar tree is typically 20-30 m tall, in exceptional cases reaching 40-50 m, and has a diameter up to 3-4 m [1,2]. The pedunculate oak is considered one of the most long-lived European trees.

^a Babeș-Bolyai University, Faculty of Chemistry and Chemical Engineering, 11 Arany Janos, RO-400028, Cluj-Napoca, Romania.

* Corresponding author: apatrut@gmail.com

^b Technological High School "Ștefan cel Mare", 526 Principală, RO-727100, Cajvana, Romania.

^c Babeș-Bolyai University, Faculty of Biology and Geology, 44 Republicii, RO-400015, Cluj-Napoca, Romania.

^d *Valor Hungariae*, Dept. of Science and Innovation, 4 Nagysándor József, 1054 Budapest, Hungary.

^e NOSAMS Facility, Dept. of Geology & Geophysics, Woods Hole Oceanographic Institution, Woods Hole, MA 02543, U.S.A.

In 2005, we started a long term research for elucidating several controversial aspects concerning the African baobab. The research is based on our new approach which enables to investigate and date standing live specimens. This approach consists of AMS radiocarbon dating of tiny wood samples collected from different areas of such trees [3-8]. We extended our research by also investigating individuals which belong to other angiosperm species, including trees from Romania.

Romania hosts several trees which have reached large dimensions and old ages. We investigated and dated by radiocarbon some remains of the historic oak of Țebea [9], the large pedunculate oak of Cajvana [10], the old black poplar of Mocod and the big grey poplar of Rafaila [11], and the old ash of Aiton [12].

Here we present the AMS radiocarbon dating results of another old Romanian tree, namely the pedunculate oak of Botoșana.

RESULTS AND DISCUSSION

The pedunculate oak of Botoșana and its area. The large oak is located in the garden of a privately-owned house in the commune Botoșana, Suceava county, at 37 km W of Suceava, in the north-eastern part of Romania. Its GPS coordinates are 47°40.690' N, 025°56.52' E and the altitude is 488 m. The mean annual rainfall in the area is around 579 mm (Suceava station). The oak of Botoșana is located at only 4 km SW from the pedunculate oak of Cajvana which is the largest and oldest oak in Romania.

The oak of Botoșana has today a maximum height of 22.5 m with a broken top and the circumference at breast height (cbh; at 1.30 m above mean ground level) is 9.14 m. Its circumference at ground level is 9.38 m, reaching a maximum value of 10.45 m at the height of 2.80 m. The calculated overall wood volume is 55 m³, out of which the trunk has 40 m³.

The very irregular trunk has many sinuosities. Seven primary branches emerge from the trunk at different heights, some of them having diameters up to 1 m. The horizontal dimensions of the remaining canopy are 18.3 (NS) x 21.2 (WE) m. A photograph taken around 1900 shows that the height of the oak exceeded 30 m and it had a much larger canopy. The tree was struck by lightning in the first half of the 20th century. The oak is in a state of decline which started more than a century ago. It has many dry branches and it is suffering from a complex disease called "chronic oak dieback or decline". In this disease, several biotic and abiotic agents interact and bring about a severe deterioration of the tree condition [13]. The percentage of dry branches in the canopy has increased continuously from 5% in 1900 (**Figure 1a**) to almost 40% today (**Figure 1b**). The Romanian Academy nominated the Botoșana oak as a Monument of Nature.

Wood samples. A number of four wood samples were extracted from the outer part of the tree around the circumference. The four samples (labelled 1 to 4) have lengths between 0.51 and 0.77 m. The heights of the sampling points were between 1.70 and 2.10 m. The deepest end of each sample (marked as 1a, 2a, 3a and 4b), as well as an intermediate segment (marked 4a) were extracted for radiocarbon dating.

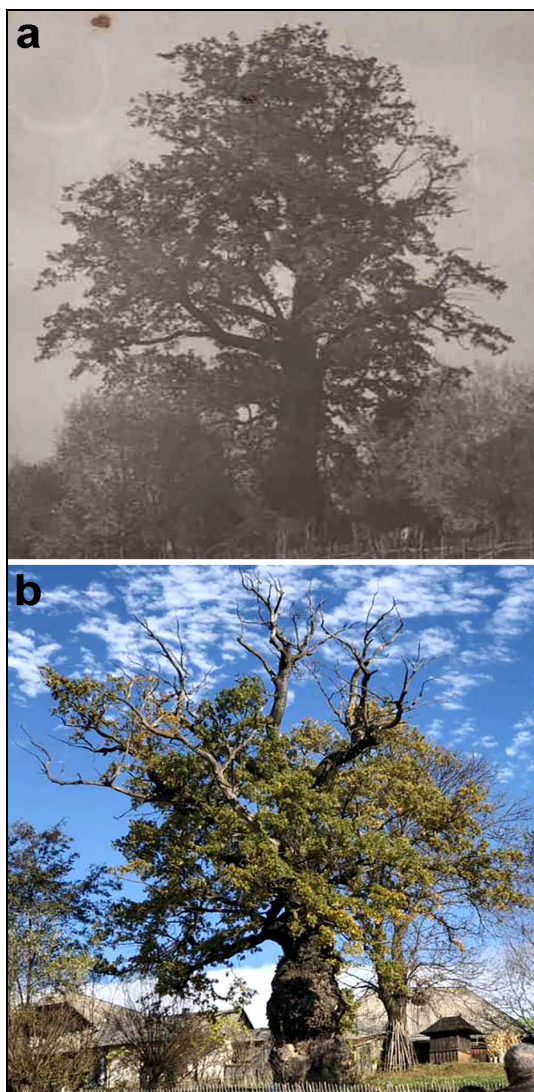


Figure 1. a. General view of the oak of Botoșana on a photograph taken around 1900; b. The oak of Botoșana in 2018.

AMS results and calibrated ages. Radiocarbon dates of the deepest segments extracted from the four samples and also of another segment of sample 4, are listed in Table 1. Radiocarbon dates and errors were rounded to the nearest year. Radiocarbon dates are expressed in ^{14}C yr BP (radiocarbon years before present, i.e., before the reference year AD 1950).

Calibrated (cal) ages, expressed in calendar years, are also shown in Table 1. The $1-\sigma$ probability distribution was selected to derive calibrated age ranges. For the oldest sample segment 4b, the $1-\sigma$ distribution corresponds to one range of calendar years. For the other four segments, the $1-\sigma$ distribution corresponds to three or four ranges of calendar years. For these segments, the confidence interval of one range is considerably greater than that of the others; therefore, it was selected as the cal AD range of the segment for the purpose of this discussion. For obtaining single calendar age values of sample segments, we derived a mean calendar age of each segment from the selected range (marked in bold). Calendar ages of segments represent the difference between AD 2018 and the mean value of the selected range, with the corresponding error. Calendar ages and errors were rounded to the nearest 5 yr.

Table 1. AMS radiocarbon dating results and calibrated calendar ages of samples/segments collected from the oak of Botoșana.

Sample (Segment) code	Depth ¹ [height ²] (10^{-2} m)	Radiocarbon date [error] (^{14}C yr BP)	Cal AD ranges $1-\sigma$ [confidence interval]	Sample age [error] (cal yr)
1a	51 [195]	161 [± 21]	1670-1685 [10.5%] 1732-1778 [38.8%] 1798-1808 [7.1%] 1928-1942 [11.8%]	265 [± 25]
2a	53 [185]	172 [± 23]	1669-1682 [12.1%] 1736-1781 [41.0%] 1798-1805 [5.6%] 1935-1946 [9.5%]	260 [± 20]
3a	56 [170]	203 [± 26]	1658-1678 [19.2%] 1764-1800 [33.4%] 1940-... [15.6%]	235 [± 20]
4a	55 [210]	175 [± 22]	1668-1682 [12.7%] 1736-1782 [39.5%] 1798-1804 [5.4%] 1936-1948 [10.5%]	260 [± 15]
4b	77 [210]	260 [± 20]	1640-1664 [68.2%]	365 [± 10]

¹ Depth in the wood from the sampling point.

² Height above ground level.

Dating results of samples (segments). The deepest part/end of the collected samples, i.e. 1a, 2a, 3a and 4b, have radiocarbon dates between 161 ± 21 BP and 260 ± 20 BP. These values correspond to calibrated ages between 235 ± 20 and 365 ± 10 yr.

The calibration, namely the conversion of radiocarbon dates into calendar ages, can be discussed in particular cases. Thus, the calibration of wood samples with calendar/dendro ages in the time frame AD 1640 – 1950 shows some uncertainties. In such cases, the calibration of one radiocarbon date may result in up to four, five or six calendar age ranges. This is due to the so-called “Suess effect”, which expresses the significant variation of the atmospheric radiocarbon concentration due to the combustion of fossil fuels [14,15].

Age of the oak of Botoșana. The radial increment of trees, measured by the radial growth rate, is typically influenced by the tree species, tree age, biological and genetic properties, environmental conditions, climatic factors, water table, etc. [16]. The pedunculate oak is one of the species for which the mean annual growth rate of an individual over several decades shows relatively constant values. Therefore, the radial increment is a parameter which can be used for the age determination of oaks.

For establishing the age of the investigated oak, we calculated the distances of the oldest dated segment, i.e., 4b, to the bark and to the geometric center of the trunk, respectively. Next, we extrapolated the age of this segment to the geometric center, by considering that the mean growth rate was almost constant. Sample 4 was collected at a height of 2.10 m, where the circumference of the trunk is 8.64 m and the bark thickness 0.05 m. These values correspond to a diameter inside bark of 2.72 m and a related radius of 1.36 m. The sample segment 4b originates from a distance of 0.77 m from the bark and 0.59 m from the geometric center. By extrapolating its age of 365 yr to the geometric center, we obtain an age of 645 yr. Calculations for the other deep segments 1a, 2a and 3a yielded similar values, hence showing that the geometric center and the true pith of the trunk, at this height, are very close to one another.

The radiocarbon dating results and their extrapolation to the pith indicate an age of 645 ± 50 yr for the investigated oak. One can state that the oak of Botoșana started growing around the year AD 1375, more precisely in the time frame 1325 – 1425.

CONCLUSIONS

Our research presents the AMS radiocarbon dating results of the pedunculate oak of Botoșana. The main aim of our investigation was to determine the age of tree. Four wood samples were collected from its trunk.

Five segments were extracted from the samples, including their deepest ends, processed and then dated by AMS radiocarbon. The five segments have radiocarbon dates between 161 ± 21 BP and 260 ± 20 BP, which correspond to calibrated ages between 235 ± 20 and 365 ± 10 yr. These results, extrapolated to the geometric center of the trunk, indicate an age of 645 ± 50 yr for the investigated oak of Botoșana.

EXPERIMENTAL SECTION

Size measurements. The height of the oak was measured using a Bosch DLE 70 Professional laser rangefinder. The circumference at different heights was measured with graduated tapes. The volume was calculated from laser measurements of the trunk and of large branches at different heights.

Sample collection. The four wood samples were collected with a Haglöf CH 800 increment borer (80 cm length, 0.54 cm inner diameter). A number of four tiny pieces/segments of the length of 0.1 cm were extracted from the deepest end of each sample. One additional segment was extracted from sample 4. The segments were processed and investigated by AMS radiocarbon dating.

Sample preparation. The standard acid-base-acid pretreatment method was used for removing soluble and mobile organic components. The pretreated samples were combusted to CO₂ by using the closed tube combustion method. Next, CO₂ was reduced to graphite on iron catalyst, under hydrogen atmosphere [17]. Finally, the resulting graphite samples were analyzed by AMS.

AMS measurements. AMS radiocarbon measurements were performed at the NOSAMS Facility of the Woods Hole Oceanographic Institution (Woods Hole, MA, U.S.A.) by using the Pelletron® Tandem 500 kV AMS system. The obtained fraction modern values, corrected for isotope fractionation with the normalized $\delta^{13}\text{C}$ value of -25‰ , were ultimately converted to a radiocarbon date.

Calibration. Radiocarbon dates were calibrated and converted into calendar ages with the OxCal v4.3 for Windows [18], by using the IntCal13 atmospheric data set [19].

ACKNOWLEDGMENTS

The research was funded by the Romanian Ministry of Research and Innovation CNCS-UEFISCDI under grant PN-III-P4-ID-PCE-2016-0776, Nr. 90/2017.

REFERENCES

1. P.H. Raven, G.B. Johnson, J.B. Losos, S.R. Singer, "Biology: Seventh Edition", McGraw Hill, New York, **2005**.
2. A. le Hardy de Beaulieu, T. Lamant, "Le guide illustré des chênes", Vol. 1-2, Huitième, Paris, **2007**.
3. A. Patrut, K.F. von Reden, D.A. Lowy, A.H. Alberts, J.W. Pohlman, R. Wittmann, D. Gerlach, L. Xu, C. Mitchell, *Tree Physiology*, **2007**, *27*, 1569.
4. A. Patrut, K.F. von Reden, R. Van Pelt, D.H. Mayne, D.A. Lowy, D. Margineanu, *Annals of Forest Science*, **2011**, *68*, 993.
5. A. Patrut, S. Woodborne, K.F. von Reden, G. Hall, M. Hofmeyr, D. Lowy, R.T. Patrut, *PLoS ONE*, **2015**, *10(1)*, e0117193, doi: 10.1371/journal.pone.0117193.
6. A. Patrut, L. Rakosy, R.T. Patrut, I.A. Ratiu, E. Forizs, D.A. Lowy, D. Margineanu, K.F. von Reden, *Studia UBB Chemia*, **2016**, *LXI*, *4*, 7.
7. A. Patrut, S. Woodborne, K.F. von Reden, G. Hall, R.T. Patrut, L. Rakosy, P. Danthu, J-M. Leong Pock-Tsy, D.A. Lowy, D. Margineanu, *Radiocarbon*, **2017**, *59(2)*, 435.
8. A. Patrut, S. Woodborne, R.T. Patrut, L. Rakosy, D.A. Lowy, G. Hall, K.F. von Reden, *Nature Plants*, **2018**, *4*, 423.
9. A. Patrut, K.F. von Reden, D.A. Lowy, S. Pasca, L. Kekedy-Nagy, I. Sovago, *Studia UBB Chemia*, **2010**, *LV*, *1*, 113.
10. A. Patrut, K.F. von Reden, V. Savu, D.A. Lowy, R. Mitea, I. Barbul, *Studia UBB Chemia*, **2011**, *LVI*, *1*, 145.
11. A. Patrut, K.F. von Reden, D.A. Lowy, R.T. Patrut, D.L. Vaida, D. Margineanu, *Nuclear Instruments and Methods in Physics Research Section B*, **2013**, *294*, 616.
12. A. Patrut, R.T. Patrut, L. Rakosy, I.A. Ratiu, D.A. Lowy, J. Bodis, K.F. von Reden, *Studia UBB Chemia*, **2018**, *LXIII*, *3*, 41.
13. J.N. Gibbs, B.J.W. Greig, *Forestry*, **1997**, *70*, 399.
14. P.P. Tans, A.F.M. de Jong, W.G. Mook, *Nature*, **1979**, *280*, 826.
15. M. Worbes, *Dendrochronologia*, **2002**, *20 (1-2)*, 217.
16. J. Ruseckas, *Ekologija*, **2006**, *1*, 16.
17. A. Patrut, S. Woodborne, R.T. Patrut, L. Rakosy, G. Hall, I.A. Ratiu, K.F. von Reden, *Studia UBB Chemia*, **2017**, *LXII*, *2*, 347.
18. C. Bronk Ramsey, *Radiocarbon*, **2009**, *51*, 337.
19. P.J. Reimer, E. Bard, A. Bayliss, J.W. Beck, P.G. Blackwell, C. Bronk Ramsey, C.E. Buck, H. Cheng, R. Lawrence Edwards, M. Friedrich, P.M. Grootes, T.P. Guilderson, H. Hafliadason, I. Hajdas, C. Hatte, T.J. Heaton, D.L. Hoffman, A.G. Hogg, K.A. Hughen, K.F. Kaiser, B. Kromer, S.W. Manning, M. Niu, R.W. Reimer, D.A. Richards, E.M. Scott, J.R. Southon, R.A. Staff, C.S.M. Turney, J. van der Plicht, *Radiocarbon*, **2013**, *55(4)*, 1869.

***Dedicated to the Memory of Assoc. Prof. RNDr.
Daniel Nižňanský (1963-2018)***

FRACTAL SURFACE MAGHEMITE NANOPARTICLES PREPARED BY CO-PRECIPITATION: THE INFLUENCE OF IRON CONCENTRATION AND BASE NATURE

**ROXANA NICOLA (CRIȘAN)^a, OTILIA COSTIȘOR^a, CĂTĂLIN IANĂȘI^a,
RADU LAZĂU^b, LIVIU SĂCĂRESCU^c, DANIEL NIŽŇANSKÝ^d,
AUREL ERCUȚA^e, ANA-MARIA PUTZA^a, CECILIA SAVII^{a,*}**

ABSTRACT. Two series of magnetic nanopowders were synthesized at room temperature starting from a mixture of iron II and III precursors, FeSO₄ and FeCl₃, respectively. Precipitation agents, as KOH and NaOH were used. While the concentration of the added ferrous and ferric solutions ranged between 0.1 M and 0.0125 M, the hydroxide solution concentration was maintained constant (1 M). TEM images of the samples showed that the particles shape changes from quasi spherical to spherical. For both series the crystallite size decreases with iron concentration, from 9 to 2 nm for KOH series and from 10 to 3 nm for NaOH series. Moessbauer Spectroscopy was signaling only Fe³⁺ in the final spinel product. BET measurements revealed the material mesoporosity and fractal structure of maghemite nanoparticles that explain the unusual high surface area, ~240 m²/g. All the samples actually exhibit superparamagnetic behavior at room temperature with saturation magnetization up to 73 emu/g value closed to those of bulk maghemite.

Keywords: *iron oxide nanoparticles, co-precipitation, fractal surface, Moessbauer Spectroscopy.*

^a *Institute of Chemistry Timișoara of Romanian Academy, Laboratory of Inorganic Chemistry, Mihai Viteazul Bd., No. 24, 300223, Timișoara, România.*

^b *"Politehnica" University of Timișoara, Faculty of Industrial Chemistry and Environmental Engineering, Vasile Pârvan Bd., No. 6, 300223, Timișoara, România.*

^c *Institute of Macromolecular Chemistry "Petru Poni", Grigore Ghica Voda Alley, No. 41A, 700487, Iași, România.*

^d *Charles University in Prague, Faculty of Science, Albertov 6, 128 43, Prague, Czech Republic.*

^e *West University of Timisoara, Faculty of Physics, Vasile Pârvan Bd., No. 4, 300223, Timișoara, România.*

* *Corresponding author: ceciliasavii@yahoo.com*

INTRODUCTION

The synthesis of superparamagnetic nanoparticles has been intensively developed because they are used in many applications, such as: magnetic storage media (e.g. magnetic carbon nanotubes composites [1], catalysts, magnetic fluids, sensors [2], as anode for lithium-ion (LIBs) [3] and sodium-ion (SIBs) [4] batteries, MRI contrast agent [5], tissue repair [6], detoxification of biological fluids, hyperthermia [7], cell and protein separation [8] and drug delivery [9][10][11].

Several synthesis methods like co-precipitation [12], microemulsion [13], thermal decomposition [14], solvothermal [15], sonochemical [16] are commonly used to produce magnetic nanoparticles. Chemical co-precipitation appears to be the most promising method, due to its simplicity, productivity and low cost [17]. In general, precipitation of magnetite requires a $\text{Fe}^{3+}/\text{Fe}^{2+}$ ratio of 2:1, and pH values between 8 and 14 [18].

Numerous studies demonstrate that several factors like pH [19], temperature [20], ionic strength [21], nature of salts [22], $\text{Fe}^{2+}/\text{Fe}^{3+}$ ratio [23], iron concentration [24], type of the precipitant agent [25] etc. affect the size and size distribution of the iron oxide nanoparticles.

Iron ion concentration is an important parameter because it has influence upon size and magnetic properties of nanoparticles. According to LaMer theory [26], at supersaturation, a critical concentration is defined as the nuclei start to grow by atomic species diffusion from solution towards the particles surfaces.

Fe oxide nanoparticles having a mesoporous structure are of interest for biomedical applications, due to the fact that the presence of mesopores facilitates high active agents loading [27]. Also, nanoparticles with high surface area can be used in catalysis [28], or as adsorbents, e.g. for heavy metal ions removal from waste water [29].

The present paper proposes a simple and economic synthesis route to obtain mesoporous maghemite nanoparticles with high surface area, exhibiting superparamagnetic behavior at room temperature.

Co-precipitation method presents advantages and disadvantages. Compared to other chemical methods, it is simple, low cost and environmentally friendly (not using organic solvents and directing agents), mild temperature conditions [30]. It is well known, the main requirements regarding magnetic nanoparticles properties with potential use in biomedical applications, such as: to be hydrophilic, nontoxic, biocompatible, near spherical, and mesoporous etc. [9][31]. Among mentioned essentials is that to be obtained in soft conditions (low temperature, aqueous media etc.).

As main disadvantage that can be mentioned was that the co-precipitation method does not always assures a perfect spherical shape of the particles and narrow particle size distribution. We agree other researchers opinion that sometimes it is worthless to expend time, money and effort designing definite particle properties (by using sophisticated preparing protocols), since co-precipitation was able to generate suitable particles for target applications [32].

The subject, the present work is dealing with, apparently was a common task, because in time, a great number of scientist published about iron oxide based magnetic nanomaterials properties (crystalline structure, magnetic properties etc.) in relationship with preparation variables (concentration of iron oxide precursor, nature of base as precipitating agent). To our best knowledge there are relatively few references where the morpho-textural properties of magnetic materials were discussed in relationship with both synthesis parameters and desired functionalities. In literature, the morpho-textural parameters are rarely reflected at the same level as crystallinity and magnetic properties. In the paper, besides crystalline and magnetic ordering, we mainly discussed morpho-textural properties related to synthesis conditions. Concerning preparation method, in order to avoid the pH local altering [33], we have chosen the reversed co-precipitation route, also less reported in iron oxide synthesis references.

RESULTS AND DISCUSSIONS

Transmission electron microscopy

In **Figure 1** the TEM images of samples $K_{0.1}$, $K_{0.025}$, $K_{0.0125}$, $N_{0.1}$, $N_{0.025}$ and $N_{0.0125}$ samples are shown. The TEM image of $K_{0.1}$ sample shows particles of spherical shape and narrow size distribution (6 -15 nm), while the particles shape in $K_{0.025}$ and $K_{0.0125}$ samples changes to quasi spherical, and the size distribution is centered on 5 nm and 3 nm respectively. The TEM images of the NaOH-base samples $N_{0.1}$, $N_{0.025}$ and $N_{0.0125}$ show the same particle size and distribution evolution pattern. It was observed that for both series, the particles size of maghemite decreases as the iron precursor concentration decreases.

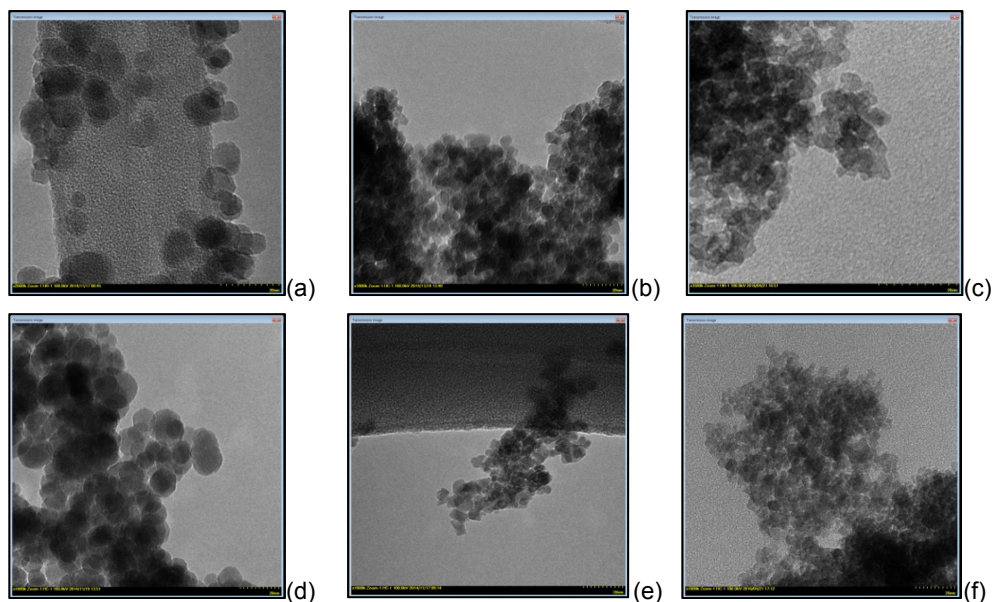


Figure 1. TEM images of samples: (a) $K_{0.1}$, (b) $K_{0.025}$, (c) $K_{0.0125}$, (d) $N_{0.1}$, (e) $N_{0.025}$ and (f) $N_{0.0125}$ (scale bar: 20 nm)

X-Ray powder diffraction analysis

The XRD spectra of the samples were recorded; as visible in **Figure 2**, all the spectra exhibit the characteristic lines of the cubic spinel structure (PDF file no. 00-039-1346).

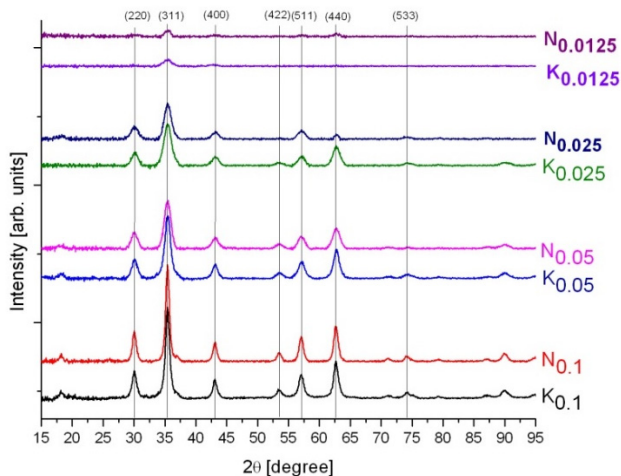


Figure 2. XRD spectra of synthesized iron oxide nanoparticles

It can be observed that the decrease of Fe concentration leads to diffraction peaks broadening, which indicates poor crystallization and/or small particle size. Also, the samples $K_{0.1}$ - $K_{0.0125}$ samples exhibit higher degree of crystallinity (the Bragg peaks are narrower) compared $N_{0.1}$ - $N_{0.0125}$ samples. The crystallite size and lattice parameter data of the two sample series are summarized in **Table 1**.

Table 1. Crystallite size and lattice parameter of the samples

KOH series	Average size of crystallite estimated by XRD [nm]*	Lattice parameter [nm]	NaOH series	Average size of crystallite estimated by XRD [nm]*	Lattice parameter [nm]
$K_{0.1}$	8.8	0.8393	$N_{0.1}$	9.8	0.8393
$K_{0.05}$	6.5	0.8389	$N_{0.05}$	5.7	0.8377
$K_{0.025}$	4.6	0.8384	$N_{0.025}$	4.6	0.8387
$K_{0.0125}$	2.0	0.8404	$N_{0.0125}$	2.7	0.8389

* calculated by using WPPF method

As the Fe concentration decreases from 0.1 M to 0.0125 M, the average crystallite size decreases from 8.8 to 2.0 nm and from 9.8 to 2.7 nm (**Table 1**), for samples synthesized with KOH and with NaOH, respectively.

The XRD data (crystallite size calculated with WPPF method) are consistent with TEM results. It can be observed that the particle size as visible in the TEM images is consistent with the crystallite size resulting from XRD data. It follows that the crystallites are slightly aggregated and a particle is composed by one or two agglomerated crystallites.

Moessbauer Spectroscopy

Both, magnetite and maghemite (except for vacancy ordered) exhibit similar XRD patterns, which makes difficult their identification. To facilitate the differentiation of the iron ionic species, Moessbauer Spectroscopy measurements were carried out for samples $K_{0.1}$, $K_{0.0125}$, $N_{0.1}$ and $N_{0.0125}$. In **Figure 3** room temperature Moessbauer spectra (MS) are shown.

It is common knowledge that MS showing sextet(s) belong to magnetically ordered phases of iron oxides [34]. Generally, in order to show sextet(s), the iron oxide particle dimension must be greater than its critical particle size having blocking temperature around room temperature. In the case of magnetite or maghemite, the critical particle size approximately corresponds to 10 nm.

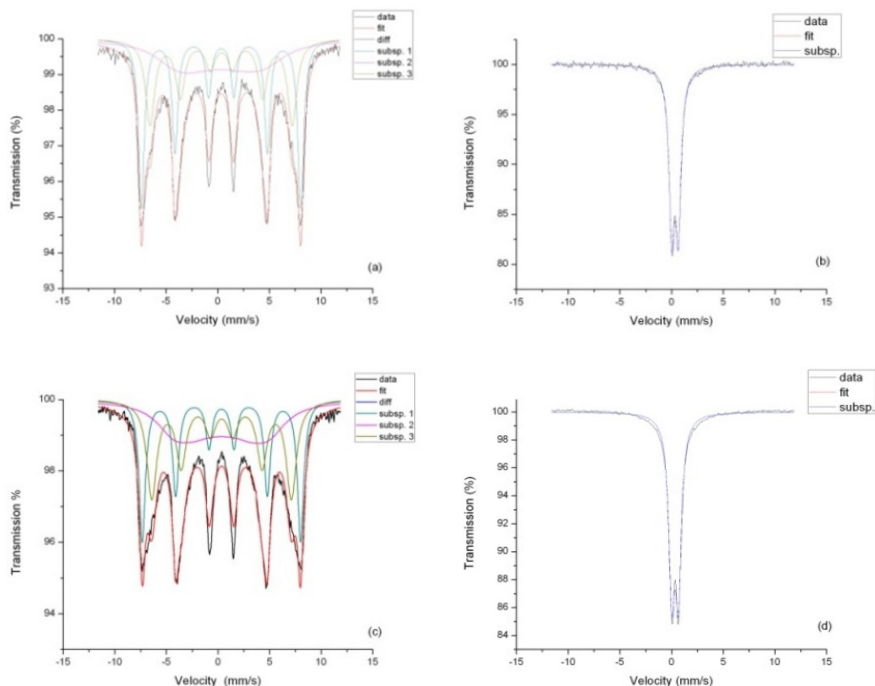


Figure 3. Room temperature MS of (a) $K_{0.1}$, (b) $K_{0.0125}$, (c) $N_{0.1}$ and (d) $N_{0.0125}$

So, we can conclude that the samples prepared using 0.1 M iron precursor solutions contain larger nanoparticles (> 10 nm) whereas using 0.0125 M solutions for the preparation leads to smaller particles (< 10 nm) as it was confirmed by the determination of crystallite size from XRD and particle size resulted from TEM.

Table 2. Parameters of $K_{0.1}$, $K_{0.0125}$, $N_{0.1}$ and $N_{0.0125}$ samples obtained from Moessbauer measurements

Sample	Isomer shift (IS) δ [mm/s]	Quadrupole splitting ΔE_Q [mm/s]	Hyperfine field B_{Hf}	Relative area (%)	Attribution
$K_{0.1}$	(1)0.33	(1)-0.0035	(1)47.70	(1)32	maghemite
	(2)0.35	(2)-0.0380	(2)28.41	(2)33	maghemite
	(3)0.34	(3)-0.0013	(3)42.00	(3)35	maghemite
$K_{0.0125}$	(1)0.33	(1)0.6394		(1)100	maghemite
$N_{0.1}$	(1)0.33	(1)-0.0061	(1)47.96	(1)39	maghemite
	(2)0.16	(2)0.1326	(2)27.08	(2)30	maghemite
	(3)0.35	(3)-0.0252	(3)42.77	(3)31	maghemite
$N_{0.0125}$	(1)0.33	(1)0.6642		(1)100	maghemite

MS give us the information about the oxidation state of iron through the value of isomer shift. In the above MS, the isomer shift (IS) values are situated in the range of 0.2– 0.4 mm/s which are characteristic values for Fe^{3+} (see **Table 2**). Reference values of IS for magnetite are around 0.26 mm/s in the case of Fe^{3+} in tetrahedral positions and 0.66 mm/s for Fe^{2+} and Fe^{3+} in octahedral sublattice. It means, that non-protected magnetite nanoparticles were oxidized by O_2 in air either in the early stage just after preparation or later during the samples storage in non-inert atmosphere.

Magnetite (Fe_3O_4) and maghemite ($\gamma\text{-}Fe_2O_3$) are common magnetic iron oxides that have spinel structure. Normal spinel structure is represented by $(A)_A[B_2]_BO_4$, where A stands for tetrahedral sites occupied by bivalent ions, and B stands for octahedral sites occupied by trivalent ions. In the case of inverse spinels, the tetrahedral positions are occupied by trivalent atoms. The unit cell formula of magnetite (inverse spinel) can be written as: $(Fe^{3+})_A[Fe^{2.5+}]_BO_4$, where the valence of iron in the octahedral sites is $Fe^{2.5+}$, due to the fast electron hopping above the Verwey transition, which take place around 121 K. Magnetite is sensitive to air expose, oxidizes, leading to nonstoichiometric magnetite, described by the formula: $(Fe^{3+})_A[Fe_{1-3x}^{2+}Fe_{1+2x}^{3+}\Upsilon_x]_BO_4$, where Υ denotes vacancy and are assumed to be located in octahedral sites in spinel structure and x ranges (0;1/3), where “0” stands for pure magnetite and “1/3” stands for pure maghemite. The fast electron hopping, which is known to be a pair-localized phenomenon in magnetite, results in $Fe^{2.5+}$ equal amounts of octahedral Fe^{2+} and Fe^{3+} : $(Fe^{3+})_A[Fe_{2(1-3x)}^{2.5+}Fe_{5x}^{3+}\Upsilon_x]_BO_4$. Maghemite is fully oxidized magnetite, where $x=0.33$ and general formula is $(Fe^{3+})_A[Fe_{5/3}^{3+}\Upsilon_{1/3}]_BO_4$ [35][36].

Textural analysis

Specific surface area, total pore volume, mean pore size, particle diameter and surface fractal dimension (D_s) are presented in **Table 3** and **Table 4** derived from N_2 adsorption-desorption isotherms presented in **Figure 4**. Assuming all the particles of spherical shape and equal size, the particle diameter was calculated using data from adsorption-desorption isotherm, using the following equation [27]:

$$(1) \quad D = \frac{6}{S_{sp}\rho_a}$$

where S_{sp} is the specific surface area and ρ_a is the density; for all maghemite samples a value of 4.9 g/cm^3 was considered.

BET derived particle size evaluations (Eq. (1)) (see **Tables 3** and **4**) are consistent with TEM results and XRD data.

Table 3. Results of textural data from adsorption-desorption isotherm for KOH series

Sample	Specific surface area [m ² /g]	Total pore volume [cc/g]	Mean pore size [nm]	Particle diameter approximated using specific surface area	D _s
K _{0.1}	91.01	0.2302	6.62	13.5	2.50
K _{0.05}	120.05	0.1871	4.92	10.2	2.61
K _{0.025}	152.21	0.1651	3.82	8.0	2.71
K _{0.0125}	239.65	0.2050	3.43	5.1	2.79

Table 4. Results of textural data from adsorption-desorption isotherm for NaOH series

Sample	Specific surface area [m ² /g]	Total pore volume [cc/g]	Mean pore size [nm]	Particle diameter approximated using specific surface area	D _s
N _{0.1}	80.50	0.2350	6.58	15.2	2.47
N _{0.05}	148.75	0.4421	6.61	8.2	2.48
N _{0.025}	160.54	0.3263	6.60	7.6	2.55
N _{0.0125}	219.52	0.4070	6.49	5.6	2.56

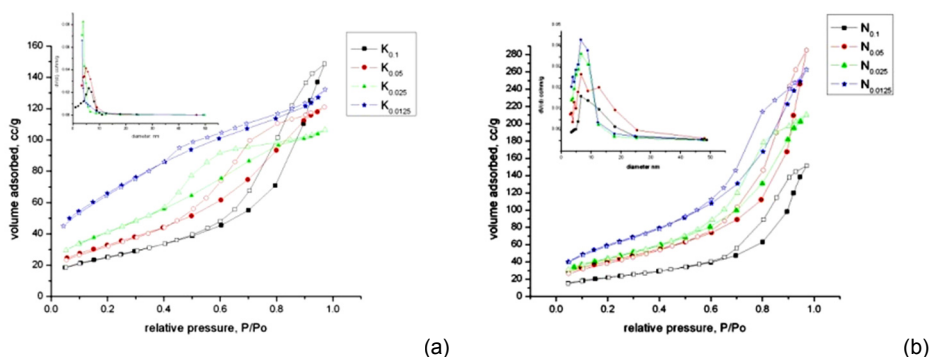


Figure 4. N₂ adsorption-desorption isotherms of (a) K_{0.1}, K_{0.05}, K_{0.025} and K_{0.0125}, and (b) N_{0.1}, N_{0.05}, N_{0.025} and N_{0.0125}. Inset: Pore size distribution curves of the samples

With the particle size decrease, in the case of sample series K_{0.1}-K_{0.0125}, the mean pore size also decrease, **Table 3**, and the specific surface area is increasing as was expected. In the case of the samples precipitated by NaOH, **Table 4**, this tendency is not so straightforward. The specific surface area regularly increases but the mean size of pores remains almost constant. So, we can see that the used basic reagents have different impact on the morphology of the aggregates.

One can see that the specific surface area is increasing with the decrease of iron precursor concentration, **Tables 3** and **4** leading to the particle size diminution. This tendency was in agreement with XRD and TEM results, the Sherrer derived crystallite size and particle size deduced from TEM also showed a decreasing trend with iron concentration.

The surface fractal dimension D_s was deduced by using Quantacrome Nova 1200e apparatus output and software, applying Frenkel-Halsey-Hill (FHH) equation [37]. All prepared samples contained iron oxide nanoparticles with apparently rough surface, having fractal structure, which can be characterized by surface fractal dimension, D_s . There was a clear increasing trend of D_s in both maghemite prepared series, specifically $2.50 \leq D_s \leq 2.79$ for KOH series and $2.47 \leq D_s \leq 2.56$, for NaOH series. A perfectly smooth surface has the value of surface fractal dimension $D_s=2$, while a highly rough surface has $D_s=3$ [38]. The obtained iron oxide particles present unusual high surface area that can be explained by its rugosity, well described by the surface fractal dimension, D_s , its evolution with iron precursor concentration was in perfect accord with the corresponding surface area trend.

The adsorption-desorption isotherms of all investigated samples correspond to a type IV-isotherm according to the Brunauer, Deming, Deming and Teller (BDDT) method, showing hysteresis [39]. The type IV isotherm was attributed to mono and multilayer adsorption and hysteresis loop is associated with capillary condensation in mesopores. These hysteresis loops are associated with mesoporous materials (containing pores between 2-50 nm diameter) [IUPAC]. In **Figure 4** are presented N_2 adsorption-desorption isotherms of the samples. Pore size distributions (calculated from desorption branch) of the samples are shown in **Figure 4** (inset). According to IUPAC classification, isotherms of $K_{0.1}$ and $N_{0.05}$ follows a H3 hysteresis loop type, as illustrated in **Figure 4**, which is observed with non-rigid aggregates of plate-like particles, giving rise to slit shape pores. For $K_{0.05}$ and $K_{0.025}$ typical hysteresis loop is type H2, and this hysteresis type is typical for materials with no uniform pore shapes and/or size. The H2 type adsorption hysteresis is associated with highly interconnected pores with ink-bottle shapes [40][41]. H1-type hysteresis loops of $N_{0.1}$, $N_{0.025}$ and $N_{0.0125}$ samples are associated with porous materials known to consisting of approximately uniform spheres aggregates in fairly regular array and hence to have narrow distribution of pore size. On the other hand $K_{0.0125}$ sample isotherm exhibits H4 hysteresis type, which appears to be associated with narrow slit-like pores [42].

A pore size distribution ranging in the mesopore domain is the main characteristic of all samples. It can be noted that samples from KOH series have a narrower pore size distribution than the samples from NaOH series.

In **Figure 4** inset, it can be seen that all the samples are characterized by mesoporous structures mainly consisting in slit-like pores. The slit-like pore geometry was recommended to be characterized using the concept of “pore width”, which value, in our case, was ranging between 2 and 15 nm [43].

Magnetic properties characterization

Table 5. Magnetic parameters

Sample	Ms [emu/g]	Hc [kOe]	Mr [emu/g]	Squareness ratio Mr/Ms	Sample	Ms [emu/g]	Hc [kOe]	Mr [emu/g]	Squareness ratio Mr/Ms
K _{0.1}	73.3	0.053	6.1	0.08	N _{0.1}	66.3	0.04	6.35	0.1
K _{0.05}	64.5	0.024	1.8	0.03	N _{0.05}	60.7	0.005	0.27	0.004
K _{0.025}	43.9	0.014	0.6	0.01	N _{0.025}	44.7	0.014	0.42	0.009
K _{0.0125}	30.1	0.03	0.17	0.005	N _{0.0125}	29.9	0.015	0.16	0.005

Room temperature magnetic measurements of all synthesized iron oxide samples indicate that the nanoparticles exhibit superparamagnetic behavior; the results are summarized in **Table 5**, **Figure 5**. According to literature, the squareness ratio of hysteresis loop, expressed by Mr/Ms ratio, less than 0.1 could categorize the magnetic material as superparamagnetic metal oxide crystals [44].

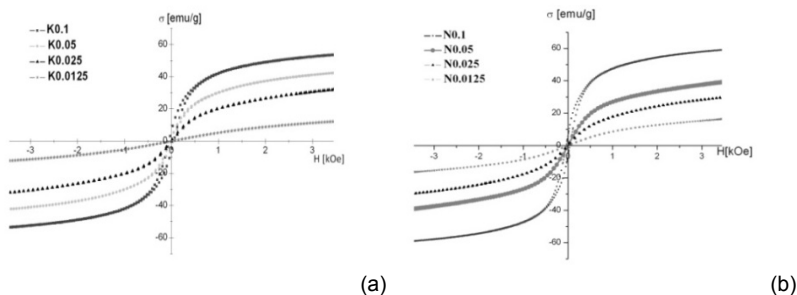


Figure 5. Magnetization curves (a) KOH series and (b) NaOH series

Saturation magnetization M_s increases, as it was expected, with the iron concentration and crystallite size respectively (see **Table 5**). Specifically, in the case of KOH based samples, M_{smax} value of 73.3 emu/g was found for the highest iron concentration sample, K_{0.1}, of 0.1 M in the given conditions. When NaOH was used, also the corresponding N_{0.1} sample showed the max M_s value of 66.3 emu/g (see **Table 5**). It can be noted that KOH series exhibited higher values of M_s comparing NaOH one. A possible explanation might be

because the KOH series maghemite particles present significantly better crystallinity. This assumption is supported by the XRD patterns features presented in **Figure 2**.

On account of the surface disorder and modified cationic distribution, smaller particles exhibit smaller values of M_s , due to the pronounced surface effects in nanoparticles [45][46]. The surface region of the nanoparticles is assumed to be composed of some canted or disordered spins that prevents the spins from aligning along the field direction, thus resulting a decrease of M_s [46][47]. The spin disorder layer increases with the decrease in crystallite size [48]. It cannot be neglected the contribution of the effect of dipolar interaction between nanoparticles [27][49] and or of the magnetic phase poor crystallinity [50] to the reduction of the material global magnetic moment.

CONCLUSIONS

Spinelic magnetic nanoparticles systems were obtained by reverse co-precipitation (Fe^{2+}/Fe^{3+}) in a large window of pH and precursors concentrations, by using KOH or NaOH.

As general conclusions, it can be noted that: pure superparamagnetic maghemite was obtained; the particles size of maghemite samples decreases with iron precursor concentration; the average crystallite size was situated up to 10 nm, slightly depending on the base nature too; the maghemite nanoparticle shape was improved from quasi spherical to spherical as Fe concentration increases.

In particular, for exclusive crystalline materials, unusual high surface area was obtained, of ~ 239 m²/g and ~ 219 m²/g, for $K_{0.0125}$ and $N_{0.0125}$ samples, respectively. N_2 adsorption – desorption isotherms data (FHH method) allowed to evaluate the apparent fractal character of obtained materials and to calculate the surface fractal dimension, D_s . Such way, by considering the fractal character of particle surface was possible to evaluate surface rugosity trend, that was consistent to corresponding surface areas and to be related to precursors concentrations. The lower precursor concentration leads to the higher rugosity and the higher surface area.

In spite of relatively low particle size, the prepared samples showed high saturation magnetization, M_s (e.g. ~ 73 emu/g), closed to the M_s value (~ 90 emu/g) of the bulk maghemite.

High surface areas and generous total pore volume of synthesized samples together with crystalline and magnetic properties, recommend them as potential candidates for catalysis domain and biomedical applications, as drug carriers.

EXPERIMENTAL SECTION

Reagents

Iron (II) sulfate-7-hydrate (Sigma Aldrich >99, 5 %, extra pure), ferric chloride hexahydrate (Merck >99%, pro analysis), potassium hydroxide (Merck, pro analysis) and sodium hydroxide (LACHEMA>98%, pro analysis) were used for the synthesis of iron oxide nanoparticles. All chemicals were used as received.

Synthesis

Magnetic iron oxide nanoparticles were synthesized in air, by room temperature co-precipitation of ferrous and ferric salts mixtures in the presence of KOH or NaOH 1 M solution; the reactions were carried out under stirring. In literature are mentioned two types of co-precipitation (I) normal co-precipitation, where alkali solution is dropped into the mixed metal solution (the pH value gradually increase), and (II) reverse co-precipitation, where mixed metal solution is added to alkaline solution (consequently, the pH which is a critical factor in synthesis could be easily controlled at high values) [31]. In order to avoid the pH local altering, reverse co-precipitation was chosen.

Two series of samples, $K_{0.1}$ to $K_{0.0125}$ labeled as the "KOH series", and $N_{0.1}$ to $N_{0.0125}$ labeled as the "NaOH series" were prepared, the indices refer to the iron concentration. Equi-molar 0.1 M ($K_{0.1}$, $N_{0.1}$), 0.05 M ($K_{0.5}$, $N_{0.5}$), 0.025 M ($K_{0.025}$, $N_{0.025}$) and 0.0125 M ($K_{0.0125}$, $N_{0.0125}$) aqueous solutions of Fe^{2+} and Fe^{3+} were separately prepared, by dissolving ferrous and ferric salts in distilled water (Fe^{2+}/Fe^{3+} 1/2 molar ratio). Compared to the calculated Fe^{2+}/Fe^{3+} molar ratio, a slight excess of Fe^{2+} was used in the synthesis. The Fe^{3+} solution was first added to the Fe^{2+} solution and stirred (at 400 rpm, for 10 min). Then the solution was rapidly added to the hydroxide solution and stirred for other 30 min. The pH values of the final solutions ranged from 11 to 13. The obtained iron oxide nanoparticles were separated by a permanent magnet, washed with distilled water and, finally, with absolute ethanol. The wet precipitates were dried in air, at 80°C.

Characterization

For particles size and shape determination, TEM investigations were carried out in high contrast operation mode, at 100 kV accelerating voltage, on a High-Tech HT7700 (HITACHI) equipment. The samples were prepared by drop casting diluted nanoparticles dispersed in ethanol, on 300

meshes holey carbon-coated Cu grids (Ted Pella) and vacuum dried. The structure and phase composition of the particles was determined by XRD, using a Ultima IV (RIGAKU) instrument operating with Cu K α radiation. The crystallite size was calculated using the WPPF method [51] and the instrument influence was subtracted using the diffraction pattern of a Si standard recorded in the same conditions. The Moessbauer spectra were recorded at constant acceleration in transmission mode, with ^{57}Co diffused into an Rh matrix as the moving source. The spectrometer was calibrated to a α -Fe foil standard at 293 K, the isomer shift being expressed with respect to this; the NORMOS program [52] was used to fit the as-recorded spectra. The specific surface area of the powders was measured using the Brunauer-Emmett-Teller (BET) method and the pore size distribution was evaluated from nitrogen desorption isotherms (at 77 K), using the Barrett-Joyner-Halenda (BJH) method; a Nova 1200e (QUANTACHROME) device was used. The magnetic properties were investigated in ac (50Hz) fields of 3.5 kOe amplitude by means of a laboratory-manufactured induction hysteresigraph [53]; the specific magnetization vs applied field curves were recorded to a PC by means of a DT-9816A (DATA TRANSLATION) acquisition card (at 16 bit analog-to-digital resolution) and fitted by assuming a superposition of Langevin functions. The saturation magnetization (technical) was estimated from extrapolating to 50kOe the fitted data.

ACKNOWLEDGEMENTS

The authors thank to Romanian Academy for the financial support: *Program 4. Inorganic compounds and hybrids with relevance in nanostructured materials science. Precursors for advanced materials.*

REFERENCES

1. M. Pastor-Belda, L. Marin-Soler, N. Campillo, P. Vinas, M. Hernandez-Cordoba, *Journal of Chromatography A*, **2018**, 1564, 102
2. K.D. Kim, S.S. Kim, Y-H. Choa, H.T. Kim, *Journal of Industrial and Engineering Chemistry*, **2007**, 13, 1137
3. S. Yu, V. M. Hong Ng, F. Wang, Z. Xiao, C. Li, L. Bing Kong, W. Que, K. Zhou, *Journal of Materials Chemistry A*, **2018**, 6, 9332
4. M. Fiore, G. Longoni, S. Santangelo, F. Panto, S. Sara, P. Frontera, P. Antonucci, R. Ruffo, *Electrochimica Acta*, **2018**, 269
5. R. Gonzales-Rodriguez, P. Granitzer, K. Rumpf, J. L. Coffey, *Royal Society Open Science*, **2018**, 5, 180697

6. S. Hu, Y. Zhou, Y. Zhao, Y. Xu, F. Zhang, N. Gu, J. Ma, M.S. Reynolds, Y. Xia, H. H. K. Xu, *Journal of Tissue Engineering and Regenerative Medicine*, **2018**, 12, e2085
7. N. V. S. Vallabani, S. Singh, *3 Biotech*, **2018**, 8, 279
8. S.P. Schwaminger, S.A. Blanck-Schim, I. Scheifele, V. Pipich, P. Fraga-Garcia, S. Berensmeier, *Biotechnology Journal*, **2018**, e:1800055
9. A.K. Gupta, M. Gupta, *Biomaterials*, **2005**, 26, 3995
10. K. El-Boubbou, *Nanomedicine*, **2018**, 13, 929
11. S. Laurent, D. Forge, M. Port, A. Roch, C. Robic, L. Vander Elst, R.N. Muller, *Chemical Reviews*, **2008**, 108, 2064
12. R. Massart, *IEEE Transaction on Magnetics*, **1981**, 17, 1247
13. C. Okoli, M. Sanchez-Dominguez, M. Boutonnet, S. Jaras, M.C. Civera, C. Solans, G.K. Rajarao, *Langmuir*, **2012**, 28, 8479
14. S. Belaid, D. Stanicki, L. Vander Elst, R.N. Muller, S. Laurent, *Nanotechnology*, **2018**, 29, 165603
15. J. Ladol, H. Khajuria, H. N. Sheikh, Y. Khajuria, *Journal of Chemical Science*, **2016**, 128, 1149
16. R. Dolores, S. Raquel, G-L. Adianez, *Ultrasonics Sonochemistry*, **2015**, 23, 391
17. N. Tresilwised, P. Pithayanukul, C. Plank, *Journal of Pharmaceutical Science*, **2005**, 32, 71
18. J. Lodhia, G. Mandarano, N.J. Ferris, P. Eu, S.F. Cowell, *Biomedical Imaging and Intervention Journal*, **2010**, 6, e12
19. W. Ramadan, M. Karim, B. Hannover, S. Saha, *Advanced Materials Research*, **2012**, 324, 129
20. N.M. Gribanov, E.E. Bibik, O.V. Buzunov, V.N. Naumov, *Journal of Magnetism and Magnetic Materials*, **1990**, 85, 7
21. J.P. Jolivet, L. Vayssieres, C. Chaneac, E. Tronc, *MRS Online Proceedings Library (OPL)*, **1996**, 432, 145
22. I.M. Bolbokh, G.S. Gunko, G. Yu Yurkov, G.P. Prokhodko, V.A. Tertykh, *Proceedings of the International Conference Nanomaterials: Applications and Properties*, **2013**, 2, 1
23. S. Alibeigi, M.R. Vaezi, *Chemical Engineering & Technology*, **2008**, 31, 1591
24. O. Kraagac, H. Kockar, S. Beyaz, T. Tanrisever, *IEEE Transactions on Magnetics*, **2010**, 46, 3978
25. M. Stoia, A. Tamas, G. Rusu, J. Morosanu, *Studia UBB Chemia LXI*, **2016**, 4, 147
26. V.K. LaMer, R.H. Dinagar, *Journal of the American Chemical Society*, 1950, **72**, 4847
27. M.C. Mascolo, Y. Pei, T.A. Ring, *Materials*, **2013**, 6, 5549
28. M. Krizek, J. Pechousek, J. Tucek, K. Safarova, I. Medrik, L. Machala, *AIP Conference Proceedings*, **2012**, 1489, 88
29. P.N. Dave, L.V. Chopda, *Journal of Nanotechnology*, **2014**, 398569, 1
30. Y.Y. Zheng, X.B. Wang, L. Shang, C.R. Li, C. Cui, W.J. Dong, W.H. Tang, B.Y. Chen, *Materials Characterization*, **2010**, 61, 489
31. J. Markhulia, S. Kekutia, Z. Jabua, V. Mikhelashvili, L. Saneblidze, *SGEM2017 Conference Proceedings*, **2017**, 17, 51

32. M. Manzano, V. Aina, C.O. Arean, F. Balas, V. Cauda, M. Colilla, M.R. Delgado, M. Vallet-Regí, *Chemical Engineering Journal*, **2008**, 137, 30
33. S. Alibeigi, M. R. Vaezi, *Chemical Engineering & Technology*, **2008**, 31, 1591
34. E. Murad, J. Cashion, "Mossbauer spectroscopy of environmental materials and their industrial utilization", Springer, Boston, MA, **2004**, chapter Iron oxides.
35. R.E. Vandenberghe, C.A. Barrero, G.M. da Costa, E. Van San, E. De Grave, *Hyperfine Interactions*, **2000**, 126, 247
36. I. Nedkov, T. Merodiiska, L. Slavov, R.E. Vandenberghe, Y. Kusano, J. Takada, *Journal of Magnetism and Magnetic Materials*, **2006**, 300, 358
37. F. Rubio, J. Rubio, J.L. Oteo, *Journal of Sol-Gel Science and Technology*, **1997**, 8, 159
38. I.M.K. Ismail, P. Pfeifer, *Langmuir*, **1994**, 10, 1532
39. S. Brunauer, L.S. Deming, W.E. Deming, E. Teller, *Journal of the American Chemical Society*, **1940**, 62, 1723
40. G. Mason, *Proceedings of the Royal Society A Mathematical, Physical and Engineering Sciences*, **1983**, 390, 47
41. N.E. Velikova, Y.E. Vueva, Y.Y. Yvanova, I.M. Salvado, M.H. Fernandes, *International Scientific Publications: Materials, Methods Technologies*, **2014**, 8, 162
42. K.S.W. Sing, D.H. Everett, R.A.W. Haul, L. Moscou, R.A. Pierotti, J. Rouquérol, T. Siemieniewska, *Pure and Applied Chemistry*, **1985**, 57, 603
43. M. Thommes, K. Kaneko, A. V. Neimark, J. P. Olivier, F. Rodroguéz-Reinoso, J. Rouquerol, K. S. W. Sing, *Pure and Applied Chemistry*, **2015**, 87, 1051
44. K. Praveena, S. Katlakunta, H.S. Virk, *Solid State Phenomena*, **2015**, 232, 45
45. B.P. Rao, O. Caltun, W.S. Cho, C.-O. Kim, C. Kim, *Journal of Magnetism and Magnetic Materials*, **2007**, 310, e812
46. H.M.H. El Ghandoor, H.M. Zidan, K. Mostafa, M.I.M. Ismail, *International Journal of Electrochemical Science*, **2012**, 7, 5734
47. K. Maaz, S. Karim, A. Mumtaz, S.K. Hasanain, J. Liu, J.L. Duan, *Journal of Magnetism and Magnetic Materials*, **2009**, 321, 1838
48. B. Wang, Q. Wei, S. Qu, *International Journal of Electrochemical Science*, **2013**, 8, 3786
49. G.F. Goya, T.S. Berquó, F.C. Fonseca, M.P. Morales, *Journal of Applied Physics*, **2003**, 94, 3520
50. M. Mandal, S. Kundu, S.K. Ghosh, S. Panigrahi, T.K. Sau, S.M. Yusuf, T. Pal, *Journal of Colloid Interface Science*, **2005**, 286, 187
51. H. Toraya, *Journal of Applied Crystallography*, **1986**, 19, 440
52. R.A. Brand, *Nuclear Instruments and Methods in Physics Research Section B*, **1987**, 28, 398
53. I. Mihalca, A. Ercuta, *Journal of Optoelectronics and Advanced Materials*, **2003**, 5, 245

KINETIC AND MECHANISTIC FEATURES OF THE THIOLACTIC ACID OXIDATION BY CHROMIUM(VI) IN ACIDIC ENVIRONMENT

DANA MARIA SABOU^{a,*}, IOAN BÂLDEA^a

ABSTRACT. Thiolactic acid, containing a reactive sulphhydryl group, has been shown to easily reduce Cr(VI) and yield disulfide as oxidation product. The reaction was studied by the use of spectrophotometry. The spectral data as well as the kinetic information showed distinct evidence of the formation of an S-bonded Cr(VI)-thiolactate intermediate that was subsequently followed by a somewhat slower, bimolecular redox process leading to the formation of the final products. The rate laws for these two stages have been determined, showing a complex dependence on substrate and hydrogen ion concentration. Small experimental Arrhenius activation energies for the two successive steps were also obtained. The involvement of paramagnetic Cr(V) species and that of some organic free radicals were evidenced by ESR and, the latter, also by initialization of polymerization. A reaction mechanism has been proposed, that leads to a rate law in convincing agreement with the experimental one.

Keywords: *kinetics, redox, chromium VI, thiolactic acid*

INTRODUCTION

The interest in the chemistry of sulphhydryl compounds and thiyl radicals is derived from their involvement in a large number of processes in natural systems, including species present in the human body. On the other hand, chromium(VI) is widely used in various industries and practical applications, however, with toxic effects for humans, that include carcinogenicity due to its conversion by intracellular reductants to more active species that initiate DNA damage [1-5]. Therefore, the understanding of the interaction mechanism

^a Babeş-Bolyai University, Faculty of Chemistry and Chemical Engineering, 11 Arany Janos str., RO-400028, Cluj-Napoca, Romania.

* Corresponding author: dsabou@chem.ubbcluj.ro

between Cr(VI) and sulphhydryl compounds is of great importance, and while considerable research has been done in the field, it remains yet a topic of interest.

Mechanistically, Cr(VI) oxidations of organic compounds (alcohols, aldehydes, thiols, hydroxy- and mercapto- acids) or inorganic compounds (sulphite, phosphite, hypophosphite) proceed by inner-sphere and the first step is an equilibrium of the type $\text{HCrO}_4^- + \text{HX} \rightleftharpoons \text{XCrO}_3^- + \text{H}_2\text{O}$ [6-13].

The condensation complex formed (XCrO_3^-) further decomposes by transfer of electrons, this being often the rate determining step. Depending on the nature of the reducing agent and the molecularity of this electron transfer step, the number of electrons changed may vary from one [14,15] (to form Cr(V)) to two [16-18] (yielding Cr(IV)) or even three in some co-oxidations [19, 20]. The involvement of the intermediate valence states Cr(V) and Cr(IV), both also oxidizing agents, as well as that of other very reactive intermediates, such as organic radicals, brings about complicated reaction schemes [6]. When thiols or thiol acids are the reducing agents, the sulphhydryl group is involved and the sulphur atom is the one to suffer a change in the oxidation state [21]. Rate laws of first-order (in the condensed complex) or second order (first order in the complex and first order in the substrate) have been reported [6].

The study of the thiolactic acid oxidation by chromium(VI) falls in line with the long lasting interest of our group in the kinetics of alcohols and thiols homogeneous oxidation reactions.

Early tests showed a rapid change of color from yellow to red-brown to take place already during the mixing of some acidic solutions of the two reactants, which then faded quite fast as well, as time elapsed. This clearly indicated that the red-brown species is an intermediate formed during the reaction process and that the reaction has two photometrically distinguishable stages, but it also suggested that the set of experimental conditions under which the reaction can be studied for reliable mechanistic insight is somewhat restrictive. The difficulties have to do with the quite fast overall rate of the process, as well as with the quite comparable relative rates of the two observable stages. These make the reaction only borderline approachable by either batch or fast-reaction techniques alone.

The findings of a stopped-flow approach aimed at explaining the formation of the condensed intermediate complex have been previously reported [22]. The stopped-flow technique was considered better suited for the study of the beginning of the reaction, as it ensures the fast and reproducible mixing of the reactants. However, with spectrophotometry employed as the detection method, the usually small path length of the mixing chamber (0.336 cm in our case) imposed the use of Cr(VI) (the monitored species) in higher

concentrations than those accessible under a batch approach, when cuvettes of a length at choice can be used. This in turn enhanced the overall rate and subsequently narrowed the range of thiolactic acid and H^+ concentrations that could be spanned.

To gain more insight on the reaction progress, a batch setup was tried out for further study of the reaction. The purpose of this paper is to report the results concerning the kinetics of both the formation and decay of the intermediate, obtained under batch conditions and by the use of spectrophotometry as the detection technique, and also to suggest a plausible overall reaction mechanism. To this end, information of extra-kinetic type was gathered as well, to clarify the matter of the involvement of further reaction intermediates.

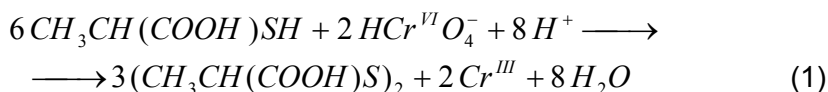
RESULTS AND DISCUSSION

Reaction stoichiometry

In a spectrophotometric approach, mixtures containing increasing molar ratios of thiolactic acid (abbreviated here as RSH) to Cr(VI) were prepared and the remaining absorbance was measured at 350 nm, after the reaction has been completed. The measured absorbance was almost zero for the ratios of 3 to 1 and higher, meaning that all Cr(VI) has reacted. This is in agreement with many literature data concerning oxidations of mono-thiols [6,10]. However, for the lower ratios the behavior was not linear, raising the question of whether further oxidation to oxygenated products might take place.

To settle this, we resorted to iodometrical titration. Six reaction mixtures were prepared, all with RSH in excess over Cr(VI), and allowed to react to completion. The concentrations of the two reactants were in this case 10 times higher therefore completion was reached within less than one minute. The mean of these experiments showed, indeed, a total of 3.09 ± 0.03 mol of thiolactic acid to react with 1 mol of Cr(VI).

Based on the above, the overall stoichiometry can be qualitatively schematized as in equation (1):



Electronic spectra giving evidence of the intermediate

Electronic spectra of $HCrO_4^-$ and thiolactic acid, as well as some qualitative ones of a reaction mixture, collected at various time intervals, are presented in Figure 1. It is clear that, as compared to $HCrO_4^-$, the mixture

exhibits lower absorbance at 350 nm, but a more pronounced absorption band around 420 nm. The progress of the reaction can be followed at either of these wavelengths, yet the absorbance of the intermediate interferes with that of the reactant at both of them.

The shift of the charge-transfer maximum from 350 in HCrO_4^- to 420 nm in the mixture argues the change of an oxygen ligand of Cr(VI) with a sulphur one, thus the formation of a condensed thiolato-chromate compound of esteric type. This takes place according to the following equilibria:

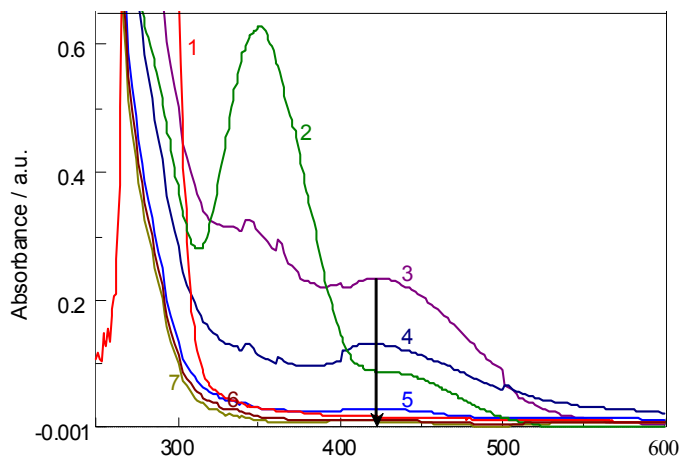
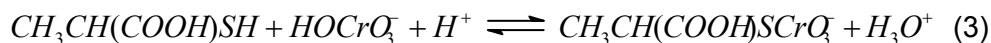
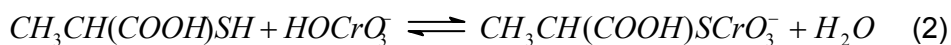


Figure 1. Spectra of the reactants and of the reaction mixture: 1 – $[\text{RSH}] = 0.1 \text{ M}$; 2 – $[\text{Cr(VI)}] = 7.22 \cdot 10^{-5} \text{ M}$; 3 - 7 – reaction mixture at some time intervals ($T = 293 \text{ K}$, $\mu = 0.5 \text{ M}$; $[\text{RSH}] = 2.67 \cdot 10^{-3} \text{ M}$, $[\text{Cr(VI)}]_0 = 6.67 \cdot 10^{-5} \text{ M}$, $[\text{H}^+] = 3.16 \cdot 10^{-3} \text{ M}$).

Reaction kinetics

Taking into account the equilibria involving Cr(VI) [23,24] species it is possible to choose such conditions of its concentration ($10^{-5} - 10^{-4} \text{ M}$), acidity (pH 1 - 5, HClO_4) and ionic strength ($< 1 \text{ M}$, NaClO_4) to ensure that HCrO_4^- is the vastly predominant species in the solution. Also, pseudo-first order conditions were ensured, with Cr(VI) always as the limiting component ($6.67 \cdot 10^{-5} \text{ M}$) and the concentrations of RSH and H^+ in high excess. In this arrangement, the reaction reaches accomplishment within several minutes. The absorbance evolution during time at both 350 nm and 420 nm is exemplified in Figure 2.

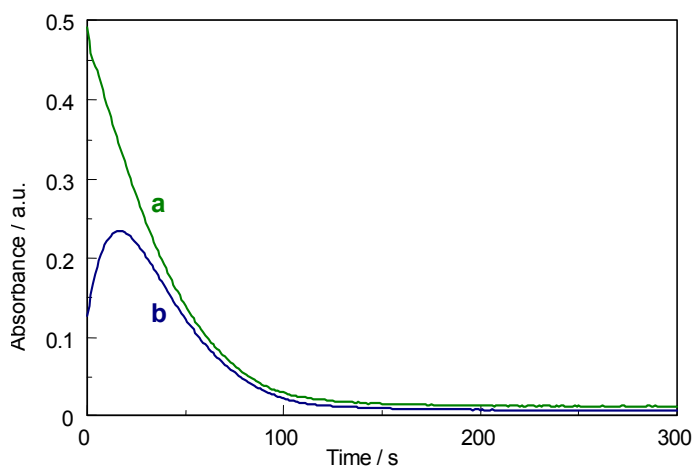
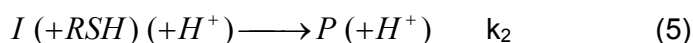
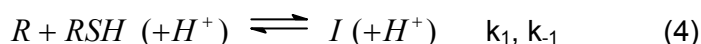


Figure 2. Experimental kinetic curves recorded at 350 nm (a) and at 420 nm (b) ($[\text{Cr(VI)}]_0 = 6.67 \cdot 10^{-5} \text{ M}$, $[\text{H}^+] = 3.16 \cdot 10^{-2} \text{ M}$, $[\text{RSH}] = 1.33 \cdot 10^{-3} \text{ M}$, $T=293\text{K}$, $\mu=0.5\text{M}$).

The kinetic curves at 350 nm show a continuous decay, while the recordings at 420 nm clearly display the biphasic shape characteristic of two consecutive steps. The differences in shape are most likely owing only to the differences in the molar absorptivities. The wavelength chosen to follow the reaction extensively was 420 nm.

The following reaction sequence has been considered:



where the parentheses are meant to suggest that the respective species may or may not partake in the process.

Under the excess concentrations of RSH and H^+ , this simplifies greatly, to:



which is a sequence of two apparent first order reactions, described by an integrated rate law containing two exponential terms.

Written in terms of absorbance, equation (6) takes the form (eq. 7):

$$A - A_\infty = [R]_0 I \left\{ \varepsilon_R + \frac{k_{2obs} \varepsilon_P - k_{1obs} \varepsilon_I}{k_{1obs} - k_{2obs}} \right\} e^{-k_{1obs} t} + [R]_0 I \left\{ \frac{k_{1obs} (\varepsilon_I - \varepsilon_P)}{k_{1obs} - k_{2obs}} \right\} e^{-k_{2obs} t} \quad (7)$$

where A and A_∞ stand for the actual and final absorbances, l is the path length of the cell and ε_R , ε_I , and ε_P are the molar absorptivities of the reactant R, intermediate I, and product P.

Since the pre-exponential terms are composed of constants, they can be combined under singular notations, to give a simpler equation:

$$A - A_\infty = \gamma_1 e^{-k_{1obs}t} + \gamma_2 e^{-k_{2obs}t} \quad (8)$$

Data processing

One milestone in extracting useful information was the processing of the kinetic curves. Three possible ways were tested, one based on sequential linear regression (over appropriate parts of the curve) and the other two being variants of non-linear regression. The detailed discussion and comparison between them made the subject of a previous report [25]. Here, a brief account will be given.

Method A – Sequential linear regression

When the condition $k_{1obs} > 5 k_{2obs}$ is fulfilled [26], at “long reaction times” (high conversions) the first step of the reaction is accomplished and only the second step proceeds. In equation (8), the first exponential term vanishes and it is possible to determine k_{2obs} and γ_2 from the linear logarithmic form (eq. 9):

$$\ln(A - A_\infty) = \ln \gamma_2 - k_{2obs}t \quad (9)$$

In the beginning of the process, the formation of the intermediate prevails. Hence, for “short reaction times” (low conversions), with the now known k_{2obs} and γ_2 , equation (10) can be derived, which permits the determination of γ_1 and k_{1obs} .

$$\ln(A - A_\infty - \gamma_2 e^{-k_{2obs}t}) = \ln \gamma_1 - k_{1obs}t \quad (10)$$

The handling of the data by using the Microsoft Excel program showed that, indeed, for “long times” (after more than 90 % of reaction) the behavior is linear with R^2 between 0.9925 and 0.9990. The plots according to equation (10) were also linear at short times after mixing ($R^2 \in [0.9911 \div 0.9999]$).

However, it became obvious that the condition $k_{1obs} > 5 k_{2obs}$ is not fulfilled. In such case, the accuracy of the k_{obs} values is expected to suffer - more so that of the k_{1obs} values, which would also be affected by the errors in k_{2obs} .

Method B – non-linear regression

Furthermore, the experimental curves were subjected to non-linear fitting with an equation derived from the same reaction model. For this, equation (7) was written in the form below (eq.11), which satisfies the requirements of the software used.

$$Y = F_1 \cdot e^{(-k_{1obs}(X+X_0))} + F_2 \cdot e^{(-k_{2obs}(X+X_0))} + Y_0 \quad (11)$$

$$\text{with } F_1 = 0.0003335 \left(\varepsilon_R - \frac{\varepsilon_I \cdot k_{1obs}}{k_{1obs} - k_{2obs}} + \frac{\varepsilon_P \cdot k_{2obs}}{k_{1obs} - k_{2obs}} \right) \quad (12)$$

$$\text{and } F_2 = 0.0003335 \cdot k_{1obs} \left(\frac{\varepsilon_I - \varepsilon_P}{k_{1obs} - k_{2obs}} \right) \quad (13)$$

and where $Y = A$ (absorbance), $X = t$ (time), $X_0 =$ time delay at the start of data acquisition, $Y_0 =$ a correction factor for base line (the translation of the curve along the Y axis, including A_∞), $0.0003335 = [\text{Cr(VI)}]_0 \cdot l$, and k_{1obs} , k_{2obs} , ε_R , ε_I and ε_P all are as described above.

Two approaches were tested: fitting the curves one by one or fitting groups of curves pertaining to various sets of concentrations. While valuable as a checkup method, the multiple curve fitting will give biased results if a curve affected by large errors happens to be part of the group, hence the single curve fitting was preferred. This was done by the program TableCurve 2D 5.0 (Systat Software). It operates by successive iterations varying the specified parameters in order to get the best fit.

Details of the initialization procedure and the limitations are given elsewhere [25]. An important mention is that the estimates of the input values for the apparent rate constants were based on the results provided by method A. From this point of view, it can be said that method B was used to refine the results of method A.

With good estimates for the input values, very good fits were obtained. The k_{obs} values obtained by method B were in general comparable to those of method A, with method A appearing to have somewhat overestimated k_{1obs} .

The method B should give more accurate results, in the least because the k_{1obs} and k_{2obs} values also satisfy the F_1 and F_2 expressions, a fact that was disregarded in the case of method A. However, it appears that methods A and B are best used in tandem, at least for such cases as the one at hand, with two consecutive steps of comparable rates.

The k_{obs} values used for the kinetic interpretation were as obtained from the nonlinear fitting of single curves (method B) at 420 nm. Tables 1 and 2 show averaged numbers of the three to seven runs (as given in parentheses) performed for each set of concentrations. However, the further kinetic interpretations are based on plots containing the individual values of the two constants.

Table 1. Average values of $k_{1\text{obs}}$ and $k_{2\text{obs}}$, obtained with $[\text{HCrO}_4^-] = 6.67 \cdot 10^{-5} \text{ M}$ and various $[\text{RSH}]$, at three H^+ concentrations ($T = 293 \text{ K}$, $\mu = 0.5 \text{ M}$, $\lambda = 420 \text{ nm}$).

$10^3 \cdot [\text{RSH}]$ (M)	$k_{1\text{obs}} \text{ (s}^{-1}\text{)}$			$k_{2\text{obs}} \text{ (s}^{-1}\text{)}$		
	$10^2 \cdot [\text{H}^+] \text{ (M)}$					
	3.12	0.98	0.31	3.12	0.98	0.31
1.33	0.051 (4)	0.045 (4)	0.029 (3)	0.048 (4)	0.032 (4)	0.028 (3)
1.67	0.070 (4)	0.043 (4)	0.034 (3)	0.057 (4)	0.040 (4)	0.033 (3)
2.66	0.086 (4)	0.060 (4)	0.055 (6)	0.066 (4)	0.052 (4)	0.050 (6)
3.33	0.111 (7)	0.076 (4)	0.067 (6)	0.088 (7)	0.064 (4)	0.059 (6)
4.00	0.130 (4)	0.098 (5)	0.079 (4)	0.101 (4)	0.074 (5)	0.071 (4)
5.00	0.179 (3)	0.113 (3)	0.094 (3)	0.100 (3)	0.079 (3)	0.084 (3)
5.33	0.182 (4)	0.116 (4)	0.100 (4)	0.129 (4)	0.083 (4)	0.091 (4)
6.66	0.216 (4)	0.125 (4)	0.126 (3)	0.148 (4)	0.098 (4)	0.110 (3)
8.00	0.253 (4)	0.160 (4)	0.146 (3)	0.177 (4)	0.102 (4)	0.125 (3)
9.99			0.185 (6)			0.148 (6)

Table 2. Average values of $k_{1\text{obs}}$ and $k_{2\text{obs}}$, obtained with $[\text{HCrO}_4^-] = 6.67 \cdot 10^{-5} \text{ M}$ and various $[\text{H}^+]$, at three RSH concentrations ($T = 293 \text{ K}$, $\mu = 0.5 \text{ M}$, $\lambda = 420 \text{ nm}$).

$10^2 \cdot [\text{H}^+]$ (M)	$k_{1\text{obs}} \text{ (s}^{-1}\text{)}$			$k_{2\text{obs}} \text{ (s}^{-1}\text{)}$		
	$10^3 \cdot [\text{RSH}] \text{ (M)}$					
	5.00	3.33	1.67	5.00	3.33	1.67
0.13			0.033 (3)			0.030 (3)
0.17	0.089 (4)			0.065 (4)		
0.19			0.033 (4)			0.031 (4)
0.23	0.093 (3)			0.066 (3)		
0.29		0.077 (3)			0.047 (3)	
0.31	0.094 (3)	0.067 (6)	0.034 (3)	0.084 (3)	0.059 (6)	0.033 (3)
0.33		0.075 (4)	0.036 (4)		0.052 (4)	0.033 (4)
0.35	0.104 (4)			0.074 (4)		
0.43		0.078 (3)			0.052 (3)	
0.51			0.039 (4)			0.035 (4)
0.53	0.097 (3)			0.074 (3)		
0.65		0.076 (3)			0.054 (3)	
0.79		0.077 (3)			0.054 (3)	
0.98	0.113 (3)	0.076 (4)	0.043 (4)	0.079 (3)	0.064 (4)	0.040 (4)
1.29		0.095 (4)			0.058 (4)	
1.60	0.119 (5)	0.111 (3)	0.052 (4)	0.090 (5)	0.060 (3)	0.047 (4)
1.97		0.105 (3)			0.075 (3)	
2.51	0.142 (4)	0.121 (4)	0.060 (4)	0.095 (4)	0.080 (4)	0.052 (4)
3.12	0.179 (3)	0.111 (7)	0.070 (4)	0.100 (3)	0.088 (7)	0.057 (4)
3.93	0.193 (4)		0.075 (4)	0.114 (4)		0.067 (4)
5.01		0.132 (4)			0.120 (4)	
6.24	0.252 (3)	0.155 (3)	0.095 (4)	0.135 (3)	0.131 (3)	0.085 (4)
7.93	0.277 (3)	0.195 (4)	0.107 (3)	0.156 (3)	0.139 (4)	0.093 (3)
9.84	0.304 (3)	0.233 (3)	0.119 (3)	0.215 (3)	0.175 (3)	0.108 (3)

Kinetic interpretation

Having established that the process consists of two observable steps, the apparent first-order rate constants for each step are functions of the reaction conditions (excess RSH concentration, acidity, temperature and ionic strength).

Intermediate formation

As the concentrations of the organic substrate and the mineral acid are in large excess, the k_{1obs} rate coefficients (dimensions s^{-1}) correspond to first order in $HCrO_4^-$, which is the limiting reactant. Based on equation (4), taking into account both directions of the equilibrium, k_{1obs} can be written as

$$k_{1obs} = k_1[RSH]_0^a[H^+]_0^b + k_{-1}[H^+]_0^b \quad (14)$$

To obtain the partial orders with respect to RSH (a) or H^+ (b), we first assume that in the beginning of the reaction, the first term prevails. Making use of log – log plots, the partial orders can be assessed. At constant acidity, the slope of the regression line will give the reaction order with respect to RSH, whose excess was varied. Conversely, at constant excess of RSH and with the mineral acid varied, the order with respect to H^+ will be found. Figure 3 illustrates those plots.

The figure shows a linear behavior when [RSH] was varied, giving an integer order of 1, and a curve when varying $[H^+]$. At low acid concentration, the order with respect to hydrogen ion is near zero and increases as the concentration of the mineral acid is raised. This behavior is systematic within all experimental conditions employed (various excesses of RSH and various temperatures). Hence, the reaction order in H^+ is fractional between zero and one, with an increasing trend as the acidity is increased.

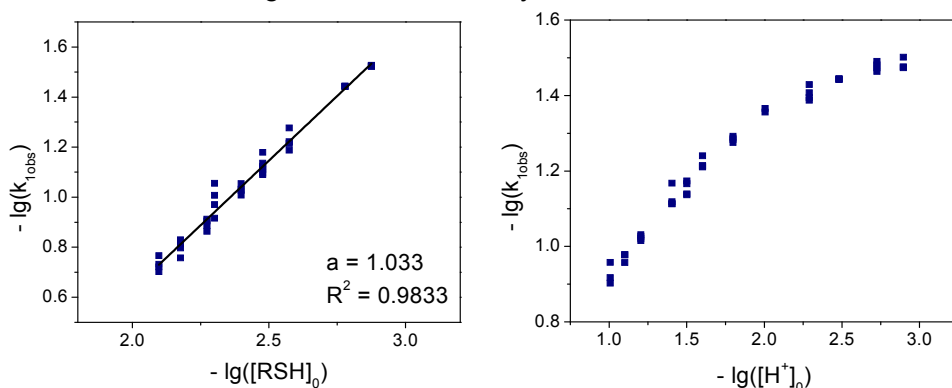


Figure 3. Log – log plots to determine the partial orders with respect to RSH (at $[H^+] = 0.0312$ M) and to H^+ (at $[RSH] = 0.0050$ M) for the intermediate formation.

From a mechanistic point of view, this result can be interpreted by the intervention of two parallel reaction paths, one of zeroth order, and one of first order in H^+ , their relative importance depending on the range of acid concentration.

This outcome is in good agreement with that obtained by us in the previous work that dealt with the buildup of the intermediate in this reaction by means of a stopped-flow experimental approach and using the initial rates method ($n_{Cr(VI)}=1.07\pm 0.08$; $n_{RSH}=1.02\pm 0.07$; $n_{H^+}=0.67\pm 0.06$) [22].

The conclusion to be drawn from these facts and the micro-reversibility principle is that the apparent first-order rate constant for the intermediate formation should be written as a sum of the two parallel paths:

$$k_{1obs} = (k_1^0 [RSH] + k_{-1}^0) + (k_1^H [H^+] [RSH] + k_{-1}^H [H^+]) \quad (15)$$

To evaluate the rate constants, the data were analyzed by plotting k_{1obs} as a function of excess thiol at constant acidity and as a function of acidity at constant thiol concentration. The graphs in Figures 4 and 5 were obtained.

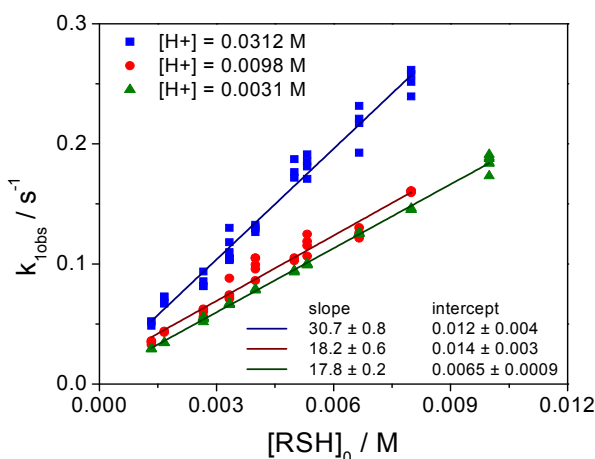


Figure 4. Linear dependence of k_{1obs} on $[RSH]_0$, with the slope $k_1^0 + k_1^H[H^+]$.

The intercepts in Figure 4 are slightly positive (statistically different from zero) but affected by large errors. In theory, they might represent the $k_{-1}^0 + k_{-1}^H[H^+]$ contribution to the apparent first-order rate constant. The slope is the $k_1^0 + k_1^H[H^+]_0$ ($M^{-1}s^{-1}$) term in k_{1obs} . From the slopes of the lines in Figure 4, rate constants $k_1^0 = (15\pm 2) M^{-1}s^{-1}$ and $k_1^H = (5\pm 1) \cdot 10^2 M^{-2}s^{-1}$ were obtained for the formation of the intermediate.

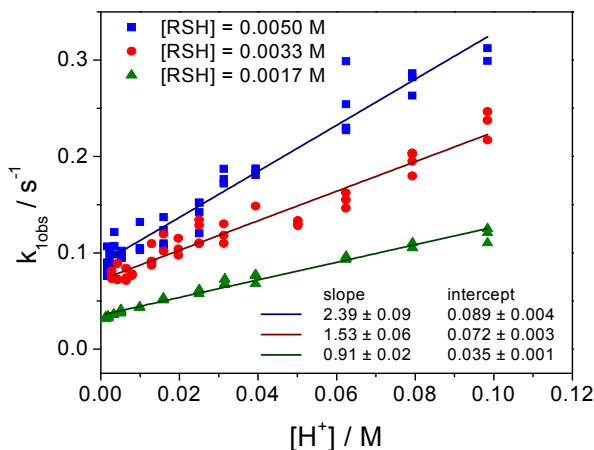


Figure 5. Linear plots of $k_{1\text{obs}}$ as a function of $[\text{H}^+]$.

From the graph in Figure 5, with the intercepts differing from zero, it is obvious that there is a term of zeroth order with respect to H^+ . The same feature was observed upon different conditions of temperature. The slopes of the straight lines correspond to a process first-order in H^+ . The linear regression parameters yield values of $k_1^0 = (16 \pm 3) \text{ M}^{-1}\text{s}^{-1}$ and $k_1^{\text{H}} = (4.4 \pm 0.6) \cdot 10^2 \text{ M}^{-2}\text{s}^{-1}$, in fairly good agreement with those obtained from the effect of thiolactic acid concentration.

Kinetics of the redox process (decay of the intermediate).

In order to determine reaction orders with respect to the reactive species, the apparent first-order rate constants $k_{2\text{obs}}$ were used as dependent on the excess concentration of thiolactic acid or hydrogen ion concentration. Graphs of the type exemplified in Figure 6 below were obtained under various conditions.

In the case of the organic substrate, the graphs were linear to a good approximation and a fractional order between zero and one was obtained in all cases. This observation can be interpreted as the occurrence of two competing processes, one of zeroth and the other of first order in RSH. From a mechanistic point of view this could be considered as a monomolecular decomposition of the intermediate, to form Cr(V) and a thiyl free radical RS^\bullet , along with a bimolecular process involving the complex and another RSH molecule, yielding the disulfide and Cr(IV) in a bi-equivalent electron transfer. On the other hand, the fractional order can be viewed as an expression of the *one-plus* form [27,28], as suggested by the presence of the pre-equilibrium of intermediate formation.

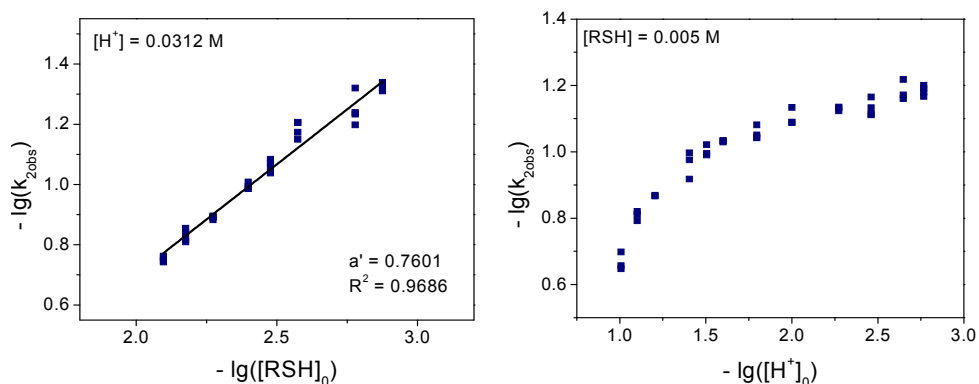


Figure 6. Log-log plots to determine the partial orders with respect to RSH and H^+ for the decay of the intermediate.

In the case of the involvement of hydrogen ions, once again a fractional order of less than 1 was found, increasing with rising acidity, as in the case of formation of the intermediate $RSCrO_3^-$. These facts can also be interpreted by two parallel paths or by a *one-plus* dependence.

Hence, there are four possibilities to describe the intermediate decay, governed by the following equations:

1) 4 parallel steps:

$$k_{2obs} = k_2^0 + k_2^H [H^+] + k_3^0 [RSH] + k_3^H [RSH][H^+] \quad (16)$$

2) 2 parallel steps (with or without H^+) and a pre-equilibrium effect on RSH

$$k_{2obs} = (k_2^0 + k_2^H [H^+]) \frac{\alpha [RSH]}{1 + \beta [RSH]} \quad (17)$$

3) 2 parallel steps (with or without a second RSH) and a pre-equilibrium effect on H^+

$$k_{2obs} = (k_2^H + k_3^H [RSH]) \frac{\alpha' [H^+]}{1 + \beta' [H^+]} \quad (18)$$

4) pre-equilibrium effect on both RSH and H^+

$$k_{2obs} = \frac{\alpha'' [H^+][RSH]}{1 + \beta'' [RSH] + \gamma'' [H^+]} \quad (19)$$

The equations (17) to (19) are of *one-plus* type. Equations (18) and (19) stipulate a decreasing effect of H^+ which was not found experimentally.

Equations (16) and (17) imply that a plot of $k_{2\text{obs}}$ as a function of the acidity should yield a line with some positive intercept. This is indeed the case, as Figure 7 clearly demonstrates.

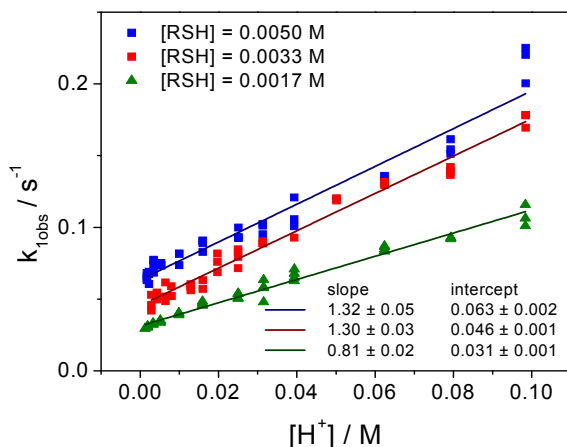


Figure 7. Linear dependence of $k_{2\text{obs}}$ on $[\text{H}^+]$.

On the other hand, for the dependence of $k_{2\text{obs}}$ on the organic substrate, equation (17) predicts a decreasing effect of RSH, meaning a curved shape with the gradient diminishing as the RSH concentration is increased. Conversely, an increasing effect of RSH would validate the linear equation (16). As shown in Figure 8, the behavior predicted by equation (17) was obtained.

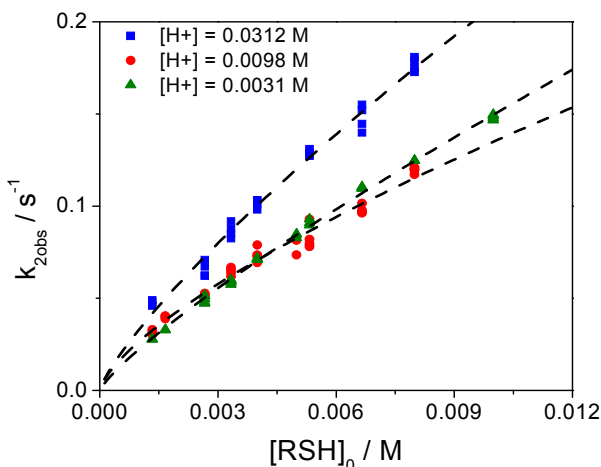


Figure 8. Dependence of $k_{2\text{obs}}$ on the thiolactic acid concentration.

Equation (17) also stipulates a slope and an intercept of the form:

$$\text{Slope} = k_2^H [H^+] \frac{\alpha[RSH]}{1 + \beta[RSH]} \quad (20) \quad \text{Intercept} = k_2^0 \frac{\alpha[RSH]}{1 + \beta[RSH]} \quad (21)$$

Once again, lines of declining slopes were obtained when plotting the intercepts and the slopes in Figure 7 against the concentration of thiolactic acid, thus giving further support to the rate equation (17).

Ionic strength effect

The increase of ionic strength showed no effect on the formation of the thioester, while it slightly diminished the rate of its consumption. This is in agreement with the involvement of a neutral molecule in building of the intermediate, and some interaction of particles with opposite charges in its decomposition by a redox process.

Determination of activation energies

Because of the complexity of the system, only experimental activation energies could be determined with our data from the dependence of either $k_{1\text{obs}}$ or $k_{2\text{obs}}$ with temperature. Seven temperatures, between 280 and 315 K, were used at five perchloric acid concentrations. The Arrhenius plots obtained had R^2 between 0.990 and 0.997. Their results are given in Table 3. The small activation energies for the electron transfer decay suggest the presence of one or more exothermal equilibria, which sustain energetically the two reaction steps.

Table 3. Experimental activation energies (each number has an error of less than 2%).

10 ² [H ⁺] (M)	E _a (kJ/mol)	
	Intermediate formation	Redox process
5.0	33.5	34.1
3.2	35.6	36.4
2.0	34.6	35.3
1.0	34.9	35.2
0.63	33.5	33.9
0.31	33.5	33.6
Mean:	34 ± 3	35 ± 2

Extra-kinetic investigations

The complexity of the system required some non-kinetic information in order to suggest a reaction mechanism. The literature mentions the implication of thiyl radicals in the majority of thiol oxidation reactions [6, 10, 29]. Therefore, we used the system to initiate the polymerization of methyl methacrylate. An increase in temperature of 1 to 1.2 °C was measured as compared to the reacting system without monomer in a small calorimeter. The concentrations were as in the kinetic runs. At the end of the process, some polymer was isolated.

ESR spectra were also recorded in order to identify paramagnetic species such as Cr(V) and thiyl or other organic radicals. The obtained results were compared to g values given in the literature [29]. Working in a flow system, with $[\text{Cr(VI)}]_0 = 2.5 \cdot 10^{-3} \text{ M}$ and $[\text{RSH}]_0 = 1.5 \cdot 10^{-2} \text{ M}$, the spectra presented in Figure 9 were obtained.

The species were assigned based on their g values: $g = 1.985$ and $g = 1.988$ were specific to oxo-complexes of Cr(V), and $g = 2.002$ to an organic radical. It should be noted that the two parts of the spectrum shown in Figure 9 were recorded using different amplification settings of the ESR spectrometer.

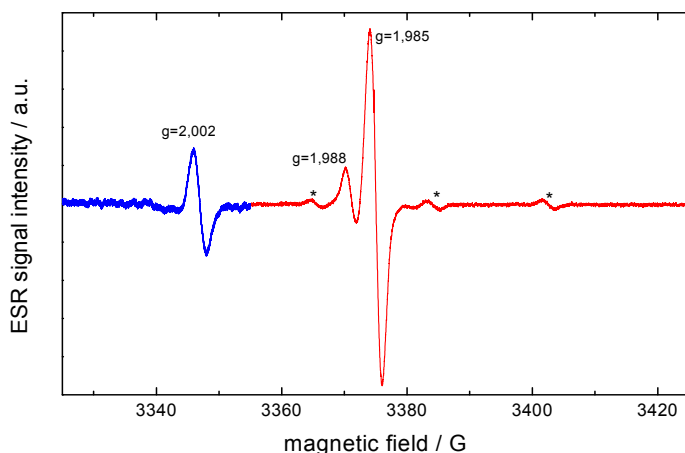


Figure 9. Paramagnetic intermediates: Cr(V) (red) and organic radical (blue). Signals marked with* are ^{53}Cr satellites of the main signal at $g = 1.985$. The last of the four expected lines overlaps with the signal of the organic radical at $g = 2.002$.

In a stopped flow variant, at $g = 1.985$ and $g = 2.002$ kinetic curves were recorded taking the normalized intensity of the signals, as presented in Figure 10. They can only be interpreted in a qualitative manner.

It is of note that Cr(V) is not an extremely active species toward the substrate; its lifetime is rather long. The signals for Cr(V) and the organic radical behave in a similar fashion. However, the occurrence of the maximum

of the organic radical at a slightly later time than that of the Cr(V) might be explained by one of the following two things: that Cr(V) is formed in a previous step than the organic radical, or that the organic radical might be formed together with Cr(V), but more is added as a result of Cr(V) own reduction, probably in a fashion similar to the reduction of Cr(VI).

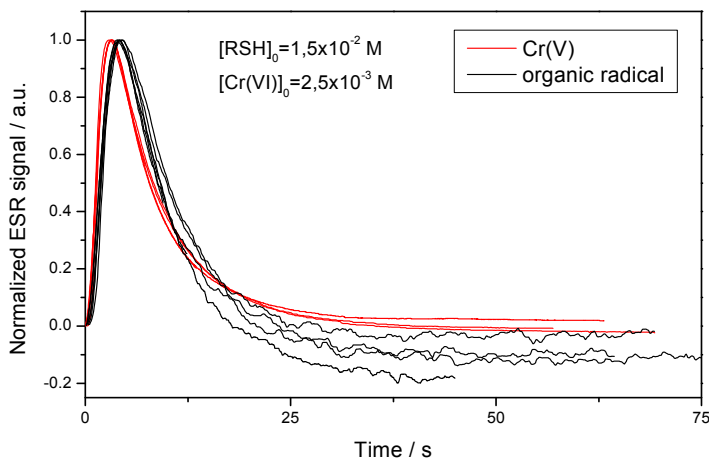
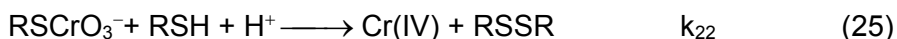
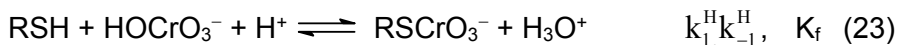
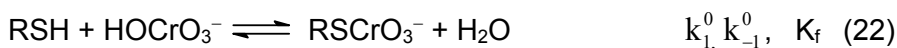


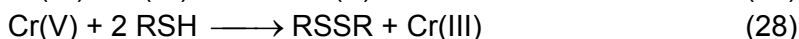
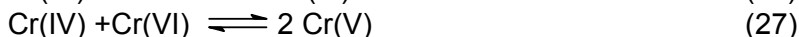
Figure 10. Kinetic curves for the paramagnetic intermediates observed during the reaction.

Reaction mechanism

Based on the kinetic and extra-kinetic results presented, the following networks of reactions seem most probable:



No precise affirmation can be made on the successive steps following the rate-determining ones. To get the correct stoichiometry, Cr(IV) species should react further to form final products and generate Cr(V). The processes are characterized by higher rate constants and take place as fast as the corresponding intermediate species are formed, with the exception of (28).



If sequence 24-28 was operative, under excess of RSH it seems likelier that the RS^{\bullet} should be formed before Cr(V), which contradicts the information in Figure 10.

An alternative and kinetically indistinguishable reaction sequence, with the rate determining steps as one-equivalent electron transfer and the formation of Cr(V) and a disulfide ion radical, is:



The disulfide radical anion is a species with an electron in the anti-bonding S-S link, first evidenced by β ray bombardment of thiol solutions [30] and is much more stable as compared to the thiyl radical. Using MO calculations, formation enthalpies of -1064 kJ/mol for $RSSR^{\bullet}$ and -268 kJ/mol for RS^{\bullet} were computed. Based on this and on the fact that, while not necessarily supported by the interpretation of Figure 10, it is also not contradicted by it, we incline to consider this way as being operative. Another argument in its favor is that an order superior to one and a *one-plus* type rate law has been found by us at the oxidation of thiolactic acid by hexacyanoferrate (III), which is a one-equivalent oxidizing agent [31].

However, the rate law deduced from each of the two variants of the mechanism, with either (24–25) or (29-30) steps as rate determining, is:

$$-\frac{d[HCrO_4^-]}{dt} = \frac{k_{21}K_f[RSH]^2}{1 + K_f[RSH]}[HCrO_4^-] + \frac{k_{22}K_f[RSH]^2[H^+]}{1 + K_f[RSH]}[HCrO_4^-] \quad (31)$$

in agreement with the experimental one.

CONCLUSIONS

The reaction between thiolactic acid (RSH) and chromium (VI) proceeds *via* the formation of an intermediate of esteric type, evidenced by spectral data. The reaction orders for both the formation and decay of the intermediate have been assessed, with respect to the species participating in each step, respectively.

For both RSH and $HCrO_4^-$ reaction orders of 1 have been found for the first step, indicating a 1:1 composition of the intermediate complex. In acidic environment, two parallel paths are available for the intermediate formation: not assisted or assisted by one hydrogen ion.

A first order has been found with respect to the thioester for its decay in an electron transfer path, and a fractional one, between 0 and 1 with thiolactic acid. Since the thioester already contains one substrate molecule,

by means of the pre-equilibrium of its formation, the overall reaction order for the thiolactic acid is between 1 and 2. The two parallel paths, involving or not the H^+ continue to be operative.

Taking into account all these, the extra-kinetic proofs of Cr(V) and of free radicals, as well as the stoichiometry, it was possible to advance a reaction mechanism which gives rise to a rate law in accordance with all these features.

EXPERIMENTAL SECTION

All chemicals employed in the study were of certified analytical reagent grade from commercial sources, and used without further purification. The solutions were prepared in demineralised and tetra-distilled water. Stock solutions of $HClO_4$ and $NaClO_4$ were prepared and standardised by titration with a $NaOH$ solution of known factor. Aliquots of the $NaClO_4$ solution were passed over a cationic resin Virolyte C-100 (Victoria, Romania) in the H-form, and then the resulted acid was titrated. The solution of thiolactic acid was freshly prepared and standardised iodometrically before each set of runs.

The course of the reaction was followed spectrophotometrically under static conditions at 420 nm, by using a Jasco V-530 spectrophotometer interfaced to a computer for data acquisition and equipped with a cell holder connected to a thermostat. A 5-cm path length quartz cuvette has been used. The process was initiated by injecting 1 ml of thermostated chromic acid solution directly into the cell, over the mixture of the other reactants. The mixing time did not exceed 1 second. The use of a calibrated syringe with a fine needle was required in order to ensure an appropriate mixing upon injection; this made some turbulence unavoidable and the first 1-3 seconds of the data recording not entirely reproducible.

Three to seven replicate runs were performed for each set of experimental conditions. These conditions usually involved $T = 293 \pm 0.1$ K, $\mu = 0.5$ M ($NaClO_4$), Cr(VI) always as the limiting reactant ($6.67 \cdot 10^{-5}$ M) and RSH and H^+ in high enough excess so that their concentrations could be considered with good approximation invariable. A few lower excesses were used as well in the case of RSH, in an attempt to enlarge the range of concentrations tested and since at higher excesses the reaction became too fast to follow for batch conditions. The range of concentrations spanned was $1.33 \cdot 10^{-3}$ to $9.99 \cdot 10^{-3}$ M for RSH and $1.3 \cdot 10^{-3}$ to $9.84 \cdot 10^{-2}$ M for H^+ .

The stoichiometry of the process was determined first by means of spectrophotometrical titration. Various mixtures, with initial known molar ratio were allowed to react to completion (at least 8 half-lives) at room temperature, constant acidity of 0.01 M and constant ionic strength of 0.5 M.

The measurements were done at 350 nm. To make sure that the completion has been reached, the mixtures were tested both after 3 and after 10 hours, with similar results. The final absorbance values were measured and compared to the one obtained with a solution containing all reactants, except for the thiolactic acid. Several experiments were made involving iodometrical titration of the remaining substrate. Six mixtures were allowed to react under excess RSH and H^+ conditions similar to the smallest ones used in the kinetic runs, but with all the concentrations being 10 times higher. In such case, the reaction had reached completion already during the mixing of the reactants. Nevertheless, the mixtures were then set to rest for about half an hour, after which the remaining thiolactic acid was titrated iodometrically. For comparison, six blank solutions (containing RSH but not $Cr(VI)$) were treated in a similar fashion and titrated as well.

Using the system to initiate polymerisation of methyl methacrylate and measuring the temperature increase in a small calorimeter, the involvement of free radicals was checked.

Also, ESR studies were made, under static or dynamic regime to detect and monitor paramagnetic species as $Cr(V)$ or organic free radicals.

ACKNOWLEDGMENTS

The authors would like to thank Prof. G. Grampp, Institute of Physical and Theoretical Chemistry, Graz University of Technology, Austria, for providing access to the ESR facility and Dr. K. Rasmussen, European Space Research and Technology Centre, European Space Agency, Netherlands, for insight on the ESR data.

REFERENCES

1. V. Bianchi, A. G. Lewis, *Toxicological & Environmental Chemistry*, **1987**, *15*, 1.
2. P. H. Connert, K. E. Wetterhahn, "Metabolism of the carcinogen chromate by cellular constituents", In: *Inorganic Elements in Biochemistry. Structure and Bonding*, Springer-Verlag, Berlin, Heidelberg, **1983**, *54*, 93.
3. M. D. Cohen, B. Kargacin, C. B. Klein, M. Costa, *Critical Reviews in Toxicology*, **1993**, *23*, 255.
5. S. Mishra, R. N. Bharagava, *Journal of Environmental Science and Health, Part C*, **2016**, *34*, 1.
4. R. Saha, R. Nandi, B. Saha, *Journal of Coordination Chemistry*, **2011**, *64*, 1782.
6. I. Bâldea, D.-M. Sabou, *Studia Universitatis Babeş-Bolyai, Chemia*, **2001**, *46(1-2)*, 17 and references therein.

7. U. Klänig, M. C. R. Symons, *Journal of the Chemical Society*, **1961**, 3204.
8. N. Bailey, A. Carrington, K. A. K. Lott, M. C. R. Symons, *Journal of the Chemical Society*, **1960**, 290.
9. M. Cohen, F. H. Westheimer, *Journal of the American Chemical Society*, **1952**, *74*, 4387.
10. A. McAuley, M. A. Olatunji, *Canadian Journal of Chemistry*, **1977**, *55*, 3328; *ibid.*, **1977**, *55*, 3335.
11. G. P. Haight, E. Perchonock, P. Emmenegger, G. Gordon, *Journal of the American Chemical Society*, **1965**, *87*, 3835.
12. K. B. Wiberg, H. Schäfer, *Journal of the American Chemical Society*, **1969**, *91*, 933.
13. J. H. Espenson, *Accounts of Chemical Research*, **1970**, *3(10)*, 347.
14. V. P. Roldán, V. A. Daier, B. Goodman, M. I. Santoro, J. C. González, N. Calisto, S. R. Signorella, L. F. Sala, *Helvetica Chimica. Acta*, **2000**, *83*, 3211.
15. D. A. Dixon, N. P. Sadler, T. P. Dasgupta, *Journal of the Chemical Society, Dalton Transactions*, **1993**, *23*, 3489.
16. G. P. Haight, G. M. Jursich, M. T. Kelso, P. J. Merrill, *Inorganic Chemistry*, **1985**, *24*, 2740.
17. J. F. Perez-Benito, C. Arias, R. M. Rodriguez, *Journal of Physical Chemistry A*, **2001**, *105*, 1150.
18. S. Signorella, M. I. Frascaroli, S. García, M. Santoro, J. C. González, C. Palopoli, V. Daier, N. Casado, L. F. Sala, *Journal of the Chemical Society, Dalton Transactions*, **2000**, 1617.
19. S. N. Mahapatro, M. Krumpolc, J. Roček, *Journal of the American Chemical Society*, **1980**, *102*, 3799.
20. P. Subramaniam, N. T. Selvi, *American Journal of Analytical Chemistry*, **2013**, *4*, 20.
21. D. C. Ramdon, D. A. Dixon, T. P. Dasgupta, *Inorganic Reaction Mechanisms*, **2004**, *5(3)*, 1.
22. D.-M. Sabou, *Studia Universitatis Babeş-Bolyai, Chemia*, **2014**, *59(4)*, 183.
23. J. Y. Tong, E. L. King, *Journal of the American Chemical Society*, **1953**, *75*, 6180.
24. N. N. Greenwood, A. Earnshaw, "Chemistry of the Elements", 2. Edition, Butterworth-Heinemann, Oxford, UK, **1997**, chapter 23.
25. D.-M. Sabou, A. Csavdári, *Muszaki Szemle (Technical Review)*, **2015**, *66*, 26.
26. T. Carrington, *International Journal of Chemical Kinetics*, **1982**, *14(5)*, 517.
27. I. Băldea, D.-M. Sabou, A. Csavdari, *Studia Universitatis Babeş-Bolyai, Chemia*, **2007**, *52(1)*, 19.
28. A. Csavdári, I. Băldea, D.-M. Sabou, *Studia Universitatis Babeş-Bolyai, Chemia*, **2007**, *52(3)*, 113.
29. A. Levina, L. Zhang, P. A. Lay, *Journal of the American Chemical Society*, **2010**, *132*, 8720 and references therein.
30. Z. M. Hoffman, E. Hayon, *Journal of the American Chemical Society*, **1972**, *94(23)*, 7950.
31. I. Băldea, D.-M. Sabou, A. Csavdári, *Revue Roumaine de Chimie*, **2009**, *54(10)*, 791.

COMPLEXES OF SELECTED TRANSITION METAL IONS WITH N-MODIFIED GLYCINE AS LIGAND

CARMEN SACALIS^{a,*}, FIRUTA GOGA^a, CRISTINA SOMESAN^b

ABSTRACT. A novel series of transitional metal complexes of Cu(II), Co(II), Ni(II), Zn(II) and Fe(II) with *N*-modified glycine as ligand provide from phenylserinol were synthesized and characterized *via* elemental analysis, MS, IR, UV-VIS thermogravimetric analysis and ESR. The thermal stability of the ligand and synthesized complexes was discussed in the 20-1000°C temperature range. The results indicate that the organic compound acts as a bidentate ligand, its coordination involving the carboxylate oxygen and the nitrogen atom belonging to the amino group of the glycine fragment. The shape of ESR spectrum for cooper complex at room temperature suggest an axial symmetry around the metallic ions ($g_{\parallel}=2.427$, $g_{\perp}=2.063$).

Keywords: *glycine, transition metal complexes, thermal behavior, spectroscopic studies.*

INTRODUCTION

Complexes of transition metals with amino acids like glycine, have received much attention because they proved biological activity such as antibacterial, antimicrobial or antifungal activities [1-4]. Glycine derivatives including complexes with different transition metals with antibacterial activity are also known [5, 6].

Other research indicated that transition metal complexes with *N*-substituted glycine act as hydrogen buffer in biological reactions [7].

N-modified glycines have a lot of applications in biomedicine as analogue of anticonvulsant and antiepileptic agent Milacemide or as *building-units* for *N*-backbone cyclic peptides [8, 9].

^a Babeş-Bolyai University, Faculty of Chemistry and Chemical Engineering, 11 Arany Janos str., RO-400028, Cluj-Napoca, Romania.

* Corresponding author: cbatiu@chem.ubbcluj.ro

^b Babeş-Bolyai University, Faculty of Physics, 1 Mihail Kogalniceanu str., RO-400084, Cluj-Napoca, Romania.

Recently studies of transition metal complexes of mixed ligand with glycine report biological activity too [10, 11].

Taking into account the important biochemical applications of *N*-modified glycine, we have recently reported a new series of transition metal complexes with an other *N*-modified glycine as a ligand, derived from *p*-nitrophenylserinol [12].

In continuation of our recent findings in the field of transition metal complexes with *N*-modified glycine as ligand, we report herein the preparation of a new series of metal complexes with other ligand (**L**) prepared and reported by us, namely 2-[(1*S*,2*S*)-1,3-dihydroxy-1-phenylpropan-2-yl-amino] acetic acid (Figure1) [13]. This work, that presents the synthesis, the spectroscopic and thermogravimetric investigation the metal complexes of ligand **L** whit Cu(II), Co(II), Ni(II), Zn(II) and Fe(II) ions, has the same objectives as the above quoted study.

The ligand **L**, an optically active *N*-modified glycine, was obtained by a literature procedure like the non-nitrated analogue, with satisfactory yield [13].

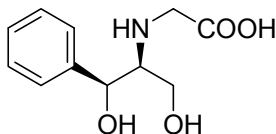


Figure 1. Structure formula of ligand **L**: 2-[(1*S*,2*S*)-1,3-dihydroxy-1-phenylpropan-2-yl-amino]acetic acid

RESULTS AND DISCUSSION

The structure of the metal complexes

The complexation reaction of Cu(II), Co(II), Ni(II) Fe(II) and Zn(II) salt with the aqueous solution of the ligand **L** in each case yields a solid product. Except Zn(II) complex which is colorless, all are colored, microcrystalline and stable at room temperature. They are also insoluble in water (the ligand is very soluble) or non-polar organic solvents but soluble in methanol or DMSO. The different and much higher melting points of these products, as well their different colors when compared to that of the ligand **L**, indicate the formation of metal complexes.

Their elemental analysis data is in agreement with the molar ratio Metal : Ligand = 1 : 2. In exchange the elemental analysis data indicate also that the ligand is hydrated with one mole of water, the copper complex with

one mole of water too, but the other metal complexes are hydrated with two mole of water. The presence of water outside or within the sphere of coordination is demonstrated by thermal analysis data (Table 2).

The UV-VIS spectra in DMSO for the complexes (**1-5**) indicate a slight hypsochromical shift by 3.5-7.5 nm, but a considerable hyperchromic increase effect of absorbance comparative to the spectrum of the initial ligand (**L**), except Zn complex, like the other similar complexes [3, 12, 14, 15].

On the other hand, the HRMS spectrum for the metal complexes proves the complexation process (Figure 2a-c). The M+1 peak supports the complexation idea with the transition metal ions, for each of them.

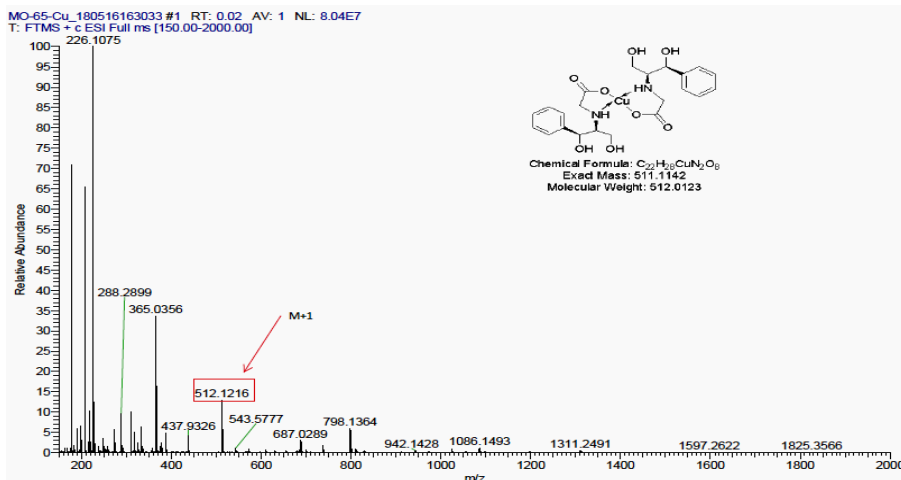


Figure 2a. HRMS spectrum (ESI) of cooper complex (**1**)

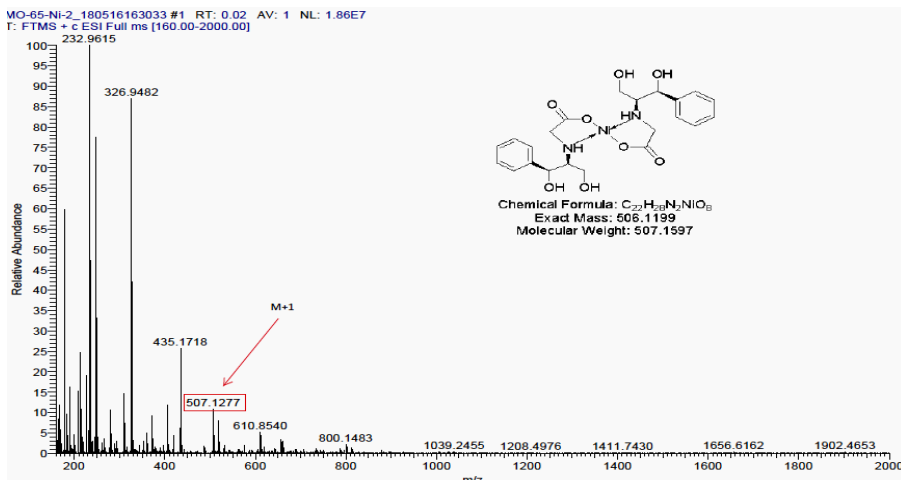


Figure 2b. HRMS spectrum (ESI) of nickel complex (**3**)

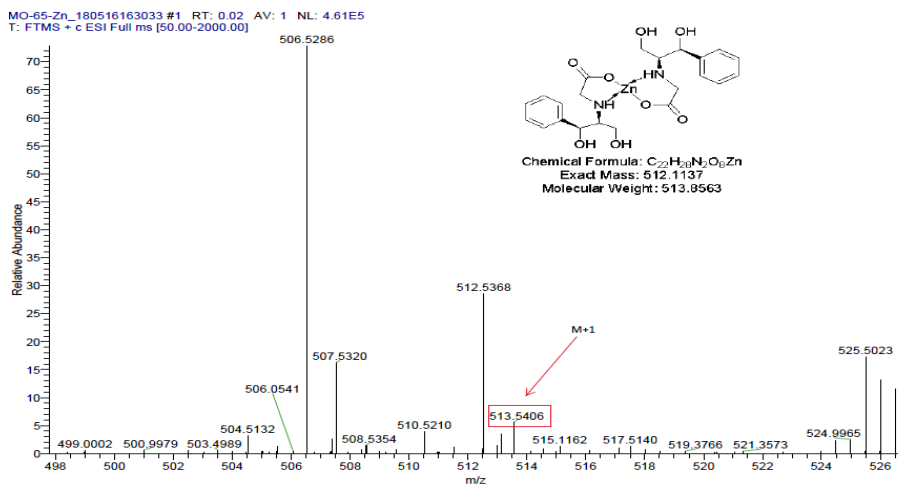


Figure 2c. HRMS spectrum (ESI) of zinc complex (**5**)

The bonding of the ligand to different metal ions was investigated also by comparing the IR spectrum of the free ligand with those of the metal complexes. IR spectrum of free ligand undergoes a certain modification when coordinated to a metal ion [15-20]. Partial assignments of the IR absorption bands observed for the free ligand and the metal complexes are given in Table 1

Table 1. Some IR absorption bands (cm⁻¹) of the ligand **L** and its metal complexes (**1-5**)

Assignment (cm ⁻¹)	<i>V</i> _{OH} , <i>V</i> _{O-H-O}	<i>V</i> _{NH}	<i>V</i> (COO ⁻) _{as}	<i>V</i> (COO ⁻) _s	$\bar{\delta}$ _{NH}	<i>V</i> _{M-O}	<i>V</i> _{M-N}	<i>V</i> _{M-H₂O}
C ₁₁ H ₁₇ NO ₅ (L)	3367	3147	1651	1411	1568 1494	-	-	-
C ₂₂ H ₃₀ CuN ₂ O ₉ (1)	3293	3034	1613	1386	1494 1456	421	541	763
C ₂₂ H ₃₂ CoN ₂ O ₁₀ (2)	3324	3086	1600	1383	1493 1456	429	561	763
C ₂₂ H ₃₂ NiO ₁₀ (3)	3316	3086	1603	1385	1494 1456	432	564	763
C ₂₂ H ₃₂ FeN ₂ O ₁₀ (4)	3393	2937	1628	1363	1495 1455	459	599	768
C ₂₂ H ₃₂ N ₂ O ₁₀ Zn (5)	3505 3402 3341 3302	2933	1608	1384	1495 1456	427	563	764

In the spectral region 3300-3500 cm^{-1} a wide band formed by 2-3 overlapped bands is observed that may be assigned to ν_{OH} and $\nu_{\text{O-H-O}}$ vibration due intra- and intermolecular hydrogen bonding in the crystalline state. The vibrational frequencies related to $\nu(\text{COO}^-)_{\text{as}}$ at 1651 cm^{-1} and $\nu(\text{COO}^-)_{\text{s}}$ at 1411 cm^{-1} in ligand is shifted toward lower value in the spectra of the complexes with 25-48 cm^{-1} for the $\nu(\text{COO}^-)_{\text{as}}$ and 23-51 cm^{-1} for the $\nu(\text{COO}^-)_{\text{s}}$, respectively [3, 18]. Modified are also observed in the case of ν_{NH} or δ_{NH} frequencies in the metal complexes comparative to the free ligand [3, 18]. These bands of the metal complexes were shifted to lower value due to chelating with metal ions. The new bands appearing in the range 421-427 cm^{-1} are assigned to $\nu_{\text{M-O}}$, while those at 541-563 cm^{-1} could be attributed to $\nu_{\text{M-N}}$ [15-21]. In the case of all metal complexes a $\nu_{(\text{M-H}_2\text{O})}$ vibration band appears at 763-768 cm^{-1} , which is characteristic for coordinated water molecules in the inner coordination sphere [15].

Thermal investigation

The thermal decomposition of the ligand **L** and its metal complexes (**1-5**) was studied by means of a derivatograph in air atmosphere. Thermal stability domains, decomposition phenomena and their assignments are summarized in Table 2 and Figure 3a-c.

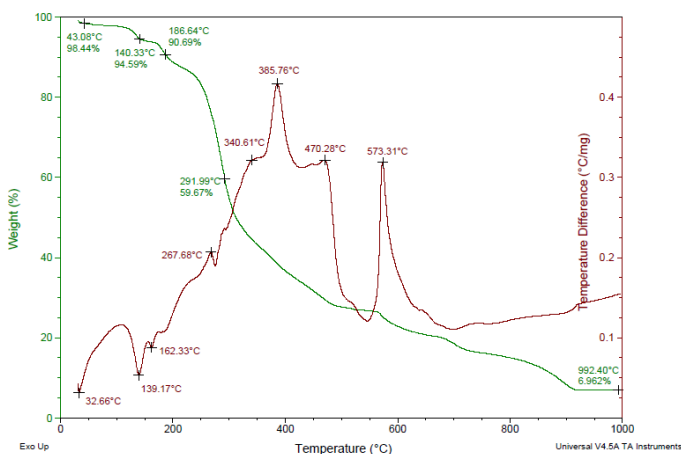


Figure 3a. TG-DTA diagram for the ligand **L**

The thermal analysis results reveal that the ligand (**L**) is hydrated with a water molecule and the decomposition involved three steps. The first step of decomposition occurs within temperature range 20-187 $^{\circ}\text{C}$ has three

endothermic peaks at 33°C, 139°C and 162°C. The first small endothermic peak with a mass loss of 1.56% represented the loss of residual water present in the pores, phenomenon which could be explained by the synthesis of the ligand from aqueous solution [13]. The next two peaks with a mass loss of 3.85% (calcd. 3.71%), respectively 3.90% (calc. 3.70%) could be assigned to loss very slowly the water molecule. Probably the water is held inside to ligand until the melting point (m.p. = 145-147°C, lit. [13].) The second stage of decomposition was observed in the temperature range 187-292°C with an exothermic at 267°C and correspond to a glycine rest splitting (exp. 31.02%, calcd. 32.86%).

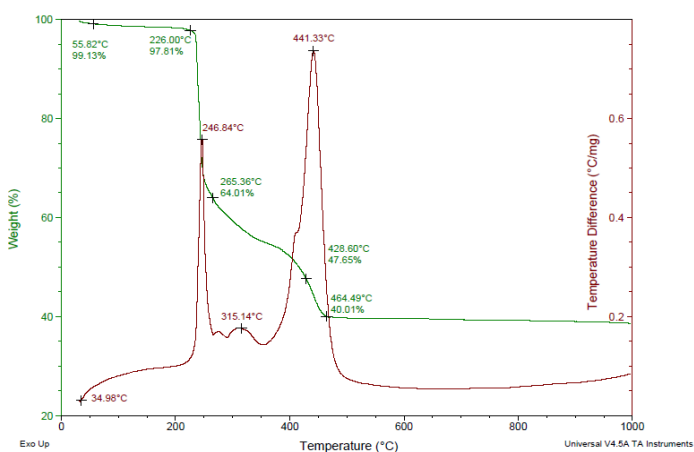


Figure 3b. TG-DTA diagram for the copper complex (1)

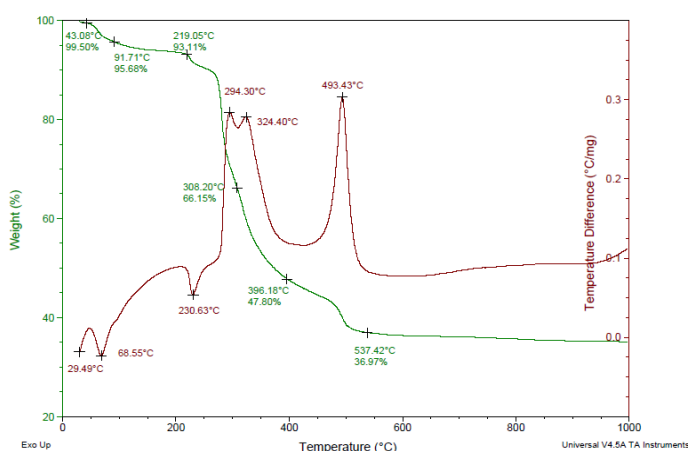


Figure 3c. TG-DTA diagram for the zinc complex (5)

Table 2. Thermal analysis data of the ligand **L** and its metal complexes (**1-5**) in air atmosphere (10°C/min)

Compound	Heat effect on DTA	Temperature (°C)			Mass loss (%)		Assignment
		T _i	T _{max}	T _f	Calcd.	Exp.	
L•H ₂ O	Endo	20	33	43	-	1.56	-residual water present inside pores
	Endo	43	139	140	3.71	3.85	-0.5 mole of hydrating water which is retained inside the molecule
	Endo	140	162	187	3.70	3.90	-melting accompanied by 0.5 mole of hydrating water loss
	Exo	187	267	292	32.86	31.02	-glycine rest (C ₂ H ₄ O ₂ N) and oxidation process
	Exo	292	341 386 470 573	1000	59.73	59.71	-pyrolysis of organic rest
[Cu(L) ₂ •H ₂ O] (1)	Endo	20	35	226	-	0.87	-residual water present inside pores
					-	1.32	-residual water present inside pores
	Exo	226	246	265	32.36	33.60	-melting, 1mole of water and 2 moles of glycine rest loss
	Exo	265	315 441	1000	67.64	24.01 40.01	-quickly cleavage and pyrolysis of organic rest CuO and ash
[Co(L) ₂ •2H ₂ O] (2)	Endo	20	36	245	-	0.61 2.71	-residual water present inside pores
	Exo	245	283	298	-	34.04	-melting, 2 moles of hydrating water, 2 mole of glycine rest
	Exo	298	313 347	1000	35.83 64.17	48.84 12.97	-quickly cleavage and pyrolysis of organic rest CoO and ash
[Ni(L) ₂ •2H ₂ O] (3)	Endo	20	59	270	-	1.13 3.84	- residual water present inside pores
	Exo	270	320	337	35.89	33.81	-2 mole water, probably melting and glycine rest loss
	Exo	337	382	1000	64.11	46.87 13.84	- pyrolysis of organic rest NiO and ash
[Fe(L) ₂ •2H ₂ O] (4)	Endo	20	43	48	-	1.73	- residual water present inside pores
	Endo	48	110	168	6.67	7.44	-2 mole of hydrating water
	Exo	168	209	206	29.36	26.85	-2 mole of glycine rest
	Exo	206	327 348	1000	63.97	26.97 36.98	- pyrolysis of organic rest FeO and ash
[Zn(L) ₂ •H ₂ O]•H ₂ O (5)	Endo	20	30	43	-	0.50	- residual water present inside pores
	Endo	43	69	92	3.28	3.82	-1mole of hydrating water
	Endo	92	231	308	3.39	2.57	-1mole of coordinating water
	Exo		294		28.90	26.94	-2 mole of glycine rest
	Exo	308	324 493	1000	64.43	29.21 36.97	- pyrolysis of organic ZnO and ash

 T_i=initial temperature, T_{max}=maximum temperature, T_f=final temperature

The aim of the thermal analysis of the metal complexes is to obtain information concerning their thermal stability of these and to decide whether the water molecules are inside or outside the coordination sphere.

The decomposition of each metal complex occurs in three steps.

The interval 20-270°C is characterized by endothermic peaks, which corresponds to the loss of residual waters present in the pores or the coordination water, except zinc complex. Between 207-337°C, the exothermic peaks indicated the breaking of the glycine rest, then all the organic fragments decompose rapidly to the metal oxide. The metal complexes are completely pyrolyzed before 500°C, except zinc complex, as follows: at 464°C for the Cu-complex, at 357°C for the Co-complex, at 392°C for the Ni-complex, at 347°C for the Fe-complex and at 537°C for the Zn-complex. Finally, the metal oxide and some ash remain in the crucible in all the cases.

For the zinc complex (**5**), the loss of one mole water at 69°C and the other at 231°C indicated that one is outside and the other inside the coordination sphere (Figure 3c).

On the other hand, the Cu(II), Co(II) and Ni(II) complex loss the water and the glycine rest simultaneous. The Fe(II) complex loss the coordination water separated from the glycine breaking.

ESR spectra

At room temperature the ESR spectrum of copper (II) compound are typical for monomeric species with axial symmetry (Figure 4). The principal values of the g tensor ($g_{\parallel}=2.427$, $g_{\perp}=2.063$) correspond to a CuN_2O_3 local symmetry [23].

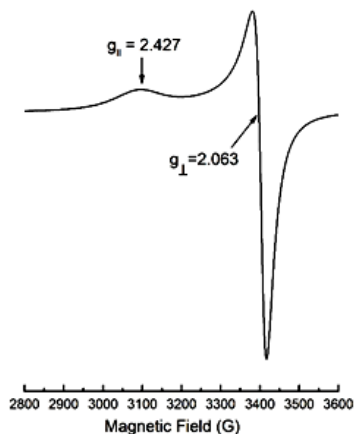


Figure 4. Powder ESR spectrum of copper complex at room temperature

CONCLUSIONS

New transition metal complexes (**1-5**) of an *N*-modified glycine (**L**) as ligand were synthesized and analyzed by elemental analysis, thermal stability in air atmosphere and spectral studies.

Mass spectra identify the M+1 peak corresponding for each of investigated compounds.

The study of UV-VIS spectra indicated a slight hypsochromic shift by 3.5-7.5 nm, but a considerable hyperchromic increase effect of absorbance comparative to the spectrum of the initial ligand (**L**), except Zn complex.

Elemental and thermal analysis lead to the idea that all the compounds, including the ligand are water hydrates. Except the ligand and the copper complex all are hydrating with two water molecules. Based on the spectroscopic studies, the ligand has been found to coordinate the metal by the carboxylate oxygen and the nitrogen atom belonging to the amino group of the glycine fragment. On the other hand, an additional band appearing at 763-768 cm^{-1} confirms the coordinative H_2O -metal bonding, like the other similar complexes [15, 20].

The thermal stability of selected *3d* transition metal complexes was studied in air atmosphere in 20-1000 $^\circ\text{C}$ temperature domain. Both the ligand and its metal complexes decompose in multistage.

On the basis of thermal and spectroscopic studies it was found that metal complexes stability: $[\text{Fe}(\text{L})_2 \cdot 2\text{H}_2\text{O}] < [\text{Co}(\text{L})_2 \cdot 2\text{H}_2\text{O}] < [\text{Ni}(\text{L})_2 \cdot 2\text{H}_2\text{O}] < [\text{Cu}(\text{L})_2 \cdot \text{H}_2\text{O}]$, except Zn complex, obeys the Irving-Williams series [17, 20, 22].

The obtained structural data allow us to propose the following molecular formulas for the studied metal complexes (Figure 5):

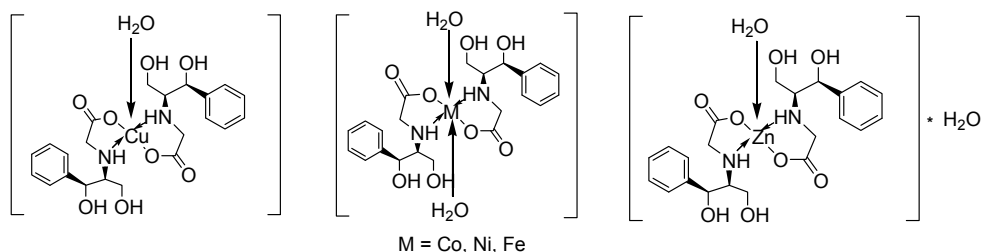


Figure 5. Suggested structure for the studied complexes

EXPERIMENTAL SECTION

Materials and instrumentation

All reagents and chemicals were purchased from commercial sources and used as received. Elemental analyses were determined on Thermo Scientific Flash EA 1112 Elemental Analyzer. Melting points were measured on an ELECTROTHERMAL[®] instrument and were not corrected. The electronic absorption spectra were performed on SHIMADZU UV-1800 spectrophotometer. Specific rotations were estimated on a Polamat A Karl Zeis Jena photopolarimeter. GC-MS spectra were recorded on a Gas Chromatograph with Mass Spectrometer Shimadzu[®] QP 2010 PLUS. Mass spectra were carried out on a LTQ ORBITRAP[®] XL (Thermo Scientific) instrument which was externally calibrated using the manufacturer's APCI for the ligand or ESI(+) calibration mix for metal complexes. The samples were introduced into the spectrometer by direct infusion. The ESR measurements were carried out on a Bruker Biospin EMX^{micro} spectrometer operating at X-band (9-10 GHz) with continuous wave at X-band (≈ 9 GHz). The spectra were recorded at room temperature with a microwave frequency of 9.4353 GHz, microwave power of 2 mW, modulation frequency of 100 kHz, modulation amplitude of 2 G. IR spectra were recorded in KBr pellets on a JASCO[®] FT-IR 6200 Spectrometer which operates with 4cm⁻¹ resolution Thermogravimetry and differential thermal analysis (TG/DTA) curves were recorded with a Thermal Analyzer TA Instruments SDT Q600 V20.9 Build 20 on an interval 20-10000C, at a heating rate of 10°C/min, in alumina crucibles and a dynamic air atmosphere.

General synthesis of the metal complexes

The ligand **L** was prepared by a literature procedure we have been working on, by treatment of [(1S,2S)-2-amino-1-phenylpropane-1,3-diol] namely phenylserinol with monochloroacetic acid/Na₂CO₃ system, TLC monitored [$R_f = 0.65$. (methanole: water = 1: 1 v/v)], then investigated by spectroscopic methods [13].

Cu(II), Co(II), Ni(II) Fe(II) and Zn(II) complexes of the ligand **L** were prepared by following a general method. The metal salt [Cu(NO₃)₂•3H₂O, Co(NO₃)₂•6H₂O Ni(NO₃)₂•6H₂O, FeSO₄•7H₂O, or ZnSO₄•7H₂O (1.24mmol) was dissolved in 10 mL distilled water. To a solution of ligand (**L**) (2mmol) dissolved in 3mL of distilled water, was added slowly, dropwise during 30 min, a solution of the metal salt, at room temperature. The mixture was let to stir at the room temperature for 24h. By adding a solution of metal ions to a solution of ligand, immediate color change was observed depending on the

metal ion. The isolated solid complexes were obtained by vacuum filtration and washed with distilled water and finally dried in air at room temperature for 48h. The dried complexes were subjected to elemental, spectroscopic and thermal analysis.

$C_{22}H_{30}CuN_2O_9$ (**1**) Pale-blue solid, MW = 530.0276, Mp = 247-248°C (desc.) Yield: 64.16%, Elemental Analysis (%) Calc.(Found) C: 49.85(48.32), H: 5.71(5.31), N: 5.29(6.11), UV-Vis (DMSO): λ_{max} = 268.5nm, A = 0.333 ϵ = 11743.96, IR(KBr): ν_{max} : 3293, 3034, 1613, 1386, 1494, 1456, 763, 541, 421, MS (ESI, CH₃OH, without hydrating water) [M+1]: 512.1216 Exact Mass: 511.1142, $[\alpha]_{546}^{25}$ = +36 (c=0.1, DMSO), Thermal Analysis: 35°C (Endo) (TG_{exp.} = 2.19%), 246°C (Exo) (TG_{calc.} = 32.36%, TG_{exp.} = 33.60%), (Exo) 315°C, 441°C (TG_{calc.} = 67.64%, TG_{exp.} = 64.01%), Molar Ratio M: L: H₂O = 1: 2: 1.

$C_{22}H_{32}CoN_2O_{10}$ (**2**) White-pink solid, MW = 543.4301, Mp = 289-290°C (desc.), Yield: 57.26%, Elemental Analysis (%) Calc.(Found) C: 48.62(46.93), H: 5.94(5.82), N: 5.15(6.03), UV-Vis (DMSO): λ_{max} = 269.5nm, A = 0.299 ϵ = 10826.66, IR(KBr): ν_{max} : 3324, 3086, 1600, 1383, 1493, 1456, 763, 561, 429, MS (ESI, CH₃OH, without hydrating water) [M+1]: 508.1255 Exact Mass: 507.1178, $[\alpha]_{546}^{25}$ = +11 (c=0.1, DMSO), Thermal Analysis: 36°C (Endo) (TG_{exp.} = 3.32%), 283°C (Exo) (TG_{calc.} = 35.83%, TG_{exp.} = 34.04%), (Exo) 313°C, 347°C (TG_{calc.} = 64.17%, TG_{exp.} = 61.81%), Molar Ratio M: L: H₂O = 1: 2: 2.

$C_{22}H_{32}N_2NiO_{10}$ (**3**) White-greenish solid, MW = 543.1903, Mp = 320-321°C (desc.), Yield: 62.87%, Elemental Analysis (%) Calc.(Found) C: 48.65(49.17), H: 5.94(5.31), N: 5.16(6.23), UV-Vis (DMSO): λ_{max} = 269.5nm, A = 0.171 ϵ = 9270.805, IR(KBr): ν_{max} : 3316, 3086, 1603, 1385, 1494, 1456, 763, 564, 432, MS (ESI, CH₃OH, without hydrating water) [M+1]: 507.1277 Exact Mass: 506.1197, $[\alpha]_{546}^{25}$ = +29 (c=0.1, DMSO), Thermal Analysis: 59°C (Endo) (TG_{exp.} = 4.97%), 320°C (Exo) (TG_{calc.} = 35.89%, TG_{exp.} = 33.81%), (Exo) 382°C, (TG_{calc.} = 64.11%, TG_{exp.} = 60.71%), Molar Ratio M: L: H₂O = 1: 2: 2.

$C_{22}H_{32}FeN_2O_{10}$ (**4**) Brown solid, MW = 540.1406, Mp = 224-225°C (desc.), Yield: 63.12%, Elemental Analysis (%) Calc.(Found) C: 48.90(48.25), H: 5.97(5.34), N: 5.18(6.02), UV-Vis (DMSO): λ_{max} = 265.5nm, A = 0.394 ϵ = 14187.97, IR(KBr): ν_{max} : 3393, 2937, 1628, 1363, 1495, 1455, 768, 599, 459, MS (ESI, CH₃OH, without hydrating water) [M+1]: 505.1233 Exact Mass: 504.1195, $[\alpha]_{546}^{25}$ = +21 (c=0.1, DMSO), Thermal Analysis: 43°C (Endo) (TG_{exp.} = 1.73%), 110°C (Endo) (TG_{calc.} = 6.67%, TG_{exp.} = 7.44%), (Exo) 209°C, (TG_{calc.} = 29.36%, TG_{exp.} = 26.85%), (Exo) 327°C, 348°C (TG_{calc.} = 63.97%, TG_{exp.} = 63.95%) Molar Ratio M: L: H₂O = 1: 2: 2.

$C_{22}H_{32}N_2O_{10}Zn$ (**5**) White solid, MW = 549.8869, Mp = 290-291°C (desc.), Yield: 55.26%, Elemental Analysis (%) Calc.(Found) C: 48.02(47.45), H: 5.87(4.98), N: 5.09(5.82), UV-VIS (DMSO): λ_{max} = 268nm, A = 0.084 ϵ = 4604.5, IR(KBr): ν_{max} : 3505, 3402, 3341, 3302, 2933, 1608, 1384, 1495, 1456, 764, 563, 427, MS (ESI, CH₃OH, without hydrating water) [M+1]: 513.5406 Exact Mass: 512.1137, $[\alpha]_{546}^{25}$ = +18 (c=0.1, DMSO), Thermal Analysis: 30°C (Endo) (TG_{exp.} = 0.50%), 69°C (Endo) (TG_{calc.} = 3.28%, TG_{exp.} = 3.82%), (Endo) 231°C, (TG_{calc.} = 3.39%, TG_{exp.} = 2.57%), (Exo) 294°C, (TG_{calc.} = 28.90%, TG_{exp.} = 26.94%) (Exo) 324°C, 493°C (TG_{calc.} = 64.43%, TG_{exp.} = 66.18%) Molar Ratio M: L: H₂O = 1: 2: 2.

ACKNOWLEDGMENTS

Authors acknowledge the financial support from a Grant provided by the Research Council Romania (project PN-II-ID-PCE-2011-3-0128).

Special thanks are addressed to Conf. Dr. Petru Pascuta from Technical University of Cluj-Napoca, Faculty of Material and Environmental Engineering, for the IR spectra measurements and to Dr. Mirabela-Ligia Golban from the Faculty of Chemistry and Chemical Engineering for the HRMS and UV-VIS spectra.

REFERENCES

1. I. Sakiyan, E. Loğoğlu, S. Arslan, N. Sari, N. Sakiyan, *BioMetals*, **2004**, 17(2), 115.
2. A. Temitayo, O. Isaac, A. Olugbenga, *International Journal of Chemistry*, **2012**, 4(2), 49.
3. A. Marcu, A. Stanila, D. Rusu, M. Rusu, O. Cozar, L. David, *Journal of Optoelectronics and Advanced Materials*, **2007**, 9(3), 741.
4. G. Indira Devi, P. Smitha, *International Research Journal of Biological Sciences*, **2013**, 2(6), 16.
5. N. Baroah, R. J. Sarma, A. S. Batsanov, J. B. Baruh, *Polyhedron*, **2006**, 25(1), 17.
6. S. Begum, S. S. Nizami, S. Saied, S. M. Shahid, F. Z. Basha, *European Journal of Chemistry*, **2014**, 5(4), 557.
7. L. Menabue, M. Saladini, *Journal of Crystallographic and Spectroscopic Research*, **1992**, 22(6), 713.
8. K. Nishimura, X. Lu, R. B. Silverman, *Journal of Medicinal Chemistry*, **1993**, 36, 446.
9. G. Byk, C. Gilon, *Journal of Organic Chemistry*, **1992**, 57, 5687.
10. C. M. Sharaby, M. F. Amine, A. A. Hamed, *Journal of Molecular Structure*, **2017**, 1134, 208.

11. F. Sevgi, U. Bagkesici, A. N. Kursumlu, E. Guler, *Journal of Molecular Structure*, **2018**, 1154, 256.
12. C. Sacalis, F. Goga, L. David, *Studia UBB Chemia*, **2017**, 62(4), Tom I, 181.
13. O. Moldovan, K. Albert, I. Nagy, C. Morar, C. Sacalis, M. Darabantu, *Tetrahedron Letters*, **2016**, 57, 5808.
14. L. Zapala, M. Kosińska, E. Woźnicka, L. Byczyński, W. Zapala, *Journal of Thermal Analysis and Calorimetry*, **2016**, 124, 363.
15. C. Batiu, L. Ghizdavu, L. David, O. Cozar, *Synthesis and Reactivity in Inorganic and Metal-Organic Chemistry*, **2003**, 33(8), 1391.
16. A. A. El-Asmy, M. A. Hafez, E. M. Saad, F. I. Taha, *Transition Metal Chemistry*, **1994**, 19, 603.
17. L. David, C. Craciun, C. Balan, O. Cozar, L. Ghizdavu, C. Batiu, *Acta Chimica Slovenica*, **2001**, 48, 407.
18. F. H. A. Al-Jeboori, T. A. M. Al-Shimiesawi, *Journal of Chemical and Pharmaceutical Research*, **2013**, 5(11), 318.
19. R. A. Ammar, S. I. Al-Saeedi, A-N. M. A. Alaghaz, *International Journal of Electrochemical Science*, **2018**, 13, 3700.
20. C. Batiu, C. Jelic, N. Leopold, O. Cozar, L. David, *Journal of Molecular Structure*, **2005**, 744-747, 325.
21. M. Castillo, E. Ramirez, *Transition Metal Chemistry*, **1984**, 9(7), 268.
22. H. M. N. H. Irving, R. J. P. Williams, *Journal of the Chemical Society*, **1953**, 3192.
23. A. Bencini, D. Gatteschi, "Transition Metal Chemistry", Marcel Dekker, New York, NY, **1982**, 8.

COMPARATIVE CYTOTOXICITY ASSAYS PERFORMED USING A FREE PORPHYRIN AND ITS Zn(II), Co(II) AND Cu(II) COMPLEXES. INFLUENCE OF OPTICAL AND AGGREGATION PROPERTIES

RADOSTINA ALEXANDROVA^{a,*}, RENI KALFIN^b, RAMONA TUDOSE^c,
EUGENIA FAGADAR-COSMA^{c,*}

ABSTRACT. Our present approach is dealing with comparative cytotoxicity assays performed with a porphyrin base, substituted with methoxy-inductive donor substituents in the *meso* position, namely: 5,10,15,20-tetrakis-(*p*-methoxy-phenyl porphyrin (TMeOPP) and with its Zn(II), Co(II) and Cu(II) complexes (Figure 1). The cytotoxicity evaluation was performed using human (HeLa, 8 MGBA, Lep-3) and bovine (MDBK) cell lines as model systems. The influence of the compounds on cell viability and proliferation was studied by (thiazolyl blue tetrazolium bromide) MTT test and further discussed taking into consideration the main optical and aggregation properties of the free porphyrin and its different metal complexes.

Keywords: Zn(II), Co(II) and Cu(II)-metalloporphyrins, cytotoxicity evaluation, UV-vis spectroscopy, STEM microscopy, MTT test.

INTRODUCTION

Substituted *meso*-tetraarylporphyrins represent an amazing class of molecular building blocks due to their large size, extended aromatic π -system and high versatility for binding various transitional metal ions. Porphyrins successfully act as photosensitizers in noninvasive photodynamic therapy (PDT) treatments. Photosensitizers are molecules which when irradiated by

^a Institute of Experimental Morphology, Pathology and Anthropology with Museum Bulgarian Academy of Sciences, Acad. G. Bonchev St., Block 25, 1113 Sofia, Bulgaria.

^b Institute of Neurobiology, Bulgarian Academy of Sciences, Acad. G. Bonchev St., Block 23, 1113 Sofia, Bulgaria.

^c Institute of Chemistry Timisoara of Romanian Academy, M. Viteazul Ave. 24, 300223-Timisoara, Romania.

* Corresponding author: efagadar@yahoo.com

light energy in the presence of oxygen might induce photochemical reactions producing lethal cytotoxic agents, due to generated reactive singlet oxygen [1].

In order to facilitate PDT, second generation of porphyrin photosensitizers have to respond to some mandatory photochemical conditions: high absorption coefficient in the red visible region of the spectrum, mainly in the field (650–800 nm) and a long lifetime of the triplet excited state in order to efficiently produce singlet molecular oxygen. In the absence of light and oxygen the photosensitizers have no effect on healthy or malignant cells and that is the reason why the time of light exposure has to be carefully monitored to ensure that the activation of the photosensitizer is occurring only when the ratio of the photosensitizer in neoplastic cells is higher than that localized in healthy tissue [2, 3].

The capacity of the free porphyrin to exist simultaneously in aggregated and protonated forms was previously investigated and brings significant influences on biological activity [4]. In this respect, experiments were focused to improve cellular uptake of the porphyrins acting as photosensitizers both by hindering their aggregation processes and by increasing their hydrophilicity [5]. A chlorin water-soluble conjugate with 4-arylaminquinazoline moiety was proven to be suitable for photodynamic therapy (PDT), exhibiting dark and photoinduced cytotoxicity at very low micromolar concentrations (IC₅₀dark/IC₅₀light ratio of 11–18), and prefers to accumulate in the tumor tissue [6].

The metallic complexes of methoxy-substituted tetraphenylporphyrins are well known for their capacity to bind axial ligands which increase their chemical versatility and enable complex structures to be generated and to be further used as biologically active systems [7-9].

The use of Zn(II), Co(II) and Cu(II) metalloporphyrins in PDT arose large attention. So, early this year, porphyrin derivatives, namely: Zn(II)-5,10,15,20-tetrakis(3,4-bis(2-(-2-(2-hydroxyethoxy)ethoxy)ethoxy)benzyl)-porphyrin, Zn(II)-5,15-bis(3,4-bis(2-(-2-(2-hydroxy-ethoxy)ethoxy)ethoxy)benzyl)-10,20-bis(2-(2-(2-(4-ethynyl-phenoxy)ethoxy)ethoxy)ethanol)-porphyrin and Zn(II)-5,15-bis(3,4-bis(2-(-2-(2-hydroxyethoxy)ethoxy)ethoxy)benzyl)-10,20-N,N-dibutyl-4-ethynyl-aniline porphyrin, were obtained aiming for more efficient cancer treatment. The three Zn-metalloporphyrins were further evaluated *in vitro* against human carcinoma of the uterine cervix (Hela) cells and exhibited negligible dark toxicity and robust phototoxicity preserving the requirements of cellular uptake [10].

Aiming to design strong near-infrared absorbing porphyrins some porphyrin derivatives substituted with methoxy groups, 5,10,15,20-tetrakis(3,4-dimethoxyphenyl) porphyrin, its Zn-derivative and a Zn-A₂B₂ porphyrin: Zn(II)-5,15-bis(3,4-dimethoxyphenyl)-10,20-bis(4-methoxy-phenyl)ethynyl)porphyrin

were obtained. The A₂B₂ asymmetrically substituted porphyrin absorbs in the near-infrared (NIR) region, promising to offer the deepest tumor tissue penetration and shows the highest singlet oxygen quantum yield (79%) and the best efficacy *in vitro* on HeLa cells [11].

Unsymmetrical porphyrinic complexes with Cu(II) and Zn(II) were used in photodynamic therapy of cancer on human histiocytic lymphoma (U937) cell line and did not damage membrane integrity, but acted as cytostatics at higher concentrations, after 24 h incubation [12]. Functionalized meso-tetraphenylporphyrin with two nitro groups were coupled with L-phenylalanine or 1-carboxymethyl-5-fluorouracil and metalated with Co(II) or Mn(II) for further use against cancer stem-like cells from human esophageal carcinoma (Ec9706) cell line in PDT trials [13].

Related to our previous work involving medical investigations on porphyrins [14, 15] our present approach is dealing with comparative cytotoxicity assays performed with a porphyrin base, substituted with methoxy-inductive donor substituents at the phenyl ring in the *meso* position, namely: 5,10,15,20-tetrakis-(*p*-methoxy-phenyl porphyrin (TMeOPP) and with its Zn, Co and Cu complexes (Figure 1). The cytotoxicity evaluation was performed using human (HeLa, 8 MG BA, Lep-3) and bovine (MDBK) cell lines as model systems. The influence of the compounds on cell viability and proliferation was studied by MTT test and further discussed taking into consideration the main optical and aggregation properties of the free porphyrin and its different metal complexes.

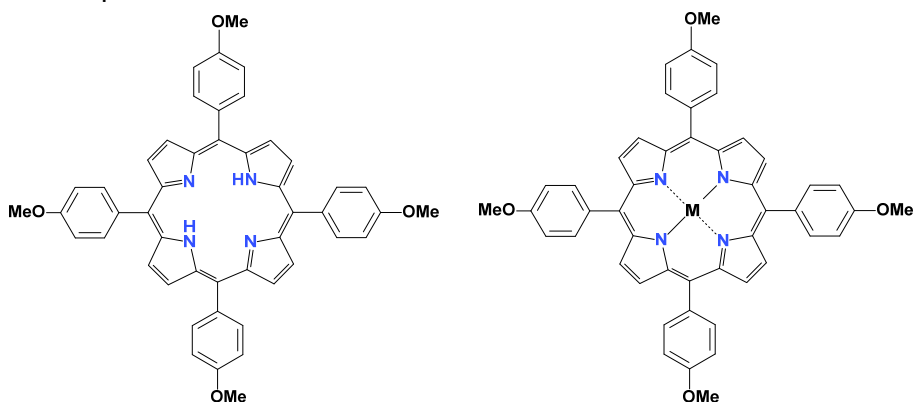


Figure 1. The structures of free base porphyrin **TMeOPP** and of its metalocomplexes with M(II) = Zn (**ZnTMeOPP**), Cu (**CuTMeOPP**) and Co (**CoTMeOPP**).

RESULTS AND DISCUSSION

The UV-vis spectrum of free porphyrin shown in Figure 2 is a typical porphyrin normal etio spectrum with four visible (Q) bands and an intense Soret (B) band.

As can be seen in Figure 3, the Soret-band of ZnTMeOPP is red-shifted by 6 nm relative to porphyrin base and all absorption bands of ZnTMeOPP are decreased in intensity relative to free porphyrin.

In comparison, the cobalt complex CoTMeOPP is characterized by the same intensity of bands with the porphyrin base, the main difference being the hypsochromic shift of its Soret band with 4 nm. Instead, UV-vis spectrum of CuTMeOPP complex has the same shape with Co complex, a significant hypochromic effect of the main Soret band, but no significant deviation of the Soret band in comparison with porphyrin-base.

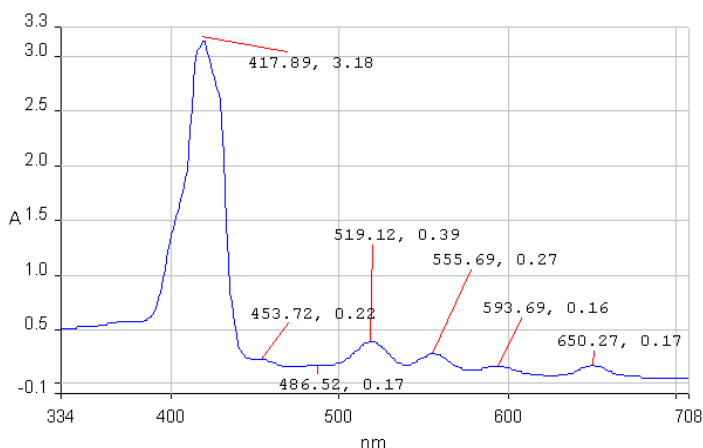


Figure 2. The UV-vis spectrum of tetrakis-(p-methoxy-phenyl)-porphyrin in chloroform

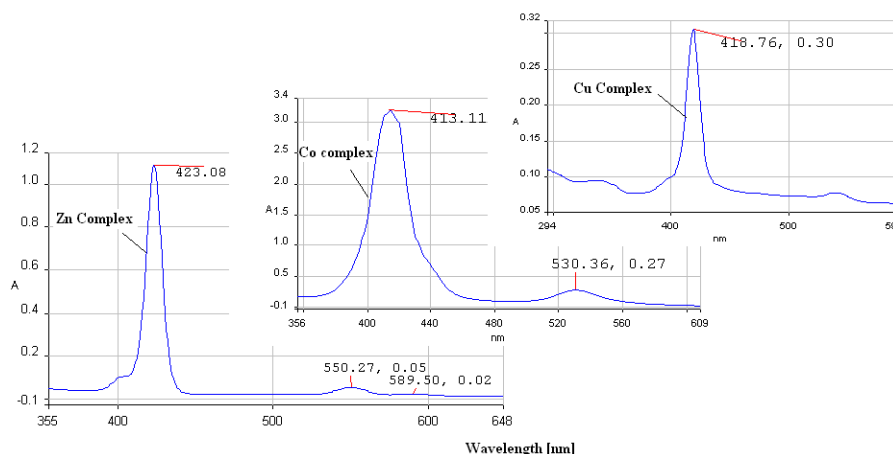


Figure 3. The UV-vis spectra of Zn(II)-; Co(II)- and respectively Cu (II)-tetrakis-(p-methoxy-phenyl)-porphyrin, in chloroform

Microscopic analysis was performed by scanning transmission electron microscopy (**STEM**) method due to the accurate and versatile information offered, with the aim to compare the aggregation behavior of all the four porphyrin derivatives.

As expected, STEM analysis showed significant differences between the aggregation behavior of the four porphyrin derivatives that we expect to influence their biological activity (Figure 4).

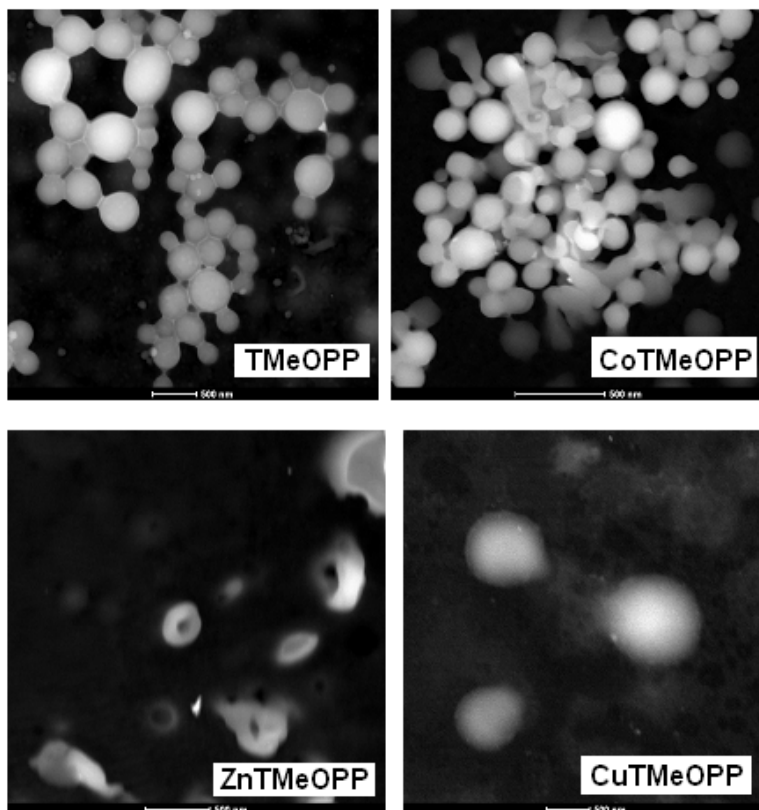
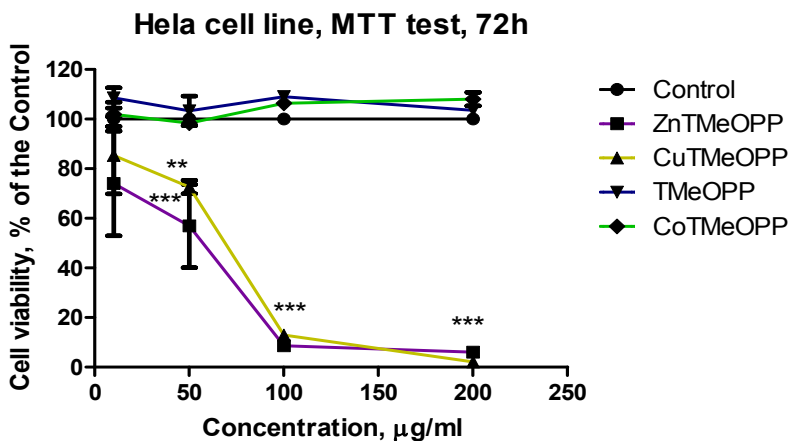


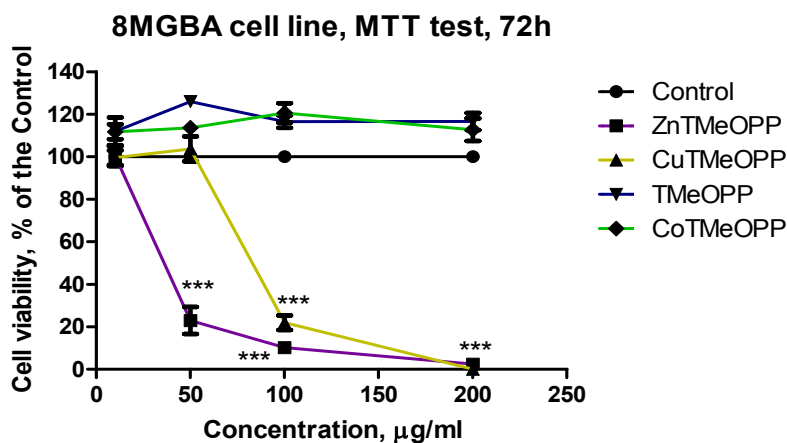
Figure 4. STEM microscopic analysis of porphyrin base TMeOPP and the metalloporphyrins CoTMeOPP, ZnTMeOPP and CuTMeOPP, at the same concentration from DMSO solvent

In both cases of porphyrin base TMeOPP and CoTMeOPP samples the images depicted in Figure 4 show spherical or ovoid aggregates with sizes in the range of 20-50 nm, irregularly connected and forming a mixture of linear and circular agglomerations. Instead, the ZnTMeOPP compound revealed rings of uniform sizes of around 100 nm. The spherical self-aggregates of CuTMeOPP metalloporphyrin, with diameters around 100-150 nm, do not have

the tendency to agglomerate or link together. All these self-assembling architectures are the result of face to face H-type aggregations and side to side J-type aggregation in which both the porphyrins' *meso*-substituents and the central metal ion play an important role.



5A



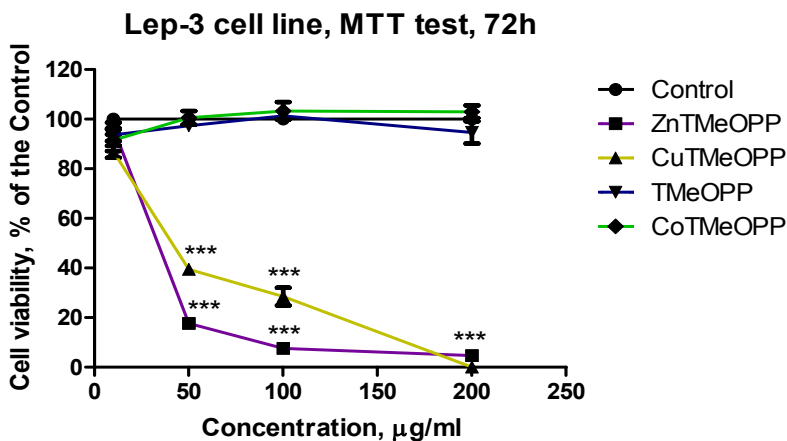
5B

Figure 5. Effect of the investigated compounds on viability and proliferation of cultured human HeLa cervical carcinoma (A) and 8MGBA glioblastoma multiforme (B) cells. The investigation was performed by MTT test after 72 h of treatment.

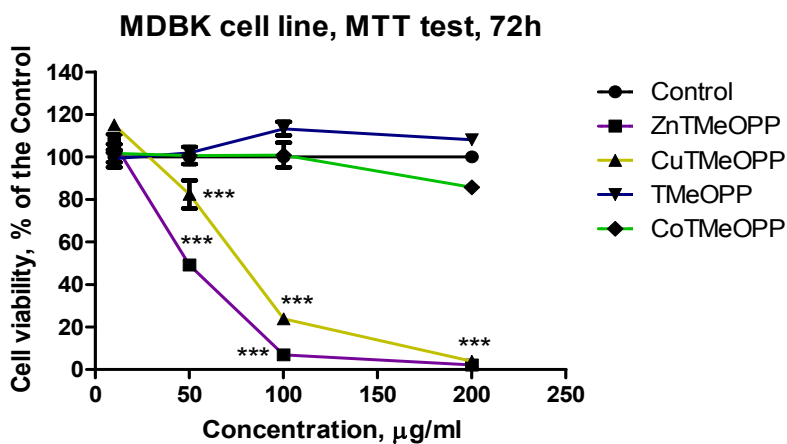
P < 0.01; *P < 0.001 vs Control

The cytotoxicity evaluation was performed using human (HeLa, 8 MG BA, Lep-3) and bovine (MDBK) cell lines as model systems. The influence of the compounds on cell viability and proliferation was studied by MTT test

and further discussed taking into consideration the main optical and aggregation properties of the free porphyrin and its different metal complexes. The results as CC50 and CC90 values ($\mu\text{g/mL}$) derived from concentration-response curves are given in Table 1. Examples of such concentration-response curves are shown in Figures 5 and 6.



6A



6B

Figure 6. Effect of the investigated compounds on viability and proliferation of cultured non-tumor human Lep-3 (A) and bovine MDBK (B) cells. The investigation was performed by MTT test after 72 h of treatment. *** $P < 0.001$ vs Control

Table 1. Cytotoxic activity (CC_{50} and CC_{90}) of compounds investigated in human and animal cell lines after 72 hours of treatment

Cell line	ZnTMeOPP	CuTMeOPP	TMeOPP	CoTMeOPP
	MTT test, 72h			
HeLa	57.16* \pm 2.30 (99.74)** \pm 4.81	60.06 \pm 3.66 (128.67 \pm 5.28)	-	-
8MGBA	36.21 \pm 2.28 (99.14 \pm 3.15)	82.72 \pm 4.83 (154.78 \pm 7.18)	-	-
Lep-3	79.81 \pm 1.69 (172.96 \pm 3.08)	40.78 \pm 2.65 (166.18 \pm 5.04)	-	-
MDBK	49.78 \pm 2.68 (95.77 \pm 5.42)	77.04 \pm 6.14 (170.10 \pm 8.63)	-	-

* CC_{50} and ** CC_{90} - Cytotoxic concentrations ($\mu\text{g/ml}$) at which the compounds investigated decrease by 50% (CC_{50}) and by 90% (CC_{90}) the viability of the treated cells as compared to the Control;

(-) - CC_{50} was not determined because at all concentrations administered (1 - 200 $\mu\text{g/mL}$) the cell viability was > 50%;

The corroborated obtained results on the basis of their ability to decrease viability and proliferation of the treated human and animal tumor and non-tumor cells revealed that the compounds investigated can be divided into two groups: ZnTMeOPP and CuTMeOPP are more pronounced cytotoxic and cytostatic agents as compared to TMeOPP and CoTMeOPP (Fig. 5; Fig. 6; Table 1).

Some possible explanations for their different cytotoxic behavior arose from their aggregation capacity and the size of the formed aggregates. Based on the STEM microscopy analyses (Figure 4), we can state that π - π interactions, that are the main factor responsible for the aggregation process in the case of porphyrin base TMeOPP and CoTMeOPP, limit the flexibility of the system.

In addition, as can be seen in Figure 2, the porphyrin base manifests the tendency to form H aggregates in solution, evidenced by the enlargement of Soret Band and these types of aggregates are considered photoinactive [16].

The lack of large aggregates formation in the case of Zn and Cu metalloporphyrins, as revealed by STEM images in Figure 4, favors the cytotoxic activity probably because there is no steric constraint regarding the intake capacity of the cells.

The cytotoxic/cytostatic effects of the compounds examined are dependent of concentration (Table 1; Figures 5 and 6); CC_{50} for ZnTMeOPP for non-tumor human Lep-3 cells (79.81 \pm 1.69 $\mu\text{g/ml}$) is higher than CC_{50} for human tumor HeLa (57.16 \pm 2.30 $\mu\text{g/ml}$) and 8 MGBA (36.21 \pm 2.28 $\mu\text{g/ml}$).

Tested independently, the same amount of DMSO as those in the solutions of the tested compounds has no significant cytotoxic effect as compared to the control – the cell viability was > 94% ($P < 0.05$).

The efficiency of the metalloporphyrin photosensitizers depends significantly, but not entirely, on the nature of the coordinated central metal ion. The increased cytotoxic activity of ZnTMeOPP might be caused by the core deformation from planar type into more appropriate S₄-saddled conformation that was already proven for Zn-porphyrin compounds [17]. It is already known that the distortion of the planarity of the porphyrin macrocycle produces a red-shift of the absorption bands, however, this bathochromic shift is accompanied by a decreasing of the extinction coefficients. Nevertheless, non-planar porphyrins act remarkably as biologically active compounds [18, 19]. ZnTMeOPP is also the only metalloporphyrin tested in the present work that manifests a significant bathochromic shift of the Soret-band (Figure 3) in the absorption spectra [20].

CONCLUSIONS

Comparative cytotoxicity assays were performed with a porphyrin base, namely: 5,10,15,20-tetrakis-(*p*-methoxy-phenyl porphyrin (TMeOPP) and with its Zn(II), Co(II) and Cu(II) complexes using human (HeLa, 8 MG BA, Lep-3) and bovine (MDBK) cell lines as model systems. The influence of the compounds on cell viability and proliferation was studied by (thiazolyl blue tetrazolium bromide) MTT test.

The best ability to decrease the viability and proliferation of the treated human tumor cells were manifested by: ZnTMeOPP and CuTMeOPP and the cytotoxic/cytostatic effects for each examined compound depend on concentration.

The efficiency of the metalloporphyrin photosensitizers depends significantly, but not entirely, on the nature of the coordinated central metal ion, the aggregation behavior and the red shifting of the absorption bands.

EXPERIMENTAL SECTION

Reagents and other materials

Dulbecco's modified Eagle's medium (D-MEM) and fetal bovine serum (FBS) were purchased from Gibco-Invitrogen (UK). Dimethyl sulfoxide (DMSO) and trypsin were obtained from AppliChem (Germany); thiazolyl blue tetrazolium bromide (MTT) was from Sigma-Aldrich Chemie GmbH (Germany).

The antibiotics (Penicillin and Streptomycin) for cell cultures were from Lonza (Belgium). Pyrrole, 4-anisaldehyde, propionic acid and acetate salts were provided by Aldrich and Merck (Germany) as purum analiticum reagents. All other chemicals of the highest purity commercially available were purchased from local agents and distributors. All sterile plastic and syringe filters were from Orange Scientific (Belgium).

Synthesized compounds

Synthesis and purification of 5,10,15,20-tetra(4-methoxy-phenyl) porphyrin (TMeOPP) was done in our laboratory by improving Adler-Longo method [21-23].

Synthesis and purification of Zn, Co and Cu complexes were done by standard procedures, through metalation reactions of free base TMeOPP porphyrin. The porphyrin-base solution, in dimethylformamide or dichloromethane, was refluxed for 1-2 hours, under vigorous stirring, with a large excess of corresponding metal acetate (20 times more than molar ratio), dissolved in methanol. The reactions were monitored by IR, UV-vis and TLC [24, 25], until the bands corresponding to NH internal signals were no more present.

The porphyrin and all three metalloporphyrins were fully characterized by UV-vis, FT-IR, H-NMR, TLC, HPLC, MS and fluorescence spectra and were in agreement with previously reported papers [24, 26].

The porphyrinic compounds were initially dissolved in dimethylsulfoxide and then diluted in culture medium. The final concentration of DMSO in the stock solutions (in which the concentration of the tested compound was 1 mg/mL) was 2%.

Apparatus

FT-IR spectra were registered on a JASCO 430 apparatus as KBr pellets. ¹H-NMR spectra were registered on a 400 MHz Bruker spectrometer in CDCl₃ and chemical shifts were reported relative to internal TMS (0.0 ppm). The HPLC analysis was performed on a JASCO apparatus equipped with NUCLEOSIL C18 nonpolar column, 240x4 mm with MD 1510 detector, at ambient temperature. UV-visible spectra were recorded on a UV/VIS PERKIN ELMER, LAMBDA 12 spectrometer in CHCl₃ at the same concentration.

The STEM measurements were recorded on Titan G2 80-200 TEM/STEM microscope from FEI Company (The Netherlands) at 200 kV for all the samples prepared on 200 mesh carbon-coated copper grids. The STEM images were obtained using Digital Micrograph v. 2.12 and TEM Imaging & Analysis v. 4.7 software [27].

Viability of cell cultures

The following permanent cell lines were used as model systems in our study:

1. Tumor – HeLa (human carcinoma of the uterine cervix), 8 MGBA (human glioblastoma multiforme);
2. Non-tumor – Lep-3 (3-month old human embryo), MDBK (bovine kidney cells).

The cell lines MDBK and HeLa were purchased from the National Bank for Industrial Microorganisms and Cell Cultures in Sofia, Bulgaria. The cell line Lep-3 was obtained from the Cell Culture Collection of the National Institute of Infectious and Parasitic Diseases in Sofia, Bulgaria. The cell line 8MGBA cell line [28] was a generous gift from Dr. A. Perzelova and Prof. C. Altaner, Cancer Research Institute, Bratislava, Slovakia.

The cells were grown as monolayer culture in D-MEM medium, supplemented with 5-10% fetal bovine serum, 100 U/mL penicillin and 100 µg/mL streptomycin. The cultures were maintained at 37 °C in a humidified CO₂ incubator (Thermo scientific, Hepa class 100). For routine passages adherent cells were detached using a mixture of 0.05% trypsin and 0.02% EDTA. The experiments were performed during the exponential phase of cell growth. The cells were seeded in 96-well flat-bottomed microplates at a concentration of 1×10⁴ cells/well. After the cells were grown for 24 h to a subconfluent state (~ 60-70%), the culture medium was removed and changed by media modified with different concentrations (1 - 200 µg/mL) of the compounds tested. Each solution was applied into 4 to 6 wells. Samples of cells grown in non-modified medium served as controls. After 72h of incubation, the effect of the compounds on cell viability and proliferation was examined by MTT (thiazolyl blue tetrazolium bromide) test.

The MTT colorimetric assay of cell survival was performed as it was previously described by [29]. Briefly, the method consisted of three hours incubation with MTT solution (5 mg MTT in 10 mL D-MEM) at 37 °C under 5% carbon dioxide and 95% air, followed by extraction with a mixture of absolute ethanol and DMSO (1:1, vol/vol) to dissolve the blue MTT formazan.

Optical density was measured at 540 nm using an automatic microplate reader (TECAN, SunriseTM, Austria). Relative cell viability, expressed as a percentage of the untreated control (100% viability), was calculated for each concentration. “Concentration – response” curves were prepared and the effective concentrations of the compounds - CC₅₀ (causing a 50% reduction of cell viability) and/or CC₉₀ (causing a 90% reduction of cell viability) were estimated (where possible) from these curves using Origin 6.1. All data points represent an average of three independent assays.

Statistical analysis

The data are presented as mean \pm standard error of the mean. Statistical differences between control and treated groups were assessed using one-way analysis of variance (ANOVA) followed by Dunnett post-hoc test and Origin 6.1TM.

ACKNOWLEDGMENTS

This study was supported by grant № DFNI Б-02/30 from 12.12.2014, National Science Fund, Bulgarian Ministry of Education and Science and a bilateral project between Bulgarian Academy of Sciences and Romanian Academy. Romanian authors are also acknowledging Romanian Academy for financing the Programmes 3 / 2018 from ICT.

REFERENCES

1. J. F. Lovell, T.W.B. Liu, J. Chen, G. Zheng, *Chemical Reviews*, **2010**, *110*(5), 2839.
2. G. Yu, T. Durduran, C. Zhou, T.C. Zhu, J.C. Finlay, T.M. Busch, S.B. Malkowicz, S.M. Hahn, A.G. Yodh, *Photochem. Photobiol.* **2006**, *82*, 1279.
3. W. Li, D. Huang, Y. Zhang, Y. Liu, Y. Gu, Z. Qian, *Ann. Biomed. Eng.* **2016**, *44*, 2737.
4. E. Fagadar-Cosma, C. Enache, R. Tudose, I. Armeanu, E. Mosoarca, D. Vlascici, O. Costisor, *Revista de Chimie-Bucharest*, **2007**, *58*(5), 451.
5. B. Pucelik, R. Paczyński, G. Dubin, M.M. Pereira, L.G. Arnaut, J.M. Dąbrowski, *PLoS ONE* **2017**, *12*(10), e0185984 <https://doi.org/10.1371/journal.pone.0185984>.
6. V.F. Otvagin, A.V. Nyuchev, N.S. Kuzmina, I.D. Grishin, A.E. Gavryushin, Y.V. Romanenko, O.I. Koifman, D.V. Belykh, N.N. Peskova, N.Y. Shilyagina, I.V. Balalaeva, A.Y. Fedorov, *European Journal of Medicinal Chemistry*, **2018**, *144* (20), 740.
7. E. Fagadar-Cosma, I. Sebarchievici, A. Lascu, I. Creanga, A. Palade, M. Birdeanu, B. Taranu, G. Fagadar-Cosma, *Journal of Alloys and Compounds*, **2016**, *686*, 896.
8. E. Fagadar-Cosma, E. Tarabukina, N. Zakharova, M. Birdeanu, B. Taranu, A. Palade, I. Creanga, A. Lascu, G. Fagadar-Cosma, *Polymer International*, **2016**, *65*(2), 200.
9. E. Fagadar-Cosma, G. Fagadar-Cosma, M. Vasile, C. Enache, *Current Organic Chemistry*, **2012**, *16*, 931.
10. D. Pan, X. Zhong, W. Zhao, Z. Yu, Z. Yang, D. Wang, H. Cao, W. He, *Tetrahedron*, **2018**, *74*(21), 2677.
11. K. Ding, Y. Zhang, W. Si, X. Zhong, Y. Cai, J. Zou, J. Shao, Z. Yang, X. Dong, *ACS Applied Materials and Interfaces*, **2018**, *10* (1), 238.

12. R. Socoteanu, M. Anastasescu, G. Dobrescu, R. Boscencu, G. Vasiliu, C. Constantin, *Chaos, Solitons and Fractals*, **2015**, *77*, 304.
13. S. Weimin, Z. Gen, D. Guifu, Z. Yunxiao, Z. Jin, T. Jingchao, *Bioorganic and Medicinal Chemistry*, **2008**, *16 (10)*, 5665.
14. S. L. Trancota, C. Enache, O. Duicu, S. N. Mirica, E. Făgădar-Cosma, D. Muntean, *Archives of Cardiovascular Diseases*, **2011**, *Suppl 3*, 31.
15. E. Fagadar-Cosma, L. Cseh, V. Badea, G. Fagadar-Cosma, D. Vlascici, *Combinatorial Chemistry & High Throughput Screening*, **2007**, *10 (6)*, 466.
16. L.B. Josefsen, R.W. Boyle, *Metal-Based Drugs*, **2008**, Article ID 276109, 24 pages.
17. N. Mehraban, H. Freeman, *Materials*, **2015**, *8(7)*, 4421.
18. B. Röder, M. Büchner, I. Rückmann, M.O. Senge, *Photochem. Photobiol. Sci.* **2010**, *9*, 1152.
19. B. L. Josefsen, R. W. Boyle, *Theranostics*, **2012**, *2(9)*, 916.
20. A. Wiehe, H. Stollberg, S. Runge, A. Paul, M. O. Senge, B. Roder, *Journal of Porphyrins and Phthalocyanines*, **2001**, *5*, 853.
21. A.D. Adler, F.R. Longo, J. Goldmacher, J. Assour, L. Korsakoff, *J. Org. Chem.*, **1967**, *32*, 476.
22. L. Xiangqing, W. Xingqiao, S. Yingya, G. Jingfu, D. Jiangwen, L. Guofa, *Chemistry Magazin Organic* **2001**, *3*, 37.
23. Z. Jing, G. Yang, C. Shaokui, Z. Wennan, W. Dongmei, C. Huifang, L. Tianxuan, *Chemistry Magazin Organic*, **2002**, *8*, 39.
24. M. E. Milanese, M. G. Alvarez, E. I. Yslas, C. D. Borsarelli, J. J. Silber, V. Rivarola, E. N. Durantini, *Photochemistry and Photobiology*, **2001**, *74(1)*, 14.
25. E. Fagadar-Cosma, I. Creanga, B. Maranescu, A. Palade, A. Lőrinczi, G. Fagadar-Cosma, M. Popescu, *Digest Journal of Nanomaterials and Biostructures*, **2011**, *6*, 75.
26. D. Vlascici, E. Fagadar-Cosma, O. Bizerea-Spiridon, *Sensors (Basel)*, **2006**, *6(8)*, 892.
27. I. Sebarchievici, A. Lascu, G. Fagadar-Cosma, A. Palade, I. Fringu, M. Birdeanu, B. Taranu, E. Fagadar-Cosma, *Compt. Rendus Chimie*, **2018**, *21(3–4)*, 327.
28. Perzelová A., I. Máčiková, P. Mráz, I. Bízik, J. Steno, *Neoplasma*, **1998**, *45(1)*, 25.
29. L. Dyakova, D. C. Culita, G. Marinescu, M. Alexandrov, R. Kalfin, L. Patron, R. Alexandrova, *Biotechnology, Biotechnological Equipment*, **2014**, *28 (3)*, 543.

DETERMINATION OF PLASMA PHENYLALANINE CONCENTRATION BY TWO DIMENSIONAL THIN LAYER CHROMATOGRAPHY AND HIGH PERFORMANCE LIQUID CHROMATOGRAPHY IN RELATION WITH DIAGNOSIS OF PHENYLKETONURIA

CIPRIAN-VALENTIN MIHALI^{a,b}, CĂLIN FLAVIU LADAȘIU CIOLACU^a,
LUCIAN FRENȚESCU^{c,d}, CONSTANTIN-MARIAN PETRESCU^a,
IULIA MÂNDRUȚIU^c, DORIN BECHET^c, TIBERIU NISTOR^e,
AUREL ARDELEAN^{a, b, e}, GHEORGHE BENGA^{a, b, c, e, f, g, *}

ABSTRACT. Phenylketonuria (PKU) is a genetic disorder which can lead to serious long-term complications in children, including intellectual impairment. The cerebral damage can be largely eliminated if hyperphenilalaninemia (HPA) and PKU is detected by newborn screening and the dietary treatment (started no later than 10 days after birth), brings within 15 days the blood Phe level in the ranges 2 - 6 mg/dL (or equivalently 120 - 360 $\mu\text{mol/L}$). Consequently, the measurement of plasma Phe level in children with PKU is of utmost importance. We present here in detail two methods for determination of plasma Phe concentrations in children with HPA (detected by newborn screening) or suspected to have PKU based on clinical symptoms. The first method, involving two-dimensional thin-layer chromatography (2D - TLC) on micro scale chromatograms, allows the identification of patients with PKU. However, the quantitation of plasma Phe concentration by the 2D - TLC video-densitometric method is only semiquantitative, because is accompanied

^a *Institute of Life Sciences, "Vasile Goldiș" Western University, 91-93 Liviu Rebreanu Street, Arad, RO-310414, Romania.*

^b *Discipline of Cell and Molecular Biology, Faculty of Medicine, "Vasile Goldiș" Western University, 94-96 Revoluției Boulevard, Arad, RO-310035, Romania.*

^c *Cluj County Clinical Emergency Hospital, Laboratory of Genetic Explorations, 6 Pasteur Street, Cluj-Napoca, RO-400349, Romania.*

^d *Department of Biochemistry, "Iuliu Hațieganu" University of Medicine and Pharmacy, 6 Pasteur Street, Cluj-Napoca, RO-400349, Romania.*

^e *Cluj-Napoca Branch, Academy of Medical Sciences of Romania.*

^f *Cluj-Napoca Branch, Romanian Academy, 9 Republicii Street, Cluj-Napoca, RO-40015, Romania.*

^g *The Gheorghe Benga Foundation, Cluj-Napoca, Romania.*

* *Corresponding author: gbgbenga@gmail.com*

by large errors. In contrast, the high performance liquid chromatography determination of the plasma Phe level is fast, very sensitive and highly accurate. Both methods are rather cheap and reliable, suitable for use in countries that cannot afford more expensive procedures for diagnosis and monitoring of PKU.

Keywords: *amino acids (AA), phenylalanine (Phe), phenylketonuria (PKU), hyperphenylalaninemia (HPA), high performance liquid chromatography (HPLC), thin layer chromatography (TLC), phenylalanine hydroxylase (PAH).*

INTRODUCTION

Phenylketonuria (PKU, *OMIM 261600*) and its milder variant hyperphenylalaninemia (HPA) are genetic disorders belonging to a rare group of inborn errors of metabolism which can lead to serious long-term complications in newborns, including intellectual impairment. PKU and HPA are caused by a deficiency in phenylalanine hydroxylase (PAH) enzyme (*EC 1.14.16.1*), that is required to metabolise the essential amino acid phenylalanine (Phe) to tyrosine (Tyr) [1 - 3]. The decreased activity of PAH (caused in most forms of PKU and HPA by mutations in the *PAH* gene on chromosome 12q23.2.) results in intolerance to the dietary intake of Phe, and consequently, abnormally high levels of Phe and its metabolites (including phenylacetate, phenylpyruvate and phenethylamine) in the blood occur. These are toxic to the brain [1-5]. Moreover, decreased or absent activity of PAH can lead to a deficiency of Tyr and its downstream products, including melanin, l-thyroxine and the catecholamine neurotransmitters [2]. Clinically, untreated PKU is manifested by growth failure, global developmental delay, severe intellectual impairment, learning disabilities, microcephaly, seizures, EEG abnormalities, motor disturbances, marked hyperactivity with purposeless movements, aberrant behaviour, autism, psychiatric symptoms, deficits in executive function (a broad term including planning, problem solving, information processing, sustained attentions), decreased verbal memory, verbal fluency, mood, social and emotional difficulties, vision loss, skin hypopigmentation, eczematous rash, a "mousy" or "musty" odor of the breath, skin and urine (due to phenylacetate, a carboxylic acid produced by the oxidation of phenylketone) [1 - 7]. PKU has a particular significance and importance from several points of view. It was discovered in 1934 by Asbjørn Følling

[8], one of the first Norwegian physicians to apply chemical methods to the study of medicine [9, 10]. Its discovery established a link between metabolic disease and intellectual impairment [1-6]. The subsequent studies led to the development of programs for newborn screening (NBS) of PKU across the globe [11 - 14] and of effective dietary treatment: low-protein foods, low-Phe diet, combined with Phe-free L-amino acid supplements. When diagnosed by NBS and treated immediately, patients essentially develop normally [15 - 19]. However, neuropsychological deficits, behavioural and social issues can occur [1 - 7, 17 - 19]. Some patients with PKU respond to tetrahydrobiopterin (BH4), a naturally occurring essential cofactor for PAH, which decreases blood Phe concentration and increases dietary Phe tolerance [17, 20]. PAH deficiency produces a spectrum of disorders, classified on the basis of blood Phe concentrations into classic PKU (Phe > 20 mg/dL or equivalently 1200 μ mol/L), mild PKU (Phe = 10 - 20 mg/dL or 600 - 1200 μ mol/L) and mild HPA (Phe = 2 - 10 mg/dL or 120 - 600 μ mol/L) [7]. The normal range of blood Phe concentrations is 0.83 - 1.83 mg/dL or 50 - 110 μ mol/L [4].

The classic PKU is the most common and the most severe disorder due to PAH deficiency. The cerebral damage can be largely eliminated if PKU is detected and the dietary treatment is started as soon as possible after birth: no later than 10 days, preferably in the first week of life with a goal of having within 15 days the blood Phe level within the ranges 2 - 6 mg/dL (or equivalently 120 - 360 μ mol/L) [6]. The treatment should be continued up to the age of 12 years maintaining the blood Phe level within these ranges. Patients with untreated Phe levels more than 10 mg/dL (or equivalently 600 μ mol/L) should be treated for life, maintaining the blood Phe level within the ranges 2 - 6 mg/dL [5 - 7]. Other authors recommend the following Phe treatment ranges: birth to 8 years, Phe 1.7 - 5.9 mg/dL (or equivalently 100-350 μ mol/L); older children and adults, Phe < 11 mg/dL (or equivalently <700 μ mol/L) [10]. Mild PKU and mild HPA are associated with lower risk of impaired cognitive development in the absence of treatment. However, regular monitoring of plasma Phe level is necessary in all subjects with PAH deficiency to control that plasma Phe level is actually within the aforementioned ranges.

A particularly special attention should be given to women with PAH deficiency considering pregnancy, since highly elevated concentrations of Phe are teratogenic and are a cause of increased risk of miscarriage. Specifically, the foetus can be affected by HPA which induce intrauterine developmental delay, growth retardation, facial dysmorphism, microcephaly,

congenital heart disease. A preconception diet is required (to maintain a blood Phe target interval of 2 - 6 mg/dL or equivalently 120 - 360 $\mu\text{mol/L}$) and weekly monitoring of blood Phe levels has to be performed [6].

NBS debuted as a public health program in the USA in the early 1960's and has expanded to countries around the world in the 1970's. PKU was the first disorder diagnosed, based on detection of the presence of HPA on a blood spot obtained from a heel prick, typically performed 2–7 days after birth. Infants with PKU are normal at birth, the disease is not detectable by physical examination of the newborn, because the mother's body (if she does not have PKU) is able to break down Phe during pregnancy. The test can reveal elevated Phe levels after one or two days of normal infant feeding. NBS is performed to detect the disease and initiate treatment before any damage is done [1 - 7, 17 - 19]. Every 4 week delay in starting treatment results in a decline of ~four intelligence quotient (IQ) points in patients with PKU [21]. The major neurologic consequences of HPA have been largely eradicated in developed (high-income) countries because the screening for PKU is performed in all newborn children, the plasma Phe level is measured in all children with HPA and the treatment is introduced in the first days of life, no later than 10 days of life [5 - 7].

A positive result in the NBS may be due to laboratory errors, to maternal PKU, to a transient HPA due to a non-PKU disease (e.g. transient 4 α -carbinolamine dehydratase deficiency) or identifies an infant with HPA (PKU). Diagnosis of persistent HPA (PKU) is made on the basis of an elevated blood Phe concentration on the second blood sample, analysed by a referral laboratory. The upper reference limit for Phe in whole blood or plasma in newborns is < 2.5 mg/dL (or equivalent 150 $\mu\text{mol/L}$). Over 98% of the children with persistent HPA, have the disorder because of mutations at the PAH locus [1, 2].

If the steps outlined above cannot be properly performed and children who present some of the aforementioned clinical symptoms are consulted by family physicians, child neurologists or pediatricians, PKU may be suspected. Consequently, in addition to the NBS there is a "clinical screening" of PKU performed by such physicians. The blood Phe concentration of such children should be measured in well equipped (referral laboratories). The upper reference limit for plasma Phe level in these children is < 2mg/dL (or equivalently 120 $\mu\text{mol/L}$) [2].

PKU screening and management practices vary widely throughout individual countries and regions; large parts of the world fall behind even the basic standards. In many less developed (low- and middle-income)

countries PKU is either not diagnosed at birth, or it is not diagnosed at all, or it is diagnosed after the irreversible mental retardation is already installed. The reasons for these unfortunate situations are multiple: the lack of the robust infrastructure in which blood is taken from all newborn babies in the first days of life, the lack (or poor management) of well equipped laboratories that can manage and assess bloodspots efficiently, and of referral laboratories where the correct determination of blood Phe level of all infants detected to have HPA should be performed [6]. The recent Key European guidelines for the diagnosis and management of PKU [6] recommend specialized metabolic centres to be set-up for treatment and follow-up of patients.

Worldwide the incidence of PKU is approximately 1:15,000 to 1:20,000 and varies among ethnic groups, countries and geographic regions [1 - 6, 14, 22]. It is highest amongst Caucasians, between 1:10,000 and 1:15,000 people. Turkey has the highest documented incidence in the world, with 1:2,600 births (explained by the high prevalence of consanguinity), while Finland and Japan have extremely low rates with fewer than 1: 100,000 births (explained by a pronounced negative founder effect in Finland and a genetic drift in the founding of the Japanese island population) [2]. The lowest incidence of PKU was found in Thailand, <1:220,000, while a study from Slovakia reported a Roma population with an extremely high incidence (1:40 births) due to extensive inbreeding [22]. Among European countries, the incidence in Ireland and Western Scotland is 1:4,500 (among the highest in the world), while in England is 1:14,000. In other countries very different ranges were reported: Sweden 1:18,000 to 1:14,000, Norway 1:14,500, Denmark 1:12,000, Estonia 1:8,000, Netherlands 1:18,000, Germany 1:10,000, Poland 1: 8,000, Czechoslovakia 1:7,000, Romania 1:10,000 Republic of Moldova 1:9,000, Portugal 1:12,000, Spain 1: 20,000, France 1:13,500, Italy 1:17,000, Hungary 1:11,000, Canada 1:20,000, China 1:12,000–1:18,000, India 1:18,000, Korea 1: 41,000, Australia 1:10,000. In the USA, the PKU incidence is from 1:10,000 to 1:25,000. In Latin American countries (a region confirmed by 20 countries), neonatal PKU incidence was assessed on a very wide range between 1:12,000 in Brazil, 1: 53,000 in Cuba to 1:160,000 in Mexico.

Romania started the national program for NBS of PKU in 1999, however probably 10 % of newborns are not screened [13]. The same percentage was reported for Bulgaria and, recently, for China [23], while many countries, perhaps all African countries [24, 25], do not perform NBS. Considering the incidence of PKU in various countries, a very high number of children in the world are not correctly treated (from birth), will

become severely retarded, and finally will need to be all the life in the care of the family or in special institutions. In addition to the tragic consequences for the patients' families and the loss of healthy individuals who could perform valuable work for society, this implies high social costs. Consequently PKU raises major public health problems [1 - 7, 26).

In order to diagnose and monitor PKU correctly and avoid the preventable major neurologic sequelae, considering the incidence of PKU in various countries (including those where are living the majority of people in the world), it appears that a huge number (perhaps billions) of measurements of the blood Phe concentration have to be performed. There is a great need for methods to detect PKU in countries (mainly low- and middle-income) where the organization and financing of health system do not allow the use of the most modern methodologies as in the developed (high-income) countries.

We describe here in details two chromatographic methods for measurement of plasma Phe in children, in relation with the diagnosis of PKU and HPA. The first method involves rapid high-resolution two-dimensional thin-layer chromatography (2D - TLC) on micro scale chromatograms. The second method uses high performance liquid chromatography (HPLC). Both methods are rather cheap and reliable, suitable for use in countries that cannot afford the more expensive procedures for diagnosis and monitoring of PKU.

RESULTS AND DISCUSSION

Figure 1 shows 2-D - TLC chromatograms of plasma AA from two infants who were found to have HPA by newborn screening and the blood has been referred to the Laboratory of Genetic Explorations (LGE) of Cluj County Clinical Emergency Hospital for confirmation of HPA. Several aspects have to be noted. On the chromatograms developed in system A, Phe is not separated from leucine and isoleucine. In system B these amino acids are obtained apart from each other. In case of one infant the spot of Phe is very pale, so that HPA (and PKU) was excluded (the control case). In case of the other infant the spot of Phe is very intense, so that HPA detected by newborn screening was confirmed; moreover, based on the intensity of Phe spot, the diagnosis of classic PKU was established. These are typical examples of the value of 2D - TLC in the diagnosis of patients with PKU among infants with HPA detected by newborn screening.

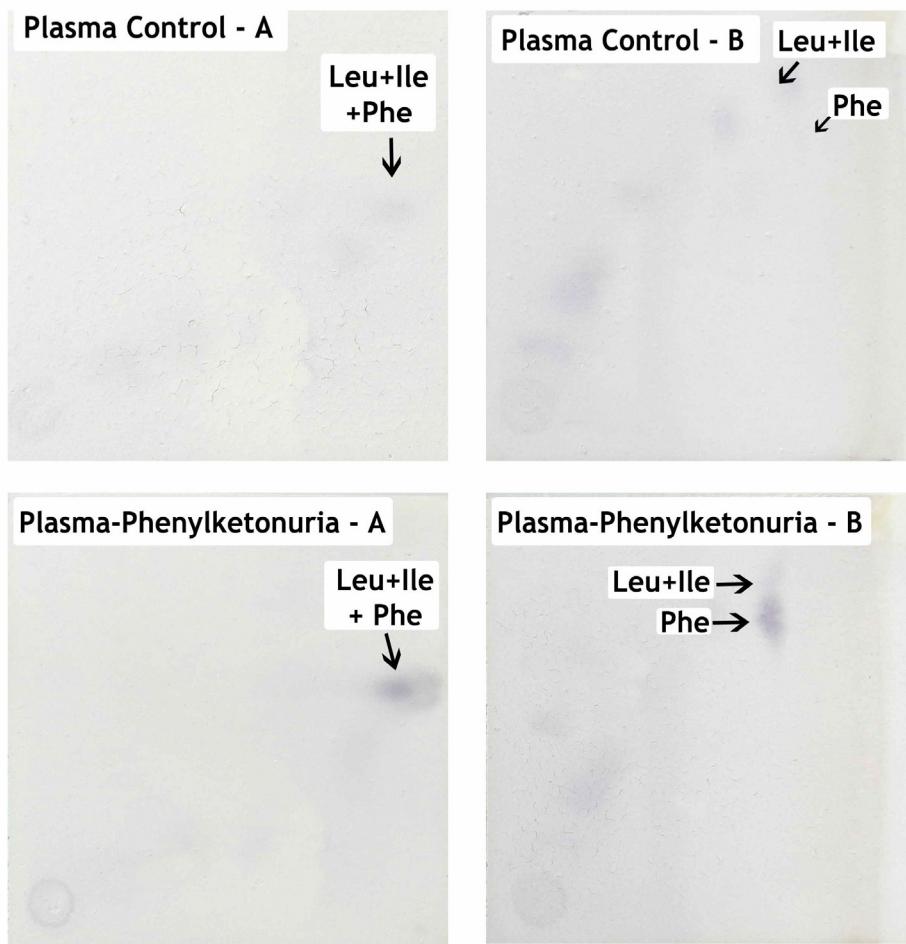


Figure 1. Aspects of 2D - TLC chromatograms of plasma amino acids from two infants who were found to have HPA by newborn screening.

In order to evaluate the possibility of quantification of Phe plasma concentration by 2D - TLC chromatography calibration curves were traced (**Figures 2a and b**), based on large numbers of measurements performed with several Phe standard solutions, prepared by several operators, who also performed the estimation of Adjusted Volume on different TLC plates (as described in **EXPERIMENTAL SECTION**).

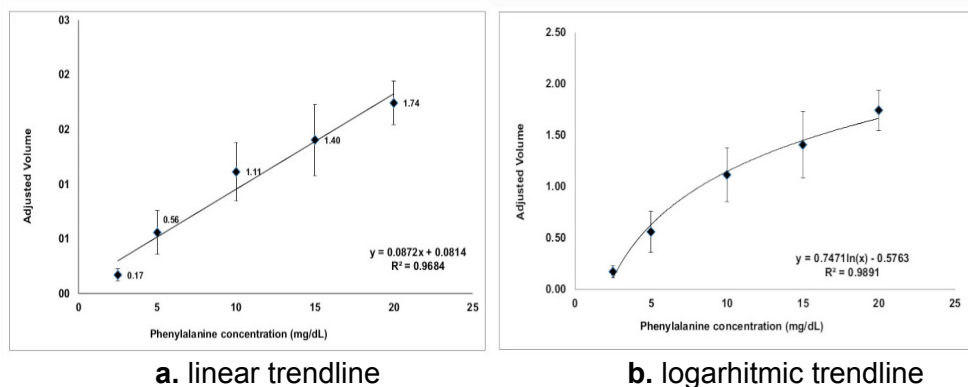


Figure 2. The standard calibration curve for measurement of Phe by quantitative 2D - TLC chromatography. The parameter Adjusted Volume vs. Phe concentration (mg/dL) is represented. The curve was obtained with Phe standard solutions having the following concentrations (in mg/dL): 2.5, 5, 10, 15, 20. The means and standard deviations (SD) of 17 - 33 determinations of Adjusted Volume at each concentration of Phe standard solutions are indicated. Microsoft Excel Software was used. The linear trendline representation was chosen in **a** and the logarithmic trendline representation in **b**.

By comparing **Figure 2a** and **b** it appears that a logarithmic representation is better, since the value of R-squared value is higher (0.989 vs. 0.968). However, neither the linear, nor the logarithmic representation appears to start in the origin of the two axes. In addition, if we take into consideration the very high value of the SD at each value of Phe concentration, it appears that a precise quantification of Phe plasma concentration by 2D - TLC chromatography is not possible.

Figure 3 shows the standard calibration curve for Phe measurement by HPLC. The ranges of concentrations have been chosen to correspond from normal plasma Phe concentrations (below 2 mg/dL) to the very high concentrations (over 20 mg/dL), as found in the severe cases of classic PKU. The curve shows linearity from the lowest concentration (0.48 mg/dL) to the highest concentration (29.4 mg/dL) of Phe and also it appears to start in the origin of the two axes. Considering also the very small values of the SD at each concentration of Phe, it appears that the procedure described here for the measurement of Phe by HPLC is very accurate. The value of R-squared value is the highest possible (1.000).

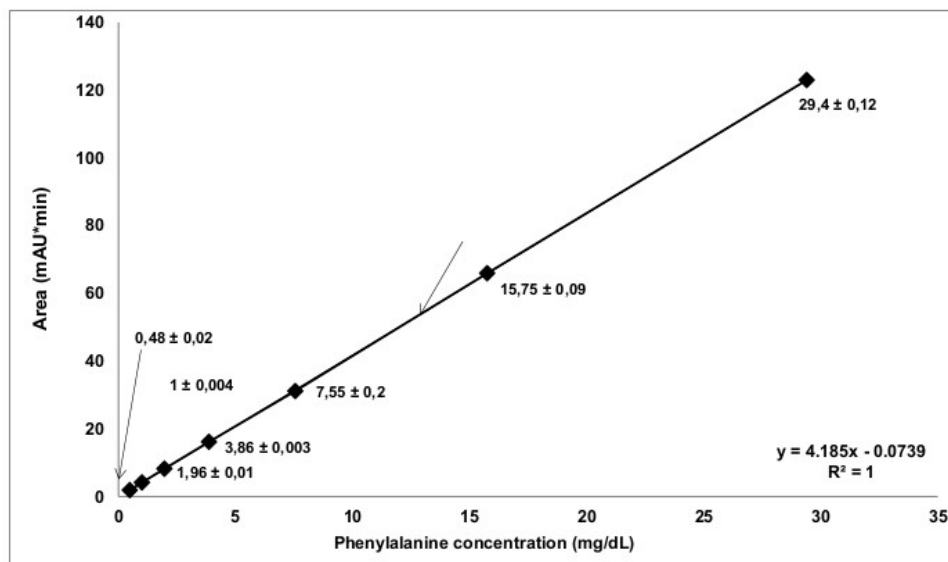


Figure 3. Graph showing the calibration curve of Phe by HPLC. The peak area given arbitrary absorption units (mAU) multiplied by time (min) for seven concentrations of Phe standard solution (means and SD) are indicated. Microsoft Excel Software was used.

The methods presented here are based by the long-term experience of our group. The corresponding author has decades-long expertise in quantitative analyses of amino acids, first by paper chromatography [27 - 29], later by amino acid analyzers [30 - 34] and TLC [35]. He founded in 1980 the the Laboratory of Genetic Explorations (LGE) of Cluj County Clinical Emergency Hospital, which became a referral lab, where thousands of blood samples from children suspected of PKU (detected by newborn screening or by "clinical screening", having the symptoms aforementioned) have been sent from all over Romania. Hundreds of children with PKU have been diagnosed and their treatment monitored. In recent years the valuable collaboration with the researchers from the Institute of Life Sciences of "Vasile Goldiș" Western University of Arad allowed the accurate measurements of plasma Phe level to be performed by HPLC.

The results presented here show the value of the 2D - TLC procedure for analysis of plasma amino acids described by Wadman and coworkers [36 - 38] as a powerful tool in identification of patients with PKU. Based on the intensity of the Phe spot on the chromatogram of plasma amino acids from the infants detected by newborn screening to have HPA, the diagnosis of PKU or HPA is confirmed. For a good interpretation of the

chromatograms (the most difficult phase of the analysis) it is necessary to have a good separations of amino acids on the chromatograms and a good experience with methodology. The decades-long use of this methodology in the lab lead by the corresponding author proved that personnel with various backgrounds working in clinical laboratories (biologists, chemists, technicians) can be trained in several weeks to perform the isolation of amino acids from blood and to identify PKU pattern.

On the other hand for quantitation of plasma Phe concentration the 2D - TLC video-densitometric methodology [39] is accompanied by large errors. The use of the logarithmic plot and the equation of the standard curve presented in this paper may decrease the errors. However, this method is only semiquantitative.

It should be mentioned that HPLC is the most widely used quantitative screening method for diagnosing the inborn errors of metabolism (PKU included), due to its speed and specificity [40 - 52]. In addition, the measurements of blood Phe levels by HPLC did not differ statistically from the determinations of blood Phe concentrations by tandem mass spectrometry (MS/MS), the technique recognized as the "gold" standard method for its sensitivity and specificity in the diagnosis of PKU and other 30 inborn errors of metabolism [50 - 52]. HPLC is used for 40 years to measure the blood concentration of Phe and other amino acids in laboratories dedicated to diagnosis and monitoring of patients with PKU, mainly from the developed (high-income) countries. A variety of approaches are presented, including the use of special columns, or performing pre- or post-column derivatization [40 - 50]. However, MS/MS and some HPLC methods are affordable only to the developed countries in the world [2 - 7, 13, 19]. It is not economic even for China [23].

The HPLC method for the determination of plasma Phe level described here requires specially trained personnel and adequate equipment, however the procedure does not involve special columns for analysis of amino acids or derivatization. Consequently, the procedure may be introduced in many clinical laboratories including those with no previous experience in diagnosis of inherited amino acid metabolic disorders.

CONCLUSIONS

Both chromatographic procedures described here may be used in laboratories from various countries, from the less developed ones (where no screening or diagnosis of PKU is performed), to countries where laboratories of genetic explorations exist, however there are not enough financial resources to measure (in all subjects who should be evaluated) the plasma Phe level by

more expensive methodologies. The major public health problems linked to PKU not being detected, including the burden of institutionalized children with preventable mental retardation may thus be avoided.

EXPERIMENTAL SECTION

Reagents and standards

Acetonitrile (HPLC grade), Phe and most other reagents (analytical grade) were purchased from Merck (Darmstadt, Germany). Dowex-50X8, 50-100 mesh was purchased from Bio-Rad Laboratories (Richmond, CA, USA). Phe standards with concentrations indicated in Figures 2 - 4 were prepared by appropriate dilution of a stock Phe solution (50 mg/dL) in deionized water.

Procedures

Blood specimen collection, separation of plasma, isolation and concentration of amino acids

Blood from infants with HPA, detected by NBS for PKU performed in the Cluj County Clinical Emergency Hospital, were collected into heparinized Vacutainer tubes (Becton Dickinson, Basle, Switzerland) and referred within 90 min to the LGE within 90 min. The samples were maintained on ice during transport. Plasma was prepared by centrifugation at 1600 g and at 22 °C. Isolation and concentration of amino acids was performed by the "desalting" procedure developed by Wadman and coworkers [36, 37] as described previously in detail [38]. Briefly, plasma was deproteinized with trichloroacetic acid, the sample was filtered and the filtrate was passed through a column of Dowex-50X8. The column was washed with distilled water and eluted with 2M ammonia. After evaporation in vacuum at 40 °C, the residue was dissolved in 50 µL of water. This is the concentrated solution of amino acids, free of salts and other interfering substances. An aliquot of the solution was used for the analysis of AA by 2D-TLC and another aliquot for the analysis of AA by HPLC.

Two-dimensional thin-layer chromatography of amino acids

2D-TLC was performed using the procedure of Wadman and coworkers [36, 37] with some changes [38]. TLC plates (5 × 5 cm) of cellulose on glass (prepared in the lab) were used. A narrow border of cellulose (~9 mm) is scratched off from the edge on each margin. 2µL of the concentrated solution of amino acids was applied in the lower left corner of the

chromatogram. The spot must be kept as small as possible. The development of chromatograms was performed in small glass tanks (tightly closed with a cover) at 20 °C. The solvents must be prepared shortly before use. The first run was performed in 96% ethanol:water (86:14, v/v) until the front reached 5 mm from the edge of the plate. After drying in air the chromatogram was developed a second time in the same direction. After drying the chromatogram was turned at right angles and the second run was performed in *t*-butyl alcohol:methylethylketone:25% ammonia:water (5:3:1:1, v/v). The development was repeated after the chromatogram was dried. After drying at 60 - 80 °C the chromatogram is stained by spraying with a solution of ninhydrin 0.42%, isatin 0.01% lutidin 1% (in acetone) then dried again at 100 °C. Maximum color is obtained after 120 min.

The final step was quantifying the level of plasma Phe by imaging-densitometric methodology applied on a Bio-Rad GS-700 imaging-densitometer (Bio-Rad Laboratories, Molecular Bioscience Group, Hercules, CA, USA), coupled to a computer. The Molecular Analyst/TM/PC Windows software for Bio-Rad's Image Analysis Systems Version 1.3 was used. The Phe spot volume (optic density x spot area) and the spot volume of a similar area of background are measured on the TLC plate. Then the parameter called Adjusted Volume was calculated as the difference between the Phe spot volume and the background spot volume (as described in ref [38]). Plasma concentration was calculated by using a calibration curve for the correspondence between the Phe concentration (mg/dL) and the Adjusted Volume.

HPLC analysis of amino acids

This was performed using a Dionex Ultimate 3000 instrument (low pressure gradient pump, Dionex 3000) equipped with a Ultimate 3000 diode array detector (DAD). The analytical column used was a Thermo Scientific Acclaim 120, C18, 5 μm Analytic (4.6 x 250 mm) column, coupled with an Acclaim C18 guard column. The working conditions were as follows: the mobile phases were acetonitrile (solution A) and water at pH 6 with formic acid (solution B), isocratic elution with 30% solvent A and 70% solvent B, elution time 5 minutes, column temperature 30 °C, injection volume 10 μL, detection wavelength 210 nm.

ACKNOWLEDGEMENTS

The corresponding author remains grateful to his former coworkers and colleagues with whom the methods of analysis of amino acids were introduced in the medical laboratories in Romania (27 - 29). He has introduced

later the TLC methods of analyses of amino acids for the diagnosis of amino acid metabolism disturbances after a visit performed in 1982 in the Laboratory of the late Professor Syde K. Wadman of The Wilhelmina Kinderziekenhuis, Utrecht, The Netherlands. Professors Gheorghe and Ileana Benga remain deeply grateful to Professor Wadman for inviting them, for his hospitality, and for training generously offered, also to Prof. Wadman's coworkers for their kindness to teach them the methods used in their lab for performing the diagnosis of inborn errors of metabolism.

Professor Gheorghe Benga founded in 1978 and coordinated the First Laboratory of Genetic Explorations (LGE) of Cluj County Clinical Emergency Hospital, Cluj-Napoca, Romania. LGE was accredited as a unit of the research platform of The Academy of Medical Sciences of Romania, also under the Aegis of The Romanian Academy. He is grateful to his former coworkers from the Center of Molecular Medicine and Neurosciences of The "Iuliu Hațieganu" University of Medicine and Pharmacy Cluj-Napoca for the decades of collaboration.

The authors thank also to Verona Pascu, Veronica Ardelean, Emese Opreș, and Livia Budișan for technical help in diagnoses of amino acid metabolism disturbances over the years in the LGE. Most of the patients who were investigated in this lab were selected and referred by the Pediatric Neurology Clinic of Cluj Clinical Emergency Children Hospital, lead by the former Chief of this Clinic, Professor Ileana Benga. Out of several thousands of samples referred to LGE for amino acid analyzes several hundreds of children with PKU were diagnosed and treated.

REFERENCES

1. C. L. Scriver, S. Kaufman, Hyperphenylalaninemia: phenylalanine hydroxylase deficiency. In C. Scriver, A. L. Baudet, W. S. Sly (eds) "The Metabolic and Molecular Bases of Inherited Disease", 8th ed., McGraw Hill, New York, **2001**, 1667- 1724.
2. R. A. Williams, C. D. S. Mamotte, Burnett, R. John, *The Clinical Biochemist*, **2008**, 29, 31.
3. J. J. Mitchell, Y. J. Trakadi, C. R. Scriver, *Genetics in Medicine*, **2011**, 13,697.
4. N. Blau, F. J. van Spronsen, H. L. Levy, *Lancet*, **2010**, 376, 1417.
5. J. Vockley, H. C. Andersen, K. V. Antschel, N. E. Braverman, B. K. Burton, D. M. Frazier, J. Mitchell, W. E. Smith, B. H. Thompson, S. A. Berry, *Genetics in Medicine*, **2014**, 16, 188.

6. F. J. van Spronsen, A. M. J. van Wegberg, K. Ahring, A. Bélanger-Quintana, N. Blau, A. M. Bosch, A. Burlina, J. Campistol, F. Feillet, M. Giżewska, S. C. Huijbregts, S. Kearney, V. Leuzzi, F. Maillot, A. C. Muntau, F. K. Trefz, M. van Rijn, J.H. Walter, A. MacDonald, *The Lancet Diabetes & Endocrinology*, **2017**, 5, 743.
7. S. A. Berry, C. Brown, M. Grant, C. L. Greene, E. Jurecki, J. Koch, K. Moseley, R. Suter, S. C. van Calcar, J. Wiles, S. Cederbaum, *Genetics in Medicine*, **2013**, 15, 591.
8. A. Følling, *Hoppe-Seylers zeitschrift für physiologische Chemie*, **1934**, 227,169.
9. I. Følling, *Acta Paediatrca*, Suppl. **1994**, 407, 4.
10. N. Blau, P. Burgard. Disorders of Phenylalanine and Tetrahydrobiopterin Metabolism. In N. Blau, J. Leonard, G. Hoffmann, J. Clarke (eds) "Physician's Guide to the Treatment and Follow-up of Metabolic Diseases", Springer Verlag, Heidelberg, **2006**, 25–34.
11. R. Guthrie, A. Susi, *Pediatrics*, **1963**, 32, 338.
12. U. Groseelj, M. Z. Tansek, T. Battelino, *Molecular Genetics and Metabolism*, **2014**, 113, 8.
13. U. Groseelj, M. Z. Tansek, A. Smon, N. Angelkova, D. Anton, I. Baric, M. Djordjevic, L. Grimc, M. Ivanova, A. Kadam, V. M. Kotori, H. Maksic, O. Mărginean, O. Mărgineanu, O. Milihanovic, F. Moldovanu, M. Mureșan, S. Murko, M. Nanu, B. R. Lampret, M. Samardzic, V. Sarnavkra, A. Savov, M. Stojiljkovic, B. Suzic, R. Tincheva, H. Tahirovic, A. Toromanovic, N. Ușurelu, T. Battelino. *Molecular Genetics and Metabolism*, **2014**, 113, 42.
14. M. Giżewska, A. MacDonald, A. Bélangee-Quintana, A. Burlina, M. Cleary, T. Coskun, F. Feillet, A. C. Muntau, F. F. Trefz, F. J. van Spronsen, N. Blau, *European Journal of Pediatrics*, **2016**, 175, 261.
15. H. Bickel, J. Gerrard, E. M. Hickmans, *Lancet*, **1953**, 265, 812.
16. I. Ahring, A. Bélanger-Quintana, K. Dokoupil, H. Gokmen Ozel, A. M. Lammardo, A. MacDonald, K. Motzfeldt, M. Nowacka, M. Robert, M. van Rijn, *Clinical Nutrition*, **2009**, 28, 231.
17. N. Blau, P. Burgard. Disorders of Phenylalanine and Tetrahydrobiopterin Metabolism. In N. Blau, J. Leonard, G. Hoffmann, J. Clarke (eds) "Physician's Guide to the Treatment and Follow-up of Metabolic Diseases", Springer Verlag, Heidelberg, **2006**, 53 - 89.
18. N. Al Hafid, J. Christodoulou, *Translational Pediatrics*, **2015**, 4, 304.
19. N. Blau, A. MacDonald, F. J. van Spronsen, *Molecular Genetics and Metabolism*, **2011**, 104, S1.
20. C. O. Harding, *Biologics Targets & Therapy*, **2010**, 4, 231.
21. I. Smith, M. G. Beasley, A. E. Ades, *Archives of Diseases in Childhood*, **1990**, 65, 472.
22. V. Ferák, D. Siváková, Z. Sieglóvá, (1987). *Bratislavské Lekárske Listy (Bratislava Medical Journal)*. **1987**, 87, 168.
23. I. Wang, H. Zou, F. Ye, X. Li, Z. Chen, J. Chen, B. Han, W. Yu, C. He, M. Shen, *Journal of Inherited Metabolic Diseases*, **2017**, 40, 369.

24. S. Khemir, M. El Asmi, H. Sanhaji, M. Feki, R. Jemaa, N. Tebib, J. L. Dhondt, M. F. Ben Dridi, A. Mebazaa, N. Kaabachi, *Clinical Neurology and Neurosurgery*, **2011**, 113, 727.
25. E. Sladkevicius, R. J. Pollitt, A. Mgdami, J. F. Guest, *Applied Health Economics and Health Policy*, **2010**, 8, 407.
26. V. Belengeanu, L. Moș, A. Covaci, Gh. Benga, *Acta Endocrinologica (Buc)* **2016**, 12, 1.
27. A. Popesco, Gh. Benga, D. Coman, V. Pop, *Revue Internationale d'Hepatology*, **1966**, 16, 1419.
28. Gh. Benga, D. Coman, *Spitalul*, 1967, 15, 312.
29. A. Hodârna, I. Chira, D. Coman, M. Căprioară, *Clujul Medical*, **1969**, 42, 519.
30. Gh. Benga, W. Ferdinand, *International Journal of Biochemistry*, **1977**, 8, 17.
31. Gh. Benga, V.I. Pop, O. Popescu, I. Benga, W. Ferdinand, *Bioscience Reports*, **1991**, 11, 53.
32. Gh. Benga, A. Hodârna, R. Tilinca, V. Borza, W. Ferdinand, *Bioscience Reports*, **1991**, 11, 95.
33. Gh. Benga, D. Poruțiu, A. Hodârna, W. Ferdinand, *Comparative Biochemistry and Physiology*, **1992**, 102 B, 123.
34. Gh. Benga, W. Ferdinand, *Bioscience Reports*, **1995**, 15, 111.
35. I. Benga, Gh. Benga, In P. Grigorescu-Sido (ed) "The Second National Symposium of Genetic, Endocrine and Metabolic Diseases in Children, Cluj - Napoca, 1998", Casa Cărții de Știință, Cluj-Napoca, **1998**, pp. 29-38.
36. S. K. Wadman, H. Fabery de Jonge, P. K. de Bree, *Clinica Chimica Acta*, **1969**, 25, 87.
37. S. K. Wadman, H. Fabery de Jonge, P. K. de Bree, *Clinica Chimica Acta*, **1969**, 25, 87.
38. H. J. Bremer, M. Duran, J. P. Kamerling, H. Przyrembel, S. K. Wadman, "Disturbances of Amino Acid Metabolism: Clinical Chemistry and Diagnosis", Urban & Schwarzenberg, Baltimore – Munich, 1981: 425.
39. R. Vulturar, "Tulburări genetice în metabolismul aminoacizilor", Ph. D. Thesis, "Iuliu Hațieganu" University of Medicine and Pharmacy, Cluj-Napoca, Romania, 2004.
40. N. D. Atherton, A. Green, *Clinical Chemistry*, **1988**, 34, 224.
41. N. D. Atherton, *Clinical Chemistry*, **1989**, 35, 975.
42. I. Czauderna, J. Kowalczyk, *Journal of Animal and Feed Sciences*, **1998**, 7, 453.
43. I. R. Allen, T. J. O. Degg, P. A. Rushworth, M. Smith, M. J. Henderson, *Annals of Clinical Biochemistry*, **1999**, 36, 207.
44. E. L. Schwarz, W. L. Roberts, M. Pasquali, **2005**, 354, 83.
45. F. Haghghi, S. Talebpour, V. Amini, A. Ahmadzadeh, M. Farhadpour, *Analytical Methods*, **2015**, 7, 7560.
46. H. Danafar, M. Hamidi, *Pharmaceutical and Biomedical Research*, **2015**, 1, 11.
47. Y. Song, K. Takatsuki, T. Sekiguchi, T. Funatsu, S. Shoji, M. Tsunoda, **2016**, *Amino Acids*, 48, 1731.
48. F. A. Abadi, A. Mirfazeli, H. Zaeri, M. Nejabat, M. Taherizadeh, M. Ariaie, A. Aliarab, H. Josaghani, *Medical Laboratory Journal*, **2016**, 10, 52.

C.-V. MIHALI, C. F. L. CIOLACU, L. FRENȚESCU, C.-M. PETRESCU, I. MÂNDRUȚIU, D. BECHET,
T. NISTOR, A. ARDELEAN, G. BENGA

- 49.A. Abbaskhanian, D. Zamanfar, A. Parvaneh, E. Asadpoor, H. Rouhanizadeh, A. Jafania, M. Shokzadeh, *International Journal of Preventive Medicine*, **2017**, 8, 93.
- 50.I. S. López, S. M. Santoyo, M. V. Amieva, *Acta Pediátrica de México*, **2012**, 33, 296.
- 51.I. Contreras, E. Alonso, L. E. Fuentes, *MEDICC Review*, **2015**, 17, 23.
- 52.A. O. Gregory, C. Yu, R. H. Singh, *Genetics in Medicine*, **2007**, 9, 761.

EVALUATION OF CAPPING AGENTS FOR SILVER NANOPARTICLES

CRISTIAN T. MATEA^a, TEODORA MOCAN^{a, b, *}, FLAVIU TABARAN^{a, c},
TEODORA POP^d, OFELIA MOSTEANU^d, LUCIAN MOCAN^{a, e},
CLAUDIU ZDREHUS^e

ABSTRACT. We have synthesized silver nanoparticles capped with: citrate, mercaptosuccinic acid, and thioctic acid respectively. Each of the obtained nanoparticles were characterized by means of: UV-Vis and ATR-FT-IR spectroscopy, dynamic light scattering (DLS), atomic force microscopy (AFM) and were found to be spherical in shape and aqueous stable.

Keywords: *silver nanoparticles, capping agents, citrate, mercaptosuccinic acid, thioctic acid*

INTRODUCTION

Silver nanoparticles (AgNPs), with their localized surface plasmon resonance (SPR) and remarkable antimicrobial properties have been a research focal point in the field of life sciences, for the past decade [1-4].

Several studies showed that the activity of noble metal nanoparticles, such as AgNPs, is strongly correlated with their colloidal stability [5, 6]. Special consideration must be given to the stabilization agents used for the synthesized nanoparticles. For example, divalent cations can induce AgNP aggregation by displacing the capping citrate layer [7], also pH significantly influences the stability of a AgNPs suspensions [8]. Adequate functionalization strategies must be undertaken in order to obtain nanostructures with specific characteristics for each biomedical application envisioned. These strategies can be divided into four

^a Department of Nanomedicine "Octavian Fodor" Gastroenterology Institute, Cluj-Napoca, Romania.

^b Department of Physiology, "Iuliu Hatieganu" University of Medicine and Pharmacy, Cluj-Napoca, Romania.

* Corresponding author: teodora.mocan@umfcluj.ro

^c Department of Pathology, Faculty of Veterinary Medicine, University of Agricultural Sciences and Veterinary Medicine.

^d 3rd Gastroenterology Department "Iuliu Hatieganu" University of Medicine and Pharmacy, Cluj-Napoca, Romania.

^e 3rd Surgery Clinic "Iuliu Hatieganu" University of Medicine and Pharmacy Cluj-Napoca Romania.

groups: a). covalent binding; b). non-covalent binding; c). using electrostatic charges between the biomolecules and the surface of the nanoparticles and d). ligand mediated binding (such as chemisorption) [4, 9, 10].

In the present paper we have synthesized aqueous stable AgNPs with capped with citrate (cit), mercaptosuccinic acid (MSA), and thiocetic acid (TA) respectively. The obtained silver colloids were investigated in terms of their size, shape, SPR band localization and stability by employing several analytical techniques: UV-Vis and FT-IR spectroscopies, dynamic light scattering (DLS) and atomic force microscopy (AFM).

RESULTS AND DISCUSSION

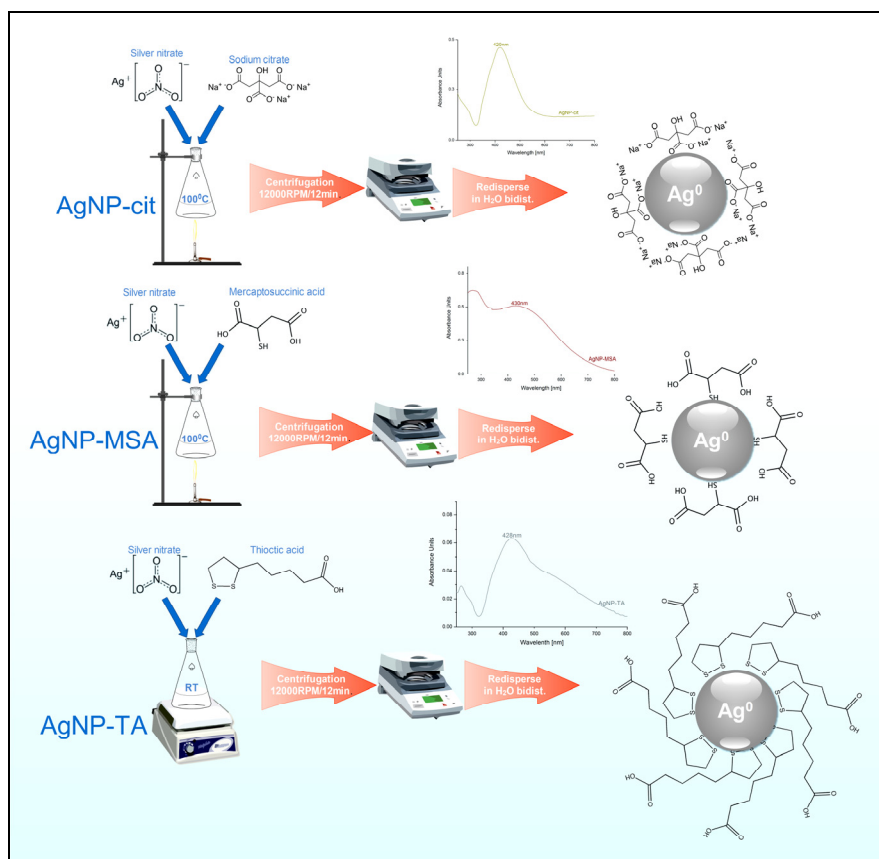


Figure 1. Graphical abstract for the synthesis routes employed for AgNP-cit, AgNP-MSA and AgNP-TA

We have proposed to evaluate 3 types of capping agents for AgNPs: citrate, mercaptosuccinic acid and thioctic acid. The synthesis routes undertaken are illustrated in fig.1. For citrate stabilized AgNPs a modified Turkevich method was used, where the citrate ions act as both reducing and stabilizing agents [11]. The same principle, where the capping agent acts both as a reducing and stabilizing agent, was employed with the mercaptosuccinic acid, yielding AgNP-MSA nanoparticles where the capping agent is linked to the nanoparticle surface through its thiol group [12]. While in the case of thioctic acid capping of AgNPs the reducing agent was NaBH_4 [13]. All three variants of AgNPs obtained were characterized in terms of aqueous stability, surface plasmon resonance band, surface chemistry, size and shape.

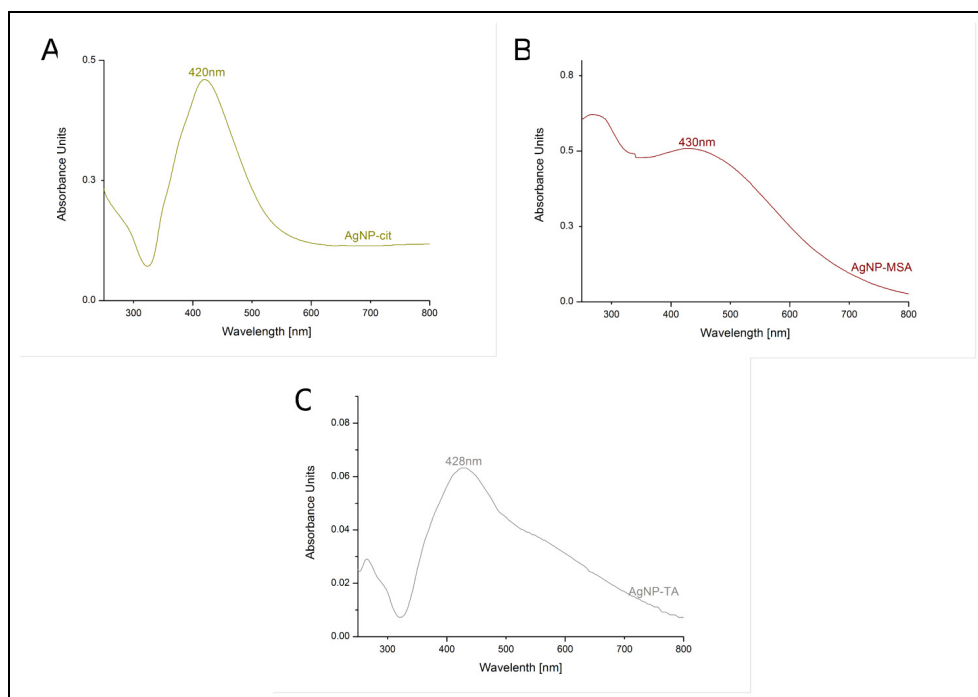


Figure 2. UV-Vis spectra of AgNP-cit (A), AgNP-MSA (B) si AgNP (C)

UV-Vis spectroscopy was used in order to determine the position of the surface plasmon band for AgNPs. In figure 2 the spectra for AgNP-cit (A), AgNP-MSA (B) si AgNP (C) are presented. The citrate stabilized silver nanoparticles presented an absorption peak at $\lambda_{\text{max}}=420$ nm, the MSA capped AgNPs had a wide peak centered at $\lambda_{\text{max}}=430$ nm, while the TA capped nanoparticles had a peak a $\lambda_{\text{max}}=428$ nm. These data are in good agreement with literature [14, 15].

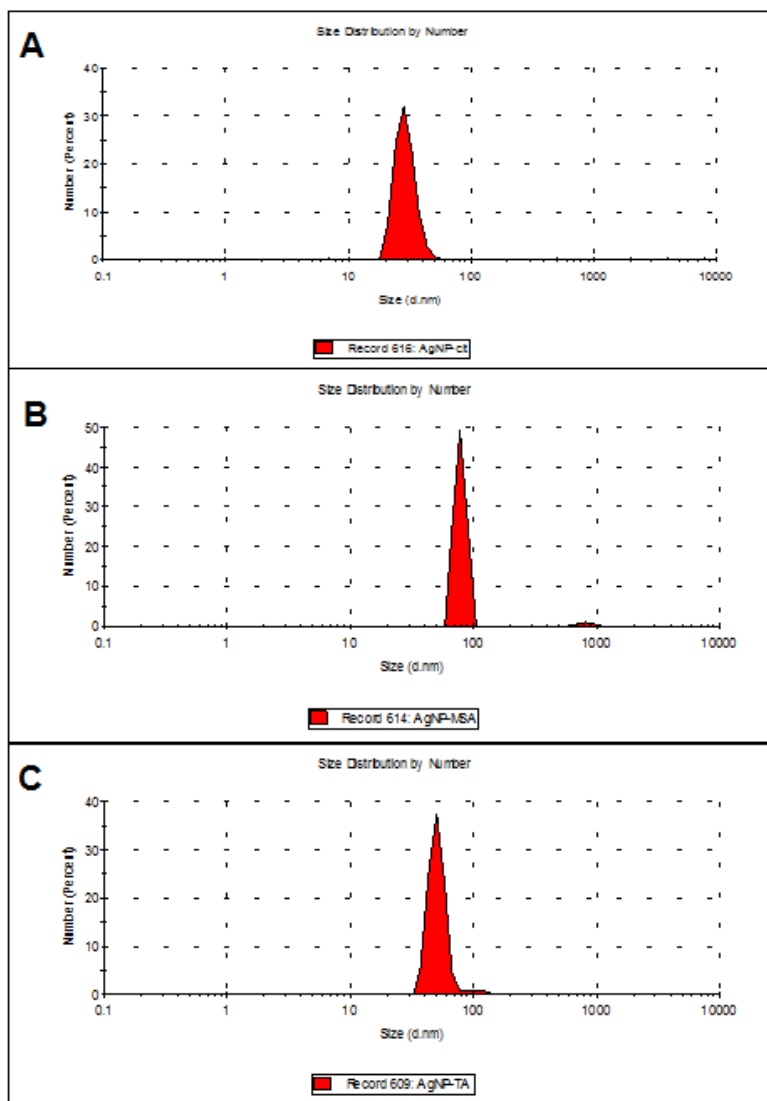


Figure 3. DLS size distribution curves AgNP-cit (A), AgNP-MSA (B) si AgNP-TA (C)

Figure 3 shows the size distribution of the hydrodynamic diameter for the citrate (A), MSA (B) and TA stabilized silver nanoparticles as measured by the DLS technique. AgNP-cit had a mean diameter of 29 nm, AgNP-MSA 69 nm and the AgNP-TA 51 nm. All three samples presented themselves as aqueous stable.

In order to confirm the presence of citrate, MSA and TA on the surface of the AgNPs the IR 'fingerprint' was acquired for each sample and are shown in figure 4. The AgNP-cit sample presented two absorption bands at 1582 and 1356 cm^{-1} which correspond to the antisymmetric and symmetric stretching vibrations of the COO^- from the citrate ions present on the surface of the silver nanoparticles. In the case of the AgNP-MSA sample the absorption band attributed to COO^- were recorded at 1567 and 1358 cm^{-1} , also the absence of an absorption band at 2550 cm^{-1} indicates the fact that the mercaptosuccinic acid is bonded on the surface of the nanoparticles via its thiolic group. For the AgNP-TA the bands at 2916 cm^{-1} , 2850 cm^{-1} , 1601 cm^{-1} si 1356 cm^{-1} are consistent with the characteristic IR spectra of thioctic acid [16].

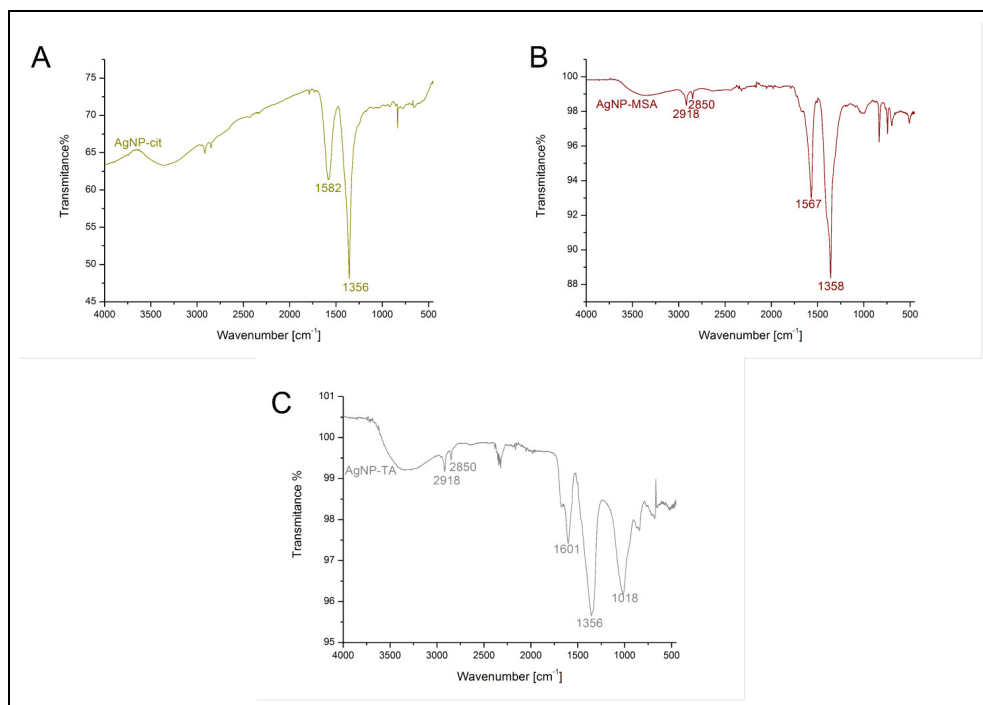


Figure 4. ATR-FT-IR spectra for AgNP-cit (A), AgNP-MSA (B) and AgNP-TA (C).

In figure 5 the AFM images, 2D and 3D representations, for the three samples are given. All capping agents used yielded nanometric, spheroidal particles. The sizes registered were: for AgNP-cit a size of ~ 23 nm; ~ 65 nm for AgNP-MSA and ~ 44 nm for AgNP-TA. The differences in sizes measured by AFM and DLS can be explained by the fact that dynamic light scattering technique provides slightly larger values due to the fact that this method

provides a mean hydrodynamic diameter of the nanoparticles surrounded by the capping agents [17].

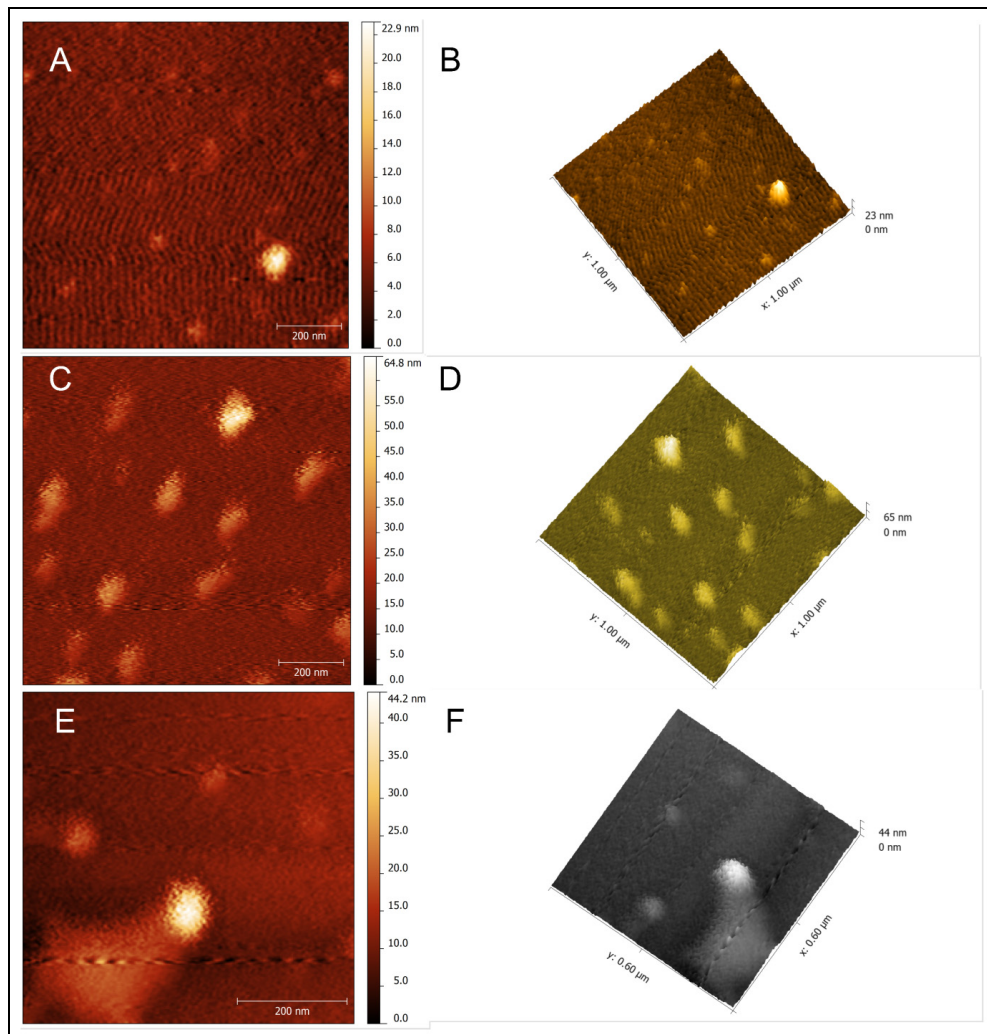


Figure 5. AFM image of r AgNP-cit (A- 2D; B- 3D), AgNP-MSA (C- 2D; D- 3D) and AgNP-TA (E- 2D; F 3D).

Each of the obtained samples can be further functionalized with proteins, peptides, drugs, and so on, depending on the biomedical application envisioned. For example for the AgNP-cit sample place exchange reactions can be employed, while for the AgNP-MSA and AgNP-TA samples EDC/NHS coupling can be used.

CONCLUSIONS

Aqueous stable silver nanoparticles were synthesized and capped with citrate, mercaptosuccinic acid, and thiocetic acid respectively. All three types of capping agents investigated yielded spherical AgNPs with different sizes. For the AgNP-cit a size of ~23 nm was registered, the AgNP-MSA had a mean size of ~65 nm, while the AgNP-TA sample ~44 nm. The surface plasmon resonance band for each sample was identified by means of UV-Vis spectroscopy. For the confirmation of the presence of each capping agent on the surface of the AgNPs IR spectra were recorded and compared. The different sizes and surface chemistries of the synthesized AgNPs can be used in different areas of biomedical research such as: antibacterial, drug delivery and sensor applications.

EXPERIMENTAL SECTION

Silver nitrate (AgNO_3 99.9%), tri-sodium citrate ($\geq 99\%$), mercaptosuccinic acid and the thiocetic acid were purchased from Sigma-Aldrich (Darmstadt, Germany) and used as received, without further purification. All glassware was cleaned with aqua regia ($\text{HCl}:\text{HNO}_3$, 3:1 v/v) prior to its use.

The citrate stabilized silver nanoparticles were synthesized by employing a modified Turkevich method. For this, 18 mg AgNO_3 were dissolved in 100 mL dist. H_2O and the solution was heated to 100°C under constant stirring. Afterwards, 2 mL sodium citrate 0.5% were rapidly injected and the reaction was allowed to continue until the solution turned pale-yellow in color. The AgNP-cit solution was allowed to cool to room temperature and subjected to a centrifugation step at 12000RPM/12min. The obtained sediment was re-dispersed in dist. H_2O with the aid of a 'in-probe' sonicator.

MSA capped AgNPs were obtained by reducing Ag^+ to Ag^0 with the aid of the mercaptosuccinic acid. Briefly, 50 mL sol. AgNO_3 0.6mM was brought to boiling and the 6 mL MSA sol. 28mM was added, where the MSA sol. was previously neutralized with NaOH 0.1M. The reaction was allowed to perfect for 30 minutes and after cooling the obtained solution was subjected to centrifugation and re-dispersing steps as described above in the case of AgNP-cit.

Thiocetic acid stabilized AgNPs were synthesized by mixing 2.5 mL AgNO_3 75 μM with 2.5 mL thiocetic 75 μM and then rapidly injecting 5 mL of freshly prepared NaBH_4 2.5mM. The reaction was allowed to perfect for 12h at room temperature and then the solution was centrifuged at 15000RPM/30min and the resulting pellet re-dispersed in dist. H_2O with the aid of a 'in-probe' sonicator.

The synthesized AgNP-cit, AgNP-MSA and AgNP-TA nanoparticles were evaluated on a UV-Vis spectroscopy Shimadzu UV-1800 spectrophotometer instrument. The spectra were recorded from 800nm to 200 nm with a spectral resolution of 0.5nm and normalized with the aid of OriginLab® software v7.0.

For dynamic light scattering (DLS) measurements of the samples a Nano ZS90 instrument (Malvern Instruments, Westborough, UK) was used at 25°C, a refractive index of 0.135 and an absorption of 3.99.

A Perkin-Elmer Spectrum Two® instrument equipped with an UATR single reflection diamond was used for the IR spectroscopy measurements. All spectra baseline corrections were done with the aid of the Spectrum10™ software.

Atomic force microscopy (AFM) data were recorded with a Workshop TT-AFM® instrument (AFMWorkshop, CA, USA), equipped with ACTA-SS (AppNano, CA, USA) cantilevers operated in vibrating mode. Samples were deposited on a mica substrate with a KLM® SCC spin-coater. The raw data collected were processed with the Gwyddion® software v2.36.

ACKNOWLEDGMENTS

This work was supported by the Romanian National Authority for Scientific Research and Innovation, CNCS-UEFISCDI, project numbers PN-III-P1-1.1-PD-2016-1831, PN-III-P2-2.1-BG-2016-0446 and PN-III-P1-1.1-TE-2016-2161.

REFERENCES

1. N. Duran; C. P. Silveira; M. Duran; D. S. T. Martinez, *Journal of Nanobiotechnology* **2015**, 13 (55), 1.
2. H. Li; D. Xu, *Trends in Analytical Chemistry* **2014**, 61, 67.
3. J. Natsuki; T. Natsuki; Y. Hashimoto, *International Journal of Materials Science and Applications* **2015**, 4 (5), 325.
4. A. Ravindran; P. Chandran; S. S. Khan, *Colloids and Surfaces B: Biointerfaces* **2013**, 105, 342.
5. K. Dastafkan; M. Khajeh; M. Bohlooli; M. Ghaffari-Moghadam; N. Shaibani, *Talanta* **2015**, 144, 1377.
6. M. Rai; A. P. Ingle; I. Gupta; A. Brandelli, *International Journal of Pharmaceutics* **2015**, 496 (2), 159.
7. B. L. Ouay; F. Stellaci, *Nano Today* **2015**, 10, 339.
8. C. Zhang; Z. Hu; B. Deng, *Water Research* **2016**, 88, 403.
9. L. Mocan; F. A. Tabaran; T. Mocan; T. Pop; O. Mosteanu; L. Agoston-Coldea; C. T. Matea; D. Gonciar; C. Zdrehus; C. Iancu, *International Journal Of Nanomedicine* **2017**, 12, 2255.
10. T. Mocan; C. T. Matea; T. Pop; O. Mosteanu; A. D. Buzoianu; S. Suciuc; C. Puia; C. Zdrehus; C. Iancu; L. Mocan, *Cellular And Molecular Life Sciences* **2017**, 74 (19), 3467.
11. A. Henglein; M. Giersig, *Journal of Physical Chemistry B* **1999**, 103, 9533.
12. K. Vasilev; T. Zhu; G. Glasser; W. Knoll; M. Kreiter, *Journal of Nanoscience and Nanotechnology* **2008**, 8 (4), 2062.
13. S. Berchams; P. J. Thomas; C. N. R. Rao, *Journal of Physical Chemistry B* **2002**, 106, 4647.
14. A. Moores; F. Goettmann, *New Journal of Chemistry* **2006**, 30, 1121-1132.
15. J. Park; J. S. Shumaker-Parry, *Journal of the American Chemical Society* **2014**, 136, 1907.
16. B. Adhikari; A. Banerjee, *Chemistry of Materials* **2010**, 22, 4364-4371.
17. G. Mandal; M. Bardhan; T. Ganguly, *Colloids and Surfaces B: Biointerfaces* **2010**, 81 178.

THE EFFECTS OF A NEW CHROMENYL-METHYLENE-THIAZOLIDINE-2,4-DIONE IN ALLEVIATING OXIDATIVE STRESS IN A RAT MODEL OF STREPTOZOTOCIN-INDUCED DIABETES

IRINA C. CHIȘ^{a,*}, ANDRA CLICHICI^b, RAMONA SIMEDREA^a,
REMUS MÔLDOVAN^a, VIORICA (LEORDEAN) LAZAR^c,
SIMONA CLICHICI^a, OVIDIU ONIGA^d, CRISTINA NASTASĂ^d

ABSTRACT. Type 1 diabetes mellitus (T1DM) is caused by the insulin deficiency resulting from the progressive destruction of pancreatic β cells. Thiazolidine-2,4-diones (TZDs) activate the peroxisome proliferator-activated receptor- γ (PPAR γ) and enhance the actions of insulin. 5-((6-methyl-4-oxo-4H-chromen-3-yl)methylene)-3-(2-(4-nitrophenyl)-2-oxoethyl)-thiazolidine-2,4-dione (TZDd) is a heterocyclic derivative synthesized in our laboratory. The purpose of this study was to examine whether TZDd has hypoglycemic and antioxidant effects in diabetic rats. Its effects were compared with those of quercetin (Que), a potent antioxidant, and with pioglitazone (Pio), a well-known antidiabetic drug. Type 1 DM was induced in Wistar rats by the intraperitoneal administration of streptozotocin (STZ) (60 mg/kg). The non-diabetic and diabetic rats were treated with Que (30 mg/kg/day), pioglitazone (30 mg/kg/day), or TZDd (30 mg/kg/day), for 5 weeks. The serum levels of malondialdehyde (MDA) and protein carbonyl (PC) groups, and the superoxide dismutase (SOD) and catalase (CAT) activities in the blood were then assessed. The results indicated that the TZDd decreased the blood oxidative stress parameters in the treated diabetic rats, compared to Que and pioglitazone. In conclusion, the hypoglycemic and antioxidant effects of TZDd in diabetic rats, suggest its therapeutic properties for the clinical treatment of T1DM.

Keywords: *diabetes mellitus; oxidative stress; quercetin; pioglitazone, thiazolidine-2,4-dione*

^a Iuliu Hațieganu” University of Medicine and Pharmacy, Department of Physiology, 1–3 Clinicilor street, RO-400023 Cluj-Napoca, Romania.

* Corresponding author: irinnaus@yahoo.com

^b Iuliu Hațieganu” University of Medicine and Pharmacy, 8 Victor Babeș street, RO-400012, Cluj-Napoca, Romania, student.

^c “Vasile Goldiș” Western University, Faculty of Medicine, 86 Liviu Rebreanu street, Arad, Romania

^d Iuliu Hațieganu” University of Medicine and Pharmacy, Department of Pharmaceutical Chemistry, 41 Victor Babeș street, RO-400012, Cluj-Napoca, Romania.

INTRODUCTION

The pathophysiological risk factor of insulin resistance, oxidative stress, hyperglycemia, hyperlipidemia and inflammation are involved in the development of diabetes mellitus (DM) and increase the incidence of diabetic complications [1,2].

Antioxidants from nutrients administered to diabetic animals, have been shown to improve the neuropathy and the endothelial dysfunction in DM [3-5]. Quercetin, one of the major flavonoids present in many fruits and vegetables, is known for its multiple biological effects such as potent vasodilator, free radical-scavenging and antioxidant action, anti-inflammatory, hypoglycemic and neuroprotective [6-9].

Thiazolidine-2,4-diones (TZDs) are the nuclear receptor peroxisome proliferator-activated receptor- γ (PPAR- γ) agonists and constitute a new class of pharmacological agents used in the management of dyslipidemia and hyperglycemia. Two TZDs, rosiglitazone and pioglitazone, are insulin sensitizers used as oral hypoglycemic agents to treat patients with type 2 DM (T2DM). PPAR- γ is highly expressed in the adipose tissue, where it plays an essential role in the regulation of lipogenesis, lipid storage, insulin sensitivity, glucose metabolism and the transcriptional regulation of a number of genes involved in these metabolic processes. Pioglitazone function as insulin sensitizer and thus, enhance the insulin action and improve hyperglycemia in patients with T2DM [10]. TZDs have also been shown to decrease pancreatic β cell destruction and therefore have a potential role in the treatment and prevention of T1DM [11].

Based on our previous experience in the synthesis of new bioactive compounds bearing the thiazolidine-2,4-dione heterocycle as an important scaffold in medicinal chemistry [12-14], in the present study, we present the synthesis of a new 5-chromenyl-methylene-thiazolidine-2,4-dione derivative (TZDd). Further, we evaluated its effect on the oxidative stress in streptozotocin (STZ)-induced diabetic rats. We hypothesized that TZDd might reduce the oxidative stress and the hyperglycemia induced by T1DM, by attenuating the fasting blood glucose levels and by free radical-scavenging, too.

RESULTS AND DISCUSSION

Chemistry

A new *N*-substituted 5-chromenyl-methylene-thiazolidine-2,4-dione derivative (Figure 1) was synthesized in our laboratory, following a procedure described previously [15].

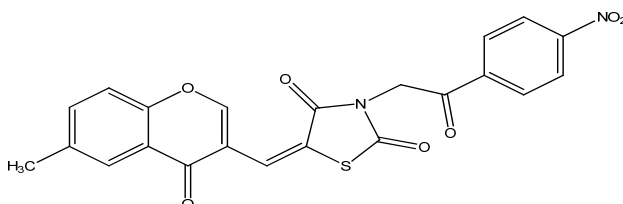


Figure 1. The new chromenyl-methylene-thiazolidine-2,4-dione derivative

Body Weight and Blood Glucose Level in Experimental Groups

The body weight and blood glucose levels of all the groups are shown in Table 1. The body weight decreased significantly ($P < 0.05$) in the diabetic rats. The administration of quercetin, pioglitazone or TZDd produced no significant change in the body weight of the non-diabetic or diabetic animals, as compared to the respective controls. The insulin treatment had significant ($P < 0.05$) effect on the body weight of diabetic rats, as compared to their respective control. The blood glucose levels were significantly increased in all STZ administered animals. The treatment with quercetin, pioglitazone or insulin produced a significant reduction in the blood glucose levels after 5 weeks, as compared to their respective control groups. The treatment of diabetic rats with TZDd (**DT** group) had cumulative effects in significantly reducing the blood glucose levels in diabetic rats.

Table 1. Body weight and blood glucose level in the experimental groups

Groups	Body weight (g)		Fasting blood glucose level (mg/dl)	
	Initial	Final	Initial	Final
CC	318.2±26.9	331±29.11	81.7±4.54	86.8±3.99
CQ	299.5±45.43	314.5±44.84	86.8±3.19	89.7±2.26
CP	288.4±24.74	307.1±26.03	85.2±2.86	90.5±2.95
CI	291.8±27.21	303±23.05	87.1±4.30	89.4±3.30
CT	298.5±31.1	312.3±30.56	87.3±3.68	90.9±1.85
DC	317.1±26.04	274.5±25.87 ^a	449.4±10.28 ^{aaa}	457.2±9.22
DQ	303.5±12.13	298.6±16.08	437.8±11.97 ^{aaa}	247.3±12.2 ^{bbb}
DP	316.9±13.4	311.4±11.09	441.9±9.26 ^{aaa}	341.9±9.26 ^{bbb}
DI	298.1±43.63	264.5±24.43 ^a	439.7±8.98 ^{aaa}	122.2±8.71 ^{bbb}
DT	306.1±37.78	299.6±38.94	445.6±6.83 ^{aaa}	303.5±12.13 ^{bbb}

CC=control+CMC, CQ=control+quercetin, CP= control+ pioglitazone, CI=control+insulin, CT=control+TZDd; DS=diabetes+CMC, DQ=diabetes+quercetin, DP=diabetes+pioglitazone, DI=diabetes+insulin; DT= diabetes+TZDd.

Results are mean± SD of 10 rats per each group. Statistically significant differences are indicated by the symbols: ^a $P < 0.05$, ^{aaa} $P < 0.001$ vs. **CC** group; ^b $P < 0.05$, ^{bbb} $P < 0.001$ vs. **DC** group.

Biochemical Parameters of Oxidative Stress in the Experimental Groups

As a measurement of the oxidative stress, we determined the malondialdehyde (MDA) and protein carbonyl content (PCC) levels in the serum of STZ-induced diabetic rats after 6 weeks of diabetes (Figure 2 a and b). The data in figures 2a and 2b demonstrate that the serum levels of MDA and PCC increased significantly ($P < 0.05$) after 6 weeks of diabetes (**DC** group). The diabetic rats treated with quercetin (**DQ** group) and pioglitazone (**DP** group), for 5 weeks, exhibited a significant decrease ($P < 0.05$) of the levels of MDA and PCC in their serum, when compared to the diabetic control rats treated with CMC (**DC** group). The administration of insulin (**DI** group) in diabetic rats for 5 weeks reduced non-significantly ($P > 0.05$) the serum levels of MDA and PCC, compared to the diabetic control rats treated with CMC (**DC** group). The diabetic rats treated with TZDd for 5 weeks (**DT** group) showed significantly reduced MDA and PC levels ($P < 0.05$) in the serum, as compared with the diabetic control rats treated with CMC (**DC** group). The results showed that TZDd decreased the MDA and PCC levels in the serum in a manner similar to quercetin and pioglitazone.

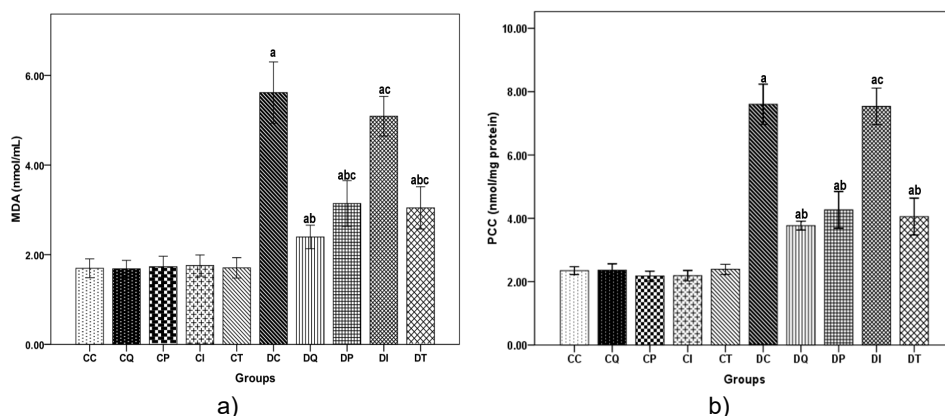


Figure 2. The effects of quercetin, pioglitazone, insulin and TZDd on (a) lipid peroxidation (MDA) (nmol/mL) and (b) protein oxidation (protein carbonyl content) (PCC) (nmol/mg protein) levels in the serum of non-diabetic and diabetic rats. Results are the means \pm SD for ten animals each group defined as in the caption of Fig. 2. Statistically significant differences are indicated by the symbols: ^a $P < 0.05$ vs. **CC** group, ^b $P < 0.05$ vs. **DC** group and ^c $P < 0.05$ vs. **DQ** group.

Figure 3 shows the effects of quercetin, pioglitazone, insulin and TZDd on the activities of superoxide dismutase (SOD) (Fig. 3a) and catalase (CAT) (Fig. 3b) in the blood of the non-diabetic control rats and

diabetic rats. The activities of SOD and CAT were significantly lowered ($P < 0.05$) 6 weeks after the STZ administration (**DC** group). The quercetin and pioglitazone treatment for 5 weeks significantly increased the SOD and CAT activities in the blood of the diabetic rats (**DQ** and **DP** groups), when compared to the diabetic control rats treated with CMC (**DC** group). The diabetic rats treated with insulin (**DI** group) for 5 weeks, exhibited a non-significant increase ($P > 0.05$) of the SOD and CAT activities in the blood, compared with the diabetic control rats treated with CMC (**DC** group). The SOD and CAT activities significantly increased ($P < 0.05$) in the blood of the diabetic rats treated with TZDd (**DT** group), when compared to the diabetic control rats treated with CMC (**DC** group).

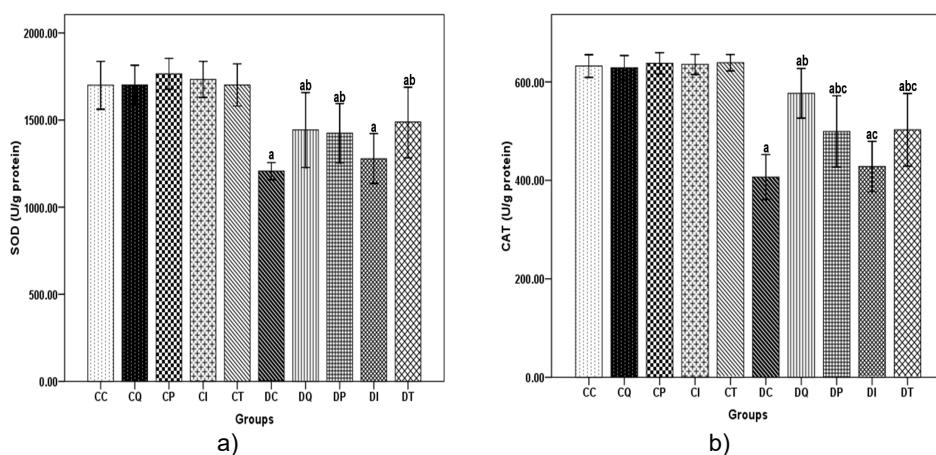


Figure 3. The effects of quercetin, pioglitazone, insulin and TZDd on the level of (a) superoxide dismutase (SOD) (U/g protein) and (b) catalase (CAT) (U/g protein) activities in the blood of non-diabetic and diabetic rats. Results are the means \pm SD for ten animals each group defined as in the caption of Statistically significant differences are indicated by the symbols: ^a $P < 0.05$ vs. **CC** group, ^b $P < 0.05$ vs. **DC** group and ^c $P < 0.05$ vs. **DQ** group.

Patients with T1DM suffer from hyperglycemia. The thiazolidine-2,4-diones (TZDs) represent a class of oral antidiabetic agents that are indicated for the treatment of patients with T2DM. Pioglitazone selectively stimulates PPAR- γ and modulates the transcription of genes involved in the control of glucose and lipid metabolism in the liver, adipose tissue and muscles [16,17]. In monotherapy or in combination with other oral antidiabetic drugs, it enhances the blood glucose levels, the long-term glucose control, and the lipid profiles [17]. Therefore, pioglitazone was chosen as a positive control drug in the analysis of glucose metabolism in our research.

Our results revealed that fasting blood glucose (FBG) levels significantly increased in the STZ-induced diabetic rats. This biochemical parameter was also improved in the diabetic rats treated with quercetin and pioglitazone, thereby suggesting that quercetin ameliorated the dysfunction of glucose metabolism in the STZ-induced diabetic rats. In our study, the thiazolidine-2,4-dione derivative (TZDd) effectively alleviated the glucose metabolism disorder in the STZ-induced diabetic rat model. The decrease in the FBG levels was interpreted as being due to the direct hypoglycemic effects.

The oxidative stress is involved in the development and progression of DM and its complications [18]. There are multiple likely sources of reactive oxygen species (ROS) in DM, including glucose autoxidation, glycation of proteins, consumption of NADPH through the polyol pathway, and activation of protein kinase C. ROS are targeted for removal by antioxidants and enzymes such as SOD and CAT. Hyperglycemia leads to elevated ROS, which dysregulates important metabolic pathways to promote micro- and macrovascular complications.

In our work, lipid peroxidation (MDA level) and oxidized proteins (PCC) were used as biomarkers of oxidative stress. This study found that the oxidative stress was higher in the serum of the STZ-induced diabetic rats, evidenced by the increased MDA and PCC levels and decreased antioxidant activities of SOD and CAT in the blood. The treatment of the STZ-diabetic rats with quercetin or pioglitazone reduced the MDA and the PCC levels in serum and increased the antioxidant SOD and CAT activities in the blood, suggesting the capacity of quercetin and pioglitazone to improve the antioxidant defenses in diabetic rats. Recent studies proved that quercetin and pioglitazone reduced the glycemia and decreased the oxidative stress in DM [2-5]. The SOD and CAT activities in the blood significantly increased and MDA and PCC levels in the serum significantly decreased in the diabetic rats treated with TZDd for 5 weeks. These findings suggest that the treatment with TZDd restores the antioxidant status in diabetes.

CONCLUSIONS

In summary, our findings suggest that the treatment with the new thiazolidine-2,4-dione derivative (TZDd) improved hyperglycemia and the antioxidant status in STZ-diabetic rats. Thus, the present study suggests that TZDd is able to produce positive therapeutic interaction in decreasing the oxidative stress produced by STZ-induced diabetes, by attenuating the fasting blood glucose level and by suppressing the oxidative stress.

EXPERIMENTAL SECTION

Drugs and Chemicals

Solvents were obtained from commercial sources (Sigma-Aldrich GmbH, Germany); the reagents were synthesized in our laboratory. Analytical thin layer chromatography was carried out on precoated Silica Gel 60F254 sheets using UV absorption for visualization. The melting points were taken with two melting point meters, Electrothermal and MPMH1 Schorpp, and are uncorrected. The ^1H NMR spectra were recorded at room temperature on a Bruker Avance NMR spectrometer operating at 400 MHz and were in accord with the assigned structures. Chemical shift values were reported relative to tetramethylsilane (TMS) as internal standard. The samples were prepared by dissolving the synthesized powder of the compounds in $\text{DMSO-}d_6$ as solvent. GC-MS analyses were realized with an Agilent gas chromatograph 6890 equipped with an apolar Macherey Nagel Permabond SE 52 capillary column. Elemental analysis was registered with a Vario EI CHNS instrument.

Streptozotocin (STZ), pioglitazone hydrochloride (Pio), quercetin (Que) (3,3',4',5,7-pentahydroxyflavone dihydrate, >98% purity powder) were purchased from Sigma-Aldrich Chemical Company Inc., (Gillingham, Dorset, UK).

Chemistry

5-((6-Methyl-4-oxo-4H-chromen-3-yl)methylene)-3-(2-(4-nitrophenyl)-2-oxoethyl)-thiazolidine-2,4-dione, was obtained according to a technique previously described [15].

5-((6-methyl-4-oxo-4H-chromen-3-yl)methylene)-3-(2-(4-nitrophenyl)-2-oxoethyl)thiazolidine-2,4-dione. Yield 86 %. Light-brown powder, mp: 262 °C. ^1H NMR ($\text{DMSO-}d_6$, 500 MHz, ppm): δ 3.04 (s, 3H, $-\text{CH}_3$); 5.20 (s, 2H, $-\text{CH}_2-$); 7.08 (d, 2H, phenyl); 7.60 (d, 1H, C8-chromone-H); 7.68 (dd, 1H, C7-chromone-H); 7.68 (s, 1H, C=CH); 7.92 (s, 1H, C5-Chromone-H); 8.12 (d, 2H, phenyl); 8.91 (s, 1H, C2-chromone-H). Anal. Calcd. (%) for $\text{C}_{22}\text{H}_{14}\text{N}_2\text{O}_7\text{S}$ (450.42): C, 58.66; H, 3.13; N, 6.22; S, 7.12. Found: C, 58.65; H, 3.13; N, 6.23; S, 7.11. MS (EI, 70 eV): m/z: 451 [M+1].

Animals

All protocols were approved by the Ethical Committee on Animal Welfare of "Iuliu Hațieganu" University (No. 44/13.03.2017), in accordance

with the Romanian Ministry of Health and complying with. The investigation conformed to the Guidelines in the Use of Animals in Toxicology. Type 1 diabetes mellitus (T1DM) was induced in Wistar rats (280-380 g), purchased from the Experimental Animal House ("Iuliu Hațieganu" University of Medicine and Pharmacy, Faculty of Medicine, Cluj-Napoca, Romania), by a single intraperitoneal (i.p.) injection of 60 mg/kg streptozotocin (STZ) dissolved in sodium citrate buffer (0.1 M, pH 4.5) as previously described [2-4]. The animals were given standard rat pellets diet and water *ad libitum*. The control group received a single i.p. injection with an equal volume of citrate sodium buffer, used to dissolve STZ. 96 H after the STZ administration, T1DM was confirmed by measuring the fasting blood glucose (FBG) concentration. Rats that had a FBG level higher than 250 mg/dL were included in the study as diabetic rats. One week after the STZ administration, the FBG level was measured and the treatment started. Blood glucose was measured from the retro-orbital venous plexus of the overnight fasting animals using the ACCU-CHEK Sensor System from Roche Diagnostics GmbH (Mannheim, Germany).

The rats were randomly divided into ten experimental groups ($n = 10$): the first group (control+CMC, **CC**)-non-diabetic control rats treated with carboxymethylcellulose (CMC); the second group (control + quercetin, **CQ**)-non-diabetic control rats treated with quercetin; the third group (control + pioglitazone, **CP**)-non-diabetic control rats treated with pioglitazone; the fourth group (control + insulin, **CI**)-non-diabetic control rats treated with insulin; the fifth group (control+TZDd, **CT**)-non-diabetic control rats treated with TZDd; the sixth group (diabetes + CMC, **DC**)-diabetic rats treated with CMC; the seventh group (diabetes + quercetin, **DQ**)-diabetic rats treated with quercetin; the eighth group (diabetes + pioglitazone, **DP**)-diabetic rats treated with pioglitazone; the ninth group (diabetes + insulin, **DI**)-diabetic rats treated with insulin; the tenth group (diabetes +TZDd, **DT**)-diabetic rats treated with TZDd.

One week after the STZ administration, the rats were treated with Que, Pio or TZDd (30 mg/kg body weight) daily by oral gavage for 5 weeks. The insulin (10 UI/kg body weight) was administered intraperitoneal (i.p.), daily, for 5 weeks. The rats from the groups: CC and DC received equal volumes of vehicle (CMC).

The FBG level was measured in all the experimental animals at the beginning of the experiment, 96 h after the STZ administration, 7 days after the STZ administration and at the end of the experiment. Upon the termination of the experiment at the end of 6 weeks, the animals were anesthetized with an i.p. injection of sodium pentobarbital (60 mg/rat) and sacrificed by cervical dislocation.

Measurement of the Biochemical Parameters of Oxidative Stress

The venous blood samples were collected from the rats' retro-orbital sinuses. Immediately after sampling, the blood was centrifuged to separate the serum. The serum was frozen with liquid nitrogen and stored in a -80°C refrigerator, until the biochemical assays.

Measurement of MDA production. Serum malondialdehyde (MDA) level, an end product of lipid peroxidation, was determined using the Conti method [19]. The MDA level was expressed as nanomole per milliliter (nmol MDA/mL).

Protein Carbonyl Content Measurement. Protein carbonyl content (PCC), a marker of oxidized proteins, was measured spectrophotometrically using the fluorimetric method with 2,4-dinitrophenyl-hydrazine (DNPH) [20]. The levels of the PCC were expressed as nanomole per milligram of protein (nmol/mg protein).

Activities of antioxidant enzymes in the erythrocytes were estimated.

Superoxide dismutase (SOD) activity was determined by the method of Flohe et al., [21]. The SOD activity was expressed as units per gram of protein (U/g protein).

Catalase (CAT) activity was determined by the method of Pippenger et al. [22]. The CAT activity was also expressed as units per gram of protein (U/g protein).

Statistical Analysis

Results are expressed as means \pm SD ($n = 10$). Statistical analysis was performed using SPSS software package version 17.0. One-way analysis of variance (ANOVA) was used to compare multiple data sets and when the P value obtained from ANOVA was significant ($P < 0.05$), Tukey's test was applied to test for differences among groups. $P < 0.05$ was taken to indicate a significant difference between group means.

ACKNOWLEDGMENTS

We gratefully thank Remus Moldovan for animal handling and experiments. We also thank Nicoleta Decea for her help regarding the assessment of the oxidative stress parameters. This study was supported by "Iuliu Hațieganu" University of Medicine and Pharmacy Cluj-Napoca internal research grant No. 4944/7/ 08.03.2016 (Cristina Nastasă).

REFERENCES

1. C.P. Domingueti, L.M. Dusse, M.D. Carvalho, L.P. de Sousa, K.B. Gomes, A.P. Fernandes, *Journal Diabetes Complic*, **2016**, 30, 738.
2. I.C. Chis, A. Muresan, O. Adrian, L.N. Andras, C. Simona, *Acta Physiologica Hungarica*, **2016**, 103(1), 49.
3. I.C. Chis, A. Coseriu, S. Ramona, O. Adrian, L.N. Andras, C. Simona, *Molecules*, **2015**, 20, 21770.
4. I.C. Chis, A. Clichici, A.L. Nagy, A. Oros, C. Catoi, S. Clichici, *Journal of Physiology and Pharmacology*, **2017**, 68(6), 877.
5. T. Kunasegaran, M.R. Mustafa, F.I. Achike, D.D. Murugan, *European Journal of Pharmacology*, **2017**, 799,160.
6. L.G. Costa, J.M. Garrick, P.J. Roquè, C. Pellacani, *Oxidative Medicine and Cell Longevity*, **2016**, 2986796.
7. W. Wang, C. Sun, L. Mao, P. Ma, F. Liu, J. Yang, Y. Gao, *Trends Food Science Technology*, **2016**, 56, 21.
8. P.M. Sha, P.V. Vishnu, R. Gayathri, *Journal Pharmaceutical Sciences Research*, **2016**, 8, 878.
9. I.C. Chiș, D. Baltaru, A. Dumitrovici, A. Coseriu, B.C. Radu, R. Moldovan, A. Mureșan, *Revista Virtual de Química*, **2016**, 8 (2), 369.
10. L. Han, W.J. Shen, S. Bittner, F.B. Kraemer, S. Azhar, *Future Cardiology*, **2017**, 13(3), 279.
11. K.S. Tafuri, M.A. Godil, A.H. Lane, T.A. Wilson, *Journal of Clinical Research in Pediatric Endocrinology*, **2013**, 5(4), 236.
12. C. Nastasă, M. Duma, C. Marie, D. Scherman, B. Tipericiu, O. Oniga, *Journal of Nanomaterials and Biostructures*, **2013**, 8 (3), 1079.
13. C.M. Nastasă, M. Duma, A. Pîrnău, L. Vlase, B. Tipericiu, O. Oniga, *Clujul Medical*, **2016**, 89 (1), 122.
14. I.C. Chis, D. Baltaru, S. Clichici, O. Oniga, I. Cojocar, C. Nastasa, *Revista de Chimie*, **2018**, 69 (9), 2361.
15. C. Nastasă, B. Tipericiu, L. Vlase, et al. *Studia UBB Chemia*, **2015**, LX (4), 239.
16. U. Smith, *International Journal of Clinical Practice*, **2001**, 121,13.
17. P. Jing, L. Qingde, L. Keye, Z. Li, L. Xiaoding, L. Xiaohong, S. Qianhui, L. Guoping, X. Xi, *Journal Diabetes Research*, **2017**, 2017, 3417306.
18. R.J. Pickering, C.J. Rosado, A. Sharma, S. Buksh, M. Tate, J.B. Haan, *Clinical and Translational Immunology*, **2018**, 7(4), e1016.
19. M. Conti, P.C. Morand, P. Levillain, *Clinical Chemistry*, **1991**, 37, 1273.
20. A.Z. Reznick, L. Packer, *Methods in Enzymology*, **1994**, 233, 347.
21. L. Flohe, R. Becker, R. Brigelius, E. Lengfelder, F. Ötting, *CRC Handbook of Free Radicals and Antioxidants in Biomedicine*, vol III, ed MiquelJ, CRCP ress, Boca Raton, **1994**, 287.
22. C.E. Pippenger, R.W. Browne, D. Armstrong, *Methods in Molecular Biology*, Amstrog, D., Ed.; Humana Press Inc.: Totowa, NJ, USA, **1998**, 108, 299.

MULTI-ELEMENT COMPOSITION OF RED AND WHITE WINES FROM BUJORU, SMULTI AND OANCEA WINE CENTER, ROMANIA

ALINA DONICI^a, EMESE GAL^b, CLAUDIA CIMPOIU^b, CLAUDIU IOAN BUNEA^{c, d}, FLORIN DUMITRU BORA^{a, *}

ABSTRACT. The ICP-MS technique was used to determine elemental composition (Pb, Sr, Cd, Ni, Co, Cu, Ni, Hg, As, Cr and Mn) of wines (Muscat Ottonel, Fetească Albă, Fetească Regală, Fetească Neagră, Merlot and Cabernet Sauvignon) wines produced in 2015, 2016 and 2017 from Bujoru, Smulti and Oancea wine-growing centers from Dealu Bujorului Vineyard. For all tested wine samples, the toxic metals contents were found in quantities below the limits established by legislation. The average data shows that the red wines contain highest concentration of Cd (0.17 µg/L), while the content of Cd in white wines are 0.11 µg/L. The concentration of U was 0.25 µg/L in red wines and 0.24 µg/L in white wines, while the concentration of Hg was 0.24 µg/L in red wines and 0.20 µg/L in white wines. The mean contents of Ni, Cr and Mn were 312.32 µg/L, 526.19±2.63 µg/L and 0.59±0.08mg/L, respectively. The concentration for Cu ranged from 0.45±0.10 mg/L to 0.90±0.04 mg/L, the last value being close to the law limit (1 mg/L). The four samples [Merlot 0.82±0.07 mg/L Bujoru wine-growing center (2015), Feteasca Alba 0.83±0.05 mg/L Smulti wine-growing center (2015), Merlot 0.83±0.05 mg/L Smulti wine-growing center (2015) and Cabernet Sauvignon 0.83±0.08 mg/L Oancea wine-growing center (2015)] showed relatively high concentration of Cu. Reporting the obtained results [Cd average 0.13±0.02 µg/L (0.1mg/kg M.L.A. = Maximum Limit Allowed) Pb average 40.64±1.85 µg/L (0.15 mg/kg M.A.L); As average 11.87±1.37 µg/L (0.2 mg/kg M.A.L); Cu average 0.67±0.09 mg/L (1 mg/kg M.A.L) to national and international legislation we can say that the wine from

^a *Research Station for Viticulture and Enology Targu Bujor, 65 G-ral Eremia Grigorescu Street, RO-805200, Galați Country Romania.*

^b *Babeş-Bolyai University, Faculty of Chemistry and Chemical Engineering, 11 Arany Janos Street, RO-400028, Cluj-Napoca, Romania.*

^c *University of Agricultural Sciences and Veterinary Medicine, Department of Horticulture and Landscaping, 3-5 Mănăştur Street, RO-400028, Cluj-Napoca, Romania.*

^d *Institute of Advanced Horticultural Research of Transylvania, 3-5 Mănăştur Street, RO-400028, Cluj-Napoca, Romania.*

* *Corresponding author: borafiorindumitru@gmail.com*

Dealu Bujorului vineyard falls within the limits set by the law. The content of potentially toxic elements such as Cd, Pb, U, Hg, As, Cu, Ni, Cr and Mn are lower than values found in literature, highlighting the safety and quality of the analysed Romanian wines.

Keywords: Dealu Bujorului vineyard, elemental composition, geographical traceability, wine.

INTRODUCTION

The origin and authenticity of food products are topics of great interest in the food industry, not only for consumers but also for producers and distributors. Additionally, the use of geographical designations allows producers to obtain market recognition and often a premium price [1]. Wine is a product widely consumed around the world and has been extensively investigated because of frauds, including adulteration, false declaration of geographical origin and false age declaration. The huge diversity of production areas poses a challenge in establishing the provenance of wine as their grape variety, soil and climate conditions, history, yeast, oenological practices, storage and transport [2, 3]. To take marketing advantage of the recent large improvements in wine quality in several „New World” wine regions, many local producers have changed to declare the specific region of origin rather than just naming the grape variety [4]. The denomination origin controlled (DOC) system are applied in many countries to control and ultimately guarantee the quality, origin and also to prevent de fraud. Chemical characterization is one of the requirements to obtain DOC certification of wines. Nowadays, there is a wide range of combined techniques to identify wine authenticity [5].

The inorganic chemical pattern of a wine is a reflection of the local geochemistry of the soil, climate and winemaking process. The elemental composition is mainly influenced by the bioavailability of inorganic compounds of the soil and the demands of the vine [6]. The initial concentration of elements can be modified during the winemaking process by the addition of bentonite or similar compounds, used to clarify the wine or by co-precipitation present in the must [7]. Not all elements are metabolized or modified during the winemaking process [8]. In wine from three southern Italian wine-producing regions were identified Li and Rb as elements facilitating a successful classification [9] wine from Spain were able to discriminate from two different Valencia by using Li and Mg content. However, factors such as environmental pollution, agricultural practices, climatic changes and winemaking process may change the multi-element

composition of wines. Nevertheless, significant correlations were obtained between the elemental composition of vineyard soil and wine [10].

The presence of lead in wine is associated with two major sources as follows: natural sources, which are due to the weathering of rocks, and human activity, which results from the use of fertilizers, pesticides and agricultural and food additives and environmental pollution [11].

The goal of this study is to determine the elemental composition (Cd, Pb, U, Hg, As, Sr, Co, Cu, Ni, Ce and Mn) of wine from Bujoru, Smulti and Oancea wine-growing centers from Dealu Bujorului vineyard and to assess their ability to discriminate between geographical origin of wines. The wines from Smulti and Oancea wine-growing centers have not been analyzed yet regarding concentration of the elemental composition.

RESULTS AND DISCUSSION

Heavy metals content in wine samples from Bujoru, Smulti and Oancea Wine Center

Table 1 and 2 summarize the total contents of Cd, U, Hg, As, Co, Cu, Ni, Cr and Mn in wine samples. Generally, the heavy metals are found in wine due to their presence in grapes, from where they are extracted during maceration [12]. These elements are found in grapes as a result of their accumulation in the plant from the soil, or they could be absorbed from the agents used in protecting the vine from diseases. In the course of the maceration, extracted elements are absorbed in the cell membrane of yeast, and in a while, their declines as a consequence of precipitation in conjunction with the yeast cell. The contact of wine with equipment, the addition of fining agents or the changing of filters during post fermentation processes could increase the content of some elements [12].

The mean contents of Cd, U and Hg were 0.13 ± 0.02 $\mu\text{g/L}$, 0.24 ± 0.03 $\mu\text{g/L}$ and 0.20 ± 0.03 $\mu\text{g/L}$. The highest concentrations of Cd and U were recorded in the wines obtained in 2016 from Smulti wine-growing center, namely Feteasca Neagra (0.22 ± 0.04 $\mu\text{g Cd/L}$ and 0.41 ± 0.06 $\mu\text{g U/L}$) and Merlot (0.21 ± 0.02 $\mu\text{g Cd/L}$ and 0.45 ± 0.05 $\mu\text{g U/L}$), while the highest concentrations of Hg were recorded in wines obtained from Bujoru wine-growing center (Feteasca Alba - 0.43 ± 0.05 $\mu\text{g Hg/L}$) in both years 2015 and 2016. The average data shows that the highest concentration of Cd was obtained to red wines (0.17 $\mu\text{g/L}$) compared to white wines white (0.11 $\mu\text{g/L}$), the highest concentration of U was obtained to red wines (0.25 $\mu\text{g/L}$) compared to white wines white (0.24 $\mu\text{g/L}$) while the highest concentration of Hg was obtained to white wines (0.24 $\mu\text{g/L}$), compared to white wines white (0.20 $\mu\text{g/L}$). The results agree with some studies [12] 0.25 $\mu\text{g/L}$ (Cd), 0.11 $\mu\text{g/L}$ (U), [13] 0.14 $\mu\text{g/L}$ (Cd), but compared with other result [14], the concentration

of Cd was significantly higher than ours 10.60 µg/L (Cd). Regarding Hg concentration the results agree with those made in Romania [15] for Sauvignon Blanc 0.56 µg/L, Feteasca Alba 0.22 µg/L and Riesling 0.16 µg/L.

Table 1. Variation of the metal content of white and red wines from Dealu Bujorului Vineyard (µg/L)

Area	Variety	Year	Cd	U	Hg	As
			M.L.A. 0.01 mg/L	M.L.A. -	M.L.A. -	M.L.A. 0.2 mg/L
Bujoru Wine Center	M Ott.	2015	0.11±0.02 ^m η	0.18±0.03 ^{klmnop} δεζ	0.34±0.08 ^{bcd} β	14.16±2.26 ^{efghijk} βγδ
		2016	0.12±0.01 ^{kim} ζη	0.27±0.04 ^{bcddefghij} αβγ	0.32±0.05 ^{bcddefg} β	15.48±0.85 ^{defghij} βγ
		2017	0.12±0.02 ^{klm} ζη	0.24±0.09 ^{cdefghijklmn} βγδε	0.30±0.02 ^{bcddefg} β	21.85±1.74 ^a α
	F A.	2015	0.12±0.01 ^m ζη	0.18±0.06 ^{klmnop} δεζ	0.43±0.05 ^a α	16.43±0.92 ^{cdefg} β
		2016	LOQ ^η θ	0.24±0.02 ^{cdefghijklmn} βγδε	0.43±0.04 ^a α	13.79±1.57 ^{ghijk} γδε
		2017	0.13±0.01 ^{ijklm} δεζη	0.17±0.02 ^{lmnop} εζ	0.31±0.03 ^{bcddef} β	13.36±1.15 ^{hijkl} γδε
	F R.	2015	LOQ ^η θ	0.21±0.05 ^{ghijklmnop} γδεζ	0.26±0.08 ^{fghij}	8.77±0.65 ^ρ θ
		2016	LOQ ^η θ	0.22±0.04 ^{efghijklmnop} βγδεζ	0.43±0.04 ^a α	13.79±1.57 ^{ghijk} γδε
		2017	0.13±0.01 ^{ijklm} εζη	0.35±0.02 ^b α	0.31±0.05 ^{bcddefg} β	15.23±1.15 ^{defghi} βγ
	F N.	2015	0.16±0.01 ^{defghijkl}	0.24±0.05 ^{cdefghijklmn} βγδε	0.33±0.04 ^{bcdde} β	14.37±2.09 ^{efghijk} βγδε
		2016	0.15±0.02 ^{defghijkl} γδε	0.26±0.03 ^{bcddefghijk} αβγδ	0.27±0.08 ^{cdefghi} β	10.03±0.47 ^{nop} ηθ
		2017	0.14±0.01 ^{efghijklm} γδεζ	0.26±0.03 ^{bcddefghijk} αβγδ	0.29±0.05 ^{bcddefg} β	10.26±0.87 ^{nop} ηθ
	M	2015	0.16±0.02 ^{cdefghijkl} γδ	0.17±0.01 ^{lmnop} εζ	LOQ ^s δ	12.02±0.50 ^{klmno} δεζ
		2016	0.21±0.02 ^{ab} α	0.16±0.01 ^{nop} εζ	0.30±0.04 ^{bcddefg} β	21.02±1.36 ^{ab} α
		2017	0.20±0.02 ^{abcd} αβ	0.17±0.03 ^{mnop} εζ	0.26±0.03 ^{efghij} β	LOQ ⁱ
	C S.	2015	0.13±0.02 ^{ijklm} εζη	0.30±0.08 ^{bcddef} αβ	LOQ ^s δ	10.45±0.81 ^{lmnop} ηθ
		2016	0.17±0.02 ^{bcddefghij} βγ	0.27±0.02 ^{bcddefghij} αβγ	0.15±0.02 ^{opr} γ	9.90±1.22 ^{nop} ηθ
		2017	0.17±0.03 ^{bcddefghij} βγ	0.23±0.03 ^{cdefghijklmno} βγδεζ	LOQ ^s δ	12.56±0.61 ^{ijklmno} ζηθ
Smulti Wine Center	M Ott.	2015	0.13±0.02 ^{ijklm} γδε	0.25±0.08 ^{bcddefghijk} αβγδ	0.13±0.02 ^{pr} ηθ	13.35±1.57 ^{hijkl} δεζη
		2016	0.13±0.01 ^{ijklm} γδε	0.25±0.06 ^{cdefghijklm} αβγδ	0.26±0.05 ^{efghij} β	13.99±2.29 ^{efghijk} δε
		2017	LOQ ^η ζ	0.15±0.04 ^{op} δε	0.19±0.03 ^{klmnop} γδεζ	17.40±1.99 ^{cd} βγ
	F A.	2015	0.13±0.01 ^{ijklm} ε	0.21±0.02 ^{ghijklmnop} βγδε	0.17±0.02 ^{mnop} δεζηθ	9.03±0.56 ^p ι
		2016	0.14±0.03 ^{efghijklm}	0.31±0.02 ^{bc} α	0.16±0.01 ^{mnop} ζηθ	10.36±0.76 ^{mnop} ηθι
		2017	LOQ ^η ζ	0.27±0.05 ^{bcddefghij} αβγ	0.22±0.04 ^{hijklm} βγδ	10.82±1.22 ^{lmnop} εζηθι
	F R.	2015	0.16±0.02 ^{bcddefghijk}	0.18±0.03 ^{klmnop} δε	0.15±0.01 ^{nopr} ζηθ	9.87±0.30 ^p ι
		2016	LOQ ^η ζ	0.28±0.07 ^{bcddefghi} αβ	0.20±0.02 ^{klmnop} γδεζ	12.86±0.69 ^{ijklm} δεζηθ
		2017	LOQ ^η ζ	0.19±0.03 ^{ijklmnop} γδε	0.12±0.01 ^r θ	10.45±0.92 ^{lmnop} ηθι
	F N.	2015	0.18±0.04 ^{abcddefgh} αβγδ	0.16±0.01 ^{nop} δε	0.20±0.03 ^{klmnop} γδεζ	15.82±3.24 ^{defgh} γδ
		2016	0.17±0.05 ^{abcddefghi} αβγδε	0.14±0.02 ^p δε	0.17±0.02 ^{lmnopr} δεζ	19.02±3.12 ^{bc} αβ
		2017	0.18±0.04 ^{abcddefg} αβγ	0.21±0.02 ^{ghijklmnop} βγδε	0.23±0.02 ^{hijkl} βγδ	21.12±1.34 ^{ab} α
	M	2015	0.18±0.04 ^{abcddefg} αβγ	0.26±0.06 ^{bcddefghijk} αβγδ	0.21±0.02 ^{ijklmno} βγδ	13.76±1.61 ^{ghijk} δεζ
		2016	0.19±0.04 ^{abcd} αβ	0.18±0.02 ^{lmnop} δε	0.22±0.03 ^{hijkl} βγδ	12.58±1.81 ^{ijklmno} εζηθ
		2017	0.13±0.02 ^{ijklm} δε	0.20±0.05 ^{ijklmnop} βγδε	0.22±0.01 ^{hijklm} βγδ	10.78±1.56 ^{lmnop} εζηθι
	C S.	2015	0.14±0.02 ^{efghijklm} βγδε	0.21±0.06 ^{ghijklmnop} βγδε	0.34±0.02 ^{bc} α	10.23±1.70 ^{nop} ηθι
		2016	0.18±0.03 ^{abcddefg} αβγδε	0.20±0.02 ^{hijklmnop} βγδε	0.31±0.06 ^{bcddefg} α	10.11±0.30 ^{nop} θι
		2017	0.21±0.03 ^{ab} α	0.21±0.04 ^{ghijklmnop} βγδε	0.25±0.03 ^{efghij} βγ	13.29±0.81 ^{hijkl} δεζηθ
Oancea Wine Center	M Ott.	2015	0.12±0.02 ^{ijklm} η	0.20±0.02 ^{hijklmnop}	LOQ ^s θ	12.66±0.46 ^{ijklmno} βγδ
		2016	0.17±0.01 ^{bcddefghij} βγδεζ	0.24±0.07 ^{defghijklmno} δεζ	0.20±0.05 ^{ijklmnop} δεζ	12.69±1.72 ^{ijklmno} βγδ
		2017	0.20±0.01 ^{abc} αβγ	0.33±0.02 ^b γ	0.21±0.05 ^{ijklmno} δε	LOQ ^ζ
	F A.	2015	0.14±0.02 ^{efghijklm} εζη	0.22±0.04 ^{ghijklmnop} εζ	LOQ ^s θ	9.59±1.69 ^{op} ε
		2016	0.17±0.01 ^{bcddefghij} βγδεζ	0.20±0.02 ^{hijklmnop} ζ	0.17±0.01 ^{lmnopr} εζ	13.21±1.45 ^{hijklm} βγ
		2017	0.13±0.02 ^{ijklm} ζη	0.48±0.03 ^s α	0.19±0.03 ^{klmnop} δεζ	10.36±0.76 ^{mnop} δε
F R.	2015	0.16±0.01 ^{bcddefghijk} γδεζ	0.30±0.02 ^{bcde} γδ	0.35±0.02 ^b α	16.97±3.84 ^{cde} α	
	2016	0.17±0.02 ^{bcddefghij} γδεζ	0.22±0.04 ^{efghijklmnop}	0.21±0.05 ^{ijklmno} δε	10.49±1.06 ^{lmnop} γδε	
	2017	0.13±0.02 ^{ijklm} ζη	0.29±0.02 ^{bcddefg} γδε	0.30±0.02 ^{bcddefg} αβ	10.33±0.80 ^{mnop} δε	

MULTI-ELEMENT COMPOSITION OF RED AND WHITE WINES FROM BUJORU ...

Area	Variety	Year	Cd	U	Hg	As
			M.L.A. 0.01 mg/L	M.L.A. -	M.L.A. -	M.L.A. 0.2 mg/L
F N.	2015	0.14±0.03 ^{ghijklm} εζη	0.28±0.03 ^{bcd} efgh γδε	0.28±0.04 ^{bcd} efgh βγ	16.67±0.84 ^{cd} ef α	
	2016	0.22±0.04 ^a α	0.41±0.06 ^a β	0.33±0.03 ^{bcd} αβ	12.24±1.22 ^{klmno} βγδε	
	2017	0.20±0.02 ^{abcd} αβγ	0.29±0.02 ^{bcd} ef γδε	0.36±0.04 ^b α	16.92±2.51 ^{cde} α	
M	2015	0.19±0.03 ^{abcd} αβγδ	0.45±0.05 ^a αβ	0.15±0.03 ^{lmnop} ζ	LOQ ^ζ	
	2016	0.21±0.02 ^{ab} αβ	0.26±0.05 ^{bcd} efghijk βγδεζ	0.17±0.01 ^{lmnop} εζ	9.41±1.16 ^{op} ε	
	2017	0.19±0.02 ^{abcd} αβγδ	0.30±0.04 ^{bcd} ef γδ	0.24±0.02 ^{ghijk} γδ	LOQ ^ζ	
C S.	2015	0.17±0.02 ^{bcd} efghij γδεζ	0.32±0.03 ^{bc} γ	0.20±0.03 ^{klmno} p δεζ	10.83±1.72 ^{lmnop} γδε	
	2016	0.19±0.02 ^{abcde} αβγδ	0.29±0.02 ^{bcd} ef γδε	0.23±0.02 ^{hijkl} γδ	14.96±1.70 ^{defghij} αβ	
	2017	0.18±0.04 ^{abcde} αβγδε	0.32±0.07 ^{bc} γ	LOQ ^s θ	LOQ ^ζ	
Average			0.13±0.02	0.24±0.03	0.20±0.03	11.87±1.37
Minimum Values			0.11±0.02	0.14±0.02	0.13±0.02	8.77±0.65
Maximum Values			0.22±0.04	0.48±0.03	0.48±0.03	21.85±1.74
F			23.242	9.324	29.901	33.878
Sig.			***	***	***	***
Area	F	87.159	71.396	56.695	80.655	
	Sig.	***	***	***	***	
Variety	F	97.092	1.469	34.672	62.417	
	Sig.	***	<i>in</i>	***	***	
Year	F	1.465	2.954	35.014	32.436	
	Sig.	<i>in</i>	<i>in</i>	***	***	
	[18]		0.86±0.55			
	[23]	0.41	0.55		7.10	
	[15]	0.22		0.56	5.24	
	[24]					

Average value ± standard deviation (n = 3). Romans letters represent the significance of the variety difference ($p \leq 0.05$). Greeks letters represent the significance of the same variety cultivated in other year's difference ($p \leq 0.05$). The difference between any two values, followed by at least one common letter, is insignificant. M.L.A. - maximum limit allowed (OIV, 2005); LOQ - lower than the limit of quantification; Cu* = (mg/L); Cu** = (μg/L); Mn*** = (mg/L). M Ott. = Muscat Ottonel; F a. = FeteascaAlba; F r. = Feteasca Regala; F n. = Feteasca Neagra; M = Merlot; C s. = Cabernet Sauvignon.

As and Co content in wine ranged from [21.85±1.74 μg As/L; 8.77±0.65 μg As/L] and [7.80±0.25 μg Co/L; 3.32±0.25 μg Co /L] with an average value of 11.87±1.37 μg As/L and 5.17±0.51 μg Co/L. In both cases the maximum concentration were recorded in wine obtained from varieties cultivated in the Bujoru wine-growing center [21.85±1.74 μg As/L (Muscat Ottonel 2017); 7.80±0.25 μg Co/L (Cabernet Sauvignon 2015)] and in Smulti wine-growing center [21.12±1.34 μg/L As (Feteasca Neagra 2017); 7.65±0.42 μg/L Co (Feteasca Alba 2016) and 7.23±0.30 μg/L Co (Feteasca Neagra 2015)]. The average data shows that a higher concentration of As was obtained in white wines (12.45 μg/L) as compared to red wines (11.42 μg/L), while the higher concentration of Co was recorded for red wines (5.58 μg/L) as compared to white wines (5.09 μg/L) (Table 1). The results are comparable with those obtained in Serbia [13] 16.1 μg/L (As) for red wines and 9.46 (As) μg/L for white wines, in Macedonia [14] 11.7 μg/L (As) by using the same microvinification technology, in Romania [15] 21.12 μg/L

(As) and 154.90 $\mu\text{g/L}$ (Sr), and higher compared to the results obtained in Italy [16] 2.91 $\mu\text{g/L}$ for As, but for Sr the results obtained are significantly lower compared to the results obtained in Italy [16] 1340 $\mu\text{g/L}$ (Sr). Regarding Co concentration the results agree with other studies made in Macedonia [12, 14] 3.9 $\mu\text{g/L}$ and 13.90 $\mu\text{g/L}$ for Co, and in Serbia [13] 3.89 $\mu\text{g/L}$ (Co) for red wines and 3.96 (Co) $\mu\text{g/L}$ for white wines.

The mean contents of Ni, Cr and Mn were 312.32 ± 2.42 $\mu\text{g Ni/L}$, 526.19 ± 2.63 $\mu\text{g Cr/L}$ and 0.59 ± 0.08 mg Mn/L , in case of Ni the highest concentrations were recorded in wine obtained from varieties cultivated in the Bujoru wine-growing centre Feteasca Alba (462.48 ± 4.02 $\mu\text{g Ni/L}$ (2017)) followed by the same variety but cultivated in the Oancea wine-growing center (433.76 ± 2.96 $\mu\text{g Ni/L}$ (2016)). Cr was recorded the highest concentrations in wine obtained from varieties cultivated in the Oancea wine-growing center (923.62 ± 2.05 $\mu\text{g Cr/L}$ (2016)), followed by the same variety but cultivated in the Bujoru wine-growing center (843.99 ± 3.89 $\mu\text{g Cr/L}$ (2016)). Regarding Mn concentration from wine samples, the highest concentrations in wine obtained from varieties cultivated in the Bujoru wine-growing center (0.92 ± 0.05 $\mu\text{g Mn/L}$ (2016)). The results agree with those made in Turkey [17] 520 $\mu\text{g Ni/L}$, in Romania [18] 147.73 $\mu\text{g Cr/L}$ and significantly higher than obtain in Serbia [8] 5.49 $\mu\text{g Cr/L}$ red wines and 6.56 $\mu\text{g Cr/L}$ white wines, in Italy [16] 54.57 $\mu\text{g Ni/L}$ and 19.68 $\mu\text{g Cr/L}$, in Macedonia [14] 32.10 $\mu\text{g Cr/L}$ and 10.20 $\mu\text{g Cr/L}$, in Romanian [18] 805.89 $\mu\text{g Mn/L}$. The results indicated that Romanian wines are moderately rich in Cr (Table 2).

The concentration for Cu ranged from 0.45 ± 0.10 mg/L to 0.90 ± 0.04 mg/L , with average values of 0.67 ± 0.09 mg/L , the latter value approaching the law limit (1 mg/L). The four samples [Merlot 0.82 ± 0.07 mg/L Bujoru wine-growing center (2015), Feteasca Alba 0.83 ± 0.05 mg/L Smulti wine-growing center (2015), Merlot 0.83 ± 0.05 mg/L Smulti wine-growing center (2015) and Cabernet Sauvignon 0.83 ± 0.08 mg/L Oancea wine-growing center (2015)] showed relatively high concentration of Cu. Wide ranges for Cu concentration in wines have been previously found and reported by other researchers in Brazil [19] 0.056-0.764 mg Cu/L , in Hungary [20] 0.031-0.313 mg Cu/L , in Italy [21] 0.50-1.00 mg Cu/L and in Greece [22] 0.076-0.114 mg Cu/L (Table 2).

Reporting the obtained results [Cd average 0.13 ± 0.02 $\mu\text{g/L}$ (0.1 mg/kg M.L.A. = Maximum Limit Allowed) Pb average 40.64 ± 1.85 $\mu\text{g/L}$ (0.15 mg/kg M.A.L); As average 11.87 ± 1.37 $\mu\text{g/L}$ (0.2 mg/kg M.A.L); Cu average 0.67 ± 0.09 mg/L (1 mg/kg M.A.L) to national and international legislation we can say that the wine from Dealu Bujorului vineyard falls within the limits set by the law (Table 2).

Table 2. Variation of the metal content of white and red wines from Dealu Bujorului Vineyard ($\mu\text{g/L}$)

Area	Variety	Year	Co M.L.A. -	Cu** M.L.A. 1 mg/L	Ni M.L.A. -	Cr M.L.A. -	Mn*** M.L.A. -
Bujoru Wine Center	M Ott.	2015	4.77±0.36 ^{klmnoprst} δεζ	0.63±0.13 ^{ghijklm} βγδ	365.61±3.67 ^l ζ	357.82±1.52 ^{rs} κλ	0.32±0.04 ^{no} η
		2016	3.34±0.28 ^u η	0.57±0.05 ^{ijklm} δ	247.11±1.69 ^l ι	475.63±2.84 ^m η	0.31±0.05 ^o η
		2017	5.28±0.24 ^{ghijklmnop} γδε	0.66±0.08 ^{defghijkl} αβγδ	258.24±3.42 st θ	629.48±4.51 ^h γ	0.49±0.05 ^{hijklm} εζ
	F A.	2015	3.41±0.21 ^u η	0.67±0.08 ^{cdefghijkl} αβγδ	450.74±1.74 ^c γ	248.33±1.05 ^w ξ	0.59±0.12 ^{efghi} δε
		2016	4.67±0.19 ^{lmnoprstu} δεζ	0.68±0.02 ^{bcdefghijkl} αβγδ	453.01±2.03 ^{bc} βγ	351.43±1.65 ^s λ	0.43±0.15 ^{klmno} ζη
		2017	4.40±0.79 ^{lmnoprstu} εζη	0.69±0.02 ^{bcdefghijkl} αβγδ	462.48±4.02 ^a α	356.59±2.38 ^s κλ	0.61±0.05 ^{efghi} δε
	F R.	2015	5.26±0.57 ^{ghijklmnop} γδε	0.66±0.08 ^{cdefghijkl} αβγδ	415.61±3.73 ^r ε	479.64±1.53 ^m η	0.30±0.05 ^o η
		2016	3.86±0.52 ^{prstu} ζη	0.76±0.20 ^{abdefghijkl} αβγδ	361.63±3.06 ^z ζ	329.35±4.51 ^l μ	0.86±0.02 ^{abc} αβ
		2017	6.42±0.81 ^{bdefghij} βγ	0.62±0.04 ^{hijklm} γδ	256.15±2.98 ^θ θ	527.25±5.41 ^ε ε	0.59±0.08 ^{efghi} δε
	F N.	2015	5.74±0.83 ^{efghijklm} γδ	0.83±0.05 ^{abcde} αβ	456.81±2.10 ^b β	458.32±1.48 ^θ θ	0.83±0.07 ^{abc} αβ
		2016	7.20±0.92 ^{abcd} αβ	0.75±0.10 ^{abdefghijk} αβγδ	455.82±0.62 ^{bc} βγ	747.70±2.34 ^z ζ	0.65±0.10 ^{defgh} γδ
		2017	5.52±1.01 ^{efghijklmnop} γδε	0.85±0.02 ^{abcd} α	146.07±0.95 ^k κ	329.35±4.51 ^l μ	0.86±0.02 ^{abc} αβ
	M	2015	7.21±0.90 ^{abcd} αβ	0.82±0.07 ^{abdefghijk} αβγ	246.47±2.32 ^{lu} ι	786.98±2.93 ^d α	0.52±0.06 ^{ghij} δεζ
		2016	5.76±0.92 ^{efghijklm} γδ	0.77±0.13 ^{abdefghijk} αβγδ	324.92±4.96 ^{kl} η	434.20±2.62 ^ι ι	0.65±0.03 ^{defghi} γδ
		2017	4.09±0.50 ^{oprstu} ζη	0.70±0.08 ^{abdefghijkl} αβγδ	327.25±5.41 ^{kl} η	362.52±4.14 ^k κ	0.64±0.13 ^{defghi} γδ
C S.	2015	4.43±0.81 ^{lmnoprstu} εζη	0.63±0.13 ^{ghijklm} γδ	328.62±3.03 ^{kl} η	543.64±7.59 ^d δ	0.77±0.02 ^{abcde} βγ	
	2016	7.80±0.25 ^a α	0.83±0.08 ^{abcde} α	426.42±5.03 ^d δ	624.55±4.12 ^h γ	0.92±0.05 ^a α	
2017	5.30±0.22 ^{ghijklmnop} γδε	0.79±0.21 ^{abdefghijk} αβγ	246.14±2.66 ^{lu} ι	256.82±5.52 ^v ν	0.80±0.07 ^{abcd} αβ		
Smulti Wine Center	M Ott.	2015	6.46±0.75 ^{abdefghijk} βγδ	0.66±0.10 ^{cdefghijkl} βγ	326.79±2.60 ^{kl} γ	567.14±1.04 ^θ θ	0.87±0.09 ^{ab} α
		2016	3.69±0.96 ^{rstu} θ	0.55±0.10 ^{lm} γδ	333.77±3.19 ^β β	843.99±3.89 ^β β	0.59±0.06 ^{efghi} δεζ
		2017	6.60±0.86 ^{abdefghijk} αβγ	0.65±0.18 ^{efghijkl} βγ	343.81±2.30 ^h γ	798.24±0.19 ^β β	0.83±0.05 ^{abc} αβγ
	F A.	2015	6.32±0.61 ^{bdefghijk} βγδε	0.83±0.05 ^{abcde} αβ	326.46±2.32 ^{kl} γ	784.21±2.94 ^d δ	0.66±0.10 ^{defgh} βγδ
		2016	7.65±0.42 ^{ab} α	0.72±0.17 ^{abdefghijk} αβγ	284.29±3.68 ^ε ε	658.70±3.85 ^z ζ	0.73±0.16 ^{bcde} αβγ
		2017	6.06±0.79 ^{cdefghijk} γδεζ	0.87±0.03 ^{ab} α	301.09±3.62 ^m η	791.29±3.25 ^v ν	0.73±0.21 ^{bcde} αβγ
	F R.	2015	4.76±0.35 ^{klmnoprst} δεζ	0.75±0.05 ^{abdefghijkl} αβ	177.40±2.47 ^λ λ	325.14±4.02 ^γ γ	0.85±0.15 ^{abc} αβ
		2016	5.74±0.54 ^{efghijklm} γδεζη	0.83±0.05 ^{abcde} αβ	201.26±4.29 ^w κ	488.30±0.81 ^λ λ	0.59±0.05 ^{efghi} δεζ
		2017	5.55±0.67 ^{efghijklm} γδεζη	0.86±0.02 ^{abc} α	205.82±0.55 ^{wv} ι	576.04±4.99 ^η η	0.65±0.10 ^{defgh} βγδ
	F N.	2015	7.23±0.30 ^{ab} αβ	0.66±0.01 ^{defghijkl} βγ	208.14±1.03 ^γ κ	216.71±2.52 ^π π	0.41±0.05 ^{klmno} ζ
		2016	6.20±0.97 ^{7cdefghijk} βγδεζ	0.71±0.15 ^{abdefghijkl} αβγ	146.26±2.53 ^λ λ	578.74±3.72 ^η η	0.60±0.04 ^{efghi} δεζ
		2017	5.66±0.63 ^{efghijklm} γδεζη	0.76±0.02 ^{abdefghijkl} αβ	178.16±1.00 ^γ λ	657.35±2.58 ^z ζ	0.79±0.10 ^{abc} αβγ
	M	2015	5.36±0.35 ^{ghijklmno} δεζη	0.72±0.15 ^{abdefghijkl} αβγ	346.68±2.17 ^h γ	494.95±2.59 ^k κ	0.54±0.11 ^{ghijk} εζ
		2016	5.07±0.42 ^{hijklmnop} ζη	0.80±0.04 ^{abdefghijk} αβ	288.40±0.86 ^ε ε	537.43±4.69 ^ι ι	0.61±0.06 ^{efghi} δε
		2017	5.56±0.66 ^{γδεζη} ζη	0.83±0.05 ^{abcde} αβ	323.49±2.08 ^γ γ	750.93±4.53 ^ε ε	0.66±0.12 ^{defgh} βγδ
C S.	2015	3.70±0.17 ^{rstu} θ	0.45±0.10 ^m δ	267.82±1.54 ^π ζ	243.00±1.76 ^ω ο	0.64±0.10 ^{defghijk} γδε	
	2016	5.20±0.34 ^{ghijklmnop} εζη	0.57±0.07 ^{ijklm} γδ	241.85±5.51 ^μ μ	316.56±3.75 ^v ν	0.66±0.10 ^{defgh} βγδ	
2017	5.89±0.29 ^{cdefghijk} γδεζη	0.80±0.04 ^{abdefghijk} αβ	255.81±4.96 ^η η	417.66±2.19 ^ε ε	0.69±0.13 ^{cde} αβγ		
Oancea Wine Center	M Ott.	2015	3.32±0.80 ^u η	0.63±0.06 ^{efghijklm} γδ	262.36±2.42 ^{ss} ζ	851.09±1.36 ^d γ	0.66±0.10 ^{defgh} βγ
		2016	3.59±0.52 ^{stu} γδ	0.60±0.13 ^{hijklm} γδ	263.92±2.54 ^{rs} ζ	923.62±2.05 ^a α	0.49±0.07 ^{hijklm} δε
		2017	4.95±0.72 ^{klmnoprs} βγδ	0.55±0.10 ^{lm} δ	177.36±2.43 ^γ ι	872.86±4.02 ^a β	0.64±0.06 ^{defghi} βγ
	F A.	2015	4.17±0.05 ^{lmnoprstu} βγδ	0.65±0.10 ^{efghijkl} βγδ	454.40±2.72 ^{bc} α	867.66±3.50 ^β β	0.57±0.02 ^{efghijk} αβ
		2016	6.93±0.69 ^{abcde} α	0.90±0.04 ^a α	433.76±2.96 ^d α	734.62±6.94 ^e ζ	0.59±0.05 ^{efghi} γδ
		2017	5.20±0.66 ^{ghijklmnop} βγ	0.71±0.06 ^{abdefghijkl} βγδ	329.59±1.41 ^{jk} γ	818.49±5.66 ^δ δ	0.65±0.01 ^{defgh} βγ
	F R.	2015	4.70±0.50 ^{lmnoprstu} βγδ	0.71±0.15 ^{abdefghijkl} βγδ	307.62±2.65 ^m δ	761.45±5.53 ^ε ε	0.65±0.10 ^{defgh} βγ
		2016	5.17±1.71 ^{ghijklmnop} βγ	0.59±0.12 ^{hijklm} δ	270.23±4.01 ^p ε	821.61±2.00 ^b δ	0.84±0.05 ^{abc} αβ
		2017	5.05±0.14 ^{hijklmnop} βγ	0.69±0.05 ^{bcdefghijkl} βγδ	303.15±4.35 ^{mm} δ	819.25±4.03 ^δ δ	0.77±0.06 ^{abcde} αβ
	F N.	2015	4.99±0.45 ^{klmnoprs} βγδ	0.63±0.13 ^{efghijklm} γδ	147.17±0.99 ^z λ	355.90±1.74 ^{ss} π	0.37±0.16 ^{mno} εζ
		2016	4.86±0.31 ^{klmnoprs} βγδ	0.79±0.09 ^{abdefghijk} αβγ	159.14±1.41 ^w κ	323.92±4.09 ^p p	0.55±0.10 ^{efghijk} γδ
		2017	5.83±1.45 ^{defghijklm} αβ	0.65±0.17 ^{efghijklm} βγδ	198.72±0.74 ^v θ	408.55±4.45 ^p p	0.59±0.12 ^{efghi} γδ
	M	2015	6.69±0.49 ^{abcdef} α	0.60±0.04 ^{hijklm} δ	268.64±4.83 ^{pr} εζ	478.45±2.86 ^m κ	0.47±0.08 ^{ijklmn} δε
		2016	5.52±1.67 ^{efghijklmno} αβ	0.62±0.08 ^{hijklm} γδ	327.49±2.07 ^{kl} γ	429.95±1.18 ^o ο	0.53±0.02 ^{ghijk} γδ

Area	Variety	Year	Co M.L.A.	Cu** M.L.A.	Ni M.L.A.	Cr M.L.A.	Mn*** M.L.A.
			-	1 mg/L	-	-	-
		2017	5.07±0.90 ^{hijklmnop} βγ	0.60±0.02 ^{hijklm} δ	338.65±1.81 ^β	520.36±1.50 ^λ	0.55±0.04 ^{ghijk} γδ
		2015	4.16±0.20 ^{noprstu} βγδ	0.83±0.08 ^{abcdef} αβ	264.48±1.53 ^{rs} ζ	651.07±1.34 ^ι η	0.66±0.10 ^{defgh} βγ
	C S.	2016	4.86±0.88 ^{kilmnoprs} βγδ	0.59±0.12 ^{ijklm} δ	180.11±2.26 ^x θ	635.97±5.22 ^θ	0.27±0.03 ^ο ζ
		2017	5.47±1.15 ^{ghijklmno} αβ	0.56±0.10 ^{klm} δ	249.66±1.50 ^ι η	530.39±1.51 ^ι	0.34±0.03 ^{mno} ζ
	Average		5.17±0.51	0.67±0.09	312.32±2.42	526.19±2.63	0.59±0.08
	Minimum Values		3.32±0.80	0.45±0.10	146.07±0.95	216.71±2.52	0.27±0.03
	Maximum Values		7.80±0.25	0.90±0.04	462.48±4.02	923.62±2.05	0.92±0.03
	F		7.227	3.259	2799.869	9054.214	9.566
	Sig.		***	***	***	***	***
Area	F		11.926	6.757	12472.658	36450.815	19.617
	Sig.		***	**	***	***	***
Variety	F		9.653	7.235	8554.109	19135.062	3.668
	Sig.		***	***	***	***	**
Year	F		2.175	0.940	2630.180	3876.973	11.399
	Sig.		<i>in</i>	<i>in</i>	***	***	***
	[18]		2.08±1.19	154.39±73.45**	18.39±1.19	146.18±70.96	
	[23]		4.65		24.90		
	[15]		2.50				
	[24]		42.06	2594.79**	322.73	1725.80	

Average value ± standard deviation (n = 3). Romans letters represent the significance of the variety difference ($p \leq 0.05$). Greeks letters represent the significance of the same variety cultivated in other year's difference ($p \leq 0.05$). The difference between any two values, followed by at least one common letter, is insignificant. M.L.A. - maximum limit allowed (OIV, 2005); LOQ - lower than the limit of quantification; Cu* = (mg/L); Cu** = (μg/L); Mn*** = (mg/L). M Ott. = Muscat Ottonel; F a. = FeteascaAlba; F r. = Feteasca Regala; F n. = Feteasca Neagra; M = Merlot; C s. = Cabernet Sauvignon.

Combining multielement analysis from wine samples for discrimination analysis

Multivariate chemometric method was used as a supervised learning technique for the differentiation of wines into groups on the basis of grape variety and year of production and finding markers which showed a significant discrimination value (variables with Wilk's lambda near zero, p value < 0.05 and higher F coefficients). Stepwise linear discriminant analysis (LDA) was used to identify significant tracers for classification to the geographical discrimination of the wines samples. Stepwise Discriminant Analysis (LDA) was used to designate suitable variables for classification of the samples, eliminating the variables that do not contribute to discrimination of the wine.

In order to validate the proposed statistic model, based on variables which showed higher significance in first LDA assessment, we performed a second Linear Discriminant Analysis (LDA) for the test set consisting of wines used to build statistical model (training set) together with data from other wine samples that are not included in the first LDA (control-set). Cross-validation was applied to determine the optimal number of variables required to obtain robust models.

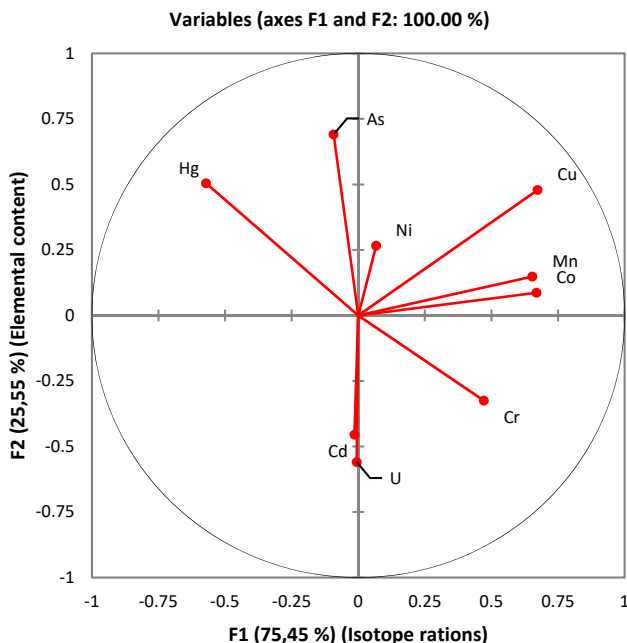


Figure 1. Correlation between analyzed parameters and the factors in discriminant analysis the origin of the wine

In this study, the content of certain wines shows high concentration of metals, but not exceeding the maximum recommended by International Organisation of Vine and Wine [25], and this mostly due to agricultural practices, fertilizers and technological winemaking processes.

Elements like Pb, Cu, Ni, Cd, U and Hg showed a high discriminatory power for geographic origin of Romanian wines, but additional new elements (Mn, Cr) have been investigate in order to identify new tracers for geographical traceability of Romanian wines. The wines obtained in the three wine-growing centers can be geographical fingerprints based on the concentration of Pb, Cu, Ni, Cd, Hg, Mn, Cr, U.

The cross-validation technique provided a 100 % percentage of predicted membership according to the origin of the wine (F1 = 75.45 % and F2 = 25.55 %). The linear correction revealed acceptable scores for the two defined discriminant factors (F1 and F2) (Figure 1). A significant differentiation of wines according to wine-growing centers and year of wine production was carried out for wines samples, which demonstrates the importance of elemental profile for the geographical traceability of wines (Figure 2).

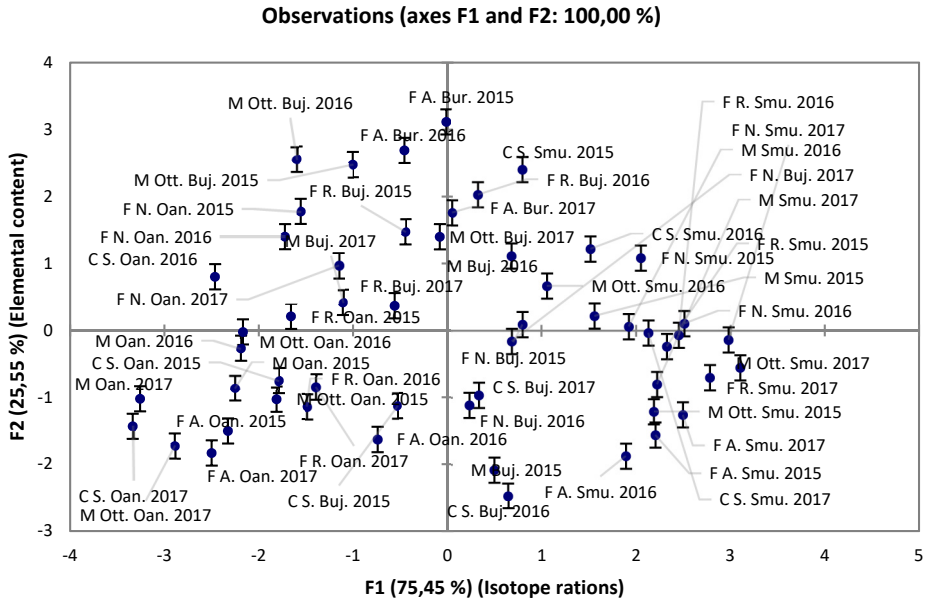


Figure 2. Differentiation of wines based on element contents

Heat map was used to discover sample groups, discover groups and also to discover related sample/feature groups. In case of elemental contents from wine, the dendrogram (horizontal dendrogram) clearly show two cluster, first cluster is formed from the Co, Cd, U, Hg, Mn, Cu, As and second cluster was formed from Ni an Cr. Based on this distribution it can be seen that the Cr recorded the highest concentration followed by Ni. The vertical dendrogram show also two cluster, the first M Smu. 2015, C S. Buj. 2015, F R. Buj. 2015, M Buj. 2017, M Oan. 2016, M Oan. 2015, F R. Smu. 2015, F R. Buj. 2017, C S. Smu. 2017, F A. Buj. 2017, F A. Buj. 2015, C S. Buj. 2017, C S. Smu. 2016, F N. Oan. 2016, F N. Oan. 2015 and second cluster was formed from F A. Smu. 2017, M Ott. Smu. 2017, M Ott. Smu. 2016, F R. Oan. 2015, M Ott. Oan. 2017, F R. Oan. 2016, M Buj. 2015, F A. Oan. 2016, F R. Smu. 2017, C S. Oan. 2016, F A. Smu. 2016, M Ott. Buj. 2017. Based on this distribution in can be seen that there is a separation of wine varieties depending on elemental contents, except for a few varieties that do not fit into this rule (F R. Buj. 2015, F R. Smu. 2016, F R. Buj. 2017, F A. Buj. 2017, F A. Buj. 2015 (which have been introduced in red wine cluster) and M Buj. 2015, C S. Oan. 2016 2015 (which have been introduced in white wine cluster) (Figure 3).

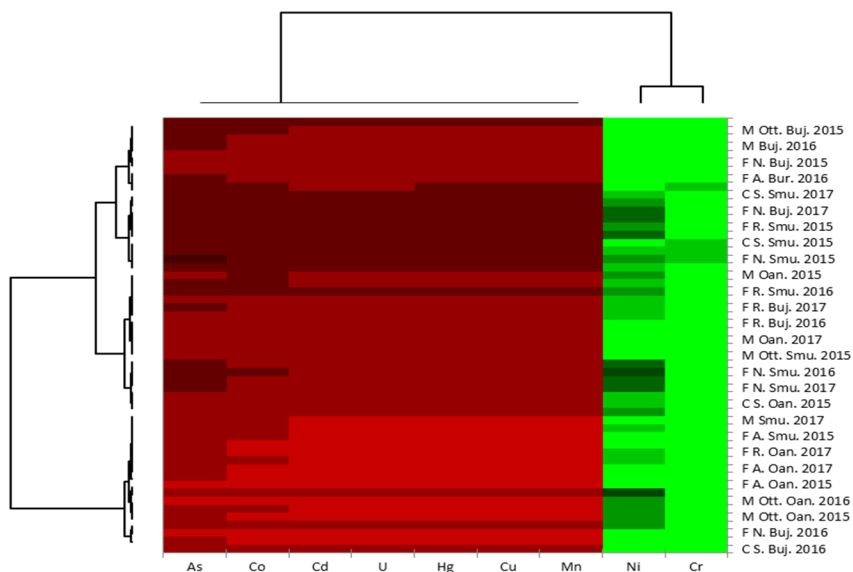


Figure 3. Heat map obtained by cluster analysis of the element contents

CONCLUSIONS

In this work the elemental composition of white wines (Muscat Ottonel, Feteasca Alba, Feteasca Regala) and red wines (Feteasca Neagra, Merlot, Cabernet Sauvignon) production years 2014-2016 from Bujoru, Smulti and Oancea wine-growing centers was studied in order to highlight geographical traceability of elemental composition for fingerprints of the wines.

Concentration of Cd, Pb, As and Cu heavy metals in analysed wine samples were under Maximum Limit Allowed (M.L.A.), respectively as published by the Organization of Vine and Wine. The content of potentially toxic elements such as Cd, Pb, U, Hg, As, Cu, Ni, Cr and Mn are lower than the recommended values found in literature, highlighting the safety and quality of the analysed Romanian wines.

EXPERIMENTAL SECTION

Study area

A total of 162 wine samples were analysed (3 white wines and 3 red wines). Samples originated from Bujoru, Smulti and Oancea wine-growing centers part of Dealu Bujorului vineyard (45°52'10" N, 27°55'8"E). The Dealu

Bujorului vineyard is characterized by an alternate landscape, from flat to hilly areas, with altitude between 100 and 225 m and the predominant soil is levigated chernozem having a clayey sand texture with pH between values 7.4 and 8.1. Although they have moisture deficit, natural conditions (ecoclimatic and ecopedological) offer viable ecosystem for the development of vineyard. The vineyard is crossed by the parallel 46° latitude north, intersected by the 28° longitude meridian. Dealu Bujorului vineyard belongs to Galați country. The specificity of the transition area is highlighted by the predominance of deposits of clays and sands. Versants were made from clay deposits and sandy sands.

Sample collection and microvinification process

The samples used in this experiment were obtained from the wines produced from Muscat Ottonel, Feteasca Alba, Feteasca Regala, Feteasca Neagra, Merlot and Cabernet Sauvignon under the conditions of 2015, 2016 and 2017. The wine samples resulted from micro-wine production. Micro-wine production was done according to the methodology describe by Bora et al. [26]. All wines were providing by the wineries as finished wines in 750 mL bottles with cork stoppers and were stored at 3-4°C before analysis. All vines were planted since 1979, and the vine plantation was organized with 2.2 x 1 m distance between rows and plants. Vines were pruned according to the Guyot system and were grown on speliers.

Reagents and solutions

Ten elements (Cd, Pb, U, Hg, As, Sr, Co, Cu, Ni, Cr and Mn) were determined in order to assess their ability to discriminate wines by geographical origin. The analysis was made using multielement analysis and ICP-MS technique, after an appropriate dilution, using external standard calibration method. The calibration was performed using XXICertiPUR multielement standard, and from individual standard solution of Cr and Hg. The working standards and the control sample were prepared daily from the intermediate standards that were prepared from the stock solution. The intermediate solutions stored in polyethylene bottles and glassware was cleaned by soaking in 10% v/v HNO₃ for 24 hours and rinsing at least ten times with ultrapure water (18.2 MΩ cm⁻¹ ultrapure water-Types 1). The accuracy of the methods was evaluated by replicate analyses of fortified samples (10 μL-10 mL concentrations) and the obtained values ranged between 0.8-13.1 percent, depending on the element. The global recovery for each element was estimated and the obtained values were between 84.6-100.9% [27].

For quality control purpose, blanks and triplicates samples ($n = 3$) were analyzed during the procedure. The variation coefficient was under 5% and detection limits (ppb) were determined by the calibration curve method. Limit of detection (LoD) and Limit of quantification (LoQ) limits were calculated according to the next mathematical formulas: $LoD = 3SD/s$ and $LoQ = 10 SD/s$ ($SD =$ estimation of the standard deviation of the regression line; $s =$ slope of the calibration curve) (Table 3).

Table 3. Instrumental conditions for the determination of each element (ICP-MS technique)

Element	Correlation coefficient	LoD* ($\mu\text{g/L}$)	LoQ*** ($\mu\text{g/L}$)	BEC** ($\mu\text{g/L}$)
Cd	0.9999	0.0202	0.0673	0.027
U	0.9999	0.0253	0.0842	0.005
As	0.9999	0.2335	0.7776	0.538
Co	0.9999	0.0365	0.1215	0.152
Ni	0.9999	0.0591	0.1968	0.091
Pb	0.9999	0.0003	0.0010	0.002
Hg	0.9999	0.0417	0.1379	0.128
Sr	0.9999	0.1434	0.4775	0.955
Cu	0.9999	0.0402	0.1339	0.237
Cr	0.9999	1.6630	5.5378	0.636
Mn	0.9999	0.0100	0.0340	0.085

*Detection limit; **Background equivalent concentration; ***Quantification limit.

Sample preparation for determination of heavy metals and isotopic riation from wine using ICP-MS.

For the determination of elements from wine samples were used an amount of 0.5 mL wine and diluted to 8 mL (7 mL HNO_3 65%+1 mL H_2O_2) the obtained solutions were placed in a clean Teflon digestion vessel, after 15-30 minutes the mineralization was performed using a microwave system Milestone START D Microwave Digestion System set in three steps: step I (time 10 min., temperature 200°C), step II (time 15 min., temperature 200°C) and step III (time 40 min., ventilation - temperature 32°C). After mineralization, samples were filtered through a 0.45 mm filter and brought to a volume of 50 mL with HNO_3 1%.

In order to confirm the best-chosen conditions for wine digestion standard additions for checking accuracy of the microwave digestion and recoveries were calculated (Table 4). The digestion seemed visually completed in all of the combinations, but the spiked recoveries showed significant differences for total elements content (p - Value = 0.005).

Table 4. Standard additions for checking accuracy of the microwave digestion ICP-MS method (n = 3) (SRM 1643e)

Element	Certified Concentration (mg/L)	Measured Concentration (mg/L)
Cd	6.568±0.073	6.473±0.106
U	9.994±0.016	9.981±0.012
As	56.85±0.37	53.09±0.31
Co	27.06±0.28	24.13±0.06
Ni	62.41±0.69	61.32±0.21
Pb	19.63±0.21	19.13±0.09
Hg	0.1016±0.0017	0.1102±0.0012
Sr	314.00±19.00	314.09±09.06
Cu	21.44±0.70	21.25±0.21
Cr	18.32±0.10	19.18±0.21
Mn	38.02±0.44	33.04±0.05

Instrumentation

The determination of metals was performed on mass spectrometer with inductively coupled plasma, (ICP-MS) iCAP Q Thermo scientific model, based polyatomic species before they reach the quadrupole mass spectrometer, using a PFA micro flow concentric nebulizer. The argon used was of 99.99% purity (Messer, Austria). The instrument was daily optimized to give maximum sensitivity for M^+ ions and the double ionization and oxides monitored by the means of the ratios between Ba^{2+}/Ba^+ and Ce^{2+}/CeO^+ , respectively, these always being less than 2%. The experimental conditions were: argon flow on nebulizer (0.82 L/min.), auxiliary gas flow 0.80 L/min., argon flow in plasma 15 L/min., lens voltage 7.30 V; RF power in plasma 1100 W, spray chamber temperature (2.42±1.00°C). Accuracy was calculated for the elements taken into consideration (0.5-5.0%).

Statistical analysis

The statistical interpretation of the results was performed using the Duncan test, SPSS Version 24 (SPSS Inc., Chicago, IL., USA). The statistical processing of the results was primarily performed in order to calculate the following statistical parameters: average and standard deviation. This data was interpreted with the analysis of variance (ANOVA) and the average separation was performed with the DUNCAN test at $p \leq 0.05$. Multivariate chemometric method was used as a supervised learning technique for the differentiation of wines into groups on the basis of grape variety and year

of production and finding markers which showed a significant discrimination value (variables with Wilk's lambda near zero, p value <0.05 and higher F coefficients). Stepwise linear discriminant analysis (LDA) was used to identify significant tracers for classification to the geographical discrimination of the wines samples. Stepwise Discriminant Analysis (LDA) was used to designate suitable variables for classification of the samples, eliminating the variables that do not contribute to discrimination of the wine. In order to validate the proposed statistic model, based on variables which showed higher significance in first LDA assessment, we performed a second Linear Discriminant Analysis (LDA) for the test set consisting of wines used to build statistical model (training set) together with data from other wine samples that are not included in the first LDA (control-set). Cross-validation was applied to determine the optimal number of variables required to obtain robust models. Linear discriminant analysis (LDA) was performed using Microsoft Excel 2016 and XLSTAT Addinsoft version 15.5.03.3707.

REFERENCES

1. D. M. A. M. Luykx, S. M. Van Rush, *Food Chemistry*, **2008**, *107*, 897.
2. C. M. R. Almeida, M. T. S. D. Vasconcelors, *Journal of Agricultural and Food Chemistry*, **2003**, *51*, 4788.
3. M. Álvarez, J. M. Moreno, A. M. Jos, A. M. Cameán, G. González, *Journal of Food Composition and Analysis*, **2007**, *20*, 391.
4. R. D. Di Paola-Naranjo, M. V. Baroni, N. S. Podio, H. R. Rubinstein, M. P. Fabani, R. G. Badini, M. Inga, H. A. Ostera, M. Cagnoni, E. Gallegos, E. Gautier, P. Peral-Garcia, J. Hoogewerff, D. A. Wunderlin, *Journal of Agricultural and Food Chemistry*, **2011**, *59(14)*, 7854.
5. I. S. Arvanitoyannis, M. N. Katsota, E. P. Psarra, E. H. Souflerous, S. Kallithraka, *Trends in Food Science and Technology*, **1999**, *10*, 321.
6. J. D. Greenough, H. P. Longerich, S. E. Jackson, *Australian Journal of Grape and Wine Research*, **1997**, *3*, 75.
7. M. M. Castiñeira-Gomez, R. Brant, N. Jakubowski, J. T. Andersson, *Journal of Agricultural and Food Chemistry*, **2004**, *52*, 2953.
8. M. Fabani, M. Toro, F. Vazquez, M. P. Díaz, D. A. Wunderlin, *Journal of Agricultural and Food Chemistry*, **2009**, *57*, 7409.
9. F. Galgano, F. Favati, M. Caruso, T. Scarpa, A. Palma, *LWT-Food Science and Technology*, **2008**, *41*, 1808.
10. P. Kment, M. Mihaljevic, V. Ettler, O. Šebek, L. Strnad, L. Rohlavá, *Food Chemistry*, **2005**, *91*, 157.
11. R. Larcher, G. Nicolini, P. Pangrazzi, *Journal of Agricultural and Food Chemistry*, **2003**, *51(20)*, 5956.

12. V. Ivanova-Petropulos, H. Wiltsche, T. Stafilov, M. Stefova, H. Motter, E. Lankmayr, *Macedonian Journal of Chemistry and Chemical Engineering*, **2013**, 32(2), 265.
13. S. Đurđić, M. Pantelic, J. Trifkovic, V. Vukojevic, M. Natic, Z. Tesica, J. Mutic, *RSC Advanced*, **2017**, 7, 2151.
14. V. Ivanova-Petropulos, B. Balavanova, S. Mitrev, D. Nedelkovski, V. Dimovska, R. Gulaboski, *Food Analytical Methods*, **2016**, 9(1), 48.
15. V. Avram, C. Voica, A. Hosu, C. Cimpoiu, C. Măruțoiu, *Revue Roumaine de Chimie*, **2014**, 59(11-12), 1009.
16. F. Galgano, F. Favati, M. Caruso, T. Scarpa, A. Palma, *LWT-Food Science and Technology*, **2008**, 41, 1808.
17. D. Karataş, F. Aydin, I. Aydin, H. Karataş, *Czech Journal of Food Sciences*, **2015**, 33(3), 228.
18. E. I. Geana, A. Marinescu, A. M. Iordache, C. Sandru, R. E. Ionete, C. Bala, *Food Analytical Methods*, **2014**, 48(2), 2064.
19. D. Schiavo, I.Y. Neira, I.A. Nóbrega, *Talanta*, **2008**, 76, 1113.
20. Z. Ajtony, N. Szoboszlai, E.K. Suskó, P. Mezei, K. György, L. Bencs, *Talanta*, **2008**, 76, 627.
21. G. Dugo, L. La Pera, T.M Pellicanó, G. Di Bella, M. D'Imperio, *Food Chemistry*, **2005**, 91, 355.
22. S. Galani-Nikolakaki, N. Kallithrakas-Kontos, A.A. Katsanos, *Science of the Total Environment*, **2002**, 285, 155.
23. G. Thiel, G. Geisler, I. Blechschmidt, K. Danzer, *Analytical and Bioanalytical Chemistry*, **2004**, 378, 1630.
24. I. Geana, A. Iordache, R. Ionete, A. Marinescu, A. Ranca, M. Culea, *Food Chemistry*, **2013**, 138, 1125.
25. OIV, *International Code of Oenological Practices, Annex: Maximum Acceptable Limits*, **2015**, Issue 2015/01. Paris, France.
26. F. D. Bora, A. Donici, T. Rusu, A. Bunea, D. Popescu, C. I. Bunea, *Notulae Botanicae Horti Agrobotanici Cluj-Napoca*, **2018**, 46(1), 223.
27. E.I. Geana, C. Sandru, V. Stanciu, R.E. Ionete, *Food Analytical Methods*, **2017**, 10(1), 63.

THE EFFECT OF HIGH PRESSURE PROCESSING ON MAJOR STRUCTURAL PROTEINS OF RAINBOW TROUT FISH FILLETS

ANA-ANDREEA CIOCA^{a,*}, SORIN DANIEL DAN^a,
VLĂDUȚA MĂRIOARA LUPĂU^a, LIORA MIHAELA COLOBATIU^b,
MARIAN MIHAIU^a

ABSTRACT. Fresh rainbow trout fillets are very perishable food products. Therefore, they cannot be stored at refrigeration temperatures for a long period of time. High pressure processing (HPP) can improve the quality of the fillets through microbial load control. As a result of this, the shelf-life of the product is extended. However, some physicochemical changes can appear. The aim of this study was to assess the degree of protein denaturation in rainbow trout fillets treated with various levels of high pressure. The results showed that protein denaturation is definitely higher for the fillets treated with higher pressure levels, in the range of 400 MPa/3 min – 600 MPa/6 min and lower for the fillets treated with lower pressure levels, in the range of 100 MPa/3 min – 200 MPa/6 min. The use of lower pressure levels is beneficial to the structural quality preservation of the fillets, but less effective concerning the microbial inactivation. Maintaining a good structural and nutritional quality of the product is not very useful in this case, because it cannot be combined with other great advantages offered by the HPP tools, namely microbial control and spoilage decline. Therefore, further studies should focus on readjusting (e. g. minimizing) the holding time and other possible parameters, without lowering the high levels of pressure.

Keywords: *high-pressure processing, microbial load, protein denaturation, rainbow trout fillets.*

^a Department of Animal Production and Food Safety, University of Agricultural Sciences and Veterinary Medicine, 3-5 Mănăștur Street, 400372, Cluj-Napoca, Romania.

^b Department of Medical Devices, Iuliu Hatieganu University of Medicine and Pharmacy, 8 Babeș Street, 400012, Cluj-Napoca, Romania.

* Corresponding author: anaandreeacioca@yahoo.com

INTRODUCTION

Fish meat is much more appreciated by consumers all over the world nowadays due to its important role in maintaining a healthy lifestyle (Pieniak et al. 2009). It provides high-quality protein, omega-3 and -6 polyunsaturated fatty acids and a variety of minerals and vitamins, which can prevent or help improving the symptoms of some illnesses (Soumia et al. 2013).

However, the main disadvantage of this type of meat is related to its spoilage characteristic. Refrigeration on ice can provide freshness for a short period of time and many times this cold chain is broken during transportation by the buyers, leaving room for a rapid decay (Sotelo et al. 1995; Trebar, 2017). Freezing ensures the safety of the product for longer periods of time, but it often interferes with the sensorial quality, especially with colour, aroma and texture.(Gökoğlu et al. 2015).

In this context, current researchers are trying to test some of the more advanced alternative processing technologies such as high pressure processing (HPP), which can potentially offer the benefit of preserving fish meat safe, with good sensorial quality and nutritional value. HPP has been used in the past for foodstuffs like smoothies, guacamole, meat products, shellfish (Bolumar et al. 2016; Heinz et al, 2010), but recently a growing interest for fish meat and fish meat products was observed (Truong et al, 2015).

While some of the nutritional and sensorial components in fish remain stable after HPP, some encounter changes. Many studies show that the colour of the fish muscle changes after HPP, becoming whiter (cooked aspect). However, the change in colour can be overcome if fish products (e.g. fish fillets) are meant to be further processed (thermal treatments or smoking treatments). Another concern is related to the level of protein denaturation after HPP (Kramer et al. 2013; Mazorra-Manzano et al. 2018; Teixeira et al. 2013). Even though HPP appeared to be a promising preserving tool for at least three decades (Balny, 1993) and optimization of the method in order to improve this aspect is still to be discovered, analyses are still conducted with diverse parameters and samples. The breaking of structural muscle proteins can lead to nutritional value loss (Lanier, 1998), but it can also influence texture and water holding capacity changes in negative ways (Skipnes et al. 2007).

Differential scanning calorimetry (DSC) is the main technique used to determine the level of protein denaturation in fish products (Kramer et al. 2013). DSC curves are dependent on the species of analyzed fish and

therefore, the degree of protein denaturation can be different (Schubring et al. 2005).

The majority of the studies conducted until today were on wild-catch, on species such as salmon, mackerel, cod, heering and ocean perch (Kramer et al. 2013; Schubring et al. 2005), while very few studies focused on the species coming from aquaculture. A very popular species among fish farmers and consumers from Europe (Timberg et al. 2011) is rainbow trout (*Oncorhynchus mykiss*), a moderately fat fish, with exceptional tenderness and aroma.

The aim of this paper was to present the effects of HPP on major structural proteins of a widely appreciated farmed fish, the rainbow trout.

RESULTS AND DISCUSSION

The thermal properties of rainbow trout proteins and the amplitude of their denaturation was measured within a range of 20 to 95°C DSC heating procedure and a scanning rate of 5 °C/min.

The two major structural proteins, myosin and actin, were illustrated in the DSC curves from the graphs of Fig 1. for each high pressure processed sample. The first peak was represented by myosin and the second one, by actin.

For the samples processed with pressure levels of 100 and 200 MPa for 6 min (Fig 1. C. and E.) pressurization time the peaks corresponding to myosin and actin were slightly lower than the peaks of the samples processed with 100 and 200 MPa at 3 min pressurization time (Fig 1. B. and D.). Apparently, these fish fillets suffered more protein denaturation. The effect of denaturation is therefore correlated with the processing time, proportionally increasing with the increment of the processing time. However, Ko Wen-Ching et al. 2006 relates the results obtained for samples treated at high pressure in between 100 and 300 MPa with reversible protein denaturation, dissociation, or precipitation, while Arnaud et al. 2015 considers that an average high pressure treatment in the range of 100-200 MPa (\approx 150 MPa) “does not oxidize or denature protein more than the natural trends”.

An important difference is spotted between the samples treated with 100 and 200 MPa and the samples treated with 400 (Fig 1. F. and G.) and 600 MPa (Fig.1 H. and I.). The DSC profile change is most of the time attributed to considerable protein denaturation (Iso Shin-ichi, 1994; Arnaud et al. 2015). Protein denaturation is more substantial for the fillets

pressurized with the high-pressure levels. This situation is demonstrated through the variation of enthalpy values (ΔH). In the same times in which the enthalpy values decrease, the peaks of myosin and actin tend to proportionally become very low, to almost nonexistent (Table 1.) This corresponds to a very high degree to almost complete degradation of myosin and actin proteins. In the present case, actin seems to be more affected by a higher level of pressure than myosin.

Comparing to the untreated sample (Fig 1. A.), the degree of protein denaturation in the samples previously HPP treated with low pressure levels (100 and 200 MPa for 3 and 6 min) was low. This was validated by their enthalpy values which were very close to the enthalpy values of the control (Table 1.)

Some samples received an additional peak or so called shoulder before the myosin peak. This situation is more obvious for the fillets treated at 100 MPa/3 min and 100 MPa/6 min (Fig 1. B and C.). These additional peaks could symbolize sarcoplasmic and connective tissue problems (Schubring R., 2008).

The overall results revealed that high levels of pressure such as 400 MPa/3 min, 400 MPa/6 min, 600 MPa/3 min and 600 MPa/6 min have a negative impact on the main proteins of rainbow trout fillets.

Table 1. Transition temperatures and enthalpies calculated from differential scanning calorimetry (DSC) curves (Perkin Elmer DSC 2920) taken on heat-treated rainbow trout fillets dependent on the heating temperatures used

No	Treatment	T _{on} (°C)	T _{max} (°C)	ΔH (J/g)	T _{on} (°C)	T _{max} (°C)	ΔH (J/g)
1.	Fresh untreated	37.7	43.6	1.2550	71.25	75.35	0.4993
2.	HPP 100 MPa (3 min)	39.75	46	0.9141	70	74.7	0.5401
3.	HPP 100 MPa (6 min)	39.7	46.1	1.0226	70	74.9	0.5350
4.	HPP 200 MPa (3 min)	36.65	46.6	0.9063	70.8	75.3	0.4502
5.	HPP 200 MPa (6 min)	39.1	45.7	0.4875	70.5	75.3	0.4751
6.	HPP 400 MPa (3 min)	38	45.5	0.3799	65	68.7	0.1492
7.	HPP 400 MPa (6 min)	38	45.8	0.3949	70	73	0.1109
8.	HPP 600 MPa (3 min)	37.3	45.25	0.4523	67.95	75.8	0.1711
9.	HPP 600 MPa (6 min)	35.05	46.7	0.479	70.2	75.95	0.2108

THE EFFECT OF HIGH PRESSURE PROCESSING ON MAJOR STRUCTURAL PROTEINS ...

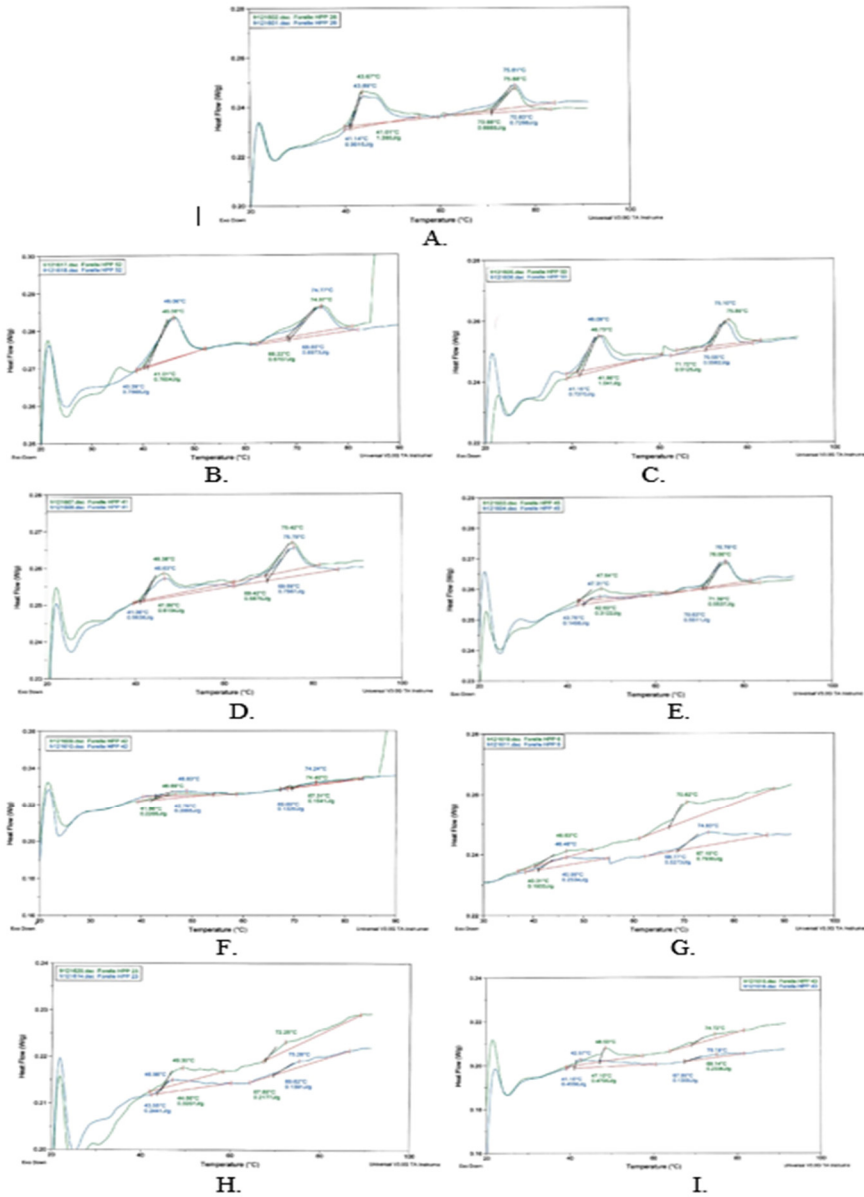


Fig 1. The variation of protein denaturation in untreated and HPP treated samples¹

¹ Legend: A. untreated sample; B. Pressure level 100 MPa/3 min; C. Pressure level 100 MPa/6 min; D. Pressure level 200 MPa/3 min; E. Pressure level 200 MPa/6 min; F. Pressure level 400 MPa/3 min; G. Pressure level 400 MPa/6 min; H. Pressure level 600 MPa/3 min; I. Pressure level 600 MPa/6 min

CONCLUSIONS

A remarkable protein denaturation process was observed in the samples treated with pressure levels in the range of 400 - 600 MPa. Obviously, this denaturation of proteins in rainbow trout fillets leads to a lower nutritive quality of the product. Therefore, despite the great benefit - a significant microbial inactivation followed by shelf life prolongation - offered by HPP when using levels such as 400 MPa and 600 MPa, it is important to consider this aspect in any research with application in the food industry and attempt to improve it.

The use of lower pressure levels is beneficial to the structural quality preservation of the fillets, but less effective concerning the microbial inactivation and shelf-life extension.

Further studies should consider readjusting the holding time for high pressure levels especially by reducing it as much as possible (from 3-6 min to maximum 1 min) in an attempt of reducing the protein denaturation process and maintaining the strong advantage of spoilage and pathogen control.

EXPERIMENTAL SECTION

Sample Collection

A total of 56 rainbow trout fish were purchased on the same day of catch from an intensive fish farming system in Osnabrück, Germany during January to February 2017. The fish was immediately slaughtered and cut in fillets. The skin was also removed on site. The skinless fillets were transported on ice to the German Institute of Food Technologies (DIL), Quakenbrück. The samples were vacuum-packed and the HPP analysis was conducted in less than 4 h post-harvest, at the time of delivery to the laboratory. All samples were stored at refrigeration temperature (4°C). The following day, within 24 h post-harvest, the samples were analyzed by DSC in order to investigate the effects of HPP on major structural proteins. Each sample was analyzed in duplicate.

Sample preparation and analytical techniques

Through DSC, the rainbow trout fillets were studied in order to observe the thermal transition temperatures for the denaturation of proteins, namely myosin and actin (Hastings R. J., 1985). This analysis in comparison with others used in the past, offers the advantage of not destroying in any chemical or mechanical way the fish proteins (Uddin Musleh, 2001).

The device used for measuring the thermal stability of rainbow trout samples collected from the same muscle part of the fillets was DSC 2920 Modulated DSC TA Instrument (USA). The fish samples consisting in ca. 10 mg pieces were weighted into a 60 μ l stainless steel pans (PerkinElmer, Germany) and sealed. The samples previously HPP treated were heated from 20 to 95°C, at a scanning rate of 5 °C/min, with a sealed empty pan as reference. Each sample was measured in duplicate. Results are presented as average curves (e.g. Fig. 1.). The average curves are used to record the onset and transition temperature (T_{on} and T_{max}) and to calculate the transition enthalpy (ΔH) expressed as J/g of the sample material from the peak area (Table 1.).

ACKNOWLEDGMENTS

This work was financially supported by DIL, Quakenbrück, Germany. We thank Dr. Kemal Aganovic and Dr. Stefan Töpfl, who provided insight and expertise that greatly assisted this research.

REFERENCES

1. C. Arnaud, M. de Lamballerie, L. Pottier, "Effect of High Pressure Processing on Fish Protein Oxidation and Denaturation", 5th Trans-Atlantic Fisheries Technology Conference, Nantes, **2015**.
2. C. Balny, P. Masson, *Food Reviews International*, **1993**, 9(4), 611.
3. Tomas B., Middendorf D., Toepfl S., Heinz V., "Structural Changes in Foods Caused by High-Pressure Processing", Springer Science+Business Media, New York, **2016**, chapter 23.
4. Gökoğlu N., Yerlikaya P., "Seafood chilling, refrigeration and freezing : science and technology" John Wiley & Sons, Chichester, **2015**.
5. R. J. Hastings, G. W. Rodger, R. Park, A. D. Matthews, E. M. Anderson, *Journal of Food Science*, **1985**, 50(2), 503.
6. Heinz V., Buckow R., *Jurnal fur Verbraucherschutz Lebensmittelsicherheit*, 2010, 5(1), 73.
7. S. Iso, Mizuno H., Ogawa H., Mochizuki Y., Iso N., *Fisheries Science*, **1994**, 60(1), 127.
8. K. Lovedeep, T. Astruc, A. Vénien, O. Loison, J. Cui, M. Irastorza, M. Bolanda, *Food & Function*, **2016**, 187(5), 2389.
9. W.-C. Ko, C.-L. Jao, J.-S.. Hwang, K.-C. Hsu, *Journal of Food Engineering*, **2006**, 77, 1007.

10. L. E. Kramer, "High Pressure Processing of Fish and Protein Denaturation", Master thesis in Biological Chemistry, Stavanger, **2013**.
11. T. C. Lanier, *Advances in Experimental Medicine and Biology*, **1998**, 434, 45.
12. M., A. Mazorra-Manzano, J., C. Ramírez-Suárez, J., M. Moreno-Hernández, R. Pacheco-Aguilar, "Seafood Proteins", Elsevier Woodhead Publishing Series in Food Science, Technology and Nutrition, Amsterdam, **2018**, 445.
13. Z. Pieniak, W. Verbeke, K. Brunso, J. Scholderer, S. O. Olsenc, *Acta Alimentaria*, **2009**, 38(2), 179.
14. R. Schubring, *Journal of Thermal Analysis and Calorimetry*, **2005**, 82, 229.
15. R. Schubring, *Journal of Food Processing and Preservation*, **2008**, 32, 190.
16. Dagbjørn S., Van der Plancken I., Van Loey A., Hendrick M. E., *Journal of Food Engineering*, 2008, 85, 51.
17. C. G. Sotelo, C. Piñeiro, R.I. Pérez-Martín, *Z Lebensm Unters Forsch*, **1995**, 200(1), 14.
18. P. Soumia, C. Sandeep, J. J. Jubbin, *Indian Journal of Endocrinology and Metabolism*, **2013**, 17(3).
19. Teixeira B., Fidalgo L., Mendes R., Costa G., Cordeiro C., Marques A., Saraiva J. A., Nunes M. L., *Journal of Agricultural and Food Chemistry*, **2013**, 61, 2851.
20. M. Trebar, "Cold Chain and Shelf Life Prediction of Refrigerated Fish – From Farm to Table", Springer Cham, New York, **2018**.
21. L. Timberg, R. Kuldjärv, K. Koppel, T., Paalme, *Agronomy Research*, **2011**, 9 (Special Issue II), 495.
22. B. Truong, R. Buckow, C. E. Stathopoulos, M. H. Nguyen, *Food Engineering Reviews*, **2015**, 7(2), 109.
23. M. Uddin, Ahmad M. U., Jahan P., Sanguandekul R. *Asian Journal of Chemistry*, **2001**, 13(3), 965.

PHYSICAL AND MECHANICAL PROPERTIES OF SOME PLASTER MORTARS WITH OXIDE WASTES

MARIA GOREA^a, LILIANA BIZO^{a,*}, ADRIANA TĂNASE^a

ABSTRACT. The present study evaluates the characteristics and performances of plaster mortars for construction, with the addition of oxide waste resulted from the filling of metal statues. Several plaster mortars using 0 %, 5 %, 10 %, 15 % and 20 % wt. of waste in composition were prepared in the laboratory and the physical and mechanical characteristics were determined. The waste oxide composition is mainly formed of 61.26 % SiO₂, 11.20 % Al₂O₃ and 23.50 % CaSO₄. The consistency water is about 75 % for mortars without waste. With increasing the waste content in the mortar composition, the amount of water decreases at about 50 %. It was also determined the setting time for all plaster mortars without any setting time retarder. The initial setting time for the control mortar was 12 minutes and with increasing the waste percentage in the composition, the setting time increased proportionally, reaching 18 minutes for the sample with 20 % wt. waste. The flexural strength of 2.03 N/mm² and compressive strength of 10.31 N/mm² were obtained for the sample with the highest amount of waste (20 % wt.).

Keywords: *oxide waste, plaster mortar, mechanical properties*

INTRODUCTION

There is growing concern in the last decades about the large amount of waste generated and the damage that this causes to the planet. At European level, waste management policies aim to reduce the environmental and health impacts of waste and to improve the EU's resource efficiency. The long-term aim of these policies is to reduce the amount of waste generated and when waste generation is unavoidable to promote it as a resource and achieve higher levels of recycling and the safe disposal of waste [1, 2].

Building mortar is a building material formed by mixing cement, fine aggregates, mixtures and water in a suitable proportion, and the use of ceramic

^a Babeş-Bolyai University, Faculty of Chemistry and Chemical Engineering, 11 Arany Janos str., RO-400028, Cluj-Napoca, Romania

* Corresponding author: lbizo@chem.ubbcluj.ro

waste in mortar production dates back to the ancient times. The development of suitable repair mortar for historic masonry requires knowledge about chemical and mineralogical composition and information about the mechanical and physical properties of individual structures [3, 4]. It has recently been suggested that mortars may be characterized by their mineralogical composition and micro structural appearance [5]. Also the understanding of all the physical chemical property is very important for this class of materials [6].

Many studies focusing on the addition of waste in a plaster matrix are found. Moreover, there are many researches about adding different types of wastes to gypsum plaster matrix.

The paper waste generated in the manufacture of paper can be a component of plaster composite material in adequate proportion. The use of paper pulp waste in plaster mortars does not involve any difficulties although it is advisable drying the paper waste before utilization. As such, the mechanical and rheological properties are enhanced and fragmenting the waste ensures a homogeneous mixture [7].

Plaster composites obtained by mixing plaster with different proportions of unburnt rice husk, blast furnace slag, calcium carbonate or poly vinyl alcohol polymer were tested. The study demonstrated that rice husk, polymer and calcium carbonate additions increased while slag decreased normal consistency water, all additives delayed the setting time, increased the apparent porosity and decreased bulk density of their corresponding composites. The compressive strength is not considerably improved, the being recommended for lightweight high-porosity building structures [8].

The mineral wools waste, both rock wool and glass wool, into a plaster matrix could be embedded in the core of plasterboards increasing their flexural strength [9].

The addition of foam ground rubber waste up to 7.5% in the lightweight plaster composite ensures a good workability, obtaining a homogeneous paste without any segregation. Also ground rubber coming from pipe foam insulation was used for obtaining a new lightweight product for building construction [10].

Saw dust, coconut fibers and tobacco waste fiber incorporated in the plaster mortar composition have improved the thermal property. Diatomaceous earth, fly ash and bottom ash improved the mechanical and thermal properties. In addition, these samples with citric retarder enhanced fire protection [11].

Del Río Merino et al. studied the physical and mechanical properties of a lightened eco-plaster mortar, manufactured with aggregates from ceramic and extruded polystyrene wastes. The mortars with these wastes reduce the water absorption by capillarity and increase the superficial hardness compared with etalon mortar [12].

The mechanical characteristics, the thermal conductivity and the sound absorption capacity of the plaster plates with wood waste (wood shavings and sawdust) were studied by Pedreño-Rojas et al. The greatest

thermal improvement occurs by adding 20% of wood shavings in the mortar composition [13].

The use of polymeric wastes as polymer additives in the manufacture of lightweight plasters has been widely studied with a view to improve the thermal behavior of these materials. The properties of plaster mortar and paste rheology containing polyurethane foam and polyamide powder waste are comparable to that of lightweight composite realized with conventional materials [14, 15].

To our knowledge there is no reference about the use of waste resulted from the filling of the metal statues incorporated into a plaster mortar. For this reason our paper aimed to study the effect of waste addition into plaster-based mortar, from point of view of physical and mechanical properties.

RESULTS AND DISCUSSION

Characterization of raw materials

Plaster

The plaster used in the experiments is a commercial modeling plaster, traditionally used in building construction due to its good properties as it provides in fire protection, as thermal isolation and its contribution to equilibrate the humidity in rooms.

Oxide waste

The oxide waste resulted from thermal treatment at 600 °C of a mixture of 50 % sand, 25 % fired clay and 25 % gypsum used in the casting process of the art metal statue was introduced as the aggregates in plaster mortars.

Chemical composition of waste

The chemical composition of the oxide waste realized by traditional wet chemistry analyses is presented in Table 1.

Table 1. Chemical composition (wt.%) of the oxide waste.

Oxide	SiO ₂	TiO ₂	Al ₂ O ₃	Fe ₂ O ₃	CaO/ CaSO ₄	MgO	Na ₂ O	K ₂ O	LOI
Waste [wt.%]	60.24	0.82	12.44	0.49	23.30	0.36	0.28	0.72	1.35

The oxide waste contains the silicon dioxide and aluminium oxide resulted from thermal treated of sand and fired clay and calcium oxide (CaSO₄) from gypsum dehydration. The minor oxides are originating from impurities presented in fired clay.

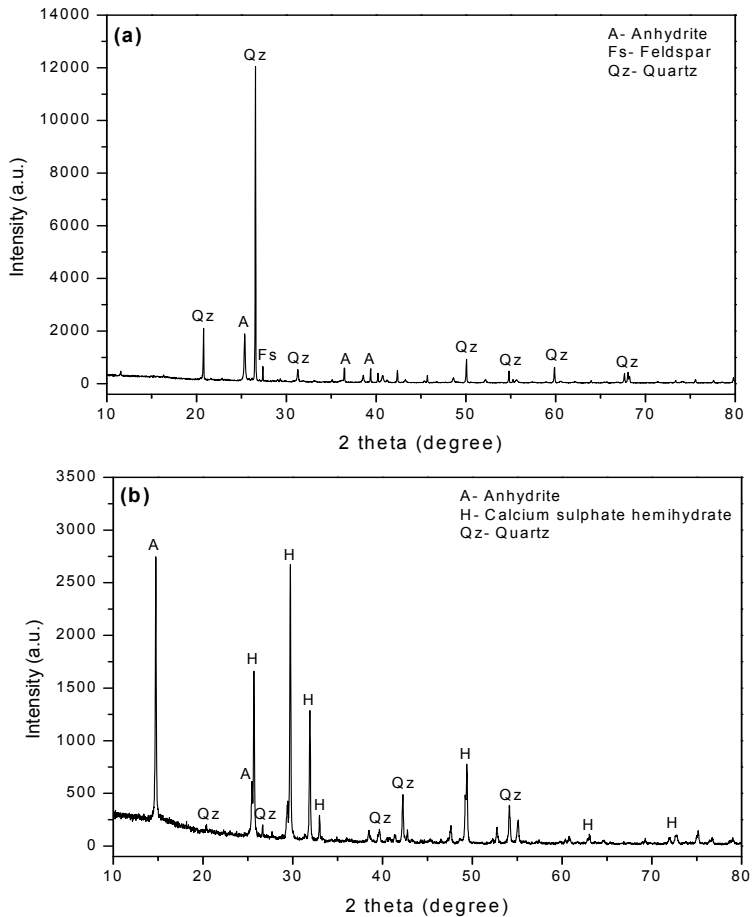
X-ray diffraction

Figure 1. X-ray diffraction pattern of oxide waste (a), plaster (b).

The mineralogical composition, presented in Figure 1(b), of plaster was investigated by X-ray diffraction using a Shimadzu 6000 apparatus. The identified compounds are calcium sulphate hemihydrate ($\text{CaSO}_4 \cdot 0.5\text{H}_2\text{O}$) as a majority, anhydrite (CaSO_4) low content and small quantities of impurities quartz (SiO_2). The quartz impurity in plaster does not influence the mortar properties, it acts as a fine aggregate.

In Figure 1(a) the X-ray diffraction pattern of oxide waste used in experiments are illustrated. The main mineralogical compounds evidenced are quartz (SiO_2), feldspar, anhydrite (CaSO_4).

Grain size distribution

For physical characterization of components of the oxide waste plaster mortars, their grain size distributions were performed by a Shimadzu laser-diffraction analyzer. Samples were immersed for 15 s in isopropyl alcohol used as a solvent, with aggregation being reduced using treatment with ultrasounds. Grain size distribution of the plaster used in experiments is represented in Figure 2 (a) and in Figure 2(b) for oxide waste.

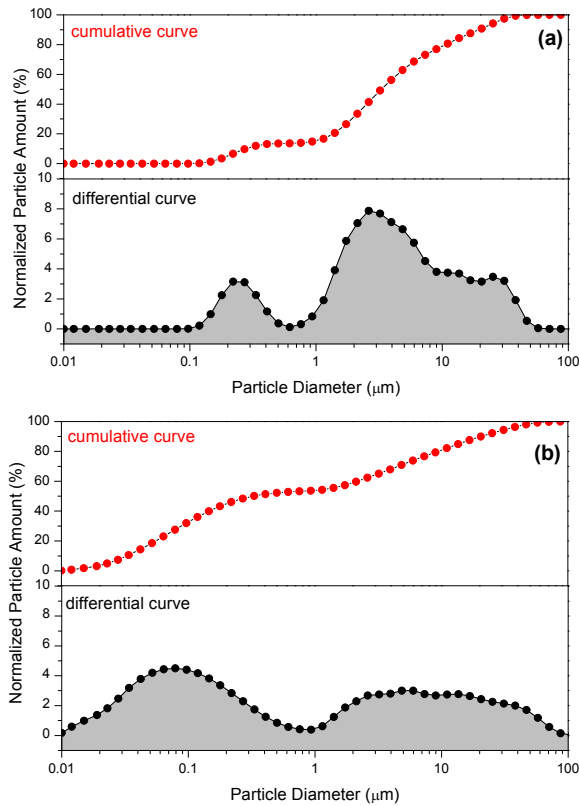


Figure 2. Grain size distribution for plaster (a) and oxide waste (b).

The size of plaster grains is less than 131 microns; 54% of the grains are less than 1 micron and the smallest value of the plaster grain is 10 nm. In the case of oxide waste, the highest value of grain size is 71 microns, only 14 % of the grains are less than 1 micron and the lowest size is of 97 nm. The size of the plaster grains close the oxide waste and ensure workability and homogeneity of the mixtures.

Characterization of mortar samples

Macroscopic aspect

Figure 3 illustrates the aspect of the experimented M5 sample, containing 20 % oxide waste. A homogeneous sample without any segregation of waste is observed. The uniform distribution of oxide waste and smooth surfaces in all studied samples were evidenced.

Consistency water

Reference plaster paste (without oxide waste) and pastes with different content of waste replacing the plaster were mixing according to the specific standard. After the rest and mixing time has passed the paste is introduced into a cylindrical ring measuring 40 mm in height and an internal diameter of 30 mm supported on a glass plate. Subsequently, the mold was removed allowing the paste to spread out. The sample diameter was measured in both directions perpendicular to each other.



Figure 3. Macroscopic aspect of M5 sample.

Table 2. Consistency water for studied samples.

Sample	Consistency Water [%]
Reference sample M1	75
5 % waste sample M2	70
10 % waste sample M3	65
15 % waste sample M4	60
20 % waste sample M5	50

The normal consistency water (Table 2) of the used plaster was determined to be of 75 % which means that each 100 g plaster powder mixes with 75 ml water for obtaining of normal consistency paste. The addition of oxide waste decreases the normal consistency water of plaster mortars. Generally, the addition of any additive in plaster mortar involves a decrease of plaster content. Thus the normal consistency water for plaster – waste composites is ranged from 70 % to 50 % for samples that contain 5, 10, 15 and 20 % oxide waste.

Setting Time

The setting times of the plaster mortars prepared with different quantities of oxide waste are given in Table 3. It can observe that the initial setting time is the same for all samples. So, the additions of oxide waste in mortar composition no influence the initial setting time.

Table 3. Setting times of the different plaster mortars compositions.

Sample/Characteristic	M1	M2	M3	M4	M5
Initial setting time [min]	12	12	12	12	12
Final setting time [min]	15	16	17	17	18

On the other hand, the final setting times increase by adding the oxide waste. This fact could be explained by the presence of CaSO_4 – soluble anhydrite, in the waste and/or in plaster composition which needs a more long time to hydrate comparing with $\text{CaSO}_4 \cdot 0.5\text{H}_2\text{O}$ hemihydrate.

Plaster mortars density

In Table 4 are presented the densities obtained for experimented mortars. It is observed that plaster mortar with additions of oxide waste achieves value higher than the reference samples (M1).

Table 4. Densities of different studied plaster mortars compositions.

Sample	M1	M2	M3	M4	M5
Density [g/cm^3]	1.09	1.21	1.25	1.28	1.32

The density of mortars with oxide waste is increased because of waste density which is higher than $2\text{g}/\text{cm}^3$. Therefore, for every 5 % of waste incorporated in the plaster mortar, the density increases with 11, 15, 17 and 21 % compared with reference mortar (M1).

Mechanical Resistance

Flexural strength

In Figure 4 are presented the flexural strength for the experimented mortars. The results shows that adding the oxide waste in gypsum plaster matrix improve the flexural strength compared to the reference sample.

Additions of 5 % waste in mortar composition no influence on flexural strength ($1.49 \text{ N}/\text{mm}^2$). 10 and 15 % waste in experimented composition increase the flexural strength to 1.72 respectively $1.80 \text{ N}/\text{mm}^2$. But adding

up to 20 % waste in the composition can increase the flexural strength up to 35 % (2.03 N/mm²). These mechanical behaviors of plaster mortars could be explained also through increasing their densities comparing the reference sample (about 11 to 21 %).

Compressive strength

The compressive strengths of the studied samples are illustrated in Figure 5.

With the addition of the oxide wastes the compressive strength values increase as the percentage of waste is increased. So, adding the 5 and 10 % waste in mortar composition the compressive strength slightly increases, from 4.72 N/mm² to 5.43 respectively 5.51 N/mm². When 15 % and 20 % waste are added the compressive strength, values are increased up to 70 % respectively 100 % (from 4.72 to 8.11 respectively 10.31 N/mm²).

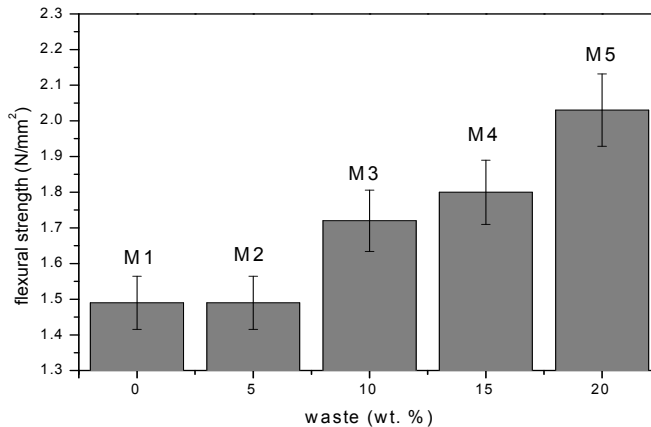


Figure 4. Flexural strength of oxide waste plaster mortar.

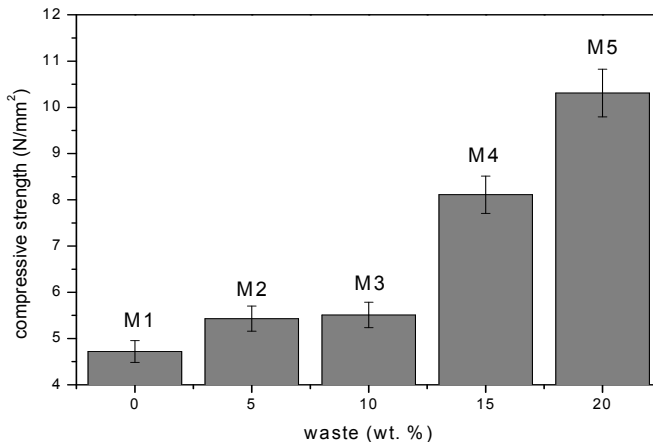


Figure 5. Compressive strength of oxide waste plaster mortar.

CONCLUSIONS

The using of oxide waste powder as a recycled and reusable material in various plaster mortars is therefore of great interest in the obtaining of new building materials. This fact would contribute to the reassessment of different waste products that are generated in large amounts.

In this respect, the addition of oxide wastes as a plaster substitute has a good influence on the final plaster mortar properties. The addition of oxide waste decreases the normal consistency water of plaster mortars. The final setting times and densities increase by adding the oxide waste. Adding up to 20 % waste in the composition can increase the flexural strength up to 35 % (2.03 N/mm²). The compressive strength values are increased up to 70 % respectively 100 % by adding 15 % and 20 % oxide waste in composition (from 4.72 to 8.11 respectively 10.31 N/mm²).

This preliminary study tries to justify the possibility of reusing this type of oxide waste as an alternative raw material in some lightweight building materials.

EXPERIMENTAL SECTION

Experimented compositions

Materials

The experimented plaster mortars are presented in the Table 5. Five blended plaster mortars with different addition of oxide waste were mixed (M1, M2, M3, M4 and M5).

Table 5. The prepared plaster mortar compositions.

Samples code		M1	M2	M3	M4	M5
Composition	Plaster (wt. %)	100	95	90	85	80
	Waste (wt. %)	0	5	10	15	20

The procedure for obtaining the pastes consisted of progressive additions of oxide waste powder to the plaster, substituting by weight different proportions of plaster for waste. The dry plaster and waste are mixed until homogenisation, about 20 minute. The consistency water is measured and put in a laboratory vessel. The homogenised mixtures sprinkle gradually for 30 seconds in the water. The resulted paste is mixed for 1 minute and then pours uniformly in three molds. The samples are kept 2 hours in molds and after hardening they are removed.

Methods

Particle size analysis in suspension was performed using Shimadzu SALD-7101 micro- and nanoparticle analyzer (Japan). The nanoparticle size analyzer can handle a broad range of measurement objects and purposes. Using this apparatus, serial measurements based on the same measurement principle are possible for particle size varying within a measurement range from 10 nm to 300 μm .

Crystalline phases were determined by X-ray diffractometer (XRD, Shimadzu 6000) using Cu-K α radiation ($\lambda = 1.5406 \text{ \AA}$) equipped with Ni-filter in a 2θ range of 10° - 80° .

The mechanical characteristics (compressive and flexural strength) are investigated on hydraulic press CONTROLS 50-C66V2 in accordance with Romanian standard SR EN 196-1.

REFERENCES

1. <http://ec.europa.eu/environment/waste/legislation/index.htm>, EU Waste Legislation.
2. http://ec.europa.eu/environment/waste/target_review.htm, Review of Waste Policy and Legislation.
3. M. Singh, S. Waghmare, S. Vinodh Kumar, *Journal of Archaeological Science*, **2014**, *42*, 430.
4. J. Schafer, H. K. Hilsdorf, "Ancient and new lime, mortars: the correlation between their composition and properties", in: Theil, M.J. (Ed.), Proceedings of the Conservation of Stone and Other Materials, vol. 2, E & FN Spon, Paris, **1993**, 605.
5. A. E. Charola, M. Dupas, R.P. Sheryll, G.C. Freund, "Scientific methodologies applied in works of arts", Proceeding of the 1st International Symposium, Firenze, **1984**, 28.
6. J. E. Adam, W. A., Kneller, "Thermal analysis of medieval mortars from Gothic Cathedrals of France", in: Marinas, Koukis (Eds.), Engineering Geology of Ancient Works, Monuments and Historic Sites. Balkema, Rotterdam, **1988**, 1019.
7. L. Agullo, A. Aguado, T. Garcia, *Building and Environment*, 2006, *41*, 821.
8. A. A. Khalil, A. Tawfik, A. A. Hegazy, M. F. El-Shahatet, *Construction and Building Materials*, **2014**, *68*, 580.
9. S. Romaniega Piñeiro, M. del Río Merino, C. Pérez García, *Advances in Materials Science and Engineering*, **2015**, article ID 854192.
10. A. Jiménez Rivero, A. de Guzmán Báez, J. García Navarro, *Construction and Building Materials*, **2014**, *55*, 146.
11. P. Chindapasirt, K. Boonserm, T. Chairuangsi, W. Vichit-Vadakan, T. Eaimsin, T. Sato, K. Pimraksa, *Construction and Building Materials*, **2011**, *25*, 3193.
12. M. del Río Merino, J. Santa Cruz Astorqui, P. Villoria Sáez, R. Santos Jiménez, M. González Cortina, *Construction and Building Materials*, **2018**, *158*, 649.
13. M. A. Pedreño-Rojas, M. J. Morales-Conde, F. Pérez-Gálvez, C. Rodríguez-Liñán, *Journal of Cleaner Production*, **2017**, *166*, 690.
14. S. Gutiérrez-González, J. Gadea, A. Rodríguez, C. Junco, V. Calderón, *Construction and Building Materials*, **2012**, *28*, 653.
15. S. Gutiérrez-González, M.M. Alonso, J. Gadea, A. Rodríguez, V. Calderón, *Construction and Building Materials*, **2013**, *38*, 407.

INFLUENCE OF THE COMPOSITION EVOLUTION OF WASTE COMPUTER MOTHERBOARDS ON THEIR RECYCLING STRATEGY

SORIN-AUREL DORNEANU^{a, b}, ALEXANDRU-ANDREI AVRAM^a,
ALEXANDRU-HORAȚIU MĂRINCAȘ^a, NICOLETA COTOLAN^a,
TIBERIU FRENȚIU^{a, b, *}, PETRU ILEA^{a, b, *}

ABSTRACT. Even if the mobile devices gain more popularity comparing to the desktop personal computers (DPCs), the last ones are still intensively used where highly computing or storage capabilities are required. Because the replacing rate of DPCs are very high, the amount of obsolete equipments is also huge, reclaiming adequate efficient and ecological recycling techniques. In this field, the main efforts are focused on the DPCs motherboards (DPCMBs) recycling because, even if they represent only 5 to 10% from the DPCs weight, they concentrate up to 80% from the recoverable value. By accounting the DPCMBs' traditional and incipient recycling technologies, it is obvious that none of them can solve alone the problem of this waste type. In this context, during the present work, the composition evolution of 10 DPCMBs released between 1998 and 2008 was evaluated and analyzed, the obtained results being used to design a feasible and eco-friendly combined strategy for integral DPCMBs recycling.

Keywords: *Waste printed circuit boards, metals recovery, composition evolution, recycling strategy, eco-friendly process*

INTRODUCTION

Obviously, the development of the modern society cannot be imagined without the support of the advanced computing systems. Among them, the portable devices (*i.e.* laptops and tables) achieve an increased popularity comparing to the desktop PCs (DPCs), with more than 162, 150 and 94 million units, respectively, forecasted to be shipped in 2018 [1]. Even if the costs of

^a Babeș-Bolyai University, Faculty of Chemistry and Chemical Engineering, 11 Arany Janos Str., RO-400028, Cluj-Napoca, Romania

^b Babeș-Bolyai University, Interdisciplinary Research Institute on Bio-Nano-Sciences, 42 Treboniu Laurian Str., RO-400271, Cluj-Napoca, Romania

* Corresponding author: pilea@chem.ubbcluj.ro

laptops manufacturing and exploiting are sensibly lower over those of DPCs [2], the last ones are still extensively used in fields where highly computing or storage capabilities are required (e.g. servers, data bases, graphical stations, processes control, research, etc.) and their development and replacing rate are very high [3]. Therefore, the amount of the resulting DPCs waste remains significant, requiring adequate efficient and ecological recycling techniques [4]. From the wasted DPCs systems, the central processing units (CPUs) represent the major component and include the main board, also known as motherboard. The DPCs motherboards (DPCMBs), representing between 5 and 10% of the DPCs weight [5] are considered the most economically interesting components due to the high value of the recoverable metals [6-8]. Despite the fact that the total amount of the precious metals (especially Au) used for DPCMBs manufacturing represents less than 1% from the boards' weight, these metals concentrate more than 80% of the recovered value [5]. As a consequence, intensive researches were dedicated to the DPCMBs recycling, being proposed various processes, e.g. physico-mechanical [7, 9], hydrometallurgical [6, 10, 11], pyrometallurgical [12, 13], pyrolytic [14] biometallurgical [15] or combination of thereof as presented in research papers [9, 16] or exhaustive reviews [17-19]. In spite of the intense efforts, confirmed by the high number of published papers [20] and patents [21], the great majority of the proposed technologies presents serious disadvantages, e.g. generation of large inter-contaminated metallic / nonmetallic fractions during the physico-mechanical treatment [22], high raw materials consumption and generation of large wastewater volumes for the hydrometallurgical approach, high energy consumption, low selectivity and generation of toxic gases during the high temperature treatments [12, 14, 23]. The true electrochemical recycling of metals from DPCMBs, that must include compulsory (i) the metals electrodeposition and (ii) the simultaneously electrochemical recycling of the leaching agent [24-27] and/or metals anodic dissolution [28], starts to represent a feasible alternative from economical [29] and ecological [30] points of view, allowing also a significant minimization of the disadvantages pointed before. Moreover, the efficiency of the DPCMBs' electrochemical recycling can be improved by the process intensification [31] or use of special electrolytes, like ionic liquids [32].

Unfortunately, due to the high heterogeneity, complexity and non-uniformity of the DPCMBs, the traditional or new-born recycling technologies mentioned before may not meet the future industry requirements because of environmental contamination, high cost, low efficiency and/or generation of new waste fluxes. Furthermore, a single technology still has several limitations and cannot solve all the DPCMBs' recycling problems, requiring combinations of more than one process or technology [33]. Practically, because the great majority of the cited technologies are focused mainly on metals recovery and high profitability, the problem of the nonmetallic parts (NMPs) recycling is

neglected or treated inadequately. For example, in the pyrometallurgical processes, the NMPs are considered as supplementary fuel and, consequently, their recycling rate is, practically, 0% [34]. Similarly, the physico-mechanical approach leads to highly inter-contaminated metallic and nonmetallic fractions, the last ones containing variable amounts of plastics, epoxy resins, glass, fiberglass, ceramics and, most often, extremely toxic compounds like heavy metals traces and flame retardants [35]. Therefore, these new generated waste fluxes, mainly as powders, are very difficult to recycle or dispose.

In this context, in the present work, we decided to study the evolution of the DPCMBs composition aiming to propose an optimal scenario for their integral recycling. Our demarche was justified by the fact that, to the best of our knowledge, the temporal evolution of the metals content in whole DPCMBs was not yet studied, a similar work being focused only on the Cu and Au content of RAM modules [36]. In our case, 10 obsolete DPCMBs released between 1998 and 2008 were selected and manually pre-treated in order to remove several unwanted components: the Li batteries (LiBs), chipset aluminium heat sinks (AHS), brass screws (BS) derived from the D-sub connectors and the cylindrical aluminium electrolytic capacitors (EC). Afterwards, the exposed metals from the DPCMBs were dissolved using the aqueous Br_2/KBr leaching system and the resulting solutions were analyzed by ICP-OES. Finally, based on the weight balance of the all contained materials and the literature data, an original flowchart for the complete DPCMBs recycling was elaborated.

RESULTS AND DISCUSSION

Because the profitability of a recycling technology represents a key factor for a successfully subsequent industrial implementation, the amount and the nature of all the recovered materials during the present work were rigorously evaluated and accounted. In our opinion, as pointed in a previous work [26], in order to reduce the recycling cost and to avoid undesirable phenomenon like hydrogen evolution, explosion risks and electrolyte contamination, it is preferable to remove some components (LiBs, AHS, BS and EC) from the DPCMBs before the main leaching step. Consequently, in the first step of our study, these unwanted parts were manually removed from each board and weighed separately, the obtained values being presented in Figure 1 as kg per ton of DPCMBs waste. Because the weight of the all removed LiBs was the same, of around 3 g each, it was not included in this comparison. Concerning the other parts, their amounts present a random distribution, without any visible increasing or decreasing tendency. Consequently, for further estimations, the mean amount values were considered.

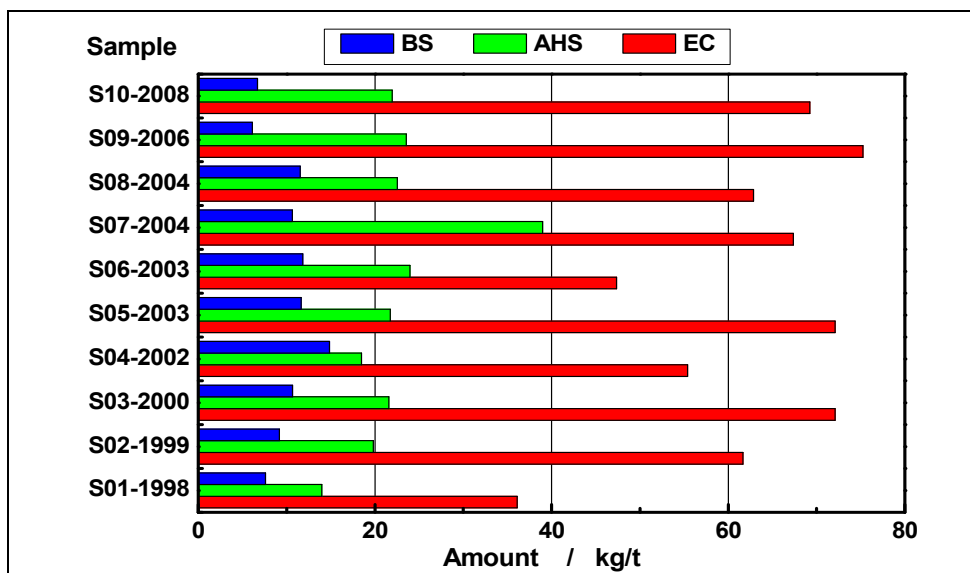


Figure 1. Amount evolution of the manually removed components from 10 studied DPCMBs

Based on data presented in Figure 1, mean amounts of 10.1, 22.7 and 61.9 kg/t of DPCMBs were calculated for BS, AHS and EC, respectively. For an electric energy price of 0.133 €/kWh [37] and a recycling energy consume of around 6.6 kWh/kg of BS (for brass leaching and metals electroextraction), an economy of ~9 €/t of DPCMBs can be obtained only by direct BS valorization. Similarly, considering energy consumptions of 12 kWh/kg for Al leaching and 12.5 kWh/kg for Al electroextraction, the direct valorization of aluminium scrap included in the AHS and EC (at least 80 kg/t of DPCMBs) can generate an economy of 260 €/t of DPCMBs.

After the pre-treatment step described before, the metals from DPCMBs were dissolved using the aqueous Br₂/KBr leaching system, liberating all the components from the boards surface. Subsequently, the leaching solutions were decanted, and the resulting solid parts were washed, dried and manually sorted on the following categories: (i) waste printed circuit boards (WPCBs), (ii) plastic parts (PPs), (iii) electronic chips and surface mounted devices (C&SMDs) and (iv) magnetic parts and undissolved metals (M&UMs). Each set of solid parts were weighed individually and the total amounts of the dissolved metals were evaluated by calculating the difference between DPCMBs mass before and after the leaching step. The resulting values are presented in Figure 2.

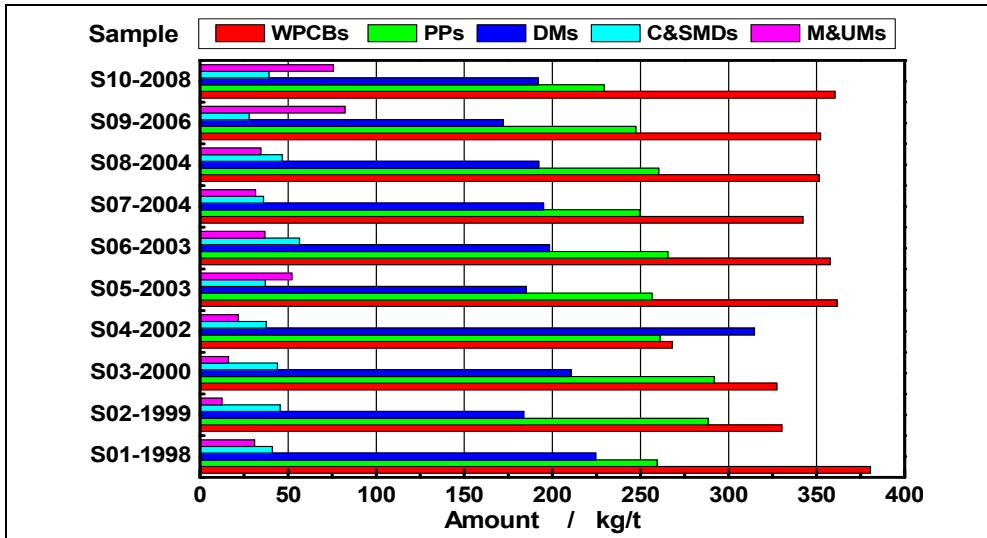


Figure 2. Amount evolution of the solid parts and total dissolved metals from 10 studied DPCMBs after the leaching step

As it can be seen from Figure 2, the amounts of solid parts and DMs presents also a random distribution, without any coherent evolution. As a consequence, for the further estimations, the mean amount values were considered.

The comparison between the mean amounts of the separated fractions, presented in Figure 3, reveal that the total quantity of WPCBs and PPs represents more than 60% from the initial DPCMBs weight, requiring the development of dedicated recycling strategies.

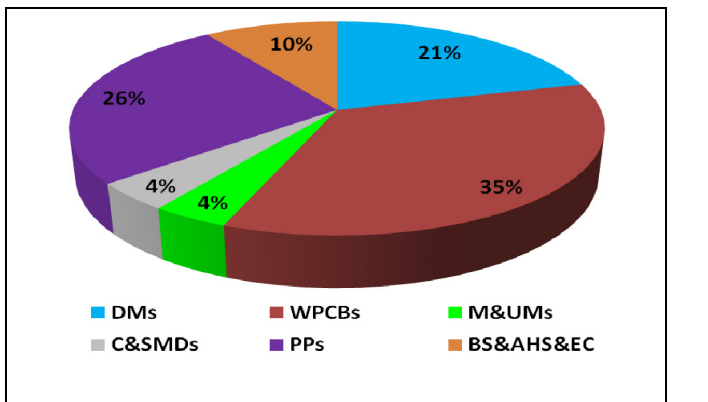


Figure 3. Distribution of the solid parts and total dissolved metals weight from 10 studied DPCMBs after the leaching step

The evolution of the DPCMBs metals' content was evaluated by ICP-OES, the obtained results being presented in Figure 4. Concerning the major (more abundant) metals amounts (see Figure 4.A), it can be observed that copper quantity presents a decrease tendency from 1998 to 2008, and, after the implementation of the UE RoHS directive in 2006, the Pb content decreased to 0, simultaneously with a small raise of the Sn content.

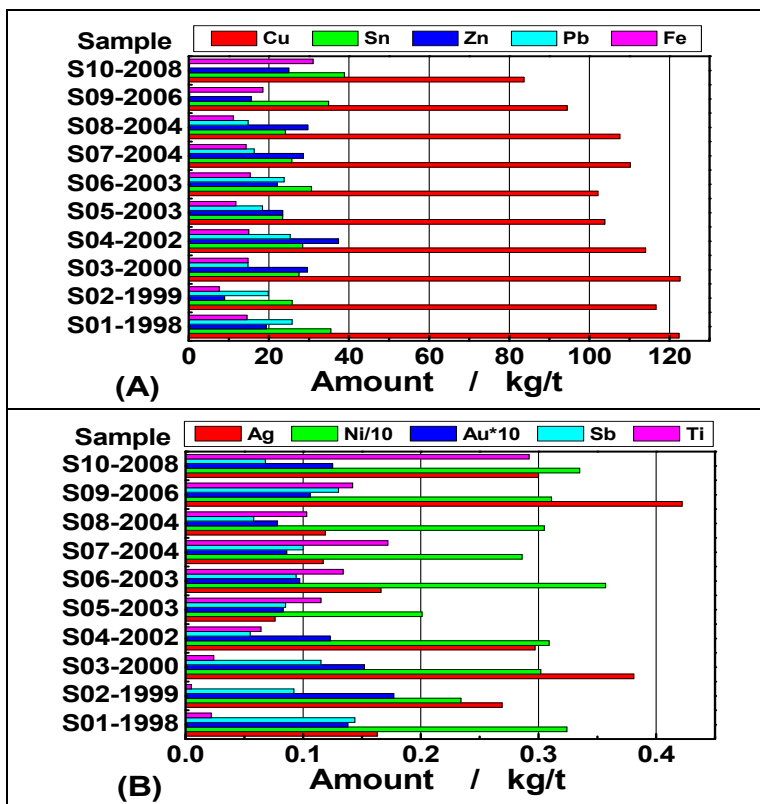


Figure 4. Amount evolution of the major (A) and minor (B) dissolved metals from 10 studied DPCMBs

Concerning the minor (less abundant) metals amounts (see Figure 4.B), Ti presents an general increase tendency, all the other elements remaining at relative constant levels.

Generally, excepting Cu, Ti and Pb, the amount of the other dissolved metals presents also a random distribution, without visible increasing or decreasing tendencies, allowing us to consider the mean values for further interpretations.

From another point of view, it is worth to note that, until this stage, the amounts of Cu remaining in the WPCBs fraction and of the other base metals (BMs) and precious metals (PMs) blocked inside of the C&SMDs parts was not evaluated. In order to solve first problem, we considered that the tested DPCMBs are of FR4 0.062' type (4 Cu layers; total thickness of 1.6 mm) [38], having an average weight of 0.5 kg and a mean area of 500 cm². In these conditions, we estimate that, for each ton of DPCMBs, at least 75 kg of undissolved Cu are still blocked under the epoxy layers.

Concerning the metals included in the C&SMDs fraction, we found, after the appropriate treatment and analysis, that the amount of Au is ~13 times higher comparing that dissolved during first leaching step. A synthesis of the obtained mean results for one ton of DPCMBs and an estimation of the potential revenues resulting from the most valuable recovered metals are presented in Table 1, together with a significant reference [39] concerning the metals content in the pins of DPCMBs.

Table 1. Mean amounts of the most valuable metals recovered during this work and their potential revenues

Metals	Au	Ag	Cu	Sn	Pb	Ni	Zn	Total
Exposed mass [kg/t]	0.012	0.231	107.7	29.5	16.0	2.96	24.0	180
Mass in WPCBs [kg/t]	-	-	75.3	-	-	-	-	75.2
Mass in C&SMDs [kg/t]	0.160	0.011	7.6	0.39	0.68	0.41	0.08	9.33
Total mass [kg/t]	0.172	0.242	190.6	29.9	16.6	3.37	24.0	265
Price [€/kg] [40]	34808	408.6	5.49	16.3	1.69	9.5	2.22	-
Total revenues [€/t]	5970	99	1045	487	28	32	54	7715
Mass in Pins [kg/t] [39]	0.015	0.037	55.7	2.54	0.84	0.82	16.7	76.7

The results of an exhaustive study focused only on the metals content of the DPCMBs connectors pins (see last row of Table 1) confirmed us that the major amount of recoverable gold is entrapped inside of the C&SMDs fraction and represents up to 80% of revenues. Moreover, in respect to the total mass of recoverable metals from DPCMBs, only 70% of Zn (as brass), 8.5% of Sn (as solder traces or bronze) and 29% of Cu (as alloys or pure metal) are included in the pins fraction, and more than 39% of Cu is entrapped in the WPCBs fraction. Consequently, the C&SMDs and WPCBs fractions must be extremely carefully and efficiently treated in order to gain a maximum profit, avoiding metals loss and secondary pollution.

Finally, we can conclude that, indifferently of the DPCs age group, applying adequate technologies, a revenue of over 7000 € can be obtained for 1 ton of recycled DPCMBs, the metal values corresponding to the series Au>Cu>Sn>Ag>Zn>Ni>Pb.

Based on applied protocols, obtained results and literature data, we succeeded to elaborate an original DPCMBs recycling flowchart able to recover all the materials included in these wastes, without generation of

new polluting fluxes. The schematic diagram of a such technology is presented in Figure 5 and starts from the obsolete DPCs. Taking into account that the final step of DPCs manufacturing is based on manual assembling and in accordance with recent studies [34, 41], it is clear that only the manual primary dismantling can assure a complete valorization of the all included materials. Subsequently, the extracted DPCMBs must be treated manually to remove the LiBs and AHS. Concerning the EC, they can be removed manually or automatically [42, 43].

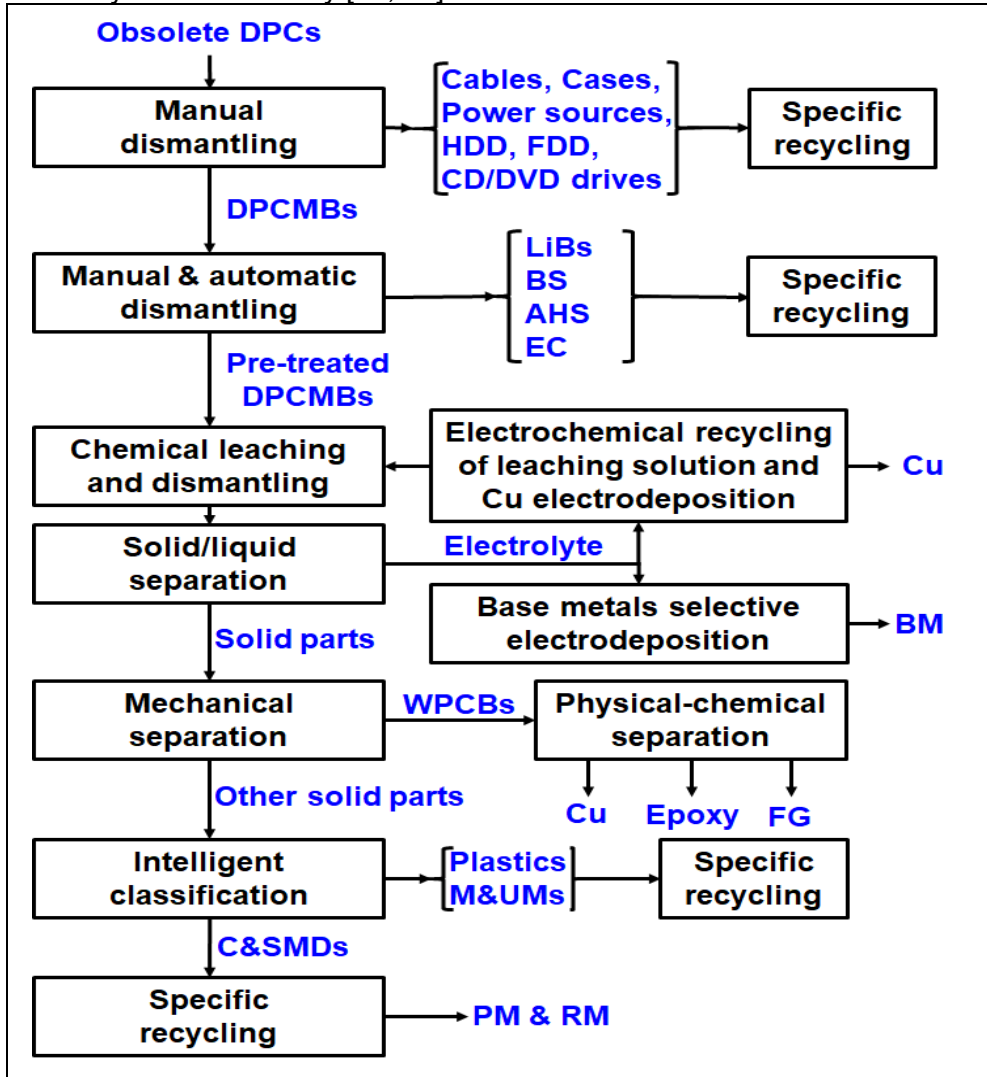


Figure 5. Proposed flowchart for the complete recycling of DPCMBs waste

The exposed metals from the whole pre-treated DPCMBs can be dissolved in appropriated equipment using electrochemically regenerated leaching solutions [26], preserving, in this manner, unaltered the solid parts. A simple mechanical separation (sieving) allows the separation of the depopulated WPCBs that can be easier recycled to recover pure Cu, epoxy and fiberglass (FG) [44]. Subsequently, an intelligent (robotized) separation can be applied to the remaining solid parts as electronic components (C&SMDs), M&UMs and plastics, the last ones able to be sorted depending on shape, composition or even color [45] and valorized superiorly with high revenues [46]. Finally, the C&SMDs fraction, containing the major amount of PM and rare metals (RM) can be appropriate recycled for their efficient recovering [47].

CONCLUSIONS

Analyzing the results concerning the composition evolution of 10 different DPCMBs released between 1998 and 2008, we concluded that the amounts of metallic and non-metallic components present, generally, a random distribution, without any evident tendency of evolution or involution. Consequently, using the mean values of the included components amounts, we estimated that the appropriate recycling of the contained metals leads to a revenue of more than 7000 € for 1 ton of recycled DPCMBs. Also, the WPCBs and plastic fractions, representing more than 60% of the DPCMBs total mass, must be carefully treated to recover supplementary materials and avoid the generation of new wastes fluxes.

Finally, combining the literature information with the practical observations we were able to propose an original flowchart combining multiples technologies able to recover ALL the components included in the DPCMBs structure. Such technology is in total agreement with the new imposed circular economy concept, leading to complete materials recycling without, theoretically, any production of secondary wastes.

EXPERIMENTAL SECTION

The starting materials for this study were represented by the obsolete CPUs discarded from the Faculty of Chemistry and Chemical Engineering (Babeş-Bolyai University, Cluj-Napoca, Romania) in 2016. Around 30 CPUs were disassembled manually, and the resulting components were sorted on different categories: cables, power sources, floppy disk and optical units, HDDs, microprocessors heat sinks systems, DPCMBs, microprocessors, RAM modules and dedicated cards (video, sound, network, data acquisition, etc.). From the resulting stock, 10 DPCMBs released between 1998 and 2008 were manually pre-treated to

remove the LiBs, AHSs, BSs and ECs. The weight of the DPCMBs before and after the pre-treatment and, also, of the dismantled components was evaluated using a laboratory electronic balance (model PLJ-510-3m, KERN&SOHN GmbH, Germany). Subsequently, each board was cut in large pieces (around 5 cm x 10 cm), introduced in sealable glass pots of 3-5 L and the exposed metals were leached for 48 h using, for each sample, 2.2 L of 2 M KBr solution containing 100 mL HCl 37% and 100 mL liquid Br₂ as oxidizing agent. After the leaching step, the resulting solutions were decanted, and the remaining solid components were washed with tap and distilled water, dried for in air 7 days, sorted manually as WPCBs, PPs, C&SMDs and M&UMs, and weighed separately. The main information concerning the selected DPCMBs samples are indicated in Table 2.

Table 2. The assigned experimental code, model, release year and the initial weight of the selected DPCMBs samples

Sample code	Model	Release year	Initial weight (g)
S01-1998	Asus P2B-S	1998	683.1
S02-1999	PRM-00801 E1	1999	554.6
S03-2000	PRM-27IV- DTK Computer	2000	520.5
S04-2002	MSI MS-6378	2002	530.7
S05-2003	Elitegroup K7VTA3/KT333	2003	657.1
S06-2003	Elitegroup P4IBASD (v3.0)	2003	646.4
S07-2004	ASRock P4i45D+	2004	539.1
S08-2004	Mercury KOB KT266a FDSX	2004	660.3
S09-2006	ASRock AliveNF6G-VSTA	2006	535.8
S10-2008	MSI P31 Neo V2	2008	573.8

The resulting leaching solutions were filtered, diluted (depending on necessities, of 10, 100 or 1000 times) and analyzed by ICP-OES using a SPECTRO CIROS CCD spectrometer (SPECTRO Analytical Instruments, Germany).

In order to evaluate the metals content in the C&SMDs fraction, a 15 g homogenous sample of chips and SMD parts was calcined at 800 °C (Heraeus GmbH, Germany) until constant weight, finely grinded and digested with 55 mL of *aqua regia*. From the resulting solution, the amount of Cu, Zn, Ni, Sn, Fe, Ag, Au and Pb was evaluated by F-AAS (AVANTA PM, GBC, Australia).

ACKNOWLEDGMENTS

This work was supported by a grant of the Romanian Ministry of Research and Innovation, CCCDI-UEFISCDI, project number PN-III-P1-1.2-PCCDI-2017-0652 / 84PCCDI/2018, within PNCDI III.

REFERENCES

1. <https://www.statista.com/statistics/272595/global-shipments-forecast-for-tablets-laptops-and-desktop-pcs/>, accessed 21.11.2018.
2. A. Puca, M. Carrano, G. Liu, D. Musella, M. Ripa, S. Viglia, S. Ulgiati, *Resources, Conservation and Recycling*, **2017**, 116, 124.
3. S.S. Suresh, S. Bonda, S. Mohanty S.K. Nayak, *Process Safety and Environmental Protection*, **2018**, 116, 477.
4. G. Chauhan, P.R. Jadhao, K.K. Pant, K.D.P. Nigam, *Journal of Environmental Chemical Engineering*, **2018**, 6(1), 1288.
5. C.A. Kohl, L. P. Gomes, *Journal of Cleaner Production*, **2018**, 184, 1041.
6. Z. Wu, W. Yuan, J.Li, X. Wang, L. Liu, J. Wang, *Frontiers of Environmental Science and Engineering*, **2017**, 11(5):8, 1.
7. M. Kaya, "Recovery of Metals and Nonmetals from Waste Printed Circuit Boards (PCBs) by Physical Recycling Techniques" in *Energy Technology 2017*, L. Zhang (Ed.), The Minerals, Metals & Materials Society, **2017**, 433–451.
8. S. Pinho, M. Ferreira, M. F. Almeida, *Resources, Conservation and Recycling*, **2018**, 132, 71.
9. A. Barnwal, S. Vishvakarma, N. Dhawan, *Materials Today: Proceedings*, **2018**, 5(9), 17046.
10. H. Li, J. Eksteen, E. Oraby, *Resources, Conservation and Recycling*, **2018**, 139, 122.
11. B. Mizero, T. Musongo, E.R. Rene, F. Battes P.N.L. Lens, *Process Safety and Environmental Protection*, **2018**, 120, 14.
12. H. Wang, S. Zhang, B. Li, D. Pan, Y. Wu, T. Zuo, *Resources, Conservation and Recycling*, **2017**, 126, 209.
13. M. Ghodrati, M.A. Rhamdhani, A. Khaliq, G. Brooks, B. Samali, *Journal of Material Cycles and Waste Management*, **2018**, 20(1), 386.
14. A. Gurgul, W. Szczepaniak M. Zabłocka-Malicka, *Science of the Total Environment*, **2018**, 624, 1119.
15. A. Priya, S. Hait, *Environmental Science and Pollution Research*, **2017**, 24(8), 6989.
16. E. Ventura, A. Futuro, S.C. Pinho, M.F. Almeida, J.M. Dias, *Journal of Environmental Management*, **2018**, 223, 297.
17. M. Kaya, *Waste Management*, **2016**, 57, 64.
18. A. İşildar, E.R. Rene, E.D. van Hullebusch, P.N.L. Lens, *Resources, Conservation and Recycling*, **2018**, 135, 296.
19. C. Ning, C.S.K. Lin, D.C. W. Hui, G. McKay, *Topics in Current Chemistry*, **2017**, 375(2), 1.
20. G. Cecere, A. Martinelli, *Research Policy*, **2017**, vol. 46(5), 925.
21. L. Rocchetti, A. Amato, F. Beolchini, *Journal of Cleaner Production*, **2018**, 178, 814.
22. G. Zhang, Y. He, Y. Feng, T. Zhang, H. Wang, X. Zhu, *Separation and Purification Technology*, **2018**, 207, 321.
23. R. Saini, R. Khanna, R.K. Dutta, R. Cayumil, M. Ikram-UI-Haq, V. Agarwala, G. Ellamparathy, K. Jayasankar, P.S. Mukherjee, V. Sahajwalla, *Waste Management*, **2017**, 64, 182.

24. S. Fogarasi, F. Imre-Lucaci, Á. Imre-Lucaci, and P. Ilea, *Journal of Hazardous Materials*, **2014**, 273, 215.
25. L.A. Diaz, T.E. Lister, J.A. Parkman, G.G. Clark, *Journal of Cleaner Production*, **2016**, 125, 236.
26. S.A. Dorneanu, *Studia Universitatis Babeș-Bolyai Chimia*, **2017**, 62(3), 177.
27. D. Yang D. Yang, Y. Chu, J. Wang, M. Chen, J. Shu, F. Xiu, Z. Xu, S. Sun, S. Chen, *Separation and Purification Technology*, **2018**, 205, 302.
28. E. Haccuria, P. Ning, H. Cao, P. Venkatesan, W. Jin, Y. Yang, Z. Sun, *Journal of Cleaner Production*, **2017**, 152, 150.
29. L. A. Diaz, T. E. Lister, *Waste Management*, **2018**, 74, 384.
30. S. Fogarasi, F. Imre-Lucaci, A. Egedy, Á. Imre-Lucaci, P. Ilea, *Waste Management*, **2015**, 40, 136.
31. K. Scott, *Renewable and Sustainable Energy Reviews*, **2018**, 81, 1406.
32. Y. Zhang, M. Chen, Q. Tan, B. Wang, S. Chen, *Hydrometallurgy*, **2018**, 175, 150.
33. S.M. Abdelbasir, C.T. El-Sheltawy, D.M. Abdo, *Journal of Sustainable Metallurgy*, **2018**, 4(2), 295.
34. J.R. Peeters, P. Vanegas, W. Dewulf, J.R. Duflou, *Journal of Cleaner Production*, **2017**, 140, 1182.
35. A. Cesaro, A. Marra, V. Belgiorno M. Guida, *Journal of Cleaner Production*, **2017**, 142, 2656.
36. R.G. Charles, P. Douglas, I.L. Hallin, I. Matthews, G. Liversage, *Waste Management*, **2017**, 60, 505.
37. https://ec.europa.eu/eurostat/statistics-explained/index.php/Electricity_price_statistics, accessed 21.11.2018.
38. <http://www.nanotech-elektronik.pl/index.php/en/42-english/support>, accessed 21.11.2018.
39. R.A. Mesquita, R.A.F. Silva, D. Majuste, *Process Safety and Environmental Protection*, **2018**, 120, 107.
40. <https://www.lme.com/Metals>, accessed 21.11.2018.
41. F. Tesfaye, D. Lindberg, J. Hamuyuni, P. Taskinen, L. Hupaa. *Minerals Engineering*, **2017**, 111, 209.
42. B. Kopacek, *IFAC-PapersOnLine*, **2016**, 49(29), 190.
43. J. Li, M. Barwood, S. Rahimifard, *Resources Conservation and Recycling*, **2019**, 140, 158.
44. H.R. Verma, K.K. Singh, T.R. Mankhand, *Waste Management*, **2017**, 65, 139.
45. S.P. Gundupalli, S. Hait, A. Thakur, *Waste Management*, **2017**, 60, 56.
46. R. Gao, Z. Xu, *Journal of Hazardous Materials*, **2019**, 364, 1.
47. Y. Liu, K. Li, J. Guo, Z. Xu, *Journal of Cleaner Production*, **2018**, 197, 1488.

AIRBORNE PARTICLES POLLUTION IN DEJ CITY

IOAN AUREL CHERECHES^a, IOAN PETEAN^b,
GERTRUD-ALEXANDRA PALTINEAN^{b,*}, AURORA MOCANU^b,
LIANA MURESAN^c, GEORGE ARGHIR^d, MARIA TOMOAI-COTISEL^{b,e}

ABSTRACT. Environmental data achieved with the Air Quality Monitoring Station in Dej city, Romania, reveal a normal state of particulate matter (PM) emissions below the standard limit in April and May 2017. These airborne particles contain a large amount of mineral fractions such as: quartz, calcite, clays (e.g., kaolinite and muscovite), and lepidocrocite. Their size varies in a wide range: from 1 to 200 μm for floating particles (FP) and from 1 to 10 μm for PM10 observed by optical microscopy and SEM. The *in vivo* testing shows the ability of PM10 to penetrate into the upper respiratory tract. Mineral fractions were found in nasal exudates. At a shorter exposure time (e.g., 1 minute), only PM10 particles were observed. Particles larger than PM10 were found in nasal exudates at prolonged exposure for up to 3 minutes.

Keywords: *Floating particles, PM10, hazard*

INTRODUCTION

Dej is a representative city in Cluj County, Romania, mainly for exploitation of sodium chloride from medieval times. Geological layers are typical for Badenian sediments associated with halite deposits [1-3]. Minerals, such as quartz, calcite, and clays, are the major components of Dej soil. Neglected green spaces are sensitive to decay and dust particles formation [4-6], which can be elevated in the atmosphere under favorable environmental

^a *Technical University of Cluj-Napoca, Faculty of Mechanics, Muncii Ave., No. 103 -105, RO-400641 Cluj-Napoca, Romania.*

^b *Babeş-Bolyai University, Faculty of Chemistry and Chemical Engineering, Arany Janos Str., No. 11, RO-400084 Cluj-Napoca, Romania.*

^c *Technical University of Cluj-Napoca, Faculty of Materials and Environment Engineering, Muncii Ave., No. 103 -105, RO-400641 Cluj-Napoca, Romania.*

^d *Technical University of Cluj-Napoca, Faculty of Materials and Environment Engineering, Muncii Ave., No. 103 -105, RO-400641 Cluj-Napoca, Romania.*

^e *Academy of Romanian Scientists, 54 Splaiul Independentei, 050094, Bucharest, Romania.*

* *Corresponding author: pgertrud@gmail.com*

conditions [7-12]. Dry and windy days are the most favorable for the mineral emission in the atmosphere, while the wet ones ensure the fixing of the dust on the soil surfaces.

The first category of pollutant air particles susceptible to being found in Dej city is floating particles (FP), which contain a large amount of mineral classes. These particles are raised in the atmosphere by strong air currents and after a short flight fall down to the soil [13-15]. Such behavior is less harmful for living beings. However the standard limit of FP is 17 g/m²/month [16-18].

PM10 are more dangerous airborne particles for living beings due to their ability to long travel in the atmosphere until their fall to the soil [19-24] with their maximum diameter of 10 μm [25, 26]. Due to their small size, they are easily inhaled in the respiratory system. The penetration capacity depends on the type, shape and size of the particles. The literature data show that minerals, as usual, in Dej city soils can form a very small fraction in the urban environment [27, 28]. PM10 contains significant amounts of micro particles called PM2.5 [29, 30] and submicron particles, even nano particles grouped in the PM1 and PM0.5 classes [31-34]. Fraction PM1 and nano require special probe techniques [35-40]. Exposure to airborne particles may lead to acute pulmonary and cardiovascular symptoms [41, 42] and for long-term exposure could lead to silicosis and lung cancer [43]. Exposure depends on the breathing manner in days with high PM emissions (windy days). Nasal breathing is more protective than oral due to the ability of the nose mucosa to catch particles from the inhaled air [44].

RESULTS AND DISCUSSION

The Air Quality Monitoring Station (AQMS) is located in the center of Dej city, at the confluence of the main transport facilities between the urban and industrial nodes around the Somes River Bridge. It refers to airborne particles caused by various sources from soil disintegration, transport, and industrial activities related to the salt and furniture industry. The measured environmental data are centralized in Table 1.

Table 1. PM emission level in Dej city in April and May 2017

Emission type		April 2017	May 2017
PM10, μg/m ³	minimum	6.34	2.53
	maximum	40.79	45.32
	average	21.51	19.42
FP, g/m ² /month	downtown	14.30	7.21
	Industrial area	13.79	26.4

PM10 values are below the standard limit in April and May 2017, demonstrating that the atmosphere in Dej city is appropriate for normal life. However, there are two-day records when the weather was dry and windy

when PM10 emissions are very close to the limit. In these days with wind, the *in vivo* tests were performed.

The FP emissions are in good parameters for the city downtown in April as well as in May, but for the industrial area the value for May 2017 exceeds the limit of 17 g/m²/month. This could result in some accidental inhalation of mineral particles. Therefore, both representative FP and PM10 samples collected with AQMS require a proper physical and chemical characterization.

Figure 1 shows the XRD spectra (a, c) and optical microscopy images (b and d) with cross-polarized optical polarization for FP, Figure 1a and Figure 1b, and for PM10, Figure 1c and Figure 1d.

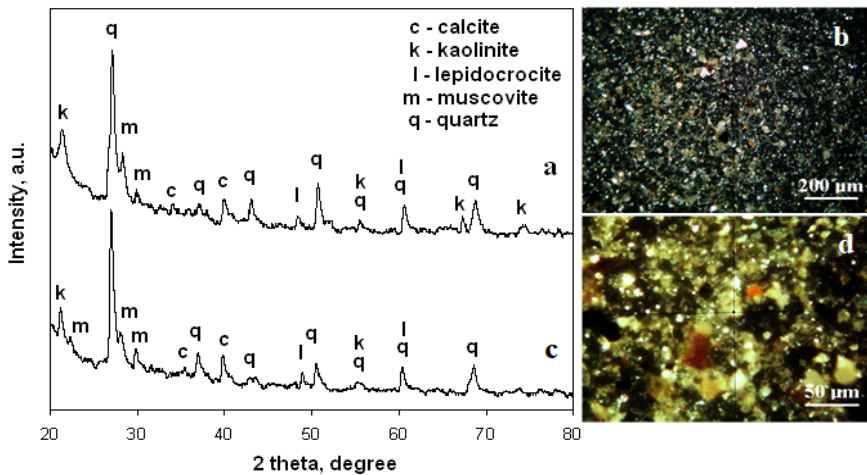


Figure 1. The mineralogical characterization of PM collected from Dej city AQMS. Floating particles: a) XRD spectrum and b) cross polarized light microscopy image; The PM10: c) XRD spectrum and d) cross polarized light microscopy image.

The XRD spectra have very well-developed, narrow-form peaks that demonstrate the crystallinity of the samples. Dominant mineral is the quartz followed by the clay mixture of kaolinite and muscovite. There is also a significant amount of calcite and traces of lepidocrocite.

The XRD data were correlated with cross-polarized light microscopy to observe the shape and size range for each identified mineral. The data are centralized in Table 2. Quartz is the dominant mineral in all particulate air samples in this investigation. Small and ultra-small fractions are found in FP and PM10 due to fragmentation of silicates [27, 29] in the urban environment.

Rounded polyhedral quartz particles are seen in the SEM images, FP of Figure 2a, and PM10 in Figure 2b. It is to be observed the higher refinement of quartz in PM10 than in the fractions found in FP. These prove to be more dangerous due to their small size and broken parts.

Table 2. Properties of minerals identified in FP and PM10 samples

Component	Quartz	Kaolinite	Muscovite	Calcite	Lepidocrocite	
Formula	SiO ₂	Al ₂ Si ₂ O ₅ (OH) ₄	KAl ₂ (AlSi ₃ O ₁₀) (F,OH) ₂	CaCO ₃	γFeO(OH)	
Size range, μm	FP	1 -200	1 - 30	1- 50	5 - 100	1 - 50
	PM10	1 - 10	1 - 5	1 - 5	5 - 10	1 - 10
Color	Green - gray	White- blue	Pink	Yellow-brown	Reddish - brown	
Shape	round	tabular	tabular	round	elongated	

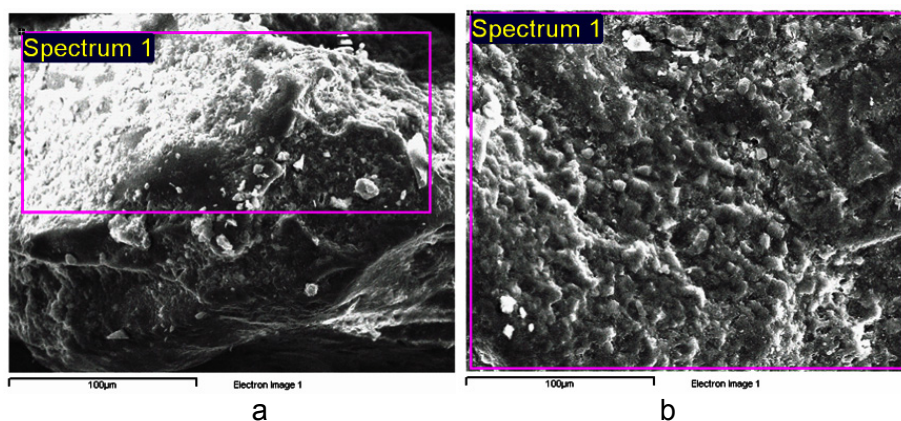


Figure 2. SEM images for particulate matter: a) FP and b) PM 10.

Clays, kaolinite and muscovite, are more often found as small fractions in airborne particles (e.g. PM10). A plenty of small clay platelet appear in PM10 sample, Figure 2b, which is in good agreement with high amount of Al, Na, and K observed for PM10 than in FP.

The large amount of quartz and silicates is supported by EDX spectrometry, the data in Table 3, where Si is one of the dominant elements.

Calcium amount is more representative for FP sample than for PM10, Table 3, confirming the optical microscopy observation that calcite is often found in FP as big particles than in PM10. Even small particles of calcite appear they have a great coalescence tendency forming clusters.

Traces of lepidocrocite observed in airborne particles are mainly related to transport activities rather than soil decay [6, 9]. The amount of Fe observed in Table 3 is in good agreement with the XRD observations.

Table 3. Elemental composition for FP and PM10 resulted from EDX

Element	FP		PM10	
	weight %	atomic %	weight %	atomic %
C	28.17	37.25	14.74	21.67
O	52.52	52.13	52.12	57.55
Na	-	-	2.97	2.29
Al	1.37	0.81	5.01	3.28
Si	15.42	8.72	22.33	14.05
K	0.21	0.09	1.10	0.50
Ca	1.16	0.46	0.99	0.43
Fe	0.57	0.16	0.74	0.23
Mg	0.58	0.38	-	-
Total	100.00	100.00	100.00	100.00

Inhalation of PM10 could be very harmful to the living organism, especially to long-term exposure. *In vivo* experiment was performed to observe the capacity of the nose mucosa to capture such mineral particles. The obtained results are shown in Figure 3.

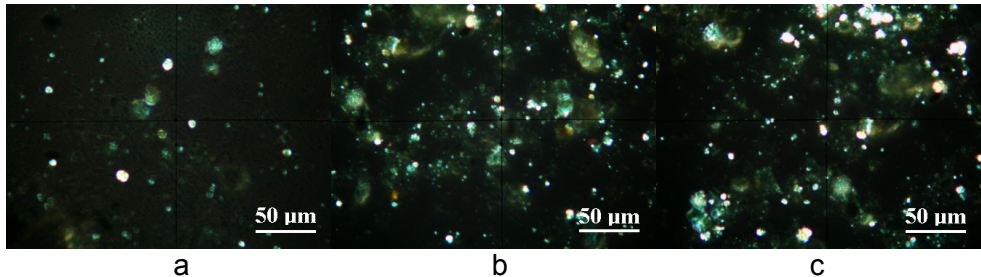


Figure 3. Nose exudates at different exposure times: a) 1 minute, b) 3 minutes and c) 10 minutes.

Exposure was performed under conditions with an FP of 26.4 g/m²/month and 45.32 µg/m³ of PM10, respectively. Several quartz and clay particles are trapped in the nose exudates at 1 minute of continuous exposure, Figure 3a. Their dimensions are in the PM10 range. Their number is significantly increased, and some clusters are formed at 3 minutes of exposure, Figure 3b. Some FP particles are observed along with many PM10 at 10 minutes of exposure, Figure 3c.

The *in vivo* test demonstrates the ability of PM10 to enter into the respiratory system, the risk increasing with exposure time. It also proves that the nose mucosa is efficient for particulate matter PM10 and larger particles trapped to prevent the penetration of airborne particles into the lower respiratory system.

CONCLUSIONS

The air quality monitoring in Dej city generally shows a normal state of particulate matter emissions with average values below of standard limit in April and May 2017. Large amounts of mineral fractions were found, containing: quartz, calcite, clays (e.g. kaolinite and muscovite), and lepidocrocite. Their size varies in a wide range: from 1 to 200 μm for floating particles and from 1 to 10 μm for PM10 as observed by optical microscopy and SEM. The *in vivo* test shows the ability of PM10 to penetrate into upper respiratory tract. Mineral fractions were found in nasal exudates. At shorter time of exposure (e.g., 1 minute) only PM10 particles were observed. Greater particles than PM10 were found in nasal exudates at prolonged exposure of 3 minutes. To prevent lungs exposure to airborne particles, the nasal breathing is recommended instead of inhalation by mouth.

EXPERIMENTAL SECTION

The experimental zone is located in the city of Dej (Cluj county), near Vasile Alecsandri street. FP and PM10 were collected by the CJ-5 Automatic Air Monitoring Station at the Environmental Protection Agency in Cluj County, and the emissions in the atmosphere were monitored in April and May 2017 and the results were centralized.

X-ray diffraction analysis was performed on a DRON 3 diffractometer equipped with the MATMEC VI.0 data acquisition and software acquisition module. A monochrome $\text{Co}_{K\alpha}$ radiation was used for all X-ray spectra. Mineral identification was performed using the standard MATCH 1.0 X - ray standard data base from Crystal Impact Co.

Optical microscopy was performed on a Laboval 2 microscope produced by Karl Zeiss Jena equipped with a Kodak 10 Mpx digital camera. Quantitative analysis of optical micro-photographic images was done using the Image J professional software as a freeware resource from the National Institutes of Health, USA.

SEM images associated with EDX spectra were performed on a Jeol JSM 5600 LV microscope in the secondary electron imaging mode coupled with the Everhart Thornley detector for EDX analysis.

REFERENCES

1. A. Szakacs, Z. Pecskay, L. Silye, K. Balogh, D. Vlad, A. Fulop, *Geologica Carpathica*, **2012**, 63(2), 139.
2. A. Codrea, O. Barbu, V. Codrea, *Contributii Botanice*, **2007**, 62, 111.

3. M. Alexe, Gh. Serban, A. Baricz, A.-S. Andrei, A. Cristea, K. P. Battes, M. Cimpean, L. Momeu, V. Muntean, S. A. Porav, H. L. Banciu, *Journal of Limnology*, **2018**, 77(1), 17.
4. S. Janhall, *Atmospheric Environment*, **2015**, 105, 130.
5. A. Przybysz, A. Saebo, H. M. Hanslin, S. W. Gawronski, *Science of the Total Environment*, **2014**, 481, 360.
6. K. V. Abhijith, P. Kumar, J. Gallagher, A. McNabola, R. Baldauf, F. Pilla, B. Broderick, S. Di Sabatino, B. Pulvirenti, *Atmospheric Environment*, **2017**, 162, 71.
7. A. Talbi, Y. Kerchich, R. Kerbachi, M. Boughedaoui, *Environmental Pollution*, **2018**, 232, 252.
8. W. Hu, H. Niu, K. Murata, Z. Wu, M. Hu, T. Kojima, D. Zhang, *Atmospheric Environment*, **2018**, 179, 201.
9. D. F. Muntean, D. Ristoiu, G. Arghir, R. F. Campean, I. Petean, *Carpathian Journal of Earth and Environmental Sciences*, **2012**, 7(3), 175.
10. R. F. Câmpian, I. Petean, M. Bărăian, G. A. Hosu-Prack, D. Ristoiu, G. Arghir, *Carpathian Journal of Earth and Environmental Sciences*, **2012**, 7(2), 57.
11. T. Moreno, T. P. Jones, R. J. Richards, *Science of the Total Environment*, **2004**, 334-335, 337.
12. P. Dagsson-Waldhauserova, O. Arnalds, H. Olafsson, *Atmospheric Environment*, **2013**, 77, 117.
13. M. Lage, H. Lopes, M. da S. Carvalho, *Journal of Computational Physics*, **2011**, 230, 7736.
14. E. Kellner, J. A. Hubbard, *Science of the Total Environment*, **2018**, 615, 1164.
15. E. C. Schiopu, *Analele Universitatii Constantin Brancusi din Targu Jiu, Seria Inginerie*, **2010**, 3, 516.
16. S. H. Tan, M. Roth, E. Velasco, *Atmospheric Environment*, **2017**, 170, 245.
17. D. Edelin, P.-C. Czujko, C. Castelain, C. Josset, F. Fayolle, *Experimental Thermal and Fluid Science*, **2015**, 68, 634.
18. European Council, 2008. *Directive 2008/50 of UE Parliament and European Council concerning atmosphere quality and a more clean atmosphere in Europe, 2008*. Official Journal of European Union, RO: L152, 1 - 44.
19. T. Banerjee, R. A. Christian, *Atmospheric Pollution Research*, **2018**, 9, 342.
20. L. Calderon-Garciduenas, A. Calderon-Garciduenas, R. Torres-Jardon, J. Avila-Ramirez, R. J. Kulesza, A. D. Angiulli, *Primary Health Care Research & Development*, **2015**, 16, 329.
21. L. Megido, B. Suarez-Pena, L. Negral, L. Castrillon, S. Suarez, Y. Fernandez-Nava, E. Maranon, *Chemosphere*, **2016**, 162, 73.
22. S. Catino, M. Tutino, S. Ruggieri, C. Marinaccio, R. Giua, G. De Gennaro, P. Corsi, G. Assennato, D. Ribatti, *Ecotoxicology and Environmental Safety*, **2017**, 140, 156.
23. C. Wen, M. Xu, D. Yu, C. Sheng, H. Wu, P. Zhang, Y. Qiao, H. Yao, *Proceedings of the Combustion Institute*, **2013**, 34(2), 2383.
24. L. Makra, I. Ionel, Z. Csépe, I. Matyasovszky, N. Lontis, F. Popescu, Z. Sümeghy, *Science of the Total Environment*, **2013**, 458-460, 36.
25. M. Diociaiuti, M. Balduzzi, B. De Berardis, G. Cattani, G. Stacchini, G. Ziemacki, A. Marconi, L. Paoletti, *Environmental Research Section A*, **2001**, 86(3), 254.
26. C. Capatina, C. M. Simonescu, N. Dadalau, D. Cirtina, *Revista de Chimie*, **2016**, 67(7), 1247.

27. G. A. Paltinean, I. Petean, G. Arghir, D. F. Muntean, M. Tomoaia-Cotisel, *Revista de Chimie*, **2016**, 67(6), 1118.
28. G. A. Paltinean, I. Petean, G. Arghir, D. F. Muntean, L. Muresan, M. Tomoaia-Cotisel, *Annals of the Academy of Romanian Scientists Series on Physics and Chemistry Sciences*, **2017**, 2(2), 43.
29. G. A. Hosu-Prack, I. Petean, G. Arghir, L.D. Bobos, M. Tomoaia-Cotisel, *Studia Universitatis Babeş-Bolyai, Chemia*, **2010**, 55(3), 93.
30. I. Petean, A. Mocanu, G. A. Paltinean, R. Tarcan, D. F. Muntean, L. Muresan, G. Arghir, M. Tomoaia-Cotisel, *Studia Universitatis Babeş-Bolyai Chemia*, **2017**, 62(4), Tom I, 33.
31. L. Zhang, Y. Ninomiya, T. Yamashita, *Fuel*, **2006**, 85(10-11), 1446.
32. I. Petean, G. A. Paltinean, A. Mocanu, D. F. Muntean, L. Muresan, G. Arghir, M. Tomoaia-Cotisel, *Studia, Universitatis Babeş-Bolyai Chemia*, **2018**, 63(3), 49.
33. G. A. Hosu-Prack, I. Petean, G. Arghir, L.D. Bobos, M. Tomoaia-Cotisel, *Carpathian Journal of Earth and Environmental Sciences*, **2016**, 11(2), 539.
34. G. A. Paltinean, I. Petean, G. Arghir, D. F. Muntean, L.D. Bobos, M. Tomoaia-Cotisel, *Particulate Science and Technology: An International Journal*, **2016**, 34(5), 580.
35. S. Rapuntean, R. Balint, G. A. Paltinean, Gh. Tomoaia, A. Mocanu, Cs. P. Racz, O. Horovitz, M. Tomoaia-Cotisel, *Studia Universitatis Babeş-Bolyai Chemia*, **2018**, 63(3), 73.
36. O. Cadar, P. T. Frangopol, Gh. Tomoaia, D. Oltean, G. A. Paltinean, A. Mocanu, O. Horovitz, M. Tomoaia-Cotisel, *Studia Universitatis Babeş-Bolyai Chemia*, **2017**, 62(4), Tom I, 67.
37. M. Tomoaia-Cotisel, A. Tomoaia-Cotisel, T. Yupsanis, Gh. Tomoaia, I. Balea, A. Mocanu, Cs. Racz, *Revue Roumaine de Chimie*, **2006**, 51 (12), 1181.
38. Gh. Tomoaia, P.T. Frangopol, O. Horovitz, L.D. Bobos, A. Mocanu, M. Tomoaia-Cotisel, *Journal of Nanoscience and Nanotechnology*, **2011**, 11 (9), 7762.
39. Gh. Tomoaia, L.B. Pop, I. Petean, M. Tomoaia-Cotisel, *Materiale Plastice*, **2012**, 49 (1), 48.
40. R.D. Pasca, A. Mocanu, S.C. Cobzac, I. Petean, O. Horovitz, M. Tomoaia-Cotisel, *Particulate Science and Technology: An International Journal*, **2014**, 32(2), 131.
41. B. J. Lee, B. Kim, K. Lee, *Toxicological Research*, **2014**, 30(2), 71.
42. S. C. Fang, A. Cassidy, D. C. Christiani, *International Journal of Environmental Research and Public Health*, **2010**, 7, 1773.
43. T. N. Perkins, P. M. Peeters, C. Albrecht, R. P. F. Schins, M. A. Dentener, B. T. Mossman, E. F. M. Wouters, N. L. Reynaert, *Toxicology and Applied Pharmacology*, **2018**, 348, 43.
44. R. G. Lucchini, D. C. Dorman, A. Elder, B. Veronesi, *Neuro Toxicology*, **2012**, 33, 838.

COMPARATIVE STUDY OF CHEMICAL COMPOSITION OF THE ESSENTIAL OILS FROM *SATUREJA CUNEIFOLIA* TEN. AND *SATUREJA MONTANA* L., LAMIACEAE COLLECTED AT NATIONAL PARK LOVČEN, MONTENEGRO

DRAGICA BOJOVIĆ^a, MIOMIR ŠOŠKIĆ^b, VANJA TADIĆ^{c,*}

ABSTRACT. The main purpose of this study was an investigation of the chemical composition of essential oils obtained from *Satureja cuneifolia* Ten. and *S. montana* L. collected at the National park Lovćen, Montenegro. The qualitative and quantitative analysis of the essential oils, performed by GC/MS and GC/FID, indicated that the most abundant compound in *S. cuneifolia* essential oil was oxygenated monoterpene linalool (20.3%). Within the sesquiterpene compounds, *trans*-(E)-caryophyllene (6.1%), germacrene D (5.8%), nerolidol (5.2%) and spathulenol (5.0%) were present in relatively high quantities. Conversely, *S. montana* essential oil was abundant in monoterpenes, with *p*-cymene being the main constituent (16.6%). Besides, limonene (10.8%), thymol (6.5%), α -pinene (6.1%) and borneol (5.5%) were present in a high percentage. The results indicated that investigated *Satureja* species essential oils possessed different chemical composition, but both might represent an interesting resource of pharmacologically active compounds.

Keywords: *Satureja cuneifolia*; *Satureja montana*; essential oil; terpenes; Montenegro.

INTRODUCTION

The medicinal plants of the genus *Satureja* (*Lamiaceae* family), commonly used herbs and shrubs, have been localised in the area of the Mediterranean region to Europe, Middle East, West Asia, North America

^a Department of Pharmacy, Faculty of Medicine, Kruševac bb, 81000 Podgorica, Montenegro.

^b Clinical Center of Montenegro, Ljubljanska bb, 81000 Podgorica, Montenegro.

^c Institute for Medicinal Plant research "Dr Josif Pančić", Tadeuša Koščuška 1, 11000 Belgrade, Serbia.

* Corresponding author: vtadic@mocbilja.rs

and Africa. As annual or perennial semi-bushy, these plants inhabit arid, stony, sunny and rocky habitats along the coast of the Adriatic Sea [1, 2, 3].

Satureja species have been traditionally used in the treatment of various diseases such as nausea, indigestion, cramps, diarrhoea, infectious diseases and muscle pains [3, 4]. Up to now, numerous literature data stated that their essential oils possess antimicrobial activity against a wide range of multidrug-resistant pathogens [4]. In line with this statement, the essential oils obtained from *S. cuneifolia* and *S. montana* showed antimicrobial activity *in vitro* against various multidrug-resistant pathogens. The maximum activity of both essential oils was observed against methicillin-resistant *Staphylococcus aureus* and Gram (-) bacteria *Escherichia coli*. Both of these oils showed fungicidal activity against *Candida albicans* and *Saccharomyces cerevisiae* [5]. The considerable antibacterial and antifungal activities of essential oils from different *Satureja* species (*S. boissieri*, *S. coerulea*, *S. icarica*, *S. pilosa* and *S. intermedia*) also were documented in recently published papers [6, 7]. Furthermore, the aqueous extracts of *S. montana* showed antiviral activities against HIV [8].

Several *Satureja* species have been well-studied and documented from various aspects of their secondary metabolites. It was found that these plants have glands on the leaf surface that produce and secrete essential oils, like other aromatic plants belonging to the mint family. As documented in recently published literature, essential oil obtained from *S. montana ssp. montana* consisted mainly of linalool, borneol and *p*-cymene, while that from *S. montana ssp. variegata* contained monoterpene phenols such as carvacrol and thymol as dominant compounds. *S. cuneifolia* essential oils are rich in limonene, linalool, α -pinene, β -cubebene, γ -terpinene and carvacrol [9].

Different extraction methods might be employed in order to obtain volatile extracts and essential oils from *S. montana* and *S. cuneifolia*, conventional extraction techniques (hydrodistillation, HD, and Soxhlet extraction, SE) being mostly used [4, 10, 11, 12]. But, these methods have been recognised to possess many disadvantages, such as a longer period of extraction, less extraction efficiency and solvent residues in the obtained extracts. Non-conventional extractions methods (supercritical fluid extraction, SFE and supercritical water extraction, SWE) might be considered the better option for obtaining the high quality and high active extracts [10, 13].

In our study, the analysis of essential oils obtained from two *Satureja* species, *S. cuneifolia* Ten. (wild savory) and *S. montana* L. (winter savory) were investigated in order to compare their chemical composition, taking into account that traditionally both species and their essential oils had application in the treatment of different health impairments. Winter savory honey is a very frequent ingredient in folk remedies known for their

beneficial effects in the treatment of bronchitis. In addition, it is used as an antiseptic in gastrointestinal complaints, might be used as choleric, digestive remedy, and in the treatment of premature ejaculation [14]. Wild savory is a medicinal and aromatic plant which essential oil commonly has application in the preparation of the aromatic water, especially in the mountainous areas of Turkey and in the Mediterranean region. In addition, this plant has application as a spice and tea due to its carminative, tonic and stimulant effects [15]. The presence of phenolic compounds in these plants' essential oil might be responsible for their taste and fragrance. Winter savory has been known for its antimicrobial activity, probably due to the presence of monoterpene, alcohols and phenolic compounds, as stated in available literature data [14, 15]. The use of wild savory in the Montenegro has been less frequent in comparison to above-mentioned areas where traditionally this plant has been well recognised.

The objective of the present study was to investigate the chemical composition of essential oils of two *Satureja* species, *S. cuneifolia* and *S. montana* collected from different locations at National park Lovćen in the south-western part of Montenegro. Further, the evaluated difference in their chemical composition was discussed in order to compare the obtained results to the data revealed in up-to-now literature regarding these two *Satureja* species' essential oils chemistry profile. The presented results might be of importance for the direction of further biological investigations.

RESULTS AND DISCUSSION

The obtained essential oils from dried aerial parts of *S. cuneifolia* and *S. montana* were yellow liquids. The yields of essential oils amounted to 0.2 and 0.9 % (v/w), respectively. Identification of chemical composition of the essential oil was performed using the gas chromatographic techniques. Based on applied techniques, more than 100 compounds were identified in both investigated essential oils, which made 98.6-98.9% of the total chemical compounds (Table 1).

GC chromatograms of analysed essential oils and representative examples of MS spectra of compounds identified in both of analysed essential oils were presented at figures 1 - 3.

Table 1. Phytochemical analysis of essential oil profiles of *S. cuneifolia* and *S. montana*

N ^o	Compound [§]	RT	KI ^a /KI ^b	<i>S. cuneifolia</i> (%)	<i>S. montana</i> (%)
1.	tricyclene	6.45	921/912	-	0.3
2.	α -thujene	6.62	924/918	-	0.2
3.	α -pinene	6.70	932/923	0.7	6.1
4.	camphene	7.13	946/937	0.2	4.5
5.	thuja-2,4(10)-diene	7.38	953/944	-	0.1
6.	sabinene	7.92	969/965	0.3	0.1
7.	β -pinene	8.00	974/966	-	1.1
8.	myrcene	8.10	988/984	0.4	1.1
9.	α -phellandrene	8.98	1002/996	-	1.2
10.	δ -3-carene	9.15	1008/1002	-	0.4
11.	α -terpinene	9.39	1018/1008	-	0.5
12.	<i>p</i> -cymene	9.59	1020/1017	0.1	16.6
13.	limonene	9.73	1024/1020	1.1	10.8
14.	1,8-cineole	9.80	1026/1022	0.6	-
15.	(<i>Z</i>)- β -ocimene	10.10	1032/1031	0.6	1.5
16.	(<i>E</i>)- β -ocimene	10.40	1044/1041	0.3	0.6
17.	γ -terpinene	10.75	1054/1050	0.1	1.4
18.	<i>cis</i> -sabinene hydrate	11.09	1065/1060	0.5	1.3
19.	camphenilone	11.13	1083/1076	-	0.1
20.	terpinolene	11.85	1086/1080	-	0.1
21.	linalool	12.33	1095/1098	20.3	1.5
22.	<i>trans</i> -sabinene hydrate	12.42	1098/1099	0.1	0.4
23.	<i>cis</i> -thujone	12.45	1101/1101	-	0.1
24.	isopentyl isovalerate	12.51	1102/1102	0.3	-
25.	2-methylbutyl isovalerate	12.68	1103/1103	0.2	-
26.	<i>trans</i> -pinene hydrate	12.81	1110/1107	0.2	-
27.	(<i>Z</i>)- <i>p</i> -menth-2-en-1-ol	12.96	1118/1115	0.1	0.2
28.	α -campholenal	13.08	1122/1118	0.3	0.6
29.	<i>trans</i> -pinocarveol	13.17	1135/1130	-	0.6
30.	<i>trans</i> -verbenol	13.52	1140/1139	0.1	0.1
31.	camphor	13.65	1141/1139	0.4	4.5
32.	myrcenone	13.83	1148/1142	-	t
33.	nerol oxide	14.13	1154/1148	0.3	-
34.	sabina ketone	14.28	1154/1154	0.1	-
35.	pinocarvone	14.41	1160/1154	-	t
36.	borneol	14.48	1165/1160	3.6	5.5
37.	terpinene-4-ol	14.87	1174/1170	1.7	1.5
38.	<i>p</i> -cymen-8-ol	15.35	1183/1182	-	0.3
39.	α -terpineol	15.40	1186/1186	3.8	1.1
40.	<i>cis</i> -dihydrocarvone	15.63	1193/1190	-	0.4
41.	myrtenol	15.88	1194/1192	0.2	0.6
42.	<i>trans</i> -dihydrocarvone	16.00	1200/1197	-	t
43.	verbenone	16.10	1204/1202	-	0.3

COMPARATIVE STUDY OF CHEMICAL COMPOSITION OF THE ESSENTIAL OILS ...

N ^o	Compound [§]	RT	KI ^a /KI ^b	<i>S. cuneifolia</i> (%)	<i>S. montana</i> (%)
44.	<i>trans</i> -carveole	16.50	1215/1215	-	0.6
45.	isobornyl formate	16.62	1223/1218	-	0.5
46.	nerol	16.72	1227/1225	2.2	-
47.	hexyl-2-methyl-butanoate	16.92	1233/1230	0.2	-
48.	pulegone	17.00	1235/1230	0.1	-
49.	neral	17.10	1235/1232	1.2	-
50.	carvacrol methyl ether	17.21	1241/1236	-	3.6
51.	geraniol	17.67	1249/1252	1.4	-
52.	geranial	18.13	1264/1264	0.1	-
53.	bornyl acetate	18.52	1287/1284	0.1	0.1
54.	thymol	19.04	1289/1289	-	6.5
55.	carvacrol	19.42	1298/1302	-	1.1
56.	<i>cis</i> -pinocaryol acetat	19.84	1309/1317	-	0.1
57.	myrtenyl acetate	19.84	1324/1324	0.7	-
58.	γ -nonalactone	20.03	1358/1358	0.2	-
59.	neiso-dihydrocarveol acetate	20.20	1358/1358	0.1	-
60.	piperitone oxide	20.46	1366/1366	0.8	-
61.	linalool isobutanoate	21.17	1373/1373	1.6	-
62.	α -copaene	21.39	1374/1373	4.5	0.1
63.	geranyl acetate	21.67	1379/1377	0.5	-
64.	β -bourbonene	21.80	1387/1374	0.8	0.8
65.	β -cubebene	21.87	1387/1387	0.5	-
66.	β -elemene	21.94	1389/1389	0.5	0.2
67.	β -longipinene	22.43	1400/1398	-	0.1
68.	<i>trans</i> -(E)-caryophyllene	22.75	1417/1407	6.1	1.6
69.	β -gurjunene	23.14	1431/1414	-	0.2
70.	χ -elemene	23.32	1434/1424	-	t
71.	aromadendrene	23.44	1439/1433	-	0.1
72.	α -humulene	23.81	1452/1442	0.3	0.1
73.	β -(E)-farnesene	24.02	1454/1448	0.1	-
74.	<i>cis</i> -cadina-1(6),4-diene	24.12	1461/1461	0.2	-
75.	4,5-di-epi-aristolochene	24.21	1471/1469	-	0.1
76.	χ -muurolene	24.53	1478/1466	-	0.1
77.	germacrene D	24.68	1484/1470	5.8	0.7
78.	<i>cis</i> - β -guaiene	24.03	1490/1472	0.3	-
79.	χ -amorphene	25.05	1495/1477	-	t
80.	bicyclogermacrene	25.16	1500/1485	2.9	0.4
81.	α -muurolene	25.27	1500/1490	0.5	t
82.	β -bisabolene	25.39	1505/1500	0.5	0.2
83.	α -bulnesene	25.56	1509/1509	0.2	-
84.	γ -cadinene	25.68	1513/1513	1.4	0.2
85.	β -cubebol	25.77	1514/1514	0.1	-
86.	endo-1-bourbonanol	25.86	1515/1514	-	t
87.	δ -cadinene	25.97	1522/1520	1.1	0.3
88.	<i>cis</i> -sesquisabinene hydrate	26.63	1542/1542	0.8	-
89.	hedycaryol	26.81	1546/1544	0.8	0.7

N ^o	Compound [§]	RT	KI ^a /KI ^b	<i>S. cuneifolia</i> (%)	<i>S. montana</i> (%)
90.	germacrene B	26.98	1559/1556	-	0.4
91.	nerolidol	27.24	1561/1561	5.2	-
92.	1-nor-bourbonanone	27.17	1561/1561	-	t
93.	caryophyllene alcohol	27.30	1570/1565	-	t
94.	germacrene D-4-ol	27.45	1574/1567	-	0.1
95.	spathulenol	27.61	1577/1567	5.0	1.4
96.	caryophyllene oxide	27.69	1582/1571	3.1	4.5
97.	globulol	27.99	1590/1580	1.8	-
98.	viridiflorol	28.31	1592/1581	0.2	5.4
99.	ledol	28.34	1602/1592	-	0.2
100.	β -oplophenone	28.50	1607/1599	-	0.5
101.	humulene epoxide II	28.50	1608/1598	0.6	-
102.	heliofolen-12-ol C	28.64	1619/1617	-	0.7
103.	1- <i>epi</i> -cubenol	29.01	1622/1622	0.3	0.1
104.	γ -desmol	29.12	1630/1630	0.9	-
105.	<i>epi</i> - α -cadinol	29.10	1638/1631	0.3	-
106.	caryophylla-4(12),8(13)-dien-5 α -ol	29.41	1639/1631	1.6	0.8
107.	<i>r</i> -cadinol	29.45	1640/1631	-	t
108.	α -muurolol	29.58	1645/1632	-	t
109.	β -eudesmol	29.64	1649/1640	4.5	t
110.	α -eudesmol	29.74	1652/1643	t	t
111.	α -cadinol	29.80	1653/1645	-	t
112.	14-hydroxy-9- <i>epi</i> -(E)-caryophyllene	29.91	1664/1648	-	0.5
113.	14-hydroxy-(E)-caryophyllene	30.10	1666/1662	t	0.1
114.	α -bisabolol	30.28	1683/1677	0.4	-
115.	germacra-4(15),5,10(14)-trien-1- α -ol	30.65	1684/1678	1.3	0.1
116.	27(14)-bisaboladien-12-ol	30.72	1760/1755	-	t
117.	β -costol	31.65	1765/1765	0.2	-
118.	α -costol	32.80	1773/1773	t	-
	The percent of the total chemical compounds			98.6	98.9
	<p>* § - The minimum acceptable match factor of experimental MS spectra with those from the libraries was specified to be 80 or more. * KI^a = Kovats index, literature data; * KI^b = Kovats index, experimentally determined; * RT = Retention time; * % = Percentage of chemical compounds; * t = Chemical compounds with percentage less of 0.05 %; * - = Chemical compounds which are not detected in the analysed sample.</p>				

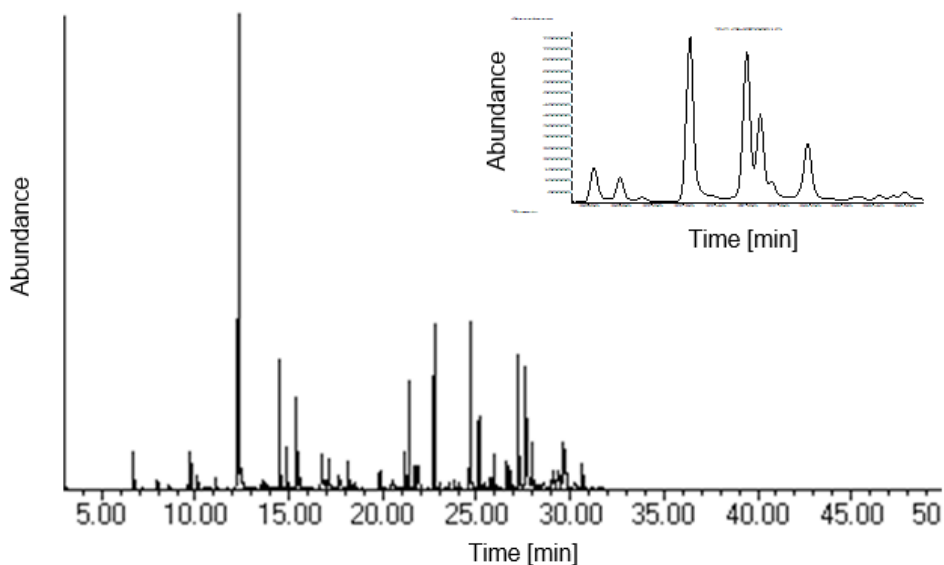


Figure 1. GC/MS chromatogram of *S. cuneifolia* essential oil

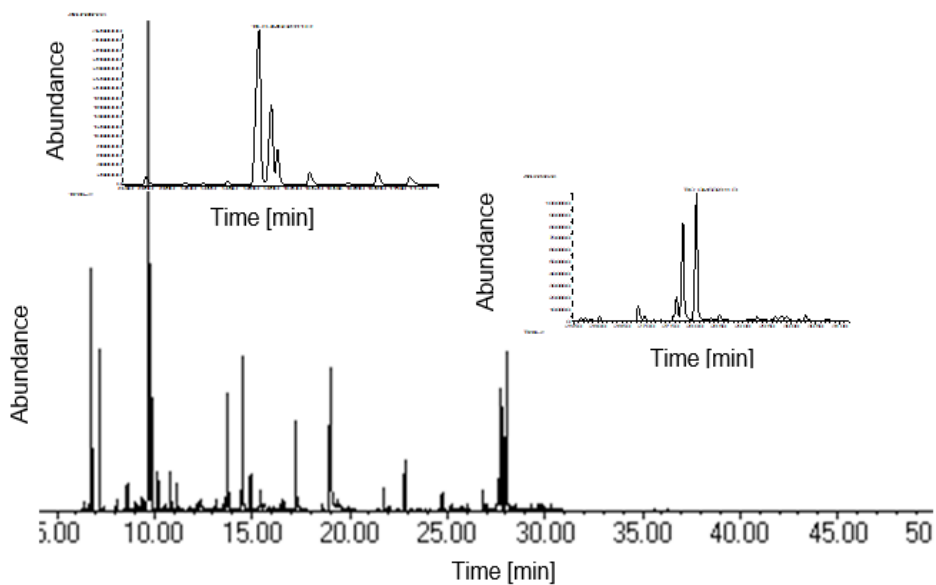


Figure 2. GC/MS chromatogram of *S. montana* essential oil

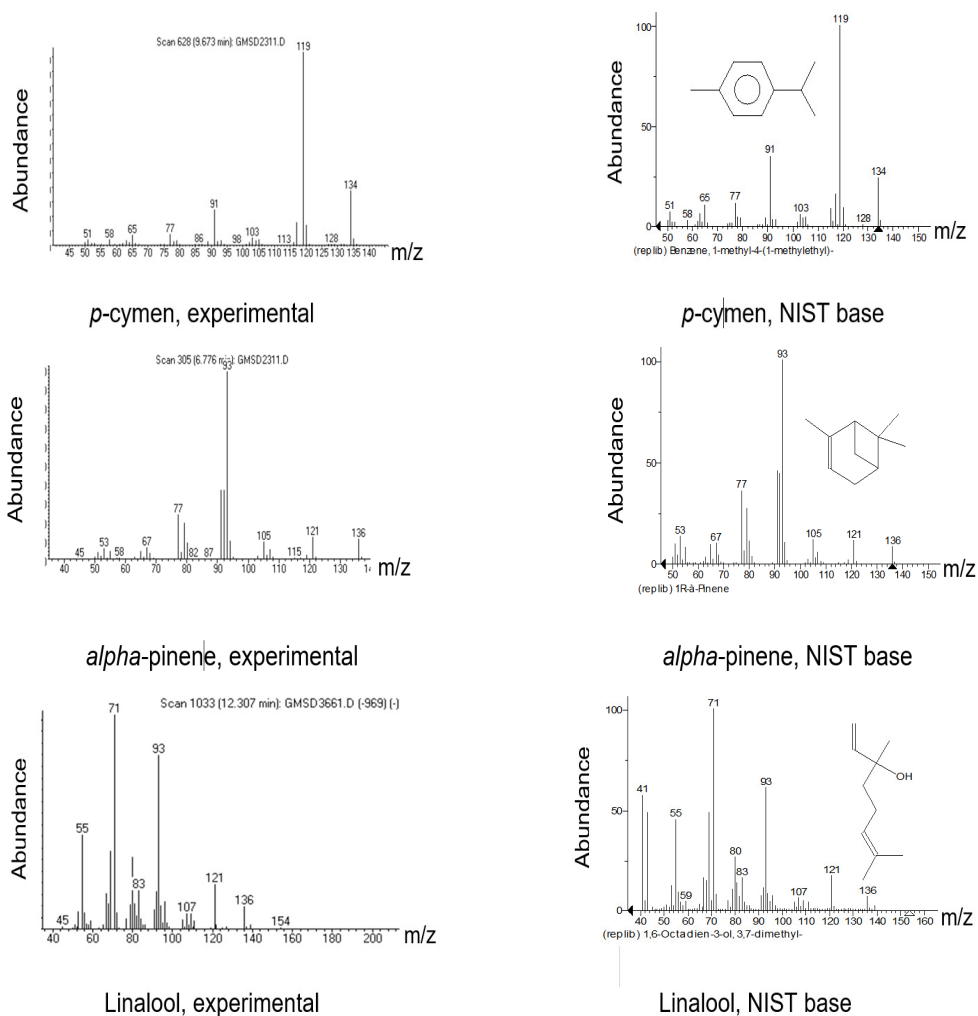


Figure 3. Some of MS spectra of compounds identified in both of analysed essential oils

The performed analysis of *S. cuneifolia* essential oil showed that the oxygenated monoterpenes (41.1%) were the predominant group of compounds, with linalool as the most abundant compound representing 20.3% of the oil. Besides, α -terpineol (3.8%) and borneol (3.6%) were present in relatively high concentrations. Within the sesquiterpene hydrocarbons, constituting 25.7% of the analysed sample, *trans*-(E)-caryophyllene (6.1%), germacrene D (5.8%) and α -copaene (4.2%) were

present in significant quantities. Oxygenated sesquiterpenes (27.1%) were represented mostly by nerolidol (5.2%), spathulenol (5.0%), β -eudesmol (4.5%) and caryophyllene oxide (3.1%). The group of monoterpene hydrocarbons were represented with only 3.8% with limonene (1.1%) and α -pinene (0.7%) as the main constituents.

Conversely, the oil of *S. montana* showed that the group of monoterpene hydrocarbons (46.6%) were the predominant group of compounds. The most abundant compound in the group was *p*-cymene representing 16.6%. Limonene (10.8%) and α -pinene (6.1%) were present in a high percentage, as well. The group of oxygenated monoterpenes constituted 31.6% of the oil. Within this group thymol (6.5%), borneol (5.5%) and camphor (4.5%) were determined to be in significant amounts. Oxygenated sesquiterpenes (15.2%) and hydrocarbon sesquiterpenes (5.5%) were present in a lower percentage in comparison to *S. cuneifolia*. Within the group of oxygenated sesquiterpenes viridiflorol (5.4%), caryophyllene oxide (4.5%) and spathulenol (1.4%) were the main constituents. Furthermore, the most abundant compounds in the group of sesquiterpenes hydrocarbons were *trans*-(E)-caryophyllene (1.6%) and β -bourbonene (0.7%).

The different classes of the chemical compounds identified in the investigated essential oils were presented in Figure 4.

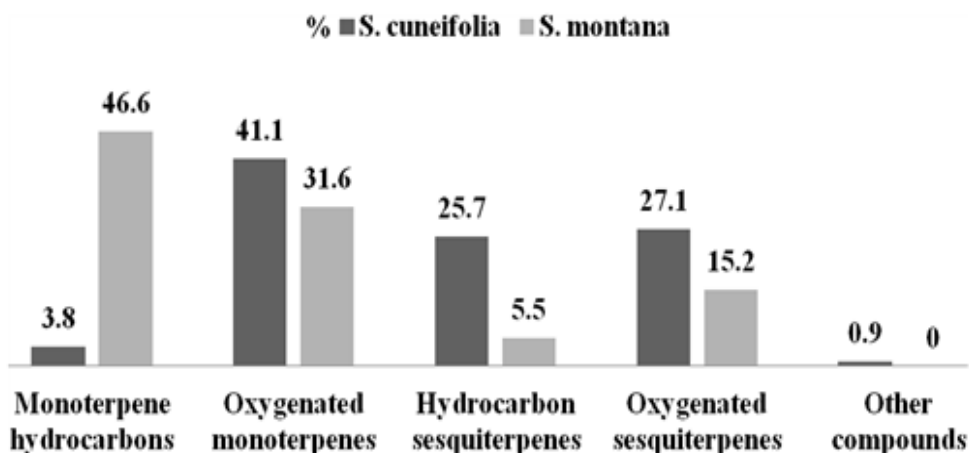


Figure 4. The comparison of the different classes of the chemical compounds of essential oils obtained from two *Satureja* species

The presented data revealed the significant difference in the qualitative and quantitative composition of essential oils obtained from *S. cuneifolia* and *S. montana*. Generally, the presented chemical profiles of the essential oils and comparison to the data presented in available literature might be important in order to evaluate the quality of the investigated plant materials and their possible applications for different therapeutic purposes.

S. cuneifolia essential oil contained linalool (20.3%), *trans*-(E)-caryophyllene (6.1%), germacrene D (5.8%), nerolidol (5.2%) and spathulenol (5.0%) as the main constituents with the concentration greater than five percent. The oil obtained from *S. montana* showed that *p*-cymene (16.6%), limonene (10.8%), thymol (6.5%), α -pinene (6.1%), borneol (5.5%) and viridiflorol (5.4%) were the main constituents (Table 2).

The search of the up to now published papers, revealed quite different chemical profile regarding the investigated essential oils. Namely, according to Bezić *et al.* [4], the main constituent of *S. cuneifolia* essential oil was carvacrol, which representing 17.7% of the oil. In addition, γ -terpinene (14.8%), *p*-cymene (9.8%), linalool (6.6%) and limonene (6.2%) were present in a high percentage. Similar results were obtained for species *S. montana*, the major compounds in the essential oil were carvacrol (13.7%), *p*-cymene (11.8%), γ -terpinene (10.6%), limonene (9.5%) and borneol (5.8%) [4]. The summary of the comparison of the main constituents determined in investigated essential oils to the literature data were presented in Table 2.

Besides Bezić *et al.* [4], Tommasi *et al.* [17] investigated the chemical composition of *S. cuneifolia* essential oil obtained from Mediterranean area, determined linalool (9.6–32.7%), borneol (12.9–24.0%) and α -pinene (9.5–11.7%) to be the main constituents [17]. The essential oil of *S. montana* originating from Albania, according to De Oliveira *et al.* [18] was characterised by a high content of thymol (28.9%), *p*-cymene (12.0%), linalool (11.0%) and carvacrol (10.7%) [18].

Based on recently published data and results presented in this study, it is evident that a significant difference existed in the chemical composition of investigated oils. The chemical composition variability of essential oils among the two *Satureja* species probably could be attributed to ecological conditions, the stages of development, life cycle and/or some genetically influenced factors [4, 18].

Table 2. Comparison of the main constituents (percentage more than 5) in the analysed essential oils of *S. cuneifolia* and *S. montana* to the results available in the recently published papers

N ^o	Compound	Investigated sample <i>S. cuneifolia</i>	Previous studies* <i>S. cuneifolia</i>	Ref.*	Investigated sample <i>S. montana</i>	Previous studies** <i>S. montana</i>	Ref.**
1.	α -pinene	<5%	5.8-20.7%	5, 15	6.1%	<5%	14, 15
2.	<i>p</i> -cymene	<5%	8.7-14.8%	4, 15	16.6%	6.61-12.6%	4, 5, 14
3.	limonene	<5%	6.2-17.4%	4, 5, 15	10.8%	9.5%	4
4.	γ -terpinene	<5%	5.6-14.8%	4, 15	<5%	8.1-13.24%	4, 5
5.	linalool	20.3%	6.6-18.2%	4, 15	<5%	15.38-32.58%	14, 15
6.	borneol	<5%	5.8-12.2%	15	5.5%	5.8-11.5%	4, 15
7.	thymol	-	<5%	4, 15, 16	6.5%	5.4-24.69%	14, 15, 16
8.	carvacrol	-	5.0-17.7%	4, 15, 16	<5%	15.19-63.4%	14, 16
9.	<i>trans</i> -(E)-caryophyllene	6.1%	5.2-9.3%	15	<5%	<5%	14, 15
10.	germacrene D	5.8%	-	4, 5, 15	<5%	<5%	14
11.	nerolidol	5.2%	-	4, 5, 15	-	9.36%	14
12.	spathulenol	5.0%	5.3-13.2%	15, 16	<5%	<5%	14, 15
13.	viridiflorol	<5%	<5%	15	5.4%	-	4, 15
* ** Ref. = Reference;							
*** <5% = Compounds with percentage less than five percent;							
**** - = Data not detected or not available in this research.							

CONCLUSIONS

The presented data revealed the significant difference in the qualitative and quantitative composition of essential oils obtained from *S. cuneifolia* and *S. montana*. Based on applied techniques, more than 100 compounds were identified in both investigated essential oils, which made 98.6-98.9% of the total chemical compounds. The results also showed that investigated essential oils of *Satureja* species have authentic terpenoid composition in comparison to other published studies. Moreover, *Satureja* species from different geographical origins showed different chemical profiles. Hence, chemical composition variability of essential oils among *Satureja* species most probably depended on the genotype of the plant, ecological conditions and the stage of plant ontogenetic development.

EXPERIMENTAL SECTION

Plant material

The plant material was collected at the end of August 2014, at the National park Lovćen, Montenegro (Figure 5). The aerial parts of two *Lamiaceae* species, wild savory (*Satureja cuneifolia* Ten.) and winter savory (*Satureja montana* L.) were air-dried in a shade at room temperature and afterwards stored in paper bags in a cool and dry place. Determination of plant species was performed by Prof. Danijela Stešević and voucher specimens kept at the Department of Biology, Faculty of Natural Science and Mathematics, University of Montenegro.



Figure 5. Map of the samples origins from National park Lovćen (A) is indicated at the map of Montenegro

Isolation procedure

The dried, powdered plant material was subjected to hydrodistillation for 3 hours by using glass Clevenger type apparatus, according to the method described by the European Pharmacopoeia and by the Yugoslav Pharmacopoeia [19, 20]. The obtained essential oils were dried over anhydrous sodium sulfate (Na_2SO_4), filtered and stored in an airtight container in a freeze until gas chromatography analyses.

Chemical analysis of essential oil profiles (GC-FID and GC-MS)

Gas chromatography (GC-FID). Gas chromatography analysis of the essential oils were carried out on an HP-5890 Series II GC apparatus [Hewlett-Packard, Waldbronn (Germany)], equipped with the split–splitless injector and automatic liquid sampler (ALS), attached to HP-5 column (25 m

× 0.32 mm i.d. and 0.52 µm film thickness) and fitted with a flame ionization detector (FID). Carrier gas was H₂ (1 ml/min), with a split ratio of 1:30, injector temperature was 250°C, detector temperature 300°C, while column temperature was linearly programmed from 40 to 260°C with a rate of change of the 4°C/min, and then kept isothermally at 260°C for 10 min. Solutions of essential oil in alcohol (10 mg/ml) were consecutively injected in an amount of 1 µl. Area percent reports, obtained as result of standard processing of chromatograms, were used as a base for the quantification analysis.

Gas chromatography / mass spectrometry (GC-MS). The same analytical conditions as those mentioned for GC-FID were employed for GC/MS analysis, along with column HP-5MS (30 m × 0.25 mm i.d. and 0.25 µm film thickness), using HP G 1800C Series II GCD system [Hewlett-Packard, Palo Alto, CA (USA)]. As the carrier gas used helium. The transfer line was heated to 260°C. The mass spectra were obtained in EI mode, with an ionisation voltage of 70 electron volt (eV); in the range from 40 to 450 m/z. The amount of the injected sample, dissolved in alcohol (10 mg/ml) was 0.2 µl. The components of the essential oil were identified by comparison of their mass spectra to those from Wiley 275 and NIST/NBS (NIST–National Institute of Standards and Technology / NBS-National Bureau of Standards) libraries, using different search engines. Identification of the compounds was achieved by comparing their Kovats' retention indices and mass spectra with those reported in the literature [21] and supplemented by the Automated Mass Spectral Deconvolution and Identification System software (AMDIS ver. 2.1), GC-MS library [22]. The experimental values for Kovats' retention indices were determined by the use of calibrated Automated Mass Spectral Deconvolution and Identification System Software (AMDIS ver. 2.1), GC-MS library [22], and also compared to those from available literature (Adams 2007) [21] and used as additional tool to approve MS findings. The relative proportion of the essential oil constituents were expressed as percentages obtained by peak area normalisation, all the relative response factors were entered as one.

ACKNOWLEDGMENTS

The authors are very grateful to the Ministry of Education, Science and Technological Development of the Republic of Serbia for the financial support of Grant No. III-45107. Authors would like to thank Prof. Danijela Stešević for determination of plant species in this research.

REFERENCES

1. A. M. El-Hagrassi, W. E. Abdallah, A. F. Osman, K. A. Abdelshafeek, *Asian Journal of Pharmaceutical and Clinical Research*, **2018**, 11, 142.
2. A. Namayandeh, N. Mokhtari, M. M. Kamelmanesh, M. T. Bedaf, *Journal of Genetics*, **2017**, 96, e5.
3. F. Jafari, F. Ghavidel, M. M. Zarshenas, *Journal of Acupuncture and Meridian Studies*, **2016**, 9, 118.
4. N. Bezić, I. Samanić, V. Dunkić, V. Besendorfer, J. Puizina, *Molecules*, **2009**, 14, 925.
5. M. Skočibušić, N. Bezić, *Phytotherapy Research*, **2004**, 18, 967.
6. D. Azaz, F. Demirci, F. Satil, M. Kürkçüoğlu, K. Başer, *Zeitschrift für Naturforschung. C, Journal of biosciences*, **2002**, 57, 817.
7. I. Sadeghi, M. Yousefzadi, M. Behmanesh, M. Sharifi, A. Moradi, *Iranian Red Crescent medical journal*, **2013**, 15, 70.
8. K. Yamasaki, M. Nakano, T. Kawahata, H. Mori, T. Otake, N. Ueba, I. Oishi, R. Inami, M. Yamane, M. Nakamura, H. Murata, T. Nakanishi, *Biological and pharmaceutical bulletin*, **1998**, 21, 829.
9. T. Dodoš, J. Aleksić, N. Rajčević, P. D. Marin, *Archives of Biological Sciences*, **2014**, 66, 285.
10. J. Vladić, O. Canli, B. Pavlić, Z. Zeković, S. Vidović, M. Kaplan, *The Journal of Supercritical fluids*, **2017**, 120, 86.
11. Y. Kan, U. S. Uçan, M. Kartal, M. L. Altun, S. Aslan, E. Sayar, T. Ceyhan, *Turkish Journal of Chemistry*, **2006**, 30, 253.
12. F. Oke, B. Aslim, S. Ozturk, S. Altundag, *Food Chemistry*, **2009**, 112, 874.
13. A. Capuzzo, M. E. Maffei, A. Occhipinti, *Molecules*, **2013**, 18, 7194.
14. T. Mihajilov-Krstev, D. Radnović, D. Kitić, V. Stankov-Jovanović, V. Mitić, Z. Stojanović-Radić, B. Zlatković, *Central European journal of biology*, **2014**, 9, 668.
15. M. Milos, A. Radonic, N. Bezic, V. Dunkic, *Flavour and fragrance journal*, **2001**, 16, 157.
16. S. Čavar, M. E. Šolić, M. Maksimović, *Botanica serbica*, **2013**, 37, 159.
17. L. C. Negro, A. Miceli, F. Mazzotta, *The Journal of essential oil research : JEOR*, **2009**, 21, 185.
18. T. L. C. De Oliveira, R. De Araújo Soares, E. M. Ramos, M. Das Graças Cardoso, E. Alves, R. H. Piccoli, *International journal of food microbiology*, **2011**, 144, 546.
19. European Pharmacopoeia 6.0., Vol. 1, Council of Europe, Strasbourg Cedex **2007**.
20. Yugoslavian Pharmacopoeia IV, Pharmacopoea Jugoslavica editio quarta, Ph. Jug. IV, Vol. I. National Institute for Health Protection, Belgrade, **1984**.
21. R. P. Adams, Identification of Essential Oil Components by Gas Chromatography / Mass Spectrometry, 4th Ed., Allured Publishing Corporation: Carol Stream, Illinois, **2007**.
22. Automated Mass Spectral Deconvolution and Identification System software (AMDIS ver. 2.1), National Institute of Standards and Technology (NIST), Standard Reference Data Program, Gaithersburg, MD, **2005**.

PRELIMINARY ASSESSMENT OF MODIFIED KAZAKH NATURAL ZEOLITES AS POSSIBLE SORBENTS FOR MnO_4^- REMOVAL FROM AQUEOUS SOLUTIONS

GULZIYA SEILKHANOVA^a, AKMARAL RAKHYM^a,
ALEXANDRA CSAVDARI^{b,*}

ABSTRACT. A natural zeolite of Kazakh origin, as well as its three different types of chemically modified versions, were assessed from the point of view of permanganate removal yield from aqueous solutions. Modification was carried out by means of di-dodecyl-dimethyl-ammonium bromide surfactant treatment type (1). Types (2) and (3) were treated prior to DDAB with HCl or NaCl, respectively. All sorbents display broad ranges of particle size distribution. Modification of the natural form enhances the specific surface as well as the pore volume, yet influences not in the same way the sorption yield. The process is slow, however, short- and long-term effectiveness are affected by preparation procedures. The most promising yield is exhibited by the natural zeolite that was subject to a combined acid - surfactant treatment.

Keywords: *Kazakh zeolite, chemical surface modification, permanganate adsorption*

INTRODUCTION

Wastewater pollution by heavy metal ions is an important issue for many industrial enterprises. Improperly treated wastewater can reach natural reservoirs, where heavy metals may accumulate as bottom sediments, precipitate as carbonates or sulfates and become hence a secondary pollution source [1,2]. Removal of such pollutants is therefore a necessity.

Within this context, sorption on solid sorbents is nowadays one of the most common ways of wastewater treatment, with results and efficacy depending on physico-chemical features of both adsorbents and adsorbates [2].

^a *Al-Farabi Kazakh National University, Faculty of Chemistry and Chemical Technology, 71 Al-Farabi Ave., KZ-050040, Almaty, Republic of Kazakhstan.*

^b *Babeş-Bolyai University, Faculty of Chemistry and Chemical Engineering, 11 Arany Janos str., RO-400028, Cluj-Napoca, Romania.*

* *Corresponding author: acsavdari@chem.ubbcluj.ro*

Natural silicate materials have several properties that recommend them as sources for sorbents, catalysts, plasticizers, reinforcing additives, etc. [1]. Their main advantages are availability and relatively low price as compared to synthetic materials. One of the most effective type of sorbents are zeolites, hydrated aluminosilicates with cage-like structures (SiO_4 and AlO_4 tetrahedrons [2]), an available surface of up to $100 \text{ m}^2/\text{g}$, and a high cation-exchange capacity. Crystals have a regular system of cavities that are interconnected by channels. Cations and water molecules are positioned in the channels, whereas cations are mobile and may be exchanged. They compensate the excess negative charge of the anionic part of the zeolite's framework. Due to the "channel-cavity" structure, these adsorbents have a well-developed inner surface that might be available for adsorbate molecules. There are around 50 types of natural and more than 150 types of synthetic zeolites used in different applications at the moment [2]. The most common type of natural zeolite is clinoptilolite.

To increase their sorption activity, zeolites may be chemically modified by a variety of different methods, such as: ion-exchange, changing of Si/Al ratio by direct synthesis in different conditions, de-cationization leading to hydrogen enriched zeolites, de-alumination by acid treatment, etc. The simplest way of modifying is by means of ion-exchange [3-6].

The ways of obtaining zeolite based sorbents that are modified by compounds which contain different functional groups, are widely studied recently. These functional groups act as additive active centers on the sorbent's surface. Examples of such modifiers are polymers, surfactants, acids, bases, etc. [7].

The permanent negative surface charge, which occurs as a result of long-lasting isomorphic replacement of Si^{4+} by Al^{3+} in the crystal framework tetrahedrons, permits the use of zeolites for effective adsorption of metal cations (Mn^{2+} , Cr^{2+} , Pb^{2+} , La^{3+}) and cationic dyes. On the other hand, as such, anions adsorb difficultly [2,8,9].

To improve the adsorption capacity of zeolites towards specific hydrophobic adsorbates, amphiphilic sorbents were developed by adsorption of cationic surfactants onto the external surface of zeolites [9]. Hence, the surfactant-modified zeolite becomes a so-called "organo-zeolite". Cationic surfactants are amphiphilic molecules which often contain a positively charged hydrophilic head (normally quaternary ammonium with a counter ion such as Cl^- , Br^- , or SO_3^{2-}) and a relatively long hydrophobic tail (8 to 24 carbon atoms) [10-13]. It has been proved that the longer the hydrophobic chain, the more stable the retention of surfactant on the zeolite's surface.

Above the critical micelle concentration (CMC), the surfactant forms a bilayer / multilayer on the zeolite's surface [3-6]. The amount of retained surfactant depends primarily on its concentration. At low concentrations, the

surfactant cations will attach to the external surface of the zeolite through an ion-exchange mechanism, till the formation of a monolayer is completed. At higher concentrations, the second layer of surfactant may attach to the first one, due to hydrophobic interactions between the alkyl chains. The positively charged groups of the second layer will be oriented towards the bulk of the aqueous solution due to electrostatic repulsive forces of head groups between internal and external layers [1]. The formation of the second layer causes an excessive positive charge (close to the surface of the adsorbent), that further enables the adsorption of anions. Thereby, surfactant-modified zeolites are considered effective towards organic anions, especially to phenol and its by-products [14-16].

The purpose of this work was to assess the possibility of using surfactant-modified organo-zeolites of natural Kazakh source for efficient heavy metal anion removal from water. Permanganate was chosen as model anion, since its concentration in aqueous solutions is easily accessible by means of photometry. Effectiveness in sorption processes of different treatment methods of the natural zeolite was also assessed, *via* a removal yield, and compared to the performance of untreated zeolite. As such, this paper is a preliminary study. If positive conclusions are drawn, the Shankanai zeolite deposit of the Almaty region, in the Republic of Kazakhstan, may develop to a reliable local source for low-cost pollutant sorbents, especially since exceeding of permissible concentrations is reported for the majority of Kazakh water reservoirs [17], for both organic pollutants and some heavy metal ions (either cations or anions).

RESULTS AND DISCUSSION

The employed zeolite comes from the Shankanai deposit, Almaty region, Republic of Kazakhstan. It belongs to the clinoptilolite type, related to the heulandite group. It is characterized by 3-dimensional alumino-silicate frameworks that mainly consist of 4-4-1-1 structural unit layers [16].

Three different types of natural zeolite (NZ) based, yet modified sorbents, were prepared (see detailed description of preparation in the experimental part). Type (1) refers to surface modified NZ by means of di-dodecyl-dimethyl-ammonium bromide (DDAB), a two-chained cationic surfactant. The main feature giving information about the shape and geometry of it, is its packing parameter of 0.620 [2]. Therefore, DDAB is expected to form on the surface of the absorbent flat structures (either lamellae or vesicle), when present in concentrations above the critical micelle concentration (CMC) [18] (1 CMC stands for 0.1 mM). Type (2) and (3) refer to sorbents that were treated

prior to DDAB surface modification, with hydrochloric acid or with sodium chloride, respectively. This kind of treatment was reported [6] to aid a more structured arrangement of surfactant molecules within the first layers on the sorbent's surface.

Sorbent characteristics

Both natural zeolite and modified NZ are fine powders of brownish color. Results of particle size and distribution analysis for all main types of sorbents are presented in Figure 1.

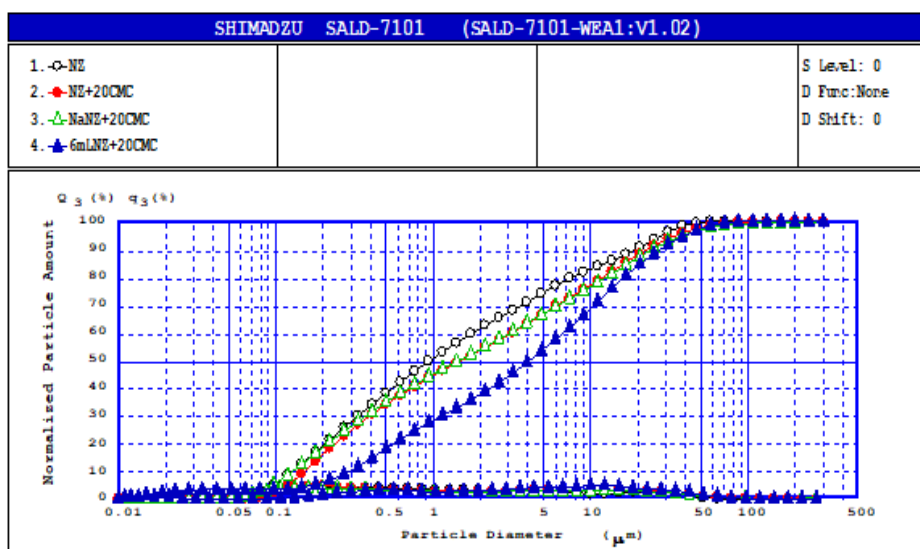


Fig. 1. Distinctive and integrated particle size distribution curves of various sorbents. Black circles – NZ; Red circles – type (1) modified NZ; Blue triangles – type (2) modified NZ; Green triangles – type (3) modified NZ.

Figure 1 shows that particle size varies with an almost uniform distribution in a wide variety of values, over 4 orders of magnitude, from 0.01 to 100 μm . Results are similar, regardless of the treatment to which NZ was subjected to. Such a broad range of particle size distribution is probably due to the manual dispersing of zeolite, without the employment of other grinding methods or granulometric fraction separation.

The values of specific surface and pore volume of both NZ and modified NZ sorbents, calculated according to the BET theory, are presented in table 1. It is obvious that DDAB surfactant treatment - type (1), and moreover, the prior acid to DDAB treatment - type (2), enhance both presented parameters. Type (3) treatment does not bring about an improvement, as compared to type (2).

Type (2) modified NZ shows best results. This is probably due to the enhancement of positive charges and/or ion-exchange on the zeolite's surface, carried out more effectively by the smaller sized H^+ than by the larger Na^+ . The result is a better and more structured coverage by DDAB, thus a favorable charged "head" and "tail" orientation for anion retention from the bulk solution.

However, the type (2) modified NZ prepared at different surfactant concentrations demonstrates that 4 times lower DDAB concentrations bring about a 50% increase of both specific surface and pore volume. This may be due to DDAB forming more dense lamellar layers at higher concentrations, and therefore block (fill in) some pores of the solid.

Table 1. Values of specific surface and pore size for unmodified and modified NZ. (Coding of samples is described in the Experimental section).

Type of sorbent	Specific	
	Surface (m^2/g)	Pore volume (cm^3/g)
<i>Unmodified zeolite</i>		
NZ	4,53	0,002
<i>Modified Zeolite at same CMC of surfactant and different types of treatment</i>		
Type (1): NZ+20CMC-DDAB	8,26	0,004
Type (2): NZ+HCl+20CMC-DDAB	21,49	0,009
Type (3): NZ+NaCl+20CMC-DDAB	7,31	0,003
<i>Modified Zeolite of type (2) with different CMC of surfactant</i>		
Type (2): NZ+HCl+20CMC-DDAB	21,49	0,009
Type (2): NZ+HCl+10CMC-DDAB	29,21	0,013
Type (2): NZ+HCl+5CMC-DDAB	31,49	0,013

Sorption experiments and assessment of sorption performance

These experiments were carried out by using the same volume of aqueous permanganate solution of initial 10 mg/L concentration. Identical amounts of all types of sorbents were added to it, in order to assess their sorption performance.

At predetermined time intervals (3, 24 and 72 hours respectively), the residual concentration **C** of MnO_4^- in the liquid phase (expressed in mg/L) was determined photometrically at 525 nm, by using the Lambert-Beer calibration in equation (1) - where A stands for absorbance.

$$A = 0.005 + 0.078 \mathbf{C} \quad (R^2 = 0.998 / 7 \text{ points}) \quad (1)$$

In order to have correct readings for the absorbance values, a time consuming procedure had to be followed for the separation of solid sorbent particles from the liquid phase. Solid sorbent particles of sizes within the 0.01 - 0.05 μm fraction disperse in aqueous solution, cannot be filtered by usual means. Hence, because of the "cloudiness" of the solution, reproductibility of photometric measurements is affected.

Thus, simple filtration of permanganate solutions containing zeolite powder, in order to determine the residual anion concentration, is not a good option since: (1) permanganate is retained by the filter, hence altering experimental results, and (2) filters with very small pore sizes must be employed, unnecessarily prolonging the filtration time (allowing further contact between the liquid and the solid phase, thus continuous sorption during filtering, and hence producing altered results). Moreover, paper should not be used for filtration, since permanganate gets reduced to Mn(II), probably by oxidizing some of its organic constituents.

Therefore, separation of the liquid phase from the solid during sorption experiments was carried out by successive centrifugation. By using a simple water – NZ mixture, a number of at least 4 to 5 successive stages were necessary to reach the same photometric results (absorbance value at 525 nm) as those of demineralized water. Hence, we standardized the procedure of solid – liquid separation to 7 successive centrifugation steps (see also the Experimental section).

The sorption performance of different sorbents was assessed *via* a yield percentage **E** as defined by equation (2), where $C_0 = 10 \text{ mg/L}$ stands for the initial permanganate concentration. Other performance indicators are also mentioned in the literature, for example the adsorption capacity, expressed as the adsorbed species / adsorbent mass ratio (usually in mg/g) [6]. However, all derive from the value of **C** in equation (1).

$$\mathbf{E} = 100 (C_0 - \mathbf{C})/C_0 \quad (2)$$

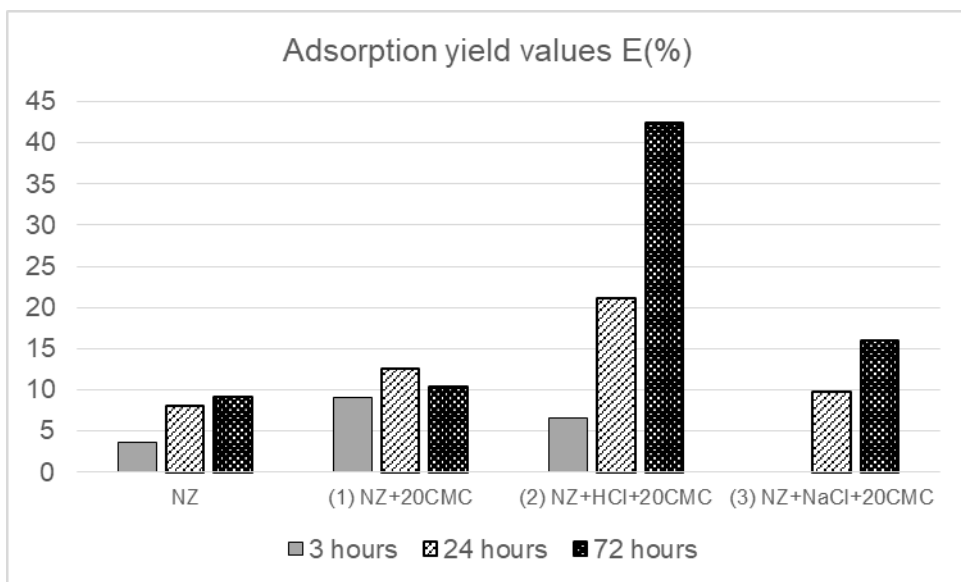


Fig. 2. Values of sorption yield E as a function of NZ modification type and total contact time between solid and liquid phases.

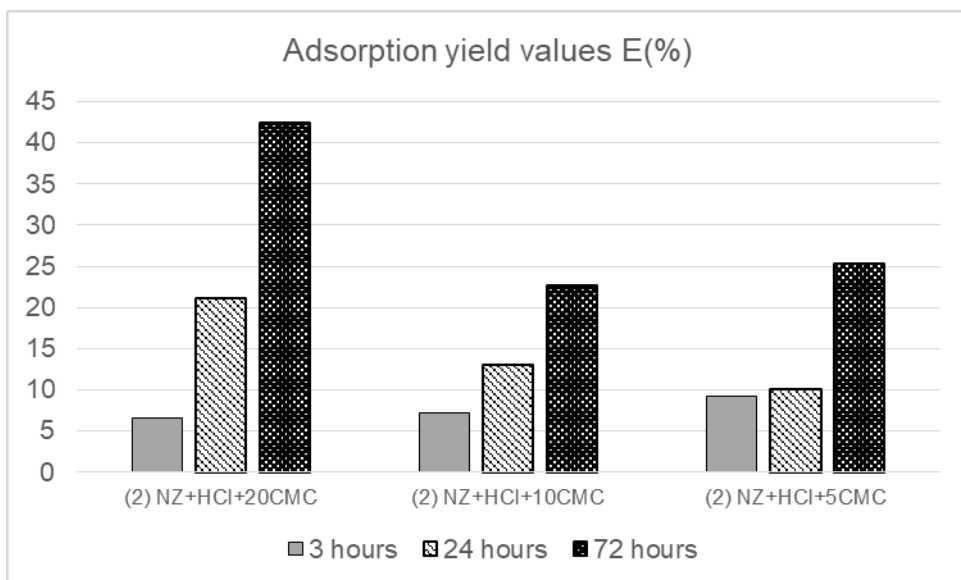


Fig. 3. Values of sorption yield E as a function of DDDBA concentration during chemical modification and total contact time between solid and liquid phases, for type (2) modified NZ.

Figures 2 and 3 present the values of sorption yields **E** for sorbents presented in Table 1, at three different total contact times between solid and liquid phases. Figure 2 compares performances of sorbents obtained by different treatment, whereas Figure 3 only the ones of type (2) having different specific surfaces and pore volumes.

At room temperature the process is quite slow and probably has not reached equilibrium even after 3 days (72 hours). A longer contact time generally brings about a higher yield, even in the case of unmodified NZ. The best adsorption capacity is seemingly proven by type (2) modified NZ, for long-term exposure. On the other hand, type (1) treatment proves to be more effective if a short-term process is targeted (see **E** values at 3 h in Figure 2). Type (3) surface modification is not recommended since it shows some sorption only after 24 or 72 hours, and even so the values of **E** are lower than in other cases. These findings are in agreement with the results in Table 1 (a higher specific surface and pore volume will favor adsorption).

Surprisingly, results in Figure 3 contradict expectations drawn from Table 1, namely that the highest specific surface obtained within the type (2) modified NZs ought to present the best yield. This might be due to the fact that results in Table 1 are based on nitrogen adsorption, a much smaller molecule than the permanganate ion, thus, even though there is a much larger surface available for adsorption processes, this is located mainly in the pores and therefore not accessible for large sized entities such as MnO_4^- .

Figure 3 further demonstrates that short-term performances (**E** values at 3 hours) are comparable, whereas the higher CMC concentration of the DDAB surfactant during preparation generates much better long-term yields (**E** values at 24 and 72 hours). Results at 5 and 10 CMC DDAB concentrations are comparable on the long-term, yet not as good as those for 20 CMC.

Results in Figures 2 and 3 are to be considered as preliminary findings. A more thorough study is necessary to draw pertinent conclusions of economic and technologic value. Experiments need repetition, control of temperature and study of its effect on the sorption performance. Modified NZ sorbents need exhaustive structural and surface characterization as well as the assessment of changes as a result of different preparation techniques. However, these results prove that the Kazakh originated natural zeolite may be developed into a performant pollutant adsorbent for wastewater. Moreover, a path to follow for the enhancement of sorption capacity by chemical modification has been identified.

CONCLUSIONS

Natural zeolite (NZ) of clinoptilolite type originating from the Almaty region of the Republic of Kazakhstan, has been chemically modified. This was carried out by means of di-dodecyl-dimethyl-ammonium bromide (DDAB) surfactant treatment of NZ – type (1). Types (2) and (3) were treated, prior to DDAB, with acid (HCl) or salt (NaCl), respectively.

Both modified and unmodified NZ display a wide range of particle size distribution. Chemical modification enhances the specific surface as well as the pore volume of the sorbent, but does not influence in the same way the sorption yield. The process is slow, yet short- and long-term effectiveness are affected by preparation procedures. However, the most promising results in terms of adsorption capacity, are exhibited by an NZ subjected to a combined HCl - DDAB chemical treatment.

Even though presented results are preliminary, the investigated Kazakh natural zeolite exhibits potential to develop into a well performing sorbent. Moreover, at least one way for the desired enhancement of sorption yield has been described.

EXPERIMENTAL SECTION

Materials and chemicals

The natural zeolite (NZ) used in this work comes from the Shankanai deposit of Almaty region, Republic of Kazakhstan. The employed surfactant was the water-soluble di-dodecyl-dimethyl-ammonium bromide (DDAB). Other reactants were hydrochloric acid, sodium chloride and potassium permanganate. All reactants were of analytical grade and provided by Aldrich Chemistry, Germany. Experiments were carried out with demineralized water.

Preparation of sorbents

Modified zeolite-based sorbents were prepared by different treatments applied to the natural form, as detailed below.

Type (1) sorbent, code: NZ + DDAB.

In this case, surface modification was achieved only by means of the surfactant. DDAB concentrations of 5, 10, and 20 CMC were used, where 1 CMC (critical micelle concentration) stands for 0.1 mM. In order to differentiate

among similar samples, the employed micellar concentration is indicated within the code.

A portion of 10 g of NZ was mixed at room temperature, in a glass conic flask, with 200 ml of DDAB aqueous solution, under continuous stirring at 500 rot/min (F20 Falc magnetic stirrer), for 24 hours. Then, the zeolite was separated by vacuum filtration, rinsed with 100 ml demineralized water, and dried at 60-70 °C in a SNOL 120-300LSN11 oven.

Type (2) sorbent, code: NZ + HCl + DDAB.

In this case, 20 g of NZ were mixed with 250 ml of 6 M HCl solution, for 2 hours and at 100 °C. Then, the solid zeolite was separated from the liquid phase by means of filtration and further rinsed with water until the pH of the rinsing water reached the value 7. The separated solid phase was dried at 70-80 °C for 4 hours. DDAB treatment was further applied as described for the type (1) sorbent.

Type (3) sorbent, code: NZ + NaCl + DDAB.

This sorbent was prepared according to the recipe described for type (2), but instead of hydrochloric acid, a 1 M NaCl solution was used, for 12 hours and at room temperature.

Both NZ and modified NZ were grained manually in a porcelain mortar. The obtained powder was further employed as such in sorption experiments.

Sorbent characterization

The specific surface area and pore volume of sorbents were determined by nitrogen sorption up to its relative pressure of 0.2 atm, at -196 °C, on a Quantachrome NOVA 4200e device.

Particle size and distribution were assessed with the aid of a Shimadzu SALD-7101 powder analyzer.

Sorption experiments

Sorption experiments were carried at approximately 20 °C room temperature, without any means of controlling it. Each experiment was started in the same way, by adding under continuous stirring a portion of 0.5 grams sorbent to a 500 ml potassium permanganate solution of 10 mg/L concentration. The entire volume (in a glass beaker) was continuously stirred at 500 rot/min by means of a F20 Falc magnetic stirrer.

After predetermined periods of time (3, 24 and 72 hours respectively), 10 ml aliquots were extracted from the bulk phase by using a pipette. In order to eliminate the fine dispersed solid particles from the solution with the aim of reproducible spectrophotometric measurements, the aliquots were centrifuged 7 times successively in glass tubes. Each centrifugation stage was carried out for 10 min at 3500 rot/min, by using a NAHITA 2610 centrifuge. After each such stage, the supernatant was collected and subjected to the next centrifugation step. The supernatant of the last stage was used to determine the unabsorbed permanganate concentration, at 525 nm, by means of double-beam 530 ABL&E-JASCO UV/VIS spectrophotometer. Quartz cuvettes of 1 cm optical path length were used. The reference cuvette contained demineralized water.

ACKNOWLEDGEMENTS

The authors gratefully acknowledge to (1) Dr. Liliana Bizo from the Babeş-Bolyai University of Cluj-Napoca for her kind help with the particle size and distribution analysis and (2) Al-Farabi Kazakh National University, Almaty, Republic of Kazakhstan, for the Internship of Akmaral Rakhym.

REFERENCES

1. G.A. Seilkhanova, A.N. Imangalieva, D.N. Akbayeva, Zh. Zh. Kenzhalina, *Studia UBB Chemia*, **2017**, 52(1), 35.
2. M.N.V. Prasad, K. Shih (Eds.), "Environmental Materials and Waste", Academic Press, Elsevier, Amsterdam, **2016**; N.S. Dionisiou, T. Matsi, "Chapter 23 - Natural and Surfactant-Modified Zeolite for the Removal of Pollutants (Mainly Inorganic) From Natural Waters and Wastewaters".
3. I.A. Bazbaz, R.I. Yousef, S.M. Musleh, *Asian Journal of Chemistry*, **2011**, 23(6), 2553.
4. Z. Li, R.S. Bowman, *Environmental Science & Technology*, **1997**, 31, 2407.
5. Z. Li, I. Anghel, R.S. Bowman, *Journal of Dispersion Science and Technology*, **1998**, 19, 843.
6. M. Ghiaci, A. Abbaspur, R. Kia, F. Seyedeyn-Azad, *Separation and Purification Technology*, **2007**, 40, 217.
7. Q. Xie, J. Xie, Z. Wang, D. Wu, Z. Zhang, H. Kong, *Microporous and Mesoporous Materials*, **2013**, 179, 144.
8. M.J. Zamzow, B.R. Eichbaum, K.R., Sandgren, D.E. Shanks, *Separation and Purification Technology*, **1990**, 25(13–15), 1555.
9. G.M. Haggerty, R.S. Bowman, *Separation and Purification Technology*, **1994**, 28(3), 452.

10. M.B. Park, S.H. Ahn, C.P. Nicholas, C.J. Lewis, S.B. Hong, *Microporous and Mesoporous Materials*, **2017**, 240, 159.
11. D. Krajišnik, A. Daković, M. Milojević, A. Malenović, M. Kragović, D.B. Bogdanović, V. Dondur, J. Milić, *Colloids and Surfaces B: Biointerfaces*, **2011**, 83(1), 165.
12. C. Serri, B. de Gennaro, L. Catalanotti, P. Cappelletti, A. Langella, M. Mercurio, L. Mayol, M. Biondi, *Microporous and Mesoporous Materials*, **2016**, 224, 143.
13. H.-P. Chao, S.-H. Chen, *Chemical Engineering Journal*, **2012**, 193, 283.
14. Q. Xie, J. Xie, L.N. Chi, K. Jie Li, D.Y. Wu, Z.J. Zhang, H.N. Kong, *China Technological Sciences*, **2013**, 56(7), 1749.
15. Y. Dong, D. Wu, X. Chen, Y. Lin, *Journal of Colloid and Interface Science*, **2010**, 348, 585.
16. C. Diaz-Nava, M.T. Olguin, M. Solache-Rios, M.T. Alarcon-Herrera, Aguilar-Elguezabal, *Journal of Hazardous Materials*, **2009**, 167, 1063.
17. RSE “Kazhydromet” Department of ecology monitoring, Ministry of Energy, Republic of Kazakhstan, “Informational bulletin of Kazakhstan environment state for 2016”, Almaty, **2016**, 421. (in Russian)
18. L.R. Griffin, K.L. Browning, C.L. Truscott, L.A. Clifton, J. Webster, S.M. Clarke, *Journal of Colloid and Interface Science*, **2016**, 478, 365.